



**HAL**  
open science

# Andreev transport in quantum dots and Josephson effect in spin-orbit coupled thin films

Alexandre Assouline

► **To cite this version:**

Alexandre Assouline. Andreev transport in quantum dots and Josephson effect in spin-orbit coupled thin films. Materials Science [cond-mat.mtrl-sci]. Sorbonne Université, 2018. English. NNT : 2018SORUS225 . tel-02483145v1

**HAL Id: tel-02483145**

**<https://theses.hal.science/tel-02483145v1>**

Submitted on 18 Feb 2020 (v1), last revised 18 Feb 2020 (v2)

**HAL** is a multi-disciplinary open access archive for the deposit and dissemination of scientific research documents, whether they are published or not. The documents may come from teaching and research institutions in France or abroad, or from public or private research centers.

L'archive ouverte pluridisciplinaire **HAL**, est destinée au dépôt et à la diffusion de documents scientifiques de niveau recherche, publiés ou non, émanant des établissements d'enseignement et de recherche français ou étrangers, des laboratoires publics ou privés.

**THÈSE DE DOCTORAT  
DE L'UNIVERSITÉ PIERRE ET MARIE CURIE**

**Spécialité : Physique**

**École doctorale n°564: Physique en Île-de-France**

réalisée

**au Laboratoire de Physique et Étude des Matériaux**

sous la direction de Hervé Aubin

présentée par

**Alexandre Assouline**

pour obtenir le grade de :

**DOCTEUR DE L'UNIVERSITÉ PIERRE ET MARIE CURIE**

Sujet de la thèse :

**Transport d'Andreev dans des boîtes quantiques et  
effet Josephson dans des couches minces à fort  
couplage spin-orbite**

**soutenue le 9 octobre 2018**

devant le jury composé de :

M. Abhay Shukla	Président du jury
M. Hervé Courtois	Rapporteur
M. Francesco Giazotto	Rapporteur
M <sup>me</sup> . Adeline Crépieux	Examinatrice
M. Marco Aprili	Invité
M. Hervé Aubin	Directeur de thèse



# Remerciements

Avant tout, je tiens à remercier dans ces quelques lignes toutes les personnes qui m'ont aidé et soutenu pendant ces trois années de doctorat.

Hervé, merci pour tout ce que tu m'as appris, pour avoir toujours donné des réponses à mes questions. Pour les connaissances et les outils scientifiques que tu partages et qui font gagner beaucoup de temps aux personnes qui t'entourent. Merci de parler de sciences avec tant de convictions et d'optimisme.

Merci aux permanents du LPEM. Cheryl, pour ton soutien pendant ces trois ans, pour m'avoir confié la diluette et pour m'avoir encouragé à candidater au prix Langlois. Alexandre, pour ton accueil à mon arrivée dans le groupe et pour être venu me soutenir au march meeting 2018. Benoit, pour tes invitations aux séminaires et workshops et pour avoir souvent pris des nouvelles sur l'avancement de ma thèse. Nicolas et Brigitte, pour votre bienveillance et vos connaissances sur les jonctions supra.

Merci aux thésards et post-docs avec qui j'ai passé de bons moments, Lucile, Rémi, Mathilde, Hung-Ju, Hengyang, Zhelu, Willem, Alexis, Paul, François, Alexandre, Mathieu et Clément. Tianzhen, thank you for going through these three years of PhD together and for the excellent tea of Wuyi mountain.

Marco, merci pour ton accueil chaleureux au LPS, pour m'avoir orienté pendant mon séjour, pour cette manip réussie et pour ton enthousiasme scientifique. Charis, Marko, Mathieu et Julien, je vous remercie pour votre sympathie et votre aide à la microsoudure tri-dimensionnelle du LPS.

Merci au professeur Hugues Pothier, pour son cours sur la supra mésoscopique et pour avoir accepté, sans hésitation, de discuter de mes résultats expérimentaux.

Merci Paola et Mahmoud, pour avoir été à l'écoute, pour les nombreux échantillons fournis et leurs caractérisations. Merci Emmanuel, pour cette première manip de transport dans une nano-plaquette colloïdale.

Je remercie aussi mes proches. Maman, Papa, merci d'avoir tout fait pour que notre famille ne manque de rien et pour m'avoir toujours encouragé pendant ces années d'études. Mikaël, pour ta confiance et nos discussions sur les maths, la physique et le reste. Tania, pour m'avoir toujours aidé quand j'en avais besoin et pour m'avoir rappelé ma citoyenneté pendant ces trois ans. Noah et Clara pour être aussi merveilleux. Xavier, pour les billets de stade et ta bonne humeur.

Merci à ma grande famille en France, au Maroc, en Israël et en Espagne pour être aussi unis et solidaires. En particulier, merci à ma génération de cousins avec qui j'ai partagé tant de moments inoubliables, Nathan, Dan, Ivan, Boris, Hanna, Deborah, Tristan, Jon, Lander, Marty et Sara ! Merci à mes grands-parents qui me manquent et qui ont réussi à unir cette famille, Papi Abner, Mami Gracia, l'Abuela Maria Teresa et l'Abuelo Manuel.

Merci à mes amis pour tout ces fous rires, ces souvenirs et les moments de détente qu'on continue de partager, Arthur, Théo, Michel, Léo, Bastian, Raffik, Nicolas, Florian, Tristan, Vincent, Bartek et Antonin.

Merci Adèle de me rendre heureux, pour ton soutien pendant ces trois ans et pour tous ces moments magiques passés ensemble.

# Table des matières

<b>Introduction</b>	<b>v</b>
<b>I Spin-orbit coupling and superconductivity in hybrid structures</b>	<b>1</b>
I.1 Spin-orbit coupled conductors . . . . .	1
I.1.1 Normal conductors . . . . .	1
I.1.2 Spin-orbit coupling . . . . .	4
I.2 Superconductors . . . . .	9
I.2.1 Ginzburg-Landau description . . . . .	9
I.2.2 Elementary excitations . . . . .	12
I.3 Hybrid devices . . . . .	14
I.3.1 Andreev reflections . . . . .	14
I.3.2 Andreev bound states . . . . .	17
I.3.3 Josephson current phase relations . . . . .	19
I.3.4 Anomalous Josephson effect . . . . .	25
<b>II Sample fabrication</b>	<b>31</b>
II.1 Electron beam lithography . . . . .	31
II.1.1 Coating . . . . .	31
II.1.2 Exposure . . . . .	31
II.1.3 Development . . . . .	32
II.1.4 Surface cleaning and metal deposition . . . . .	33
II.1.5 Lift-off . . . . .	34
II.1.6 Correction of the proximity effect . . . . .	34
II.2 Connections to the devices . . . . .	35
II.3 InAs Nanowire devices . . . . .	35
II.3.1 Growth and Crystal structure . . . . .	35
II.3.2 Fabrication . . . . .	38
II.4 Bi <sub>2</sub> Se <sub>3</sub> thin film devices . . . . .	41
II.4.1 Growth and Crystal structure . . . . .	41
II.4.2 Fabrication . . . . .	42
II.5 Measurement stations . . . . .	46
II.5.1 Glove box . . . . .	46
II.5.2 Dilution fridge . . . . .	47

<b>III Andreev Quantum Dot in doped InAs nanowire</b>	<b>49</b>
III.1 Coulomb blockade transport . . . . .	50
III.1.1 Single electron transistors . . . . .	50
III.1.2 Excited state spectroscopy . . . . .	55
III.2 Random matrix theory . . . . .	57
III.3 Mobility edge . . . . .	61
III.4 Superconducting correlations . . . . .	62
III.4.1 Ground state transitions . . . . .	63
III.4.2 Shiba states across the mobility edge . . . . .	65
III.5 State of the art . . . . .	67
III.5.1 Conclusion . . . . .	71
<b>IV Anomalous Josephson effect in Bi<sub>2</sub>Se<sub>3</sub></b>	<b>75</b>
IV.1 State of the art . . . . .	75
IV.2 Thin films characterization . . . . .	79
IV.2.1 Carrier density modulation with an electrolyte gate . . . . .	82
IV.3 Josephson effect in Bi <sub>2</sub> Se <sub>3</sub> . . . . .	83
IV.3.1 Supercurrent interferences . . . . .	84
IV.3.2 Shapiro steps . . . . .	88
IV.3.3 RSJ model . . . . .	89
IV.3.4 Current phase relation . . . . .	91
IV.4 Josephson effect with in-plane magnetic field . . . . .	93
IV.4.1 Anomalous Fraunhofer pattern . . . . .	94
IV.4.2 Simulation of an anomalous pattern . . . . .	97
IV.4.3 Detection of the anomalous Josephson effect . . . . .	100
IV.5 Current injection across a Bi <sub>2</sub> Se <sub>3</sub> Josephson junction . . . . .	105
IV.5.1 Current induced spin polarization . . . . .	105
IV.5.2 Effect of heating . . . . .	107
IV.6 Anomalous Shapiro steps . . . . .	107
IV.7 Conclusion and perspectives . . . . .	108
<b>Conclusion</b>	<b>111</b>
<b>A - Josephson <math>\varphi_0</math> interferometer</b>	<b>113</b>
<b>Publications</b>	<b>115</b>
<b>Bibliographie</b>	<b>116</b>

# Introduction

Josephson junctions are widely used in superconducting electronics as sensors[1, 2] and quantum units of information[3, 4]. They are based on superconducting tunneling across an insulating barrier which separates two superconductors, a quantum phenomena discovered in the seventies[5, 6, 7, 8]. This tunneling drives a (super)current free from dissipation across the barrier and a phase difference between the superconductors. The relation between the supercurrent and the phase is at the heart of all devices relying on the Josephson effect. In this thesis, we study experimentally Josephson junctions where the insulating barrier is replaced by a semiconducting material. On the one hand, such hybrid devices attract interest in the development of SQUID magnetometers capable of detecting the magnetization of single molecules[9]. In that context, the use of a semiconductor quantum dot as a barrier material is promising as the device operation depends on the microscopic configuration of the quantum dot. On the other hand, hybrid semiconductor-superconductor devices have received tremendous attention as possible candidates to host non-abelian excitations which allow for quantum information processing[10]. Once a practical physical system is found to realize and manipulate such excitations, quantum computing in this system should not suffer from coupling to the external environment.

Using a conductor as the weak link between two superconductors allows new research directions, distinct from what is done with Josephson tunnel junctions made with insulating barriers. This includes the realization of supercurrent transistors as the carrier density in a semiconductor can be modulated by a field effect[11], the design of Josephson arrays allowing the investigation of the superconductor-insulator transition[12, 13]. Also, as the supercurrent does not rely on tunneling, it can flow on large distances such that multi-terminal Josephson junctions[14, 15], where multiple superconductors are connected through the same weak link, can be fabricated.

Recently, this field has led to advances in material science which have made possible to grow both the semiconductor and the superconductor in ultra high vacuum chamber realizing an epitaxial contact between the two, in situ[16, 17]. This approach overcomes difficulties, encountered by researchers, of making good and reproducible electrical contacts between the two materials. It will be of great interest for future developments in the field.

During these three years we fabricated and studied, through electronic transport measurements, hybrid devices based on InAs nanowires and Bi<sub>2</sub>Se<sub>3</sub> thin films coupled

with superconducting aluminum electrodes.

In contrast with previous studies, the InAs nanowires provided by the Nanosciences and Nanotechnologies Center (C2N) have small diameter of 20 nm and are conducting at low temperature because they are doped during growth with Si atoms. This allowed us to observe the proximity effect of the superconductor across a metal insulator transition induced by an electrical field effect. We were not able to measure the Josephson supercurrent in these devices. However, owing to the large disorder induced by the dopants, we observed in the same device, different coupling regimes between the semiconductor and the superconductor, including an intermediate coupling regime where a quantum dot is formed between the electrodes and can be used to control the supercurrent.

We also fabricated Josephson junctions and Superconducting Quantum Interference Devices (SQUID) with  $\text{Bi}_2\text{Se}_3$  thin films. These films are grown by molecular beam epitaxy at the Nanosciences Institute of Paris (INSP) and capped, in the growth chamber, by a protecting Se layer which avoids exposition of the film surface to air. We elaborated a fabrication process where the protecting layer is removed just before the aluminum deposition, which gives very reproducible results in the device resistances and the magnitude of the supercurrent measured at low temperature. This allowed us to study the Josephson effect in great detail in this material and obtain experimental evidence of an effect predicted in 2008[18]. It concerns the coupling between the Josephson current and a spin polarization induced by a magnetic field, through the spin-orbit interaction of the semiconductor. This effect produces an "anomalous" current in the absence of a phase difference between the two superconductors forming the junction. We find and demonstrate experimentally that this anomalous Josephson effect modifies the operating frequency of the SQUID where two Josephson junctions are fabricated in parallel on the semiconducting film.

In the first chapter, we present the theory describing the spin-orbit interaction in semiconductor as well as the coupling between superconductors and diverse non superconducting materials. In the second, we detail the lithography techniques used to fabricate the devices and describe the crystalline structures of InAs and  $\text{Bi}_2\text{Se}_3$ . The last two chapters are dedicated to the description of the experiments carried on the nanowires and on the thin films, respectively. We conclude with some perspectives.

# I – Spin-orbit coupling and superconductivity in hybrid structures

In this chapter, we describe hybrid devices composed of superconductors coupled to normal conductors in the presence of spin-orbit interaction.

We will first describe a normal conductor and the role played by quantum confinement in nanostructures. Then, we will introduce the spin-orbit interaction which couples the electron motion to its spin. This coupling attracts interest as an essential ingredient for the discovery of new phases of matter. It plays an important role in hybrid devices where a normal conductor is coupled with a superconductor.

The superconductor will be described in two parts. First, its superconducting condensate will be characterized by the Ginzburg-Landau theory, which describes the behaviour of a superconductor in a magnetic field. Then, the elementary excitations of the superconductor will be described by the microscopic BCS theory. The description of these excitations is essential to understand the properties of hybrid structures made of superconductors (S) and normal conductors (N).

Finally, we will describe such hybrid structures. First, the Andreev reflection process which allows charges to be transferred across a SN interface. Secondly, the case of SNS interfaces where Andreev bound states form in the N region. These states carry the Josephson current in SNS devices. Prior to the description of the results obtained in this thesis, we will describe theoretical works which predict a direct relation between the spin-orbit interaction in the semiconducting material and the Josephson effect in a SNS junction.

## I.1 Spin-orbit coupled conductors

### I.1.1 Normal conductors

As a result of Landau theory of Fermi liquids, a metal can be described as a gas of non-interacting quasi-particles. Thus, the total energy of this gas is the sum of the single particle energies. A quasi-particle is described by a wave function  $\psi_k$  solution of Schrödinger equation :

$$H\psi_k = \epsilon_k\psi_k$$

where  $H$  is the single particle Hamiltonian and reduces to the kinetic operator  $H = \frac{\mathbf{p}^2}{2m} = \frac{(-i\hbar\nabla)^2}{2m}$  when no potential is present,  $m$  is the electron mass. In that case, the electron wave function is a plane wave of the form  $\psi_k \propto e^{i\vec{k}\vec{r}}$  and its energy is solely determined by its wave vector  $\vec{k}$  in the absence of spin dependent interaction :

$$\epsilon_k = \frac{\hbar^2\vec{k}^2}{2m}$$

In virtue of Pauli exclusion principle, only two electrons can have the same wave vector provided that their spins are opposite. Therefore, by adding electrons to a three dimensional system, one builds a sphere in reciprocal space composed of all electron wave vectors  $\vec{k}$ . The last electron added to the system has an energy defined as the Fermi energy  $E_F = \frac{\hbar^2 k_F^2}{2m}$  where  $\vec{k}_F$  is the wave vector of the last electron added to the system.

If an electron is confined in a finite size region, boundary conditions are imposed on its electronic wave function and results in forbidden values for its wave vector  $\vec{k}$ . For a system of dimensions  $L_x$ ,  $L_y$  and  $L_z$  in the three spatial directions, the allowed wave vector components are :

$$k_{x,y,z} = \frac{2\pi}{L_{x,y,z}}n_{x,y,z}$$

where  $n$  is an integer. Therefore, the volume in reciprocal space of two spin degenerate electron states is  $V_s = \frac{(2\pi)^3}{L_x L_y L_z}$  and the number of states in the Fermi sphere is  $N = 2\frac{V_F}{V_s}$  where  $V_F = \frac{4}{3}\pi k_F^3$  is the volume of the Fermi sphere. Thereby, the Fermi wave vector is linked with the electronic density  $n = \frac{N}{L_x L_y L_z}$  by the relation :

$$k_F = (3\pi^2 n)^{1/3}$$

The density of states in three dimensions is obtained from  $\rho(E) = \frac{1}{V} \frac{dN}{dE}$  and reads :

$$\rho_{3D}(E) = \frac{\sqrt{2m^3 E}}{\pi^2 \hbar^3}$$

In a metal such as aluminum, the Fermi energy is so large  $E_F > 10$  eV that the density of states and the carrier density are highly stable with respect to perturbations, such as the presence of impurities, strain and so on. This is not the case in doped semiconductors  $E_F \approx 100$  meV where the carrier density is widely tunable with gate voltages and electronic level distribution can be modulated by quantum confinement.

If the size of the system in a given direction, say  $z$ , is such that  $E(k_x = 0, k_y = 0, k_z = \frac{2\pi}{L_z}) > E_F$  the electron momentum is restricted in a plane and the system can be considered as two-dimensional. Such systems are realized for example at the conducting AlGaAs/GaAs interface and in graphene. However, the dispersion relation

$\epsilon_k$  is different for these two systems. For the AlGaAs/GaAs interface it is parabolic as given above, while for graphene it is linear in momentum :

$$\epsilon_k = \hbar v_F |k|$$

where  $v_F$  is the Fermi velocity. This gives two distinct relations for the density of states :

$$\text{parabolic : } \rho_{2D}(E) = \frac{m}{\pi \hbar^2} \mathcal{H}(E - E_c) \quad \text{linear : } \rho_{2D}(E) = \frac{2E}{\pi \hbar^2 v_F^2}$$

where  $\mathcal{H}$  is the Heaviside step function and  $E_c$  is the energy of the bottom of the conduction band. The density of states corresponding to these two different dispersion relations is shown in Fig. I.1. In the next section, we will discuss three dimensional topological insulators. Theoretically, these materials are expected to have, at their surfaces, a linear dispersion relation like graphene, and an insulating bulk. Nevertheless, unavoidable defects present in real materials often lead to a residual conduction of the bulk. These bulk electrons are characterized by a parabolic dispersion. Therefore, two kinds of electronic states coexist and electronic transport in the system depends on the position of the Fermi energy. If the Fermi energy is below the bottom of the conducting band, states with a linear dispersion are dominating electronic transport, while if the Fermi energy is within the conduction band, bulk states with a parabolic dispersion will dominate electronic transport.

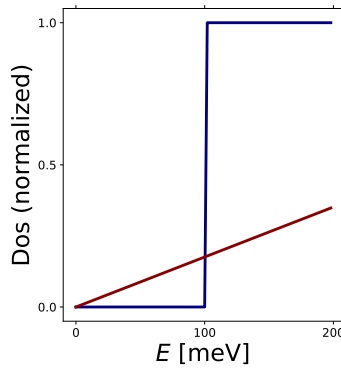


Fig. I.1 *Density of states in two dimensions. In blue for a parabolic and in red for a linear dispersion relation.*

In a quantum wire where the electron momentum is restricted to one dimension, the Fermi liquid theory does not apply, instead, the system should be rather described by the theory of Luttinger liquid, which is beyond the scope of this thesis. In a quantum dot the electron is confined in the three spatial directions. Therefore, spin-orbit coupling, the interaction between the electron spin and its momentum, is not so relevant to understand transport phenomena in a quantum dot as it is in higher dimensional systems.

### 1.1.2 Spin-orbit coupling

As spin-orbit coupling is understood as the coupling between the electron spin and an effective magnetic field, we start by the usual description of a spin in a magnetic field.

Each electron possesses a magnetic dipole moment  $\mu$  due to the electronic spin. The spin operator is defined as :

$$\mathbf{S} = \frac{1}{2}\sigma$$

where the components of  $\sigma = \sigma_x\mathbf{x} + \sigma_y\mathbf{y} + \sigma_z\mathbf{z}$  are the Pauli matrices :

$$\sigma_x = \begin{pmatrix} 0 & 1 \\ 1 & 0 \end{pmatrix} \quad \sigma_y = \begin{pmatrix} 0 & -i \\ i & 0 \end{pmatrix} \quad \sigma_z = \begin{pmatrix} 1 & 0 \\ 0 & -1 \end{pmatrix}$$

The electron magnetic moment is related to its spin by the relation :

$$\mu = -g\mu_B\mathbf{S}$$

where  $\mu_B = 57.88 \mu\text{eV}\cdot\text{T}^{-1}$  is the Bohr magneton and  $g \approx 2$  is the Landé g-factor for an electron in vacuum. The effective g-factor value can significantly change for an electron in a crystal [19, 20].

Applying a magnetic field leads to a precession of the magnetic moment which is described by the Zeeman Hamiltonian  $H_z = -\mu\mathbf{B} = \frac{1}{2}g\mu_B\sigma\mathbf{B}$ . Its eigenstates are two-component spinors  $|\chi\rangle = \begin{pmatrix} \chi_0 \\ \chi_1 \end{pmatrix}$  describing spin wave functions. Two eigenvalues  $\pm E_z$  are found for a static magnetic field  $\mathbf{B}$ , where  $E_z$  is the Zeeman energy :

$$E_z = \frac{1}{2}g\mu_B B$$

In spin-orbit coupled system, an effective magnetic field emerges due to the motion of a charged particle in an electric field. In an atom, an electric field  $\vec{E}_n$  is caused by the nuclei. In the inertial frame where the electron is at rest, this electric field generates a magnetic field which couples to the electron spin. This is a relativistic effect that comes from the transformation of the fields between two frames moving at relative velocity  $\vec{v}$ . The spin-orbit interaction in an atom is derived from the Dirac equation, in the non relativistic limit [21] :

$$H_{\text{SO}} = -\frac{g\mu_B}{2c^2}(\vec{v} \times \vec{E}_n)\vec{S}$$

where  $c$  is the speed of light and  $\vec{v}$  is the electron velocity. As  $\vec{E}_n$  is the electric field generated by the electrostatic potential of the charged nucleus, the spin-orbit interaction is larger for heavier elements with high  $Z$  number.

In solid state physics, spin-orbit interaction is important to calculate the correct band structure of crystals. If the crystal is invariant under time and spatial reversal (or

parity) symmetries, all energy bands are doubly degenerate in energy. Indeed, spatial inversion symmetry insures that the energy is the same when going in two opposite directions :

$$\text{Parity symmetry : } E_{\downarrow}(\vec{k}) = E_{\downarrow}(-\vec{k})$$

Furthermore, in the presence of time reversal symmetry, Kramers theorem insures degeneracy of time-reversed states, i.e two states with both opposite momentum and spin have the same energy :

$$\text{Time reversal symmetry : } E_{\uparrow}(\vec{k}) = E_{\downarrow}(-\vec{k})$$

Together, these two symmetries protect the spin degeneracy of all energy bands :

$$\text{Parity and time reversal symmetry : } E_{\downarrow}(\vec{k}) = E_{\uparrow}(\vec{k})$$

Nevertheless, spin degenerate energy bands do not imply the absence of spin-orbit related phenomena, as we will see for three dimensional topological insulators.

Spin degeneracy for a given momentum can be lifted if spatial inversion symmetry is broken by bulk inversion asymmetry (BIA) or structural inversion asymmetry (SIA). BIA is present in non centrosymmetric material, where no inversion center leaving the crystal lattice invariant can be found. This leads to the Dresselhaus spin-orbit coupling term in the Hamiltonian.

SIA is found at the surface of all materials due to the broken symmetry at the interface with the vacuum or another material. It can also be induced when two surfaces of a solid are submitted to a potential difference. SIA leads to an electric field  $\vec{E}$  which points in the direction perpendicular to the interface and the resulting spin-orbit coupling term is described by the Rashba Hamiltonian :

$$H_R = \frac{\alpha}{\hbar}(\vec{p} \times \vec{e}_z) \vec{\sigma}$$

where  $\alpha$  is the Rashba spin-orbit coupling strength and  $\vec{e}_z$  is the direction perpendicular to the interface. In such a system, the spin is mostly coupled to the momentum components  $k_x$ ,  $k_y$  and the Rashba Hamiltonian in 2D reads [22] :

$$H_R = \frac{p_x^2 + p_y^2}{2m} + \frac{\alpha}{\hbar}(p_y \sigma_x - p_x \sigma_y) = \begin{pmatrix} -\frac{\hbar^2}{2m}(\frac{\partial^2}{\partial x^2} + \frac{\partial^2}{\partial y^2}) & \alpha(\frac{\partial}{\partial x} - i\frac{\partial}{\partial y}) \\ -\alpha(\frac{\partial}{\partial x} + i\frac{\partial}{\partial y}) & -\frac{\hbar^2}{2m}(\frac{\partial^2}{\partial x^2} + \frac{\partial^2}{\partial y^2}) \end{pmatrix}$$

The two eigenstates are the spinors :

$$|\chi+\rangle = \frac{1}{\sqrt{2}} e^{i\vec{k}\vec{r}} \begin{pmatrix} \frac{i}{k}(k_x - ik_y) \\ 1 \end{pmatrix} \quad \text{and} \quad |\chi-\rangle = \frac{1}{\sqrt{2}} e^{i\vec{k}\vec{r}} \begin{pmatrix} -\frac{i}{k}(k_x - ik_y) \\ 1 \end{pmatrix}$$

where the spinor components depend on momentum with  $k = \sqrt{k_x^2 + k_y^2}$ . One can calculate the expectation value of the spin operators on these eigenstates. For example,

in the present case, there is no out of plane spin component :  $\langle \chi + |\sigma_z| \chi + \rangle = 0$ . These two orthogonal eigenstates have opposite expectation value for the spin :  $\langle \chi + |\sigma_x| \chi + \rangle = \frac{k_y}{k}$ , while  $\langle \chi - |\sigma_x| \chi - \rangle = -\frac{k_y}{k}$ . The expectation value changes sign with the momentum  $k_y$ . Therefore, these Rashba eigenstates are spin textured.

Moreover, due to spin-orbit coupling the eigenstates acquire a finite Berry phase, even in the absence of magnetism in the system. In 2003, the intrinsic spin Hall effect has been predicted for Rashba systems[23, 24]. It leads to a spin Hall conductivity in clean system,  $\sigma_{SH} = \frac{e\phi_B}{8\pi^2}$ , related to the Berry phase[25] :

$$\phi_B = i \oint_C \langle \chi | \vec{\nabla}_k | \chi \rangle d\vec{k}$$

This phase is equal to  $\pi$  for both Rashba eigenstates<sup>1</sup> and is analogous to the Aharonov-Bohm phase acquired by an electron when traversing a loop enclosing a magnetic flux. Thus, one also defines the Berry curvature which is analogous to the magnetic field :

$$\vec{\Omega}(k) = i \vec{\nabla}_k \times \langle \chi | \vec{\nabla}_k | \chi \rangle$$

This curvature leads to a spin dependent bending of the electron trajectories when an electric field  $\vec{E}_a$  is applied to the system, characterized by the anomalous velocity :

$$\vec{v}_a = -\frac{e}{\hbar} \vec{E}_a \times \vec{\Omega}(k)$$

This anomalous velocity is responsible for the intrinsic spin Hall effect, i.e a spin current transverse to the applied electric field. There is no dissipation associated with the intrinsic spin Hall effect.

However, impurity scattering in spin-orbit coupled system also leads to two mechanisms responsible for an extrinsic spin Hall effect : the skew scattering which leads to a spin Hall conductivity  $\sigma_{SH}^{sk} \propto \tau$  which increases with the relaxation time  $\tau$  and the side-jump which leads to a spin Hall conductivity  $\sigma_{SH}^j$  independent of  $\tau$ . The extrinsic spin Hall effects also result in a transverse spin current due to a longitudinal charge current. This transverse spin current can lead to a transverse spin accumulation at the edges of the sample as shown in Ref. [26]. A related but different effect is known as the Edelstein effect[27], where a charge current leads to a steady spin polarization[28] due to asymmetries in the spin relaxation<sup>2</sup>. The inverse effect also occurs and is known as the spin galvanic effect where a spin polarization generates a transverse charge current. In Ref. [29] the spin accumulation is generated by optical pumping with circularly polarized light. It should be possible to generate a spin accumulation simply by a magnetic field inducing a difference in spin population[30] :

---

1. The calculation is conveniently done by writing  $k_x = \cos \theta$  and  $k_y = \sin \theta$ .  
2. There is two spin relaxation mechanisms : The Elliot-Yafet where the spin relaxes as it scatters, thus the spin relaxation time is proportional to the relaxation time. The other is the Dyakonov-Perel mechanism where the spin relaxes as it travels due to an internal field, thus, the more frequently it scatters, the less it travels in a fixed internal field and the spin relaxation time is inversely proportional to the relaxation time.

$$n_{\uparrow} - n_{\downarrow} = \frac{1}{2}g\mu_B B\rho(E_F)$$

Nevertheless, this effect has never been demonstrated.

We come back to the eigenenergies of the Rashba Hamiltonian :

$$E_{\pm} = \frac{\hbar^2 k^2}{2m} \pm \alpha k$$

This energy dispersion is shown in Fig. I.2a, where the sign of the spin expectation value  $\sigma_y$  is represented by arrows. This dispersion is directly observed in angle resolved photoemission spectroscopy (ARPES) when the Rashba coefficient is large. From an ARPES spectra, the Rashba coefficient  $\alpha$  can be extracted from the slope of the E vs k spectrum when  $k \rightarrow 0$ . Large Rashba coefficient has been reported by ARPES in BiTeI ( $\alpha = 4.4$  eVÅ)[31], in Bi ( $\alpha = 0.56$  eVÅ)[32] and in Bi<sub>2</sub>Se<sub>3</sub> ( $\alpha = 0.36$  eVÅ)[33]. Surface deposition can strongly enhance the Rashba coefficient such as in BiAg surface alloy ( $\alpha = 3$  eV.Å)[34]. In material promising for spintronics such as InAs, which possesses long spin lifetime, the splitting is too small to be resolved by ARPES[35]. In chapter 4 we propose a new experimental method to infer the Rashba coefficient, it can readily be applied to InAs. Furthermore, it could be used to measure the Rashba coefficient while changing the electronic density with an electrostatic gate.

Usually, when the Rashba spin-orbit term or the Zeeman term are considered separately, at a given energy, one can find two k vectors with the same spin, Fig. I.2ab. Due to the interplay between spin-orbit coupling and a Zeeman field, a helical spin texture can be realized, where a single momentum corresponds to a given spin, Fig. I.2c. Indeed, when an in-plane magnetic field is present, the Hamiltonian of the Rashba system reads[36] :  $H_R = \frac{p^2}{2m} + \frac{\alpha}{\hbar}(p_y\sigma_x - p_x\sigma_y) + \frac{1}{2}g\mu_B(\sigma_x B_x + \sigma_y B_y)$ . And the eigenenergies are :

$$E_{\pm} = \frac{\hbar^2 k^2}{2m} \pm \sqrt{(\alpha k_y + \frac{1}{2}g\mu_B B_x)^2 + (\alpha k_x - \frac{1}{2}g\mu_B B_y)^2}$$

The previous simple Rashba case is obtained for  $B_x = B_y = 0$ . The dispersion relations with magnetic field are shown in Fig. I.2bc.

Therefore, by considering a quasi 1D system  $k_y = 0$ , with a magnetic field along x, as shown in Fig. I.2c, when the Fermi level resides between two energy bands, the helical state is realized where a given spin orientation corresponds to a single momentum  $k_x$ . Such states attract interest as they are protected against back-scattering by non magnetic impurity as a change in momentum requires a spin flip. The energy gap at  $k_x = 0$  in Fig. I.2c, where this helical spin texture is realized, has been probed by transport measurements in nanowires[37, 38].

The helical spin texture has been predicted at the edges of materials in the absence of magnetic field. Firstly in 2005, a quantum spin Hall insulating phase is predicted for graphene in presence of spin-orbit interaction[39]. In this phase, an energy band gap opens in the bulk while states with a helical spin texture exist at the edges. Soon

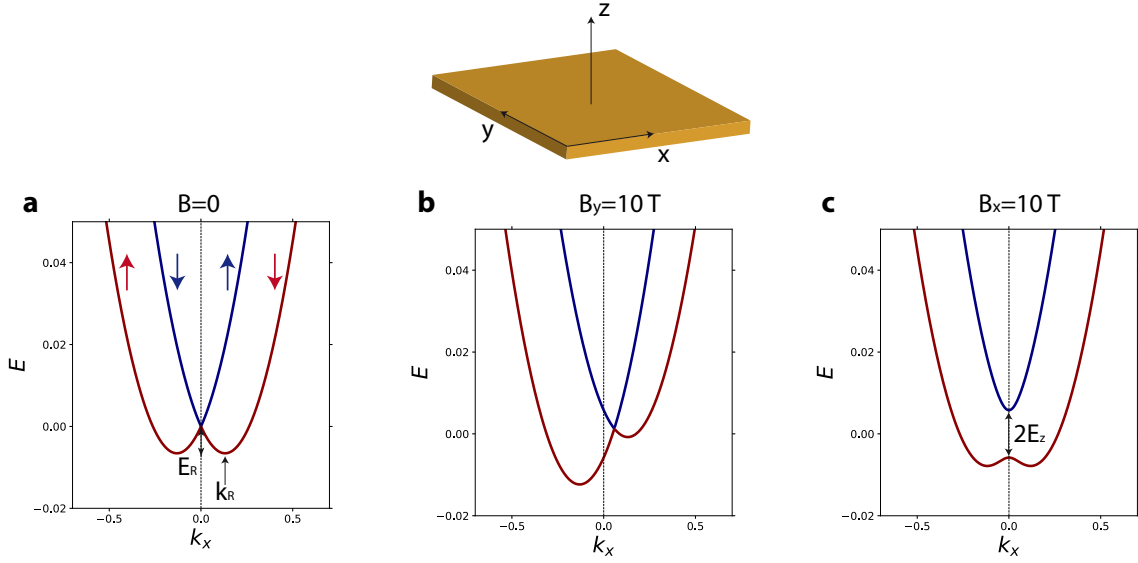


Fig. I.2 **Rashba and Zeeman effect.** **a** Energy dispersion along  $k_x$  showing the Rashba effect without magnetic field. **b** Energy dispersion with a magnetic field applied in the  $y$  direction. **c** Energy dispersion for a magnetic field applied in the  $x$  direction. A Zeeman gap opens at  $k_x = 0$ .

after, quantum spin Hall insulating phases have been predicted and discovered in HgTe/CdTe[40, 41] and InAs/GaSb[42] heterostructures. These materials are referred to as 2D topological insulators or quantum spin Hall insulators.

Three dimensional topological insulators (3D TIs) constitute an extension of the quantum spin Hall insulating phase[43] to the third dimension. The 1D edge channels are replaced by 2D surface states with a helical spin texture. Unlike Rashba systems, the existence of these surface states do not require broken inversion symmetry[44]. Thereby, as previously discussed, the relation  $E_{\uparrow}(\vec{k}) = E_{\downarrow}(\vec{k})$  applies. In other words, two states with same momentum and opposite spin have the same energy. Nevertheless, in 3D TIs, such states are spatially separated on the two opposite surfaces of the material, as sketched in Fig. I.3. The Hamiltonian describing a 3D TI is a  $4 \times 4$  matrix as 2 orbitals and two spins for each orbitals are considered[45]. As the two surfaces are decoupled due to the absence of electronic states in the bulk, one can focus on the properties of a single surface state described by the Hamiltonian[46],  $H_{\text{surface}} = \hbar v_F(\sigma_x k_y - \sigma_y k_x)$ , with eigenvalues :

$$E_{\pm} = \pm \hbar v_F k$$

Such dispersion describes a Dirac cone in momentum space where the energy is linear in momentum. By identifying the Hamiltonian  $H_{\text{surface}}$  with the Rashba Hamiltonian  $H_R$ , we can identify an "effective" Rashba coefficient for the surface states of a 3D TI which is directly related to the Fermi velocity,  $\alpha_{\text{eff}} = \hbar v_F$ .

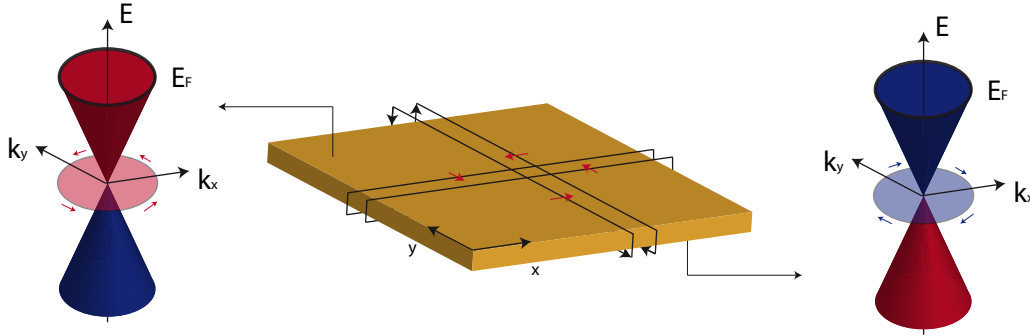


Fig. I.3 **Three dimensional topological insulator.** Two states  $\vec{k}$  with opposite spin are degenerate in energy but spatially separated on the two opposite surfaces of the material.

$\text{Bi}_2\text{Se}_3$  and related compounds are predicted to be 3D TIs[47]. The Dirac cone has been observed by ARPES in  $\text{Bi}_2\text{Se}_3$  crystals and in thin films grown by molecular beam epitaxy. Furthermore, it was shown[48] that the Dirac states disappear below a critical film thickness of  $\approx 5$  nm, interpreted as due to the coupling of the two opposite surfaces by tunneling. Also, the spin texture of the Dirac cone was observed by our partner[49]. A major complication in highlighting the properties of the surface states is that 3D TI are often doped such that the bulk is also conducting. Therefore, making the distinction between the surface states and the bulk states in electronic transport experiments is challenging. Nevertheless, the supercurrent carried by the surface states when coupled to a superconductor is expected to differ significantly than the supercurrent carried by the bulk states.

## I.2 Superconductors

### I.2.1 Ginzburg-Landau description

A superconductor is characterized by a wave function  $\psi$  that describes a quantum coherent superfluid condensate. Ginzburg and Landau (GL) introduced this wave function as the order parameter in a Landau theory of a second-order phase transition. It is related to the local density of superconducting electrons  $n_s = |\psi(\mathbf{r})|^2$  and is used to express the free energy of the superconductor as[50] :

$$f = f_{n0} + \int d^3r \left[ a|\psi|^2 + \frac{b}{2}|\psi|^4 + |\vec{D}\psi|^2 + \frac{B^2}{8\pi\mu^2} \right]$$

with :

$$\vec{D} = \frac{1}{\sqrt{4m}} \left( \frac{\hbar}{i} \nabla - \frac{2e}{c} \vec{A} \right)$$

The parameters of the theory  $a \propto B_c^2 \lambda_L^2$  and  $b \propto B_c^2 \lambda_L^4$  are linked to the critical magnetic field  $B_c$  where the phase transition to the normal state occurs and to the London penetration depth  $\lambda_L$  over which the field penetrates in the superconductor, as sketched in Fig. I.4. The expression of  $\lambda_L$  can be calculated from GL theory and agrees with the expression given by London in its earlier theory describing the local electrodynamics of superconductors :

$$\lambda_L = \sqrt{\frac{m}{\mu_0 n_s e^2}}$$

Beyond this length, in the bulk of a superconductor, the magnetic field is fully screened and the GL wave function is constant  $\psi_{\text{bulk}} = -\frac{a}{b}$ .

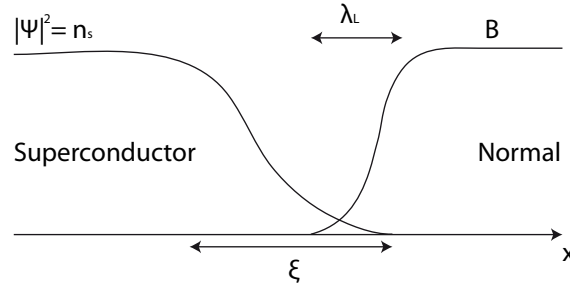


Fig. I.4 **Interface between a superconductor and a normal state.** In the normal state a magnetic field  $B$  is present. It decreases in the superconductor over the London penetration depth  $\lambda_L$ . The superconductor is characterized by a macroscopic wave function  $\psi$  related to the density of superconducting electron  $n_s$ . It changes over the coherence length  $\xi$  which is larger than  $\lambda_L$  for type I superconductor.

In order to obtain the GL equations, one can take the free energy variation with respect to  $\psi^*$  [51] :

$$df = \int d^3r \left[ a\psi\delta\psi^* + \frac{b}{2}|\psi|^2\psi\delta\psi^* + (\vec{D}\psi)(\vec{D}\delta\psi)^* \right]$$

Using an integration by part for the last term, one can show that this expression can be separated into an integral over the volume of the superconductor,  $I_V$  and an integral over its surface  $I_S$  that is  $df = I_V + I_S$  with

$$I_V = \int_V d^3r \left[ a\psi\delta\psi^* + \frac{b}{2}|\psi|^2\psi\delta\psi^* - \delta\psi^* \vec{D}^2\psi \right]$$

and

$$I_S = \frac{1}{\sqrt{2m^*}} \int_S d\sigma \left[ \delta\psi^* \vec{D}\psi \right]$$

By considering only the volume contribution we have  $df = I_V$ . At equilibrium, the free energy is kept constant  $df = 0$  and we obtain the first Ginzburg-Landau equation :

$$a\psi + \frac{b}{2}|\psi|^2\psi - \vec{D}^2\psi = 0$$

From this equation, the GL coherence length is naturally defined in the absence of potential vector  $\vec{A} = 0$  as  $\xi_{GL} = \sqrt{\frac{\hbar^2}{4m|a|}}$ . A disturbance of the GL wave function from its bulk value  $\psi_{\text{bulk}}$  will be attenuated over  $\xi_{GL}$ . This coherence length diverges near  $T_c$  but, well below  $T_c$ , is equal to the Pippard coherence length  $\xi_0$  which is independent of temperature for a pure superconductor :

$$\xi_0 = 0.18 \frac{\hbar v_F}{k_B T_c}$$

For a dirty superconductor, where the mean free path  $l$  is less than  $\xi_0$ , the coherence length  $\xi$  is obtained from :

$$\frac{1}{\xi} = \frac{1}{\xi_0} + \frac{1}{l}$$

The second Ginzburg-Landau equation is found similarly. A small variation  $d\vec{A}$  induced a free energy variation  $df$ . At equilibrium, the Ginzburg-Landau current equation is found from Maxwell equation  $\nabla \times \vec{B} = \mu_0 \vec{j}$  :

$$\vec{j} = -\frac{e^* \hbar}{2m^* i} (\psi^* \nabla \psi - \psi \nabla \psi^*) - \frac{e^{*2}}{m^* c} \psi^* \psi \vec{A}$$

By writing  $\psi(r) = |\Delta(r)| e^{i\varphi(r)}$  and inserting in the above equation we understand that the current solely depends on a phase gradient  $\nabla \varphi$  and does not imply a modulus variation of the order parameter  $\nabla |\Delta(r)|$ .

$$\vec{j} = \frac{e^*}{m^*} |\psi|^2 (\hbar \nabla \varphi - \frac{e^*}{c} \vec{A})$$

To guarantee that the wave function  $\psi$  is single valued, the phase variation around a closed path must satisfy :

$$\oint \nabla \varphi dl = 2\pi n$$

with  $n$  integer. By replacing  $\nabla \varphi$  with the previous expression and the current by  $\vec{j} = |\psi|^2 e^* \vec{v}$ , one obtains the quantization of the "fluxoid" introduced by London :

$$\oint \frac{c}{e^*} \left( m^* \vec{v} + \frac{e^* \vec{A}}{c} \right) \cdot dl = n \phi_0$$

where  $\phi_0 = \frac{hc}{e^*}$  is the flux quantum. From Stokes theorem and the relation between the vector potential and the magnetic field, the second part of the last expression is the magnetic flux enclosed in the area. Therefore, if one chooses an integration contour

for  $\oint$  deep inside the superconductor, far with respect to  $\lambda_L$  from its edges, then the supercurrent is zero  $\vec{v} = 0$  and it is the flux that is quantized :

$$\oint \vec{A}.dl = \int \vec{B}.ds = n\phi_0$$

If we consider a superconducting loop interrupted by a junction we can express the gauge invariant phase difference across the junction by :

$$\varphi_j = 2\pi n - 2\pi \frac{\phi}{\phi_0}$$

## 1.2.2 Elementary excitations

Superconductivity is a phenomena involving many electrons in interactions. Its microscopic description has been given by Bardeen, Cooper and Schrieffer in 1957[52]. They understood that an attractive interaction between electrons will induce an instability of the Fermi liquid. Many-body problems are usually described in the frame of second quantization, where an occupied state is specified by the use of creation operators such as  $c_{\mathbf{k}\uparrow}^+$  which creates an electron of momentum  $\mathbf{k}(=\vec{k})$  and spin up. The annihilation operator  $c_{\mathbf{k}\uparrow}$  empty the corresponding states. In this notation the pairing Hamiltonian reads :

$$H = \sum_{\mathbf{k},\sigma} \epsilon_{\mathbf{k}} c_{\mathbf{k}\sigma}^+ c_{\mathbf{k}\sigma} - V \sum_{\mathbf{k},\mathbf{k}'} c_{\mathbf{k}'\uparrow}^+ c_{-\mathbf{k}'\downarrow}^+ c_{-\mathbf{k}\downarrow} c_{\mathbf{k}\uparrow}$$

where  $\epsilon_{\mathbf{k}} = \frac{\hbar^2 k^2}{2m} - \mu$  are the single particle Hamiltonian energies and  $V$  is an attractive interaction.

The BCS mean-field approximation consists in neglecting fluctuations in the number of particles. Defining  $D = \sum_{\mathbf{k}} c_{-\mathbf{k}\downarrow} c_{\mathbf{k}\uparrow}$ , this approximation corresponds to :

$$D^+ D \simeq -D^+ \frac{\Delta}{V} - D \frac{\Delta^*}{V} - \frac{|\Delta|^2}{V^2}$$

with  $\Delta = -V \langle D \rangle$ . Due to this approximation, the Hamiltonian does not conserve particle number. By using the anti-commutation rule for fermions :

$$c_{\mathbf{k}\downarrow}^+ c_{\mathbf{k}\downarrow} = 1 - c_{\mathbf{k}\downarrow} c_{\mathbf{k}\downarrow}^+$$

One finds the mean field Hamiltonian :

$$H_M = \sum_{\mathbf{k}} \begin{pmatrix} c_{\mathbf{k}\uparrow}^+ & c_{-\mathbf{k}\downarrow} \end{pmatrix} \begin{pmatrix} \epsilon_{\mathbf{k}} & \Delta \\ \Delta^* & -\epsilon_{\mathbf{k}} \end{pmatrix} \begin{pmatrix} c_{\mathbf{k}\uparrow} \\ c_{-\mathbf{k}\downarrow}^+ \end{pmatrix} + \sum_{\mathbf{k}} \epsilon_{\mathbf{k}} + \frac{|\Delta|^2}{V}$$

This Hamiltonian is diagonalized by the transformation :

$$\gamma_{\oplus} = uc_{\mathbf{k}\uparrow} + vc_{-\mathbf{k}\downarrow}^+ \quad \text{and} \quad \gamma_{\ominus} = -vc_{\mathbf{k}\uparrow} + uc_{-\mathbf{k}\downarrow}^+$$

These operators describe the elementary excitations of superconductors. As  $c_{\mathbf{k}\uparrow}$  describes the creation of a hole, the excitations, called Bogoliubons, are made of both electron and hole excitations, with respective contributions  $u$  and  $v$  that depends on energy as :

$$u = \sqrt{\frac{1}{2} \left( 1 + \frac{\epsilon_k}{E_k} \right)} \quad \text{and} \quad v = \sqrt{\frac{1}{2} \left( 1 - \frac{\epsilon_k}{E_k} \right)}$$

The eigenenergies of this Hamiltonian are given by :

$$E_k = \pm \sqrt{\epsilon_k^2 + |\Delta|^2} \quad (\text{I.1})$$

At large energy  $\frac{\epsilon_k}{E_k} \rightarrow 1$ , we recover the excitations of the normal state  $u = 1$ ,  $v = 0$ .

From Eq. (I.1), it is clear that the excited states can not have an energy smaller than  $\Delta$ . Therefore,  $\Delta$  is called the superconducting energy gap. It defines a natural energy scale for superconductivity and is linked to the critical temperature  $T_c$  by the BCS relation at zero temperature :

$$\Delta = 1.764 k_B T_c$$

where  $k_B$  is the Boltzmann constant.

The density of states (DOS) of a BCS superconductor  $N_s$  is calculated from the DOS of the normal metallic state  $N_n$  :

$$N_s(E)dE = N_n(\epsilon)d\epsilon$$

As we are interested in a small energy range  $\Delta$  compared to the Fermi energy, the normal DOS is assumed to be constant and the superconducting DOS is expressed :

$$N_s(E) = N_n(0) \frac{d\epsilon}{dE} = N_n(0) \frac{|E|}{\sqrt{E^2 - \Delta^2}}$$

It is shown in Fig. I.5. The striking departure from the normal DOS is that no states are present near the Fermi energy for  $|E| < \Delta$ . Regarding the DOS, a superconductor looks more like an insulator than a metal.

The vacuum state of a superconductor  $|\text{vacuum}\rangle$ , is the state without Bogoliubon excitations, thus it satisfies  $\gamma_{\ominus} |\text{vacuum}\rangle = 0$  and  $\gamma_{\oplus} |\text{vacuum}\rangle = 0$ . The vacuum state is given by :

$$|\text{vacuum}\rangle = \prod_k c_{-\mathbf{k}\downarrow}^+ |0\rangle$$

where the state empty of electron is denoted  $|0\rangle$ .

The application of the Bogoliubon operator  $\gamma_{\ominus}^+$  on this vacuum state leads to a state of lower energy by the amount  $E_k$ . Thus, the BCS ground state is obtained from :

$$|BCS\rangle = \prod_k \gamma_{\ominus}^+ |\text{vacuum}\rangle$$

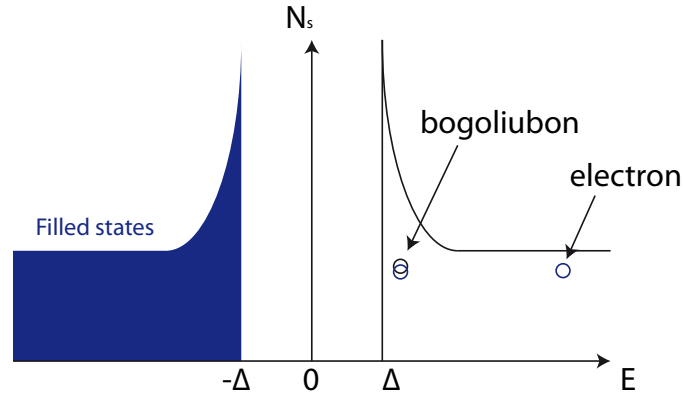


Fig. I.5 **BCS Density of states.** Superconducting density of states  $N_s$  as a function of energy  $E$ . The zero energy is the Fermi energy. No states exist in a superconductor at energy below the superconducting gap  $|E| < \Delta$ . The lowest energy excitations are the Bogoliubons. At high energy, we recover the excitations of the normal state.

Using the definition for the Bogoliubon operator, the BCS ground state reads :

$$|BCS\rangle = \prod_k (-v c_{\mathbf{k}\uparrow}^+ c_{-\mathbf{k}\downarrow}^+ + u) |0\rangle$$

It is composed of electron pairs having opposite momentum and spin : the so-called Cooper pairs.

We have seen that no state exists in the superconductor at energy lower than the superconducting gap  $|\Delta|$ . Therefore, at the interface between a superconductor and a normal material, the superconductor should reflect electrons coming from the normal material. Nevertheless, charge transfers do occur across the interface through the mechanism of Andreev reflection.

## I.3 Hybrid devices

### I.3.1 Andreev reflections

The Andreev reflection is a general property of the interface between a superconductor and a conducting material, which we refer to as SN interface. Its description is provided by the Bogoliubov de Gennes equation[53] where the order parameter  $\Delta(x)$  is allowed to vary in space to go from a finite value in the superconductor to zero in the non superconducting material :

$$\begin{pmatrix} H & \Delta(x) \\ \Delta^*(x) & -H \end{pmatrix} \begin{pmatrix} e \\ h \end{pmatrix} = E \begin{pmatrix} e \\ h \end{pmatrix}$$

where  $H$  is the single particle Hamiltonian and  $e$ ,  $h$  are the electron and hole

amplitude respectively of the spinor  $\begin{pmatrix} e \\ h \end{pmatrix}$  defined in electron hole space. For a system invariant by translation along  $x$ , where  $\Delta$  is constant, we recover the BCS result where  $e$  and  $h$  describe the Bogoliubons :

$$\begin{pmatrix} e \\ h \end{pmatrix} = \begin{pmatrix} e_k \\ h_k \end{pmatrix} e^{ikx} = \begin{pmatrix} -v \\ u \end{pmatrix} \quad \text{or} \quad \begin{pmatrix} u \\ v \end{pmatrix}$$

when  $\Delta$  is set to zero the waves of the normal states are solutions of the Bogoliubov de Gennes equation. We assume that the interface is at  $x = 0$ , the region  $x < 0$  describes the normal material, the region  $x > 0$  describes the superconductor as shown in Fig. I.6. We can write the wave function of an incident quasi-particle of the normal region propagating toward the superconductor by :

$$\psi_k^i(x) = \begin{pmatrix} 1 \\ 0 \end{pmatrix} e^{ik_e x}$$

It can be reflected as an electron with a probability  $b$  or as a hole with a probability  $a$  :

$$\psi_k^r(x) = b \begin{pmatrix} 1 \\ 0 \end{pmatrix} e^{-ik_e x} + a \begin{pmatrix} 0 \\ 1 \end{pmatrix} e^{ik_h x}$$

which are solutions of the Bogoliubov de Gennes equation with  $H = \frac{p^2}{2m}$ ,  $\Delta = 0$  and wave vectors :

$$k_e = k_F \sqrt{1 + \frac{E}{\epsilon_F}} \quad \text{and} \quad k_h = k_F \sqrt{1 - \frac{E}{\epsilon_F}}$$

The transmitted wave in the superconductor is :

$$\psi_k^t(x) = c \begin{pmatrix} u \\ v e^{-i\varphi} \end{pmatrix} e^{ik_e^s x} + d \begin{pmatrix} -v \\ u e^{-i\varphi} \end{pmatrix} e^{-ik_h^s x}$$

which are solutions of the Bogoliubov de Gennes equation with  $\Delta = |\Delta|e^{i\varphi}$ . At low energy  $|E| < \Delta$ , the waves in the superconductor are evanescent with wave vectors :

$$k_e^s = k_F \sqrt{1 + i \sqrt{\frac{\Delta^2 - E^2}{\epsilon_F^2}}} \quad \text{and} \quad k_h^s = k_F \sqrt{1 - i \sqrt{\frac{\Delta^2 - E^2}{\epsilon_F^2}}}$$

At the interface ( $x = 0$ ) the continuity equation for the wave function are :

$$\psi_k^i(0) + \psi_k^r(0) = \psi_k^t(0) \quad \text{and} \quad \frac{\partial}{\partial x} \psi_k^i(0) + \frac{\partial}{\partial x} \psi_k^r(0) = \frac{\partial}{\partial x} \psi_k^t(0)$$

The continuity of the derivative is satisfied when using Andreev approximation : by considering low energies with respect to the Fermi energy, all wave vectors  $k_e, k_h, k_e^s, k_h^s$  are approximate as equal to  $k_F$ . Thereby, one finds the coefficient :

$$a = \frac{v}{u} e^{-i\varphi} \quad b = 0 \quad c = \frac{1}{u} \quad d = 0$$

The amplitude  $a$  corresponds to the Andreev reflection amplitude where an electron of the normal metal is reflected as a hole. If the incident electron energy is less than  $|\Delta|$ , this reflection must occur ( $|a|=1$ ). Thus, two electron charges are lost in the normal metal, no excitation can be created in the superconductor due to the superconducting gap, the wave vector  $k_e^s$  has an imaginary part describing evanescent wave in the superconductor and charge conservation implies that a Cooper pair of charge  $2e$  is added to the condensate. Therefore, the transfer of charge and so the conductance of the interface is doubled at low energy compared to the normal state. This simple model describes perfect SN interfaces, where normal reflections are not allowed ( $b=0$ ).

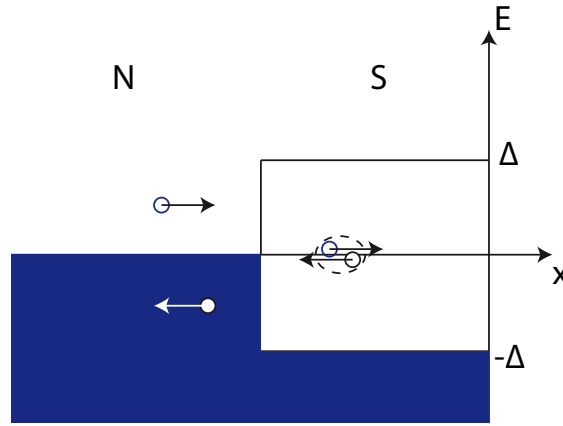


Fig. I.6 **Andreev reflection at a normal-superconductor interface.**

Blonder, Tinkham and Klapwijk have provided a framework to take into account imperfect interfaces [54]. They add a repulsive potential in the Hamiltonian

$$H = \frac{p^2}{2m} - \mu + Z\hbar\sqrt{\frac{2\mu}{m}}\delta(x - x_1)$$

at position  $x_1 < 0$  in the normal material and calculate the conductance of the interface as a function of  $Z$ . At low  $Z$  value, they found that the conductance is twice the conductance of the normal state for voltage corresponding to  $eV < \Delta$ . For high  $Z$ , they found that the conductance is strongly suppressed near zero bias and a conductance peak at the gap edge  $eV = \Delta$ , consistent with calculation involving tunneling, for a normal metal separated from the superconductor by a tunnel barrier [50].

Even in the presence of normal reflections, no wave from the normal material can be transmitted into the superconductor far from the interface at low energy  $|E| < \Delta$ . Thereby, if the normal material is sandwiched between two superconductors its wave functions will be confined and bound states will form under resonant condition.

### I.3.2 Andreev bound states

In SNS junctions, the electronic states are confined in the N region at low energy, and stationary states, known as Andreev bound states, can form. The resonant condition for their formation can be obtained with the scattering matrix formalism. A scattering matrix (S-matrix)[55], describes a scattering region between two leads denoted L and R. We discuss the case of a single transverse mode even so an arbitrary number of transverse modes can be described by the same formalism. The scattering matrix relates the outgoing wave amplitudes to the incoming wave amplitudes through the scattering region :

$$\begin{pmatrix} \text{out}_L^e \\ \text{out}_R^e \end{pmatrix} = S^e \begin{pmatrix} \text{in}_L^e \\ \text{in}_R^e \end{pmatrix}$$

where the electron states from the left lead, incident on the scattering region are denoted  $\text{in}_L^e$ , while electron states going to the right lead, emergent from the scattering region are denoted  $\text{out}_R^e$ .

Similarly for hole states :

$$\begin{pmatrix} \text{out}_L^h \\ \text{out}_R^h \end{pmatrix} = S^h \begin{pmatrix} \text{in}_L^h \\ \text{in}_R^h \end{pmatrix}$$

As the normal region does not couple electrons and holes the  $4 \times 4$  scattering matrix  $S_N$  can be written in a block diagonal form, as shown in the left part of Fig. I.7 :

$$S_N = \begin{pmatrix} S^e & \mathbf{0} \\ \mathbf{0} & S^h \end{pmatrix}$$

Due to Andreev reflection ([56] or p.777 [57]), one can define an Andreev scattering matrix  $S_A$  that relates electron states to hole states at the same lead, as shown in the right part of Fig. I.7. The coefficients of this matrix are the Andreev reflection amplitudes found in the last section. Written in the basis of the normal scattering matrix  $S_N$  it reads :

$$S_A = \begin{pmatrix} 0 & 0 & a_{hL} & 0 \\ 0 & 0 & 0 & a_{eR} \\ a_{eL} & 0 & 0 & 0 \\ 0 & a_{eR} & 0 & 0 \end{pmatrix}$$

The Andreev bound states are stationary states, bound in the SNS region. Therefore, they can be regarded as incident states which remain unchanged after the scattering process :

$$\begin{pmatrix} \text{in}_L^e \\ \text{in}_R^e \\ \text{in}_L^h \\ \text{in}_R^h \end{pmatrix} = S_A S_N \begin{pmatrix} \text{in}_L^e \\ \text{in}_R^e \\ \text{in}_L^h \\ \text{in}_R^h \end{pmatrix}$$

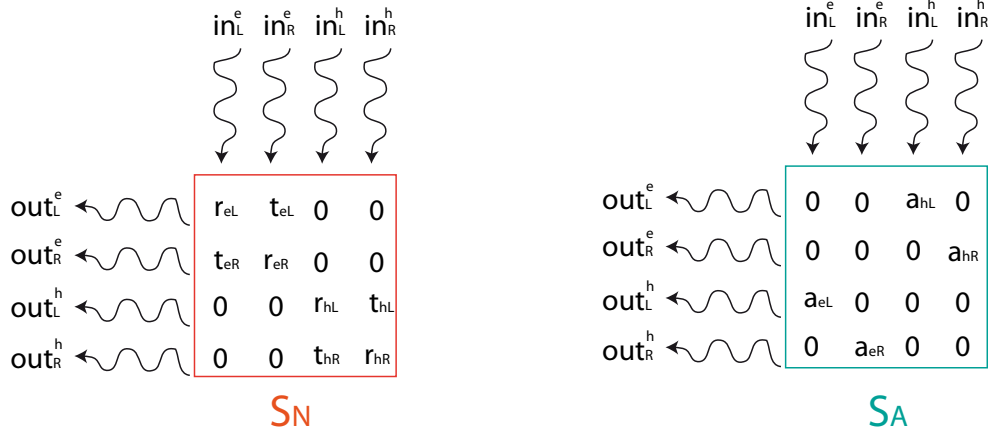


Fig. I.7 **Scattering matrix.** **Left** Normal scattering matrix, which does not couple electron and hole. **Right** Andreev scattering matrix, which couples electron and hole at the same lead.

which is satisfied when  $\det(I - S_A S_N) = 0$ . This requirement gives the Andreev bound states energy as the coefficients of the scattering matrices depend on energy. The scattering matrices for electron and hole are related by  $S^e(\epsilon) = S^h(-\epsilon)^*$  in system with time reversal and particle hole symmetry. The scattering matrix coefficients are related to the coefficients  $a$ ,  $b$ ,  $c$  and  $d$  obtained in the previous section. For  $|E| < \Delta$ , as the wave vectors in the superconductor have an imaginary part, the Andreev reflection amplitude  $a = \frac{v}{u} e^{-i\varphi} = \sqrt{\frac{E-\epsilon}{E+\epsilon}} e^{-i\varphi}$  defined in the previous section, can be re-written by defining  $\epsilon = i|\epsilon|$  :

$$a = \frac{E - i|\epsilon|}{\Delta} e^{-i\varphi} = e^{-i(\varphi+\theta)}$$

with  $\theta = \arccos \frac{E}{\Delta}$ . Therefore, the Andreev scattering matrix coefficients are phase factors,  $a_{eL} = e^{-i(\varphi_L+\theta)}$ ,  $a_{eR} = e^{-i(\varphi_R+\theta)}$ ,  $a_{hL} = e^{i(\varphi_L+\theta)}$  and  $a_{hR} = e^{i(\varphi_R+\theta)}$ . In the case of short junctions, where the scattering matrix in the N region reads :

$$S^e = \begin{pmatrix} ir & t \\ t & ir \end{pmatrix}$$

One obtains the Andreev bound states energy :

$$\epsilon = \pm \Delta \sqrt{1 - \tau \sin^2 \frac{\varphi}{2}}$$

with  $\tau = |t|^2 = 1 - |r|^2$ . These states are shown in Fig. I.8 for different transmission  $\tau$ . They have been probed by Josephson microwave spectroscopy in SNS junctions with N being an atomic aluminum contact[58], where the short junction condition is well fulfilled; and with N being an InAs nanowire  $L \approx 100$  nm[59]. As the carrier density

can be modulated in InAs, it was shown that Andreev states can be added in the system by tuning the gate voltage and increasing the number of transverse modes.

In a long junction  $L > \xi$  a phase term is also acquired due to propagation in the N region. It corresponds to the phase difference between the electrons at the right interface and the holes at the left interface  $(k_e - k_h)L = \frac{2\epsilon L}{\hbar v_F}$ . In the case of perfect transmission across the N region, the equation to get the bound states can be obtained by summing the phase acquired during a cyclic process where an electron is Andreev reflected as a hole which is subsequently reflected as an electron, it reads[60] :

$$\frac{2\epsilon L}{\hbar v_F} - 2 \arccos\left(\frac{\epsilon}{\Delta}\right) \pm \varphi = 2\pi n$$

with  $n$  integer. For long junction  $L \gg \xi$ , the first term dominates over the second term which is omitted :

$$\epsilon = (2\pi n \mp \varphi) \frac{\hbar v_F}{2L}$$

While for short junction  $L \ll \xi$ , the first term is omitted :

$$\epsilon = \pm \Delta \cos \frac{\varphi}{2}$$

### I.3.3 Josephson current phase relations

As the Andreev reflections describe charge transfer across a SN interface, the Andreev bound states that form in SNS junctions carry a supercurrent. Moreover, it has been shown that the Andreev states carry most of the supercurrent in short junctions[56]. The supercurrent depends on the occupation of the states, which is given by the Fermi Dirac distribution :

$$f_D(E, T) = \frac{1}{\exp((E - E_F)/k_B T) + 1}$$

At  $T=0$ , all the states below the Fermi energy are occupied and the states above are empty. Thus, only the Andreev states below the Fermi energy carry a current which, for a single pair of Andreev states, is given by :

$$I = \frac{2e}{\hbar} \frac{\partial \epsilon}{\partial \varphi} = \frac{e\Delta}{2\hbar} \frac{\tau \sin \varphi}{\sqrt{1 - \tau \sin^2 \frac{\varphi}{2}}}$$

For a low transmission coefficient  $\tau$ , the Josephson current phase relation is sinusoidal and  $2\pi$  periodic in phase  $\varphi$ , as expected for Josephson tunnel junctions. This sinusoidal dependence can be obtained by writing a solution of the GL equation in a system where two superconductors are separated by a weak-link[50], it leads to the first Josephson equation :

$$I_J = I_c \sin(\varphi)$$

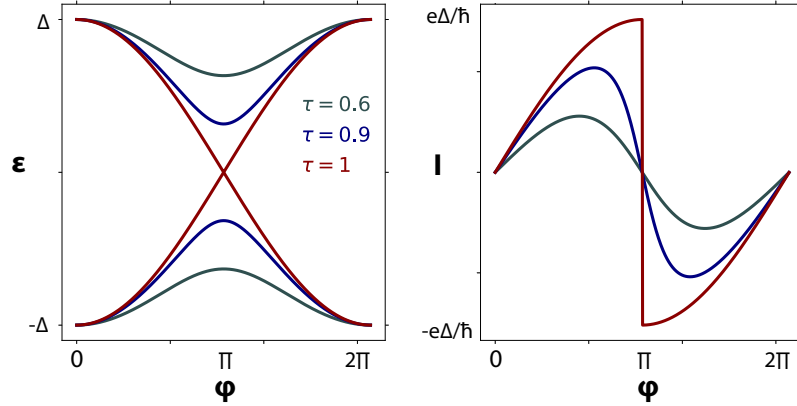


Fig. I.8 **Andreev bound states and current phase relation.** *Left* Energy of Andreev states  $\epsilon$  as a function of the phase difference between two superconductors  $\varphi$ , for different transmission coefficient  $\tau$ . **Right** Corresponding current carried by these states.

It has been shown experimentally that changing the states occupation by inducing a non equilibrium Fermi Dirac distribution in the normal region can modulate the Josephson current[61].

In hybrid devices, such as those involving large g-factor material, one can generate large Zeeman energy in the N region while maintaining superconductivity in the electrodes. As the Pauli matrices describing the Zeeman Hamiltonian acts in spin space, one has to explicit the spin states of electron and hole. Thus, the wave function solutions of the single particle Hamiltonian which enters in the Bogoliubov de Gennes equation has four components :

$$H_{\text{BdG}} \begin{pmatrix} \psi_{e\uparrow} \\ \psi_{e\downarrow} \\ \psi_{h\uparrow} \\ \psi_{h\downarrow} \end{pmatrix} = E \begin{pmatrix} \psi_{e\uparrow} \\ \psi_{e\downarrow} \\ \psi_{h\uparrow} \\ \psi_{h\downarrow} \end{pmatrix}$$

Analytic solutions for the Andreev states energy considering the Zeeman energy have been found in Ref. [62] using the scattering matrix formalism in the short junction limit. The energy of the states depends on a parameter  $\theta_B = \frac{g\mu_B BL}{\hbar v_F}$ . The spin degeneracy of the Andreev states is only preserved when the magnetic field is such that  $\theta_B = [\pi]$ , spin degeneracy is lifted otherwise and four distinct states appear in the spectrum  $\epsilon$  vs  $\varphi$ . The values  $\theta_B = 0$  and  $\theta_B = \pi$  correspond to two Andreev spectrum shifted by  $\pi$ . As the Josephson current results from the derivative of these states, an Andreev spectrum shifted by  $\pi$  results in a sign reversal of the Josephson current :

$$I \sin(\varphi) \rightarrow I \sin(\varphi + \pi) = -I \sin(\varphi)$$

It has been observed in planar Josephson junctions made with large g-factor materials[63, 64].

This shift of  $\pi$  in the Josephson current phase relation is well known when the N material is a ferromagnet[65]. In a superconductor/ferromagnet/superconductor (SFS) junction the 0 and the  $\pi$  states are separated by a critical thickness of ferromagnet where the supercurrent vanishes[66]. The supercurrent reversal can be understood as an oscillation of the order parameter due to the exchange field experienced by the Cooper pair traversing the junction. An intuitive picture to understand this oscillation is given in Ref. [67]. A Cooper pair is composed of two electrons with opposite momentum and spin. The two-particle state is given by the anti-symmetric singlet wave function :

$$|S\rangle = |p \uparrow, -p \downarrow\rangle - |-p \downarrow, p \uparrow\rangle$$

Due to the exchange field in the ferromagnet, the electron acquires a potential energy  $+E_z$  or  $-E_z$  depending on its spin orientation. Thereby, its kinetic energy is modified by a shift in momentum  $\Delta p$ , in order to conserve its total energy. Considering that this momentum shift is small compared to the Fermi momentum  $\Delta p \ll p_F$ , the Cooper pair acquires a center of mass momentum  $q = \pm \frac{2E_z}{v_F}$  depending on its spin configuration and the singlet state becomes :

$$|S_E\rangle = e^{iqx/\hbar}|p \uparrow, -p \downarrow\rangle - e^{-iqx/\hbar}|-p \downarrow, p \uparrow\rangle = \cos(qx/\hbar)|S\rangle + i \sin(qx/\hbar)|T\rangle$$

with the triplet state defined as  $|T\rangle = |p \uparrow, -p \downarrow\rangle + |-p \downarrow, p \uparrow\rangle$ . As the singlet component changes sign when  $qx/\hbar = \pi$ , a minimum of critical current is observed for a junction thickness  $d = \frac{\pi\hbar v_F}{2E_z}$ , in agreement with the Andreev description.

The Josephson current is also strongly affected when it occurs across a confined region. This is the case when the normal material is a quantum dot (QD) where the  $0-\pi$  transition can be induced by an electric field. In QD, electron-electron interaction plays a major role and leads to a charging energy  $U$  as detailed in chapter 3. As electron-electron interaction involves at least two particles, S-QD-S junction can not be described by the Bogoliubov de Gennes equation which takes as input single particle Hamiltonian. Therefore, the study of Andreev QD is a challenging theoretical problem. Confinement of the electronic states in the QD leads to an energy difference  $\delta$  between energy level. If this spacing is sufficiently large, the analysis can be restricted to a single spin degenerate level and is described by the Anderson impurity model with the Hamiltonian[68] :

$$H = H_{\text{QD}} + \sum_{i=L,R} H_M^i + \sum_{l=L,R} H_T^l$$

where the uncoupled QD is described by :

$$H_{\text{QD}} = \sum_{\sigma} \epsilon_0 d_{\sigma}^{\dagger} d_{\sigma} + U d_{\uparrow}^{\dagger} d_{\uparrow} d_{\downarrow}^{\dagger} d_{\downarrow}$$

where  $d_{\downarrow}^{\dagger}$  creates an electron in the QD orbital at energy  $\epsilon_0$  defined with respect to the Fermi energy. A BCS mean-field Hamiltonian  $H_M^l$  is used to describe the superconducting lead  $l$ . In a given lead  $l$ , the superconducting gap is  $\Delta_l = |\Delta|e^{i\varphi_l}$ . Finally,

the coupling between the QD and the electrodes is described by :

$$H_T^l = \sum_{\mathbf{k}, \sigma} (t c_{\mathbf{k}\sigma, l}^+ d_\sigma + H.c)$$

where  $t$  is a hopping amplitude between the QD and the superconducting lead, which is assumed to be symmetric and independent on the wave vector  $\mathbf{k}$ . The coupling parameter  $\Gamma$  depends on the density of states  $\rho$  of the electrodes in the normal state and on the hopping amplitude  $t$  between the lead states and the QD state :

$$\Gamma = 2\pi\rho t^2$$

Solving this Hamiltonian is a challenging theoretical problem and different approaches and approximations have been used[69].

An interesting physical situation occurs when  $\Delta$ ,  $\Gamma$  and  $U$  are of the same order of magnitude, where the  $\pi$  transition can be induced by an electric field. In this situation, a perturbation expansion in one of the parameters is hardly justified. Numerical calculations are however possible, such as the numerical renormalization group, and have provided good agreements between theory and experiments[70, 71, 72]. This method is computationally demanding and we rather present some analytic approaches, relevant to the parameters determined experimentally in the third chapter.

The  $\pi$  transition in a S-QD-S junction can be described by removing the many body part of  $H_{QD}$ , responsible for the charging energy, and by including the charging energy into the orbital energy  $\epsilon_0 \rightarrow \epsilon_\sigma$ , with  $\epsilon_{\sigma=\uparrow} = \epsilon_0 + U/2$  and  $\epsilon_{\sigma=\downarrow} = \epsilon_0 - U/2$ . In the limit  $\Delta \ll \Gamma$ , the Andreev states are determined analytically in Ref. [73], and shown in Fig. I.9. The effect of the on site energy is to split the Andreev states such that four states appear in the spectrum. By increasing the on site energy, the states cross zero energy and the Josephson current abruptly changes sign as a consequence of the sign reversal of the slope of the occupied states. By increasing further the on site energy, the Andreev spectrum will correspond to a Josephson current of lower amplitude shifted by  $\pi$ .

Another approach, followed in Ref. [74], treats the coupling Hamiltonian  $H_T$  as a perturbation. This method allows the authors to directly calculate the Josephson current and predicts its sign reversal as a function of the QD orbital energy  $\epsilon_0$ , in the limit  $U \rightarrow \infty$  :

$$I(\varphi) = \lambda \frac{e}{\hbar} \frac{\Gamma_1 \Gamma_2}{\Delta} F\left(\frac{|\epsilon_0|}{\Delta}\right) \sin \varphi$$

Where  $\lambda = 2$  for  $\epsilon_0 > 0$  and  $\lambda = -1$  for  $\epsilon_0 < 0$ . Experimentally, the QD orbital energy  $\epsilon_0$  can be shifted with respect to the Fermi level by applying a gate voltage on a metallic electrode capacitively coupled to the QD. Therefore, the sign reversal of the Josephson current can be obtained through an electrical field effect[75].

As the Josephson current flowing through a S-QD-S junction can be reversed by tuning the relevant parameters, an important achievement in the study of Andreev

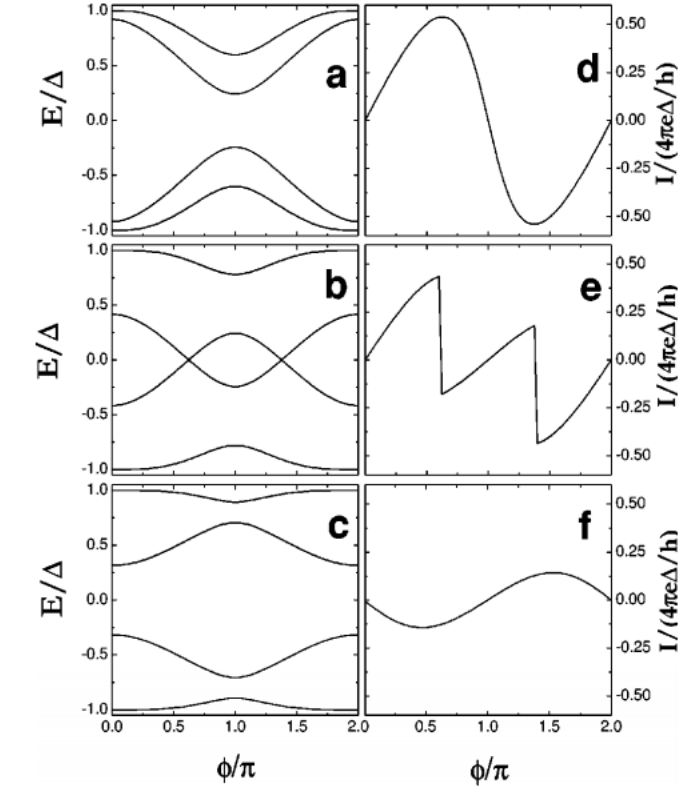


Fig. I.9 Model for a S-QD-S junction, from Ref. [73], which shows the Andreev bound states and the corresponding current phase relation in the presence of an on-site Coulomb energy. The parameters are  $\frac{\epsilon_0}{2\Gamma} = -0.5$  and  $\frac{E_{\text{ex}}}{2\Gamma} = 0.25$  (upper panel), 0.75 (middle panel) and 1.5 (lower panel).

QD has been to draw a phase diagram as a function of  $\Delta$ ,  $\Gamma$  and  $\epsilon_0$ , which separates the 0 and the  $\pi$  state. This diagram can be obtained by the self-consistent description described in Ref. [68] where a single particle effective Hamiltonian is derived :

$$H_{\text{eff}} = \sum_{\sigma} \xi_d d_{\sigma}^{\dagger} d_{\sigma} - |\Gamma_{\varphi}| (d_{\uparrow}^{\dagger} d_{\downarrow}^{\dagger} + H.c) + \frac{U}{2} (\sum_{\sigma} d_{\sigma}^{\dagger} d_{\sigma} - 1)^2$$

where  $\xi_d = \epsilon_0 + \frac{U}{2}$ . This Hamiltonian can be diagonalized by a Bogoliubov-like transformation. It has four eigenstates, two singly occupied spin  $\frac{1}{2}$  states with energy  $E_{\uparrow}^0 = E_{\downarrow}^0 = \xi_d$  and two BCS like states with energy  $E_{\pm}^0 = \frac{U}{2} \pm \sqrt{\xi_d^2 + \Gamma_{\varphi}^2} + \xi_d$ . The ground state of the system can be one of the two singly occupied states (doublet) or the lowest energy BCS state (singlet). Therefore, two ground states of the Andreev QD can be identified and are separated by a phase transition where the two low energy states are equal,  $\xi_d = E_{-}^0$ , that is when :

$$\left(\frac{\xi_d}{U}\right)^2 + \left(\frac{\Gamma_{\varphi}}{U}\right)^2 = \frac{1}{4}$$

which leads to the phase diagram in Fig. I.10. This phase diagram allows to capture a large part of the physics observed in Andreev QD. As we will see in chapter 3, S-QD-S junctions are often in the Coulomb blockade regime and conductance peaks, or Coulomb peaks, occur regularly as a function of gate voltage when the energy  $\xi_d$  is shifted by  $U$ , independently of superconductivity. The phase diagram allows for example to understand that at low coupling  $\Gamma \ll U$  the ground state of the Andreev QD changes at each Coulomb peak which results in a modification of the conductance spectrum at voltage  $eV < 2\Delta$ .

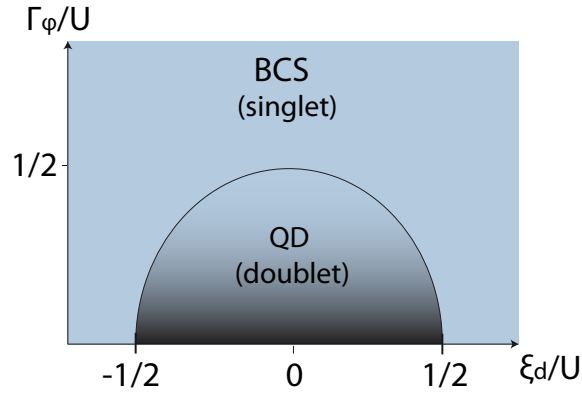


Fig. I.10 **Phase diagram of an Andreev QD.** At low coupling  $\Gamma_\varphi$ , the ground state changes at each charge degeneracy points which correspond to  $\frac{\xi_d}{U} = \pm\frac{1}{2}$ . At large coupling the ground states is always a singlet.

Nevertheless, the phase diagram obtained as it is does not capture the  $0-\pi$  transition when the Andreev QD ground state changes because the energy of the doublet  $\xi_d$  does not depend on the superconducting phase and thus does not carry supercurrent. To solve this issue, in the same study Ref. [68], a perturbation expansion is performed in the term which are missing in the effective Hamiltonian  $H_{eff}$ , to recover the phase dependence of the states and to describe the sign reversal of the Josephson current when the QD ground states changes. When the ground states is a doublet another complication arises when the Kondo temperature expressed as [69] :

$$T_K = \sqrt{\frac{U\Gamma}{2}} \exp\left(-\frac{\pi|\epsilon_0(\epsilon_0 + U)|}{2U\Gamma}\right)$$

leads to a Kondo energy  $k_B T_K$  larger than the Coulomb energy  $U$ . In that case, the local spin of the doublet can be screened by the Kondo effect, and the system will stay in the 0 state. The Kondo effect can be characterized in the normal state as it leads to a zero bias conductance peak independent of gate voltage for odd occupancy of the QD. We did not consider it in chapter 3 as we did not observed the Kondo effect in the gate voltage range studied experimentally. The study of Andreev QD, when the ground states is a doublet and when the Kondo effect is neglected, is analogous to the study of single magnetic impurity in superconductors (see section 6 and 10 of

the review[76]). In particular, it was shown by Shiba that a bound state forms on the impurity site at an energy below the superconducting gap energy :

$$\epsilon = \frac{1 - (JS\pi N_0/2)^2}{1 + (JS\pi N_0/2)^2}$$

where  $S$  is the impurity spin,  $N_0$  is the normal density of states at the Fermi energy and  $J$  is the exchange energy. When the exchange energy is large the Shiba state is found at zero energy and the conductance, which is a measure of the density of states, exhibits a peak at zero bias as shown by STM in Ref. [77].

In the 0 or in the  $\pi$  state, the system symmetries insure that no "anomalous" Josephson current flows without a phase difference between the superconductors. Indeed, for both current phase relation  $I_J = I \sin(\varphi)$  or  $I_J = I \sin(\varphi + \pi)$ , the relation  $I_J(\varphi) = I_J(-\varphi)$  holds and insures that  $I_J(\varphi = 0) = 0$ . However, another type of junctions exist where this condition is broken, these junctions allow a finite current to flow in the absence of phase difference. This phenomena is known as the anomalous or  $\varphi_0$  Josephson effect.

### 1.3.4 Anomalous Josephson effect

In the original paper where Cooper pair tunneling were predicted [5], Josephson noticed that, in the presence of time reversal symmetry, all contributions to the supercurrent are in phase. Forty years later, in a study related to the long range triplet proximity effect observed in ferromagnet-superconductor heterostructures, the authors of Ref. [78] found that different magnetization direction in a SFS junction would result in a finite Josephson current in the absence of phase bias between two superconductors. One year later, the anomalous Josephson effect is predicted in a simple system where two superconductors are separated by a magnetic weak link with spin-orbit coupling[18]. It is also noticed that a magnetic field would result in the same effect when the weak link is non magnetic.

To understand how the spin-orbit coupling and the exchange field affect the proximity effect, one adds a spin-orbit term  $f_{\text{SO}}$  to the GL free energy[18] :

$$f_{\text{SO}} = - \int d^3r \left[ \epsilon \vec{n} \cdot \{ \vec{h} \times [\psi(\vec{D}\psi)^* + \psi^*(\vec{D}\psi)] \} \right]$$

where  $\vec{n}$  is the direction of the Rashba electric field,  $\vec{h}$  is in the direction of the applied magnetic field and  $\epsilon$  is the spin-orbit coupling parameter. In the case of a Rashba spin-orbit coupling this parameter is the Rashba parameter  $\alpha$ , defined in section 1.1.2.

In order to see how this term modifies the Ginzburg-Landau equation, which describes a weak link, we consider the variation of the spin-orbit term due to a small variation  $\delta\psi^*$  :

$$df_{\text{SO}} = - \int d^3r \left[ \epsilon \vec{n} \cdot \{ \vec{h} \times [\psi(\vec{D}^* \delta\psi^*) + \delta\psi^*(\vec{D}\psi)] \} \right]$$

As in the derivation of the GL equation, this expression can be separated into an integral over the volume of the superconductor,  $I_V$  and an integral over its surface  $I_S$  that is  $df_{SO} = I_V + I_S$ . We are interested in a particular solution of  $\psi$  in a direction where  $\vec{A} = 0$ , thereby we find  $I_S = 0$  and

$$I_V = -\epsilon\vec{n} \cdot \left\{ \vec{h} \times \int d^3r \left[ \delta\psi^* \vec{D}\psi - \psi \vec{D}\delta\psi^* \right] \right\}$$

Therefore, the one dimensional Ginzburg-Landau equation describing the weak-link is modified, we neglect  $\frac{\psi \vec{D}\delta\psi^*}{\delta\psi^*} = 0$  :

$$a\psi + \frac{b}{2}|\psi|^2\psi - \vec{D}^2\psi + \epsilon h\vec{D}\psi = 0$$

To illustrate the difference between the proximity effect in a metal and in a ferromagnet, this one dimensional equation is widely used[65]. In a simple derivation of the Josephson current phase relation given in Ref. [50], the last term due to spin-orbit coupling is not present, thus one can choose a general solution for  $\psi$  which is real as all the equation coefficients are real. This solution is of the form  $\psi = \psi_0 e^{-x/\xi}$  and describes the decaying order parameter at a SN interface. The phase degree of freedom enters when choosing the boundary condition, for example  $\psi(x=0) = |\Delta|e^{i\varphi}$  which results in  $\psi = |\Delta|e^{i\varphi}e^{-x/\xi}$ . In the case where the weak link is a ferromagnet without spin-orbit interaction, the one dimensional equation describing the bridge is modified to account for the paramagnetic effect which becomes dominant over the orbital one[65]. In that case the solution is of the form  $\psi = \psi_0 e^{-x/\xi_f} \cos(x/\xi_{osc})$  such that the order parameter oscillates while it decays. The length  $\xi_f$  and  $\xi_{osc}$  are defined in Table. I.3.4. For a SN junction with the same boundary conditions we obtain  $\psi = |\Delta|e^{i\varphi}e^{-x/\xi_f} \cos(x/\xi_{osc})$ . In both SN and SF proximity effect, there is a spatial dependence of the order parameter modulus  $|\psi|(x)$  but no spatial dependence of its argument  $\arg(\psi)$ , in other words there is no spatial dependence of the superconducting phase in the weak link. In the case where the spin-orbit term is present, one must choose a complex general solution of the form  $\psi = \psi_0 e^{ix/\xi_{zso}}$ , such that, with the same boundary condition, one obtains  $\psi = |\Delta|e^{i(\varphi+x/\xi_{zso})}$ . In that case,  $\arg(\psi)(x)$  is position dependent, as sketched in Fig. I.11, and a phase shift accumulates along the weak link. This phase shift results in an anomalous phase difference between the two superconductors as calculated in Ref. [18] :

$$\varphi_0 = \frac{4E_z\alpha L}{(\hbar v_F)^2} \quad (I.2)$$

where  $L$  is the length of the weak link. This  $\varphi_0$  term result in the anomalous current phase relation :

$$I_J = I_c \sin(\varphi + \varphi_0)$$

which leads to an anomalous current  $I_J(\varphi_0)$  at zero phase difference.

	Ballistic	Diffusive
Superconducting coherence length, $\xi$	$\frac{\hbar v_F}{2\pi k_B T_c}$	$\sqrt{\frac{\hbar D}{2\pi k_B T_c}}$
Coherence decay length in an exchange field, $\xi_F$	$\frac{\hbar v_F}{2\pi k_B T}$	$\sqrt{\frac{\hbar D}{E_z}}$
Coherence oscillation length in an exchange field, $\xi_{\text{osc}}$	$\frac{\hbar v_F}{2E_z}$	$\sqrt{\frac{\hbar D}{E_z}}$
Phase oscillation length in an exchange field with Rashba SOI, $\xi_{zSO}$	$\frac{\pi(\hbar v_F)^2}{2E_z\alpha}$	$\left(\frac{6\pi\hbar^6 D}{\tau m^*2 E_z\alpha^3}\right)^{\frac{1}{3}}$

Table I.1 *Characteristic length scales for the proximity effect. The three first lines are taken from Ref. [65]. The first line is the superconducting coherence length in the superconductor. On the normal side, for the same diffusion coefficient, this length is longer as the critical temperature is replaced by the actual temperature. For the last line, the phase oscillation length corresponds to the junction length necessary to induce a phase difference of  $2\pi$  across a Josephson junction. For the ballistic case Eq. (I.2) is used, while for the diffusive case Eq. (IV.3) is used.*

This anomalous current is related to the inverse Edelstein effect observed in metals or semiconductors with strong spin-orbit coupling. While the Edelstein effect consists in the generation of a spin polarization in response to an electric field[27], the inverse Edelstein effect[79], also called spin-galvanic effect, consists in the generation of a charge current by a steady spin polarization induced by a magnetic field[80].

The effect of spin-orbit interaction has also been investigated using the microscopic theory describing the proximity effect in term of Andreev reflections. Spin-orbit interaction alone modifies the Andreev bound states spectrum[81, 82]. Nevertheless, the

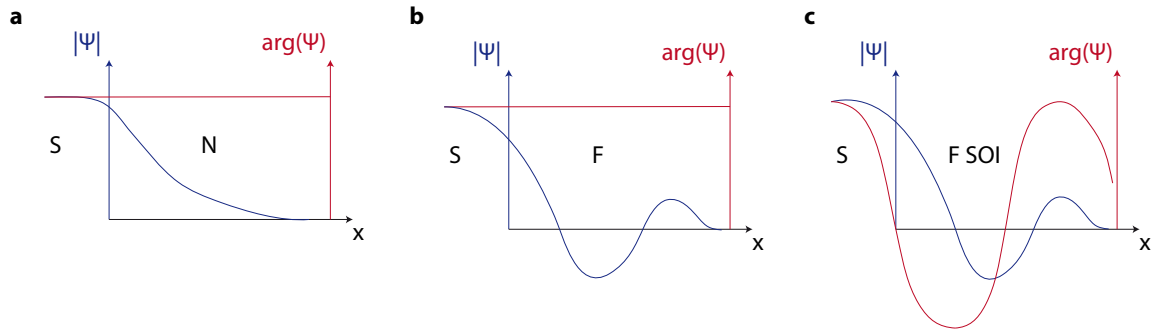


Fig. I.11 *Sketch of the order parameter at (a) a superconductor-normal interface (b) a superconductor-ferromagnet interface and (c) a superconductor-ferromagnet with spin-orbit coupling interface.*

Josephson current, which results from the summation over the derivative of the occupied Andreev states, is not affected by the modification of the Andreev spectrum[81] in the absence of magnetic field. The anomalous Josephson current is found using the Bogoliubov de Gennes equation by including both a Rashba spin-orbit interaction of the form  $H_R = \frac{\alpha}{\hbar}(p_y\sigma_x - p_x\sigma_y)$  and the Zeeman term in the single particle Hamiltonian. In Ref. [83] the Andreev bound state spectrum is calculated using the scattering matrix formalism, it is shown in Fig. I.12a, for a Rashba spin-orbit parameter  $k_\alpha/k_F = 0.15$ , where  $k_\alpha = \frac{m^*\alpha}{\hbar^2}$ . By increasing the magnetic field, the Andreev states split and present a finite slope at  $\varphi = 0$ , resulting in an anomalous current at zero phase difference Fig. I.12b.

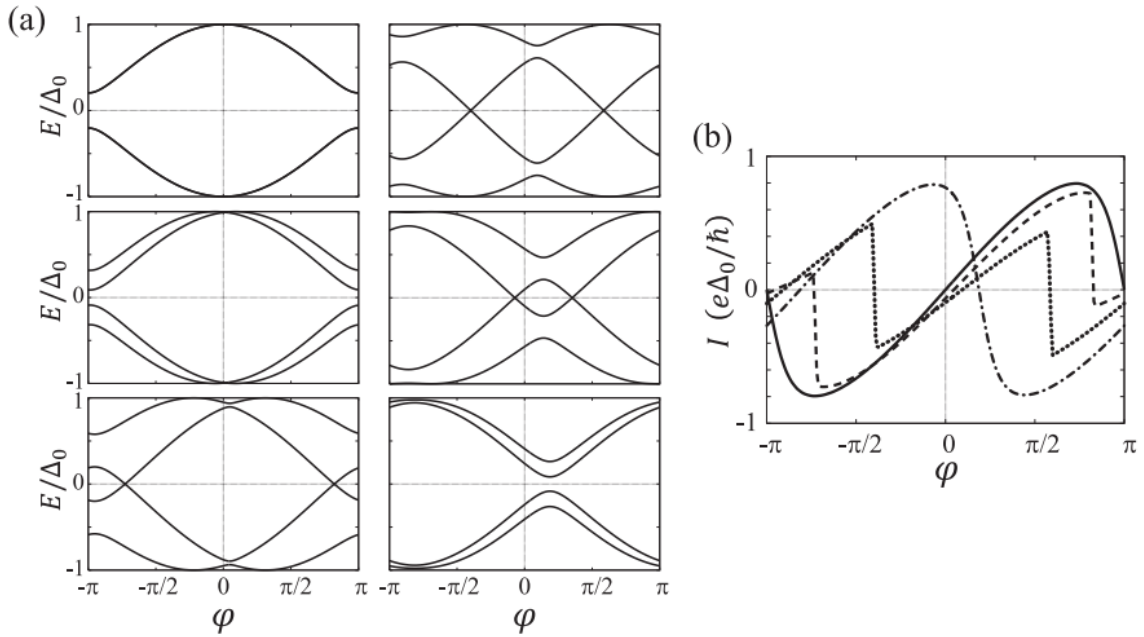


Fig. I.12 Results from Ref. [83]. The Andreev states are calculated in the short junction limit and in the ballistic regime  $\frac{L}{\ell} = 1$ . The magnetic field is applied perpendicular to the current. **a** The different current phase dependence are calculated for different value of the parameter  $\theta_B = g\mu_B L/(\hbar v_F)$ , (top left)  $\theta_B = 0$ , (middle left)  $\theta_B = 0.1\pi$ , (down left)  $\theta_B = 0.35\pi$ , (up right)  $\theta_B = 0.7\pi$ , (middle right)  $\theta_B = 1.05\pi$  and (bottom right)  $\theta_B = 1.4\pi$ . **b** Josephson current for  $\theta_B = 0$  (solid),  $\theta_B = 0.35\pi$  (broken),  $\theta_B = 0.7\pi$  (dotted) and  $\theta_B = 1.4\pi$  (dotted broken lines).

The anomalous Josephson effect is not completely trivial to measure. When we increase the current passing through a Josephson junction in an actual measurement, in some ways, we increase the phase difference between the two superconductors forming the junction. We measure simultaneously the voltage drop across the junction, which is zero until the junction critical current is reached. When the critical current is reached, the junction switches to a dissipative state and a finite voltage difference is measured.

In the case of a usual current phase relation  $I_J = I_c \sin(\varphi)$ , the critical current is reached for a phase difference of  $\pi/2$ , while for an anomalous current phase relation  $I_J = I_c \sin(\varphi + \varphi_0)$  the critical current is reached for  $\varphi = \pi/2 - \varphi_0$ . As we do not know for which phase we get the critical current, the anomalous Josephson effect can not be detected without requiring to phase sensitive measurement as described in chapter 4.



## II – Sample fabrication

In order to study the Josephson effect in a semiconductor, it is necessary to fabricate superconducting contacts on its surface, spaced by a distance of the order of the superconducting coherence length, which is about 100 nm. In this chapter, we describe the fabrication procedure and the characterization of the semiconducting materials. We conclude the chapter with the presentation of the experimental setup.

### II.1 Electron beam lithography

Electron beam lithography allows to pattern a sample at the nanoscale. This technique is sketched, step by step, in Fig. II.1. We pursue with a general description of each step of the process. The exact parameters corresponding to a specific sample are detailed in the fabrication sections.

#### II.1.1 Coating

The lithography process starts by coating the substrate with poly(methyl methacrylate), referred to as PMMA. As shown in Fig. II.1ab, we deposit a PMMA droplet on the substrate and use a spin coater that spins the sample at 4000 round per minute for 30 s with an acceleration of  $2000 \text{ rpm.s}^{-1}$ . The sample is then baked at  $160 \text{ }^\circ\text{C}$  for 15 min. After this step, the PMMA surface is flat and the sample is ready to be loaded in the scanning electron microscope. The choice of PMMA thickness depends on how much material needs to be deposited and on the precision needed for lithography. It can be reduced by diluting PMMA in anisol. Using the PMMA from an A6 bottle yields a thickness of about 400 nm. The PMMA thickness should be approximately 4 times larger than the metal thickness deposited such that, after metal deposition, the metal in contact with the substrate is well separated from the metal on the PMMA.

#### II.1.2 Exposure

As sketched in Fig. II.1c, we expose the PMMA resist to an electron beam in a scanning electron microscope (SEM), from FEI Magelan. A software, namely Raith Elphy Quantum, controls the exposure of pattern pre-defined in GDSII files. An electron

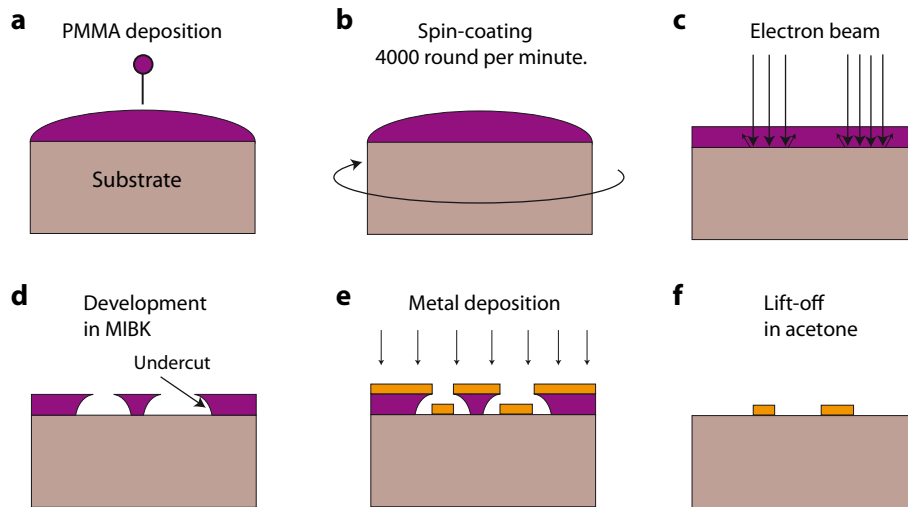


Fig. II.1 **Lithography method.** **a** A PMMA droplet is deposited on the substrate. **b** A spin-coater is used to spin the sample at high speed; then, the sample is baked. **c** The resist is exposed to an electron beam in a scanning electron microscope. **d** The exposed resist is washed away by a solution of MIBK. The undercut regions are due to resist exposure by the spread of the electron beam. **e** A metal is deposited by e-beam thermal evaporation in a Plassys evaporator. **f** The resist is removed by dipping the sample in acetone, the deposited metal in contact with the substrate remains.

beam is focused along the microscope column and accelerated with a voltage of 27 kV. The PMMA polymer chains exposed to the electron beam are broken and these exposed regions will be removed during development. The exposure dose needed,  $D = \frac{It_D}{S}$ , depends on the electrical current,  $I$ , delivered by the SEM, as well as the exposure time,  $t_D$ , and the surface exposed,  $S$ . We use a dose of  $230 \mu\text{C}\cdot\text{cm}^{-2}$  for PMMA resist. We can adjust the current depending on the precision of lithography. Indeed, a smaller current allows a better focusing of the electron beam. However, it requires to increase the exposure time,  $t_D$ , to keep the exposure dose,  $D$ , constant. For small and precise design, we use a low current of 13 pA and an exposure line spacing of 6 nm yielding an exposure surface  $S$  of  $6 \text{ nm} \times 6 \text{ nm}$ . While for larger design, we use a current of 26 nA and a line spacing of 100 nm.

### II.1.3 Development

After exposure, the sample is dipped in methyl-isobutyl ketone (MIBK) diluted 1 :3 in volume with isopropanol (IPA) for the development. This solution removes the PMMA which has been exposed to the electron beam, as shown in Fig. II.1d. We dip the sample in MIBK for 70 s. Then, we rinse the sample in IPA for 30 s and dry it using a nitrogen gas flow. After development, the designed patterns are reproduced on the sample as region without PMMA. They can be checked with an optical microscope.

Then, the sample is loaded in an evaporator for metal deposition.

### II.1.4 Surface cleaning and metal deposition

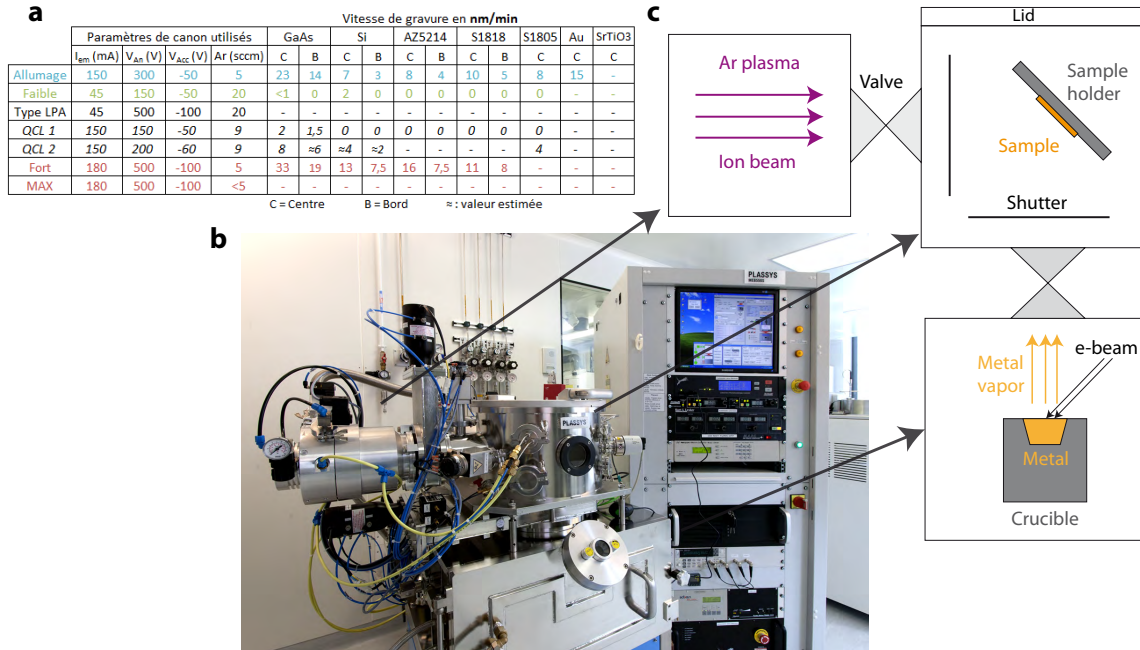


Fig. II.2 **Plassys evaporator.** **a** Different programs for the ion milling and corresponding etching rate on different materials. *C* and *B* denotes the sample position on the Plassys sample holder, center and edge respectively. We usually use the program QCL1 for 40 s. **b** Picture of the Plassys evaporator from MPQ Paris Diderot website. **c** Sketch of the evaporator. The sample holder rotates. It is vertical during the ion milling and horizontal for the metal deposition.

The sample is loaded in a Plassys evaporator shown in Fig. II.2b, for metal deposition. When a vacuum  $< 10^{-6}$  mbar is reached in the evaporator chamber, we use the Plassys Argon plasma to clean the surface. Different ion milling programs are listed in Fig. II.2a, we typically use the weak argon milling program QCL1 for 40 s. Without breaking the vacuum, we subsequently deposit the desired metal as sketched in Fig. II.1e. To do so, the metal, contained in a crucible, is heated with an electron beam and starts to evaporate on the sample as shown in Fig. II.2c. We use different evaporation rates depending on the metal : for Ti  $0.2 \text{ nm.s}^{-1}$ , for Au  $0.3 \text{ nm.s}^{-1}$  and for Al  $1 \text{ nm.s}^{-1}$ . This large evaporation rate for Al is known to make good superconducting Al grains. We always start with the deposition of a small Ti layer (5 nm) as Ti is reactive and improves the adhesion of the metal to the substrate. The evaporated thickness is precisely measured with a quartz crystal. When the desired thickness is reached, a shutter protects the sample from further deposition. After this step, the

deposited metal is present on top of the remaining resist and on the sample surface, where the resist has been removed, as shown in Fig. II.1e.

### II.1.5 Lift-off

The resist is removed by dipping the sample in acetone for 5 min in the case of a thick resist ( $\approx 400$  nm). For thinner resist ( $\approx 100$  nm), one should wait for several hours in order to remove the resist. We can see that the metal on top of the resist crumples in acetone as the resist is washed away. We use a pipette to induce a current flow in the acetone which lifts off the metal layer on top of the resist. The deposition of a thin (5 nm) Ti adhesive layer helps the metal, in contact with the substrate, to stick to the sample. We rinse the sample in IPA and dry it using a nitrogen gas flow.

### II.1.6 Correction of the proximity effect

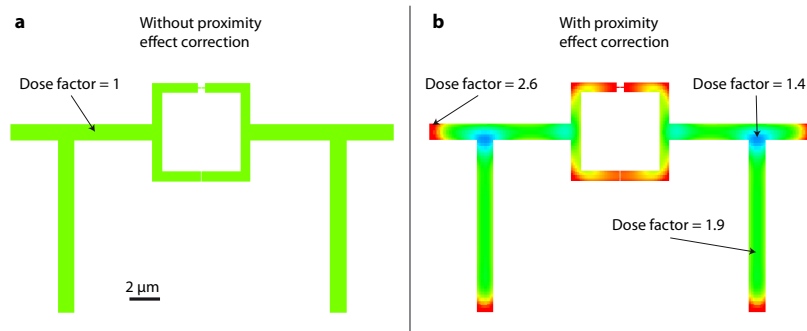


Fig. II.3 **E-beam proximity effect correction.** GDSII datafile containing the design of a device for lithography. **a** Without proximity effect correction, the exposure dose is the same in each points of the design. We start the lithography with a dose of  $230 \mu\text{C.cm}^{-2}$ . **b** With proximity effect correction, the exposure dose is adjusted. We start the lithography with a dose of  $90 \mu\text{C.cm}^{-2}$ . At the edge of the design (red), the dose delivered is  $90 \times 2.6 = 234 \mu\text{C.cm}^{-2}$ . In the center (blue) it is  $90 \times 1.4 = 126 \mu\text{C.cm}^{-2}$ .

After the development procedure, section II.1.3, the developed pattern can be larger than the pattern which has been scanned with the electron beam due to the exposure proximity effect : During exposure, the primary electrons incident on the resist lead to back-scattered electron by the substrate. These secondary back-scattered electrons lead to a subsequent unintentional exposure of the resist. This effect is large for substrate made of heavy nuclei elements because the substrate back-scatters electron with a large scattering angle. It can be corrected by modifying the exposure dose of the design. Indeed, due to the proximity effect, the center of the design needs less exposure than its edges. It is comprehensive as the edges have less nearest neighbors exposed to the electron beam. Therefore, the dose needs to be increased at the edge of a design and decreased in its center. We use a module of Raith quantum elphy software to correct

the proximity effect when a high precision lithography is needed. A GDSII datafile containing a design without and with proximity effect correction is shown in Fig. II.3a and b, respectively. The proximity effect correction takes some parameters as input which depend on the resist used, its thickness, the substrate and the acceleration voltage used during lithography.

## II.2 Connections to the devices

After fabrication, the samples consist in nano-circuits connected to microscopic metallic pads. We can test the sample resistances at room temperature using tip probes connected to measurement instruments in a glove box filled with argon, see section II.5.1. Once a sample is ready to be measured at low temperature, we glue it on a chip as shown in Fig. II.4. We use a wire-bonder to make connections between the chip and the microscopic metallic pads on the sample. These nano-devices (especially the nanowires) are extremely fragile. Therefore, all connections to these devices must be kept at the same potential to avoid unintentional potential differences and currents which would damage the devices. To do so, a first set of connections is made to connect all connections of the chip together. Then, the chip connections are connected to the sample. Once the sample is connected to the dilution fridge, we remove the first set of connection to address separately the different connections on the sample, as shown in Fig. II.4.

We now pursue with the description and characterization of the semiconducting materials as well as the description of the final designed fabrication process for each device.

## II.3 InAs Nanowire devices

### II.3.1 Growth and Crystal structure

The InAs nanowires (NWs) are provided by J.C. Harmand from the Center of Nanosciences and Nanotechnologies (C2N). They are grown by the vapor-liquid-solid mechanism in a molecular beam epitaxy chamber[84, 85]. Catalyst nano-particles of Au are deposited on a GaAs substrate and remain liquid during growth. The atoms of In and As forming the gas in the chamber are deposited preferentially on the liquid droplet. Thereby, crystalline NWs grow on the droplet. The size of the Au nano-particle determine the NW diameter. The InAs NWs studied in the next chapter are doped with silicon atoms during growth.

InAs is a semiconductor of the III-V family. In bulk crystals and thin films it has a zincblende crystal structure, as shown in Fig. II.5a, and a direct band gap of  $\approx 350$  meV at the  $\Gamma$  point which corresponds to the Brillouin zone center. Nevertheless, it is conducting due to the bending of its electronic energy band at its surface that leads to a surface accumulation layer of charges. This two dimensional electron gas is widely used

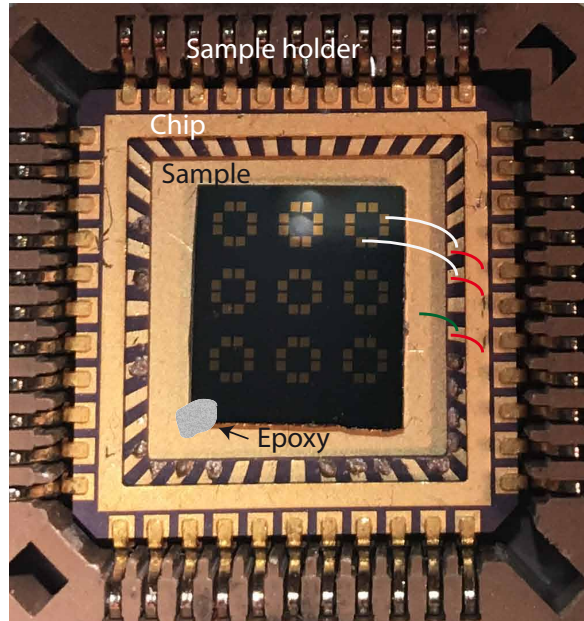


Fig. II.4 **Picture of a sample mounted on the sample holder.** The sample is glued to a chip. Electrical connections are made with a wire bonding machine and are represented in red, green and white. The red connections are done first to insure that all sample connections stay at the same electrical potential. This insures that the sample does not suffer from a potential difference during the wire bonding or when we plug it on the cryostat. These red connections are removed once the sample is connected on the cryostat. Connections to the sample are represented in white. A connection is also made to the gold below the sample, represented in green. This allows to apply a gate voltage or a radio frequency signal to the sample via capacitive coupling. For the gate voltage, an electrical connection is made with epoxy between the doped substrate and the gold below the sample.

in electronic devices such as transistors since the electronic density can be adjusted by a gate voltage. Furthermore, it allows to make electrical contacts with negligible contact resistance due to the absence of Schottky barrier at the semiconductor/metal interface, as it is required to observe the Josephson effect. These properties have led to the observation of a quantized conductance which is doubled by Andreev reflection when a quantum point contact is fabricated at a InAs/Aluminum interface[86].

In a NW form, InAs can be found in the wurtzite crystal structure, shown in Fig. II.5b. This structure is often observed in III-V NWs[88, 89], instead of the usual zincblende lattice of thin films and bulk crystals. In wurtzite InAs NW, the energy gap at the  $\Gamma$  point has been found to be enlarged by  $\approx 60$  meV compared to the bulk zincblende phase[89, 90]. The effective mass value at the bottom of the conduction band is expected to increase by 20 % for the wurtzite phase compared to zincblende[91]. In the next chapter, we use the effective mass of bulk InAs.

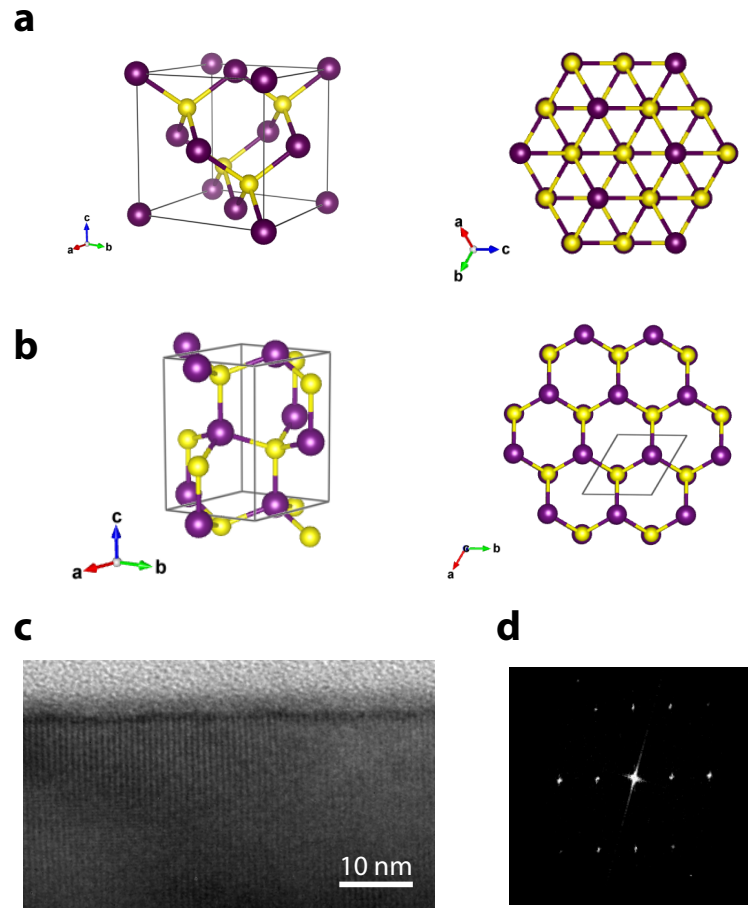


Fig. II.5 **Structure of the MBE grown InAs nanowires.** **a** Crystallographic structure of InAs drawn with Vesta[87]. The structure is imported from the Crystallography Open Database (COD). Bounds between As (purple) and In (yellow) are represented. InAs bulk crystals form in the zincblende crystal structure. **b** In III-V semiconducting nanowires, the wurtzite crystal structure is often found, in contrast with bulk and thin film materials where only the zincblende phase is observed. Here, the wurtzite crystal structure of ZnS is imported from COD. **c** Transmission electron microscopy (TEM) image of an InAs nanowire. **d** Fourier transform of the TEM image.

The transmission electron microscope (TEM) image in Fig. II.5c shows the crystalline nature of a large NW (diameter 100 nm) not doped with Si. We could study this large NW by TEM as the transfer of large NWs from their growth substrate can be done simply by scratching the growth substrate on top of a TEM metallic grid.

Previous study has shown that InAs NWs become insulating below a typical diameter of 50 nm[92]. The NWs measured at low temperature in the next chapter are shown in Fig. II.6a, their diameter is about 20 nm and are conducting at low temperature because they are doped with Si. We did not study them with TEM as the transfer from their growth substrate is not as simple as for the large NW, probably because they are more strongly bound to their substrate by Van der Waals forces.

### II.3.2 Fabrication

In this section, we will detail the fabrication of a nanowire (NW) device which is done in four steps :

- Preparation of the substrate.
- NWs transfer on the substrate.
- Localization of the NWs.
- Deposition of metallic contacts on the NWs.

We begin with the substrate preparation which is a doped silicon wafer covered with a 300 nm thick silicon dioxide layer. Before transferring the NWs on that substrate, a first lithography is performed to pattern alignment gold marks which are essential to localize the NWs. Therefore, 9 grids of  $10 \times 10$  small,  $\approx 1 \mu\text{m}$ , crosses are patterned on the substrate, these crosses are shown in the optical microscope image in Fig. II.7b. During this lithography, 8 large gold marks of  $100 \mu\text{m}$  are patterned at the corners of the chip to be able to align with the sample during the next lithography step, where we will pattern electrodes on the NWs. We also pattern large gold pads, as shown in Fig. II.7a, during this lithography. We will do the wire bonding of the sample on these large pads when the device is finished. This first lithography is done with PMMA of thickness 400 nm. The small crosses are done with a write-field of  $25 \mu\text{m}$  at a current of 13 pA. The large crosses and pads are done with a write-field of  $100 \mu\text{m}$  and a current of 26 nA. After this first lithography the PMMA is developed as described in section II.1.3 and loaded in the Plassys evaporator. Before metal deposition, the sample surface is cleaned in the Plassys for 3 min using the weak argon milling program QCL1, as described in section II.1.4. Then 5 nm of Ti and 75 nm of Au are deposited. The resist is then removed as described in section II.1.5.

We can now transfer some NWs from their growth substrate to the prepared Si substrate. To do so, we use a polydimethylsiloxane (PDMS) stamp. PDMS is a soft material, when it is submitted to a plasma it becomes sticky due to the creation of free radicals at its surface and can be used to grab nano-objects. We let a small cube of PDMS in a plasma cleaner (O<sub>2</sub>-Ar) for 5 min at the lowest power. Then, we stamp the GaAs growth substrate and the Si substrate several times, as shown in Fig. II.6b. This procedure transfers some nanowires on the Si substrate.

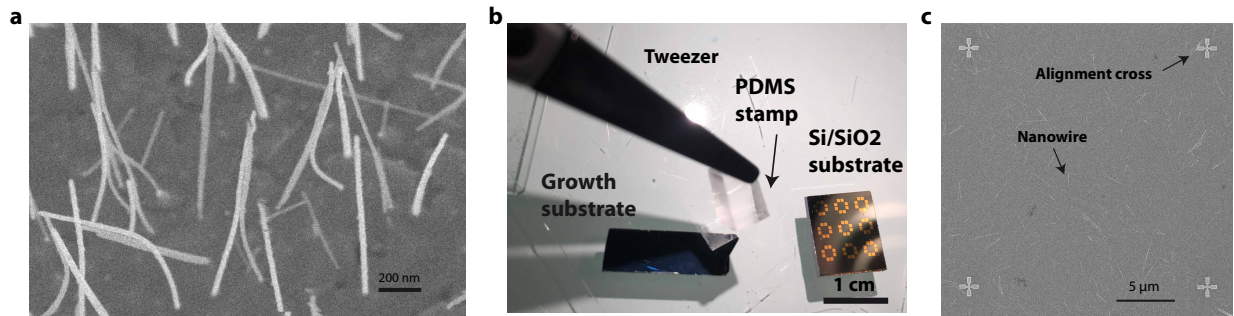


Fig. II.6 **Nanowire transfer from their growth substrate to a Si/SiO<sub>2</sub> substrate.** **a** Scanning electron microscope image of the Si doped InAs nanowires on their growth substrate. The scale bar is 200 nm. **b** Picture of the nanowire transfer. A PDMS stamp is used to transfer the nanowires. **c** Scanning electron microscope image of the Si/SiO<sub>2</sub> substrate. Alignment crosses are patterned on this substrate to localize the nanowires (barely visible on that scale).

Once the NWs are on the substrate of interest, we image the sample with the SEM with a low current of 13 pA and voltage of 5 kV to avoid carbon contamination. The SEM software provides an automatic acquisition of 225 images of the sample. Each image size is  $25\mu\text{m} \times 25\mu\text{m}$ , one is shown in Fig. II.6c. A couple of well isolated NWs are selected from these images (9 to 18 per chip). The corresponding images can be open with the lithography software (Raith) and the lithography design is drawn directly on the image.

The second lithography step to pattern the aluminum contacts on the NWs is performed with PMMA diluted in anisole to get a PMMA thickness of 200 nm after spin-coating, see section II.1.1. This lithography requires a high precision, therefore, it is done with a small current of 13 pA to have the electron beam well focused and with a write-field of  $25\mu\text{m} \times 25\mu\text{m}$ . This write-field size corresponds to the surface over which the electron beam can be oriented using the lenses of the SEM. If a design is larger than the writefield size, the SEM plate needs to be mechanically moved with piezoelectric motors in order to complete the exposure. This mechanic motion is precise within 200 nm which is not enough to aim correctly the NW. Therefore, we use the motor to align the SEM with the crosses shown in Fig. II.6c, then, without requiring to the plate motor, we can start the exposure procedure. This procedure needs to be repeated for each NWs that we have choose to connect on the sample. When it is done, the PMMA is developed as described in section II.1.3. Before metal deposition, the NW surface is cleaned in the Plassys evaporator for 45 s using a weak argon milling program QCL1 which parameters are shown in Fig. II.2a. Without breaking the vacuum, 5 nm of Ti and 60 nm of Al are deposited. The PMMA is lifted off in acetone as described in section II.1.5. Some optical and SEM images of the final devices on different scales are shown in Fig. II.7.

We reproduced the same fabrication procedure to fabricate electrical contacts on

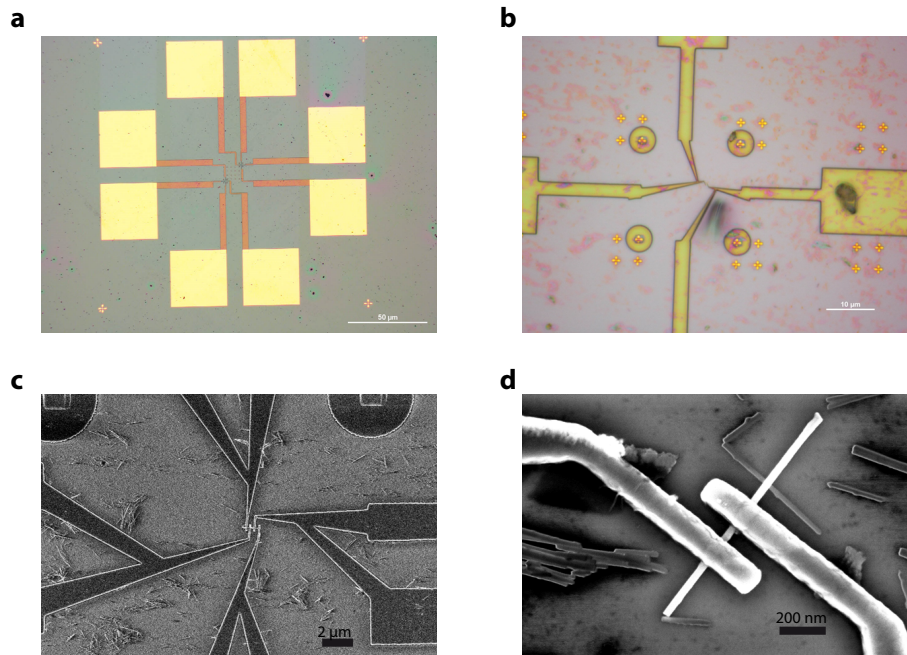


Fig. II.7 **Nanowire devices on different scale.** **a** Scale bar :  $50\ \mu\text{m}$ . Optical image showing the large gold pads on which the wire bonding is done. The gold crosses present at the corners of the image are used for a first alignment procedure during lithography. These gold pads and alignment crosses are done in the first lithography prior to the nanowires deposition. **b** Scale bar :  $10\ \mu\text{m}$ . The smaller gold crosses are used for a precise alignment during lithography. The four gold crosses surrounding the selected nanowire are pictured during the alignment procedure, thus the resist is removed on these crosses and the metal is also deposited on them. The connections between the large gold pads and the smaller electrodes on the nanowire are visible. **c** Scale bar :  $2\ \mu\text{m}$ . Scanning electron microscope image of the nanowire contacted with multiple aluminum electrodes. **d** Scale bar :  $200\ \text{nm}$ . A narrow InAs nanowire of  $20\ \text{nm}$  diameter is contacted with metallic electrodes spaced by  $100\ \text{nm}$ .

$\text{Sb}_2\text{Te}_3$  colloidal nanoplates grown in solution at the INSP by the group of E. Lhuillier.  $\text{Sb}_2\text{Te}_3$  is a three dimensional topological insulator similar to  $\text{Bi}_2\text{Se}_3$  described in the next section. Electrical transport properties of such colloidal particles are usually probed by deposition of a bunch of particles between two electrodes, which makes the distinction between the particle itself and the contact between different particles difficult. We manage to contact electrically a single particle and to show that it was p-doped as reported in Ref. [93] and shown in Fig. II.8.

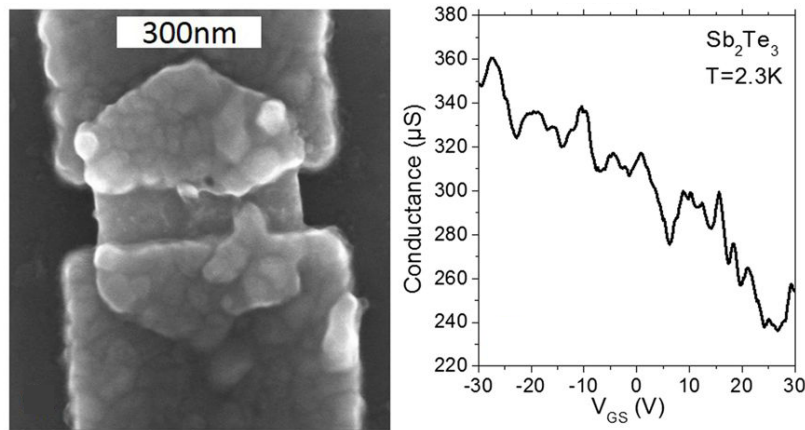


Fig. II.8  **$\text{Sb}_2\text{Te}_3$  colloidal nanoplate device.** The gate voltage  $V_{GS}$  is applied on the metallic side of the  $\text{SiO}_2/\text{Si}$  substrate on which the nanoplate is deposited. The conductance measured at zero bias shows a decrease with increasing gate voltage which confirmed the p doping of the material.

## II.4 $\text{Bi}_2\text{Se}_3$ thin film devices

### II.4.1 Growth and Crystal structure

The  $\text{Bi}_2\text{Se}_3$  thin films are provided by the INSP. They are grown in a multichamber molecular beam epitaxy (MBE) on GaAs substrate. The thickness of the film is atomically controlled by x-ray reflectivity measurements. Following growth, in the MBE chamber, the samples are capped with a Se protective layer to avoid exposure of the  $\text{Bi}_2\text{Se}_3$  surface to air.

Bismuth (Bi) is the heaviest stable element of the periodic table ( $Z=83$ ) and therefore has a strong spin-orbit interaction, see section I.1.2. It is metallic and its electronic configuration is  $6s^26p^3$ . Selenium (Se) is an element of the oxygen family, it is insulating, its electronic configuration is  $4s^24p^4$ . Together, these two elements form the V-VI semiconductor  $\text{Bi}_2\text{Se}_3$ .

$\text{Bi}_2\text{Se}_3$  crystal structure is drawn with VESTA[87] in Fig. II.9a, it is rhombohedral with the space group  $D_{3d}^5$  ( $R\bar{3}m$ ). The crystal is centrosymmetric because it contains

inversion centers where the parity transformation leaves the crystal lattice invariant.<sup>1</sup>  $\text{Bi}_2\text{Se}_3$  has a layered structure. A quintuple layer (QL) consists in 5 atomic planes where each plane contains the same element (Bi or Se). It corresponds to a thickness of  $\approx 1$  nm. Chemical bonds form within a QL between the Bi and the Se atoms, the QL are weakly stucked together by van der Waals forces. The layered structure is observed on the transmission microscope image in Fig. II.9c. The X-ray diffraction spectrum of the  $\text{Bi}_2\text{Se}_3$  thin film grown on GaAs, shown in Fig. II.9d, can be compared with the spectrum of GaAs and  $\text{Bi}_2\text{Se}_3$  generated using the Vesta software. The measured spectrum shows the peak expected for both material separately.

To calculate the band structure of  $\text{Bi}_2\text{Se}_3$ , one considers the outermost shell of Bi and Se which are p orbitals. If each elements are considered separately, the Se p orbitals have a lower energy than the Bi p orbitals, because Se has less electron than Bi. Nevertheless, in a  $\text{Bi}_2\text{Se}_3$  crystal, a Se p orbital have a higher energy than a Bi p orbital due to crystal field splitting and spin-orbit coupling[94]. This is a key signature of the topological insulator phase in  $\text{Bi}_2\text{Se}_3$  and its related compounds,  $\text{Bi}_2\text{Te}_3$  and  $\text{Sb}_2\text{Te}_3$ . This topological phase is characterized by a bulk band gap of 0.3 eV and gapless Dirac states at the material surfaces. Furthermore, these Dirac states have their spin locked perpendicular to their momentum such that, at the surface, a given momentum corresponds to a unique spin. The band gap and the Dirac state are present at the  $\Gamma$  point in reciprocal space which corresponds to the Brillouin zone center. An angle resolved photoemission spectroscopy (ARPES) spectra from Ref.[33], is shown in Fig.II.10. It shows the Dirac cone at the surface of a  $\text{Bi}_2\text{Se}_3$  crystal. It also shows that the Fermi level is well in the conduction band. A large Rashba splitting of the conduction band is observed after 8 hours after cleaving in UHV. The Dirac cone and its spin texture have been observed by ARPES with circularly polarized light in the  $\text{Bi}_2\text{Se}_3$  thin films grown by the INSP[49].

## II.4.2 Fabrication

The fabrication of Josephson junctions on  $\text{Bi}_2\text{Se}_3$  thin film is done in three steps :

- Contact the  $\text{Bi}_2\text{Se}_3$  with superconducting electrodes.
- Isolate electrically the  $\text{Bi}_2\text{Se}_3$  area containing the Josephson junction from the rest of the film, by etching.
- Connect the junction to large metallic pads for the wire bonding.

We begin with the first lithography, performed to pattern the Josephson junction on the thin film and alignment crosses for the next lithography steps. As the superconducting electrodes defining the Josephson junction can be relatively wide (several  $\mu\text{m}$ ) and spaced by a small distance (100 nm), we correct the exposure proximity effect for this lithography, as detailed in section II.1.6. We use PMMA diluted in anisol to get a PMMA thickness of 200 nm after spin-coating, as described in section II.1.1. We develop the PMMA by dipping the sample in MIBK for 55 s. Then, the Se protecting

---

1. The parity transformation consists in reversing the three spatial directions  $x,y,z$  into  $-x,-y,-z$ .

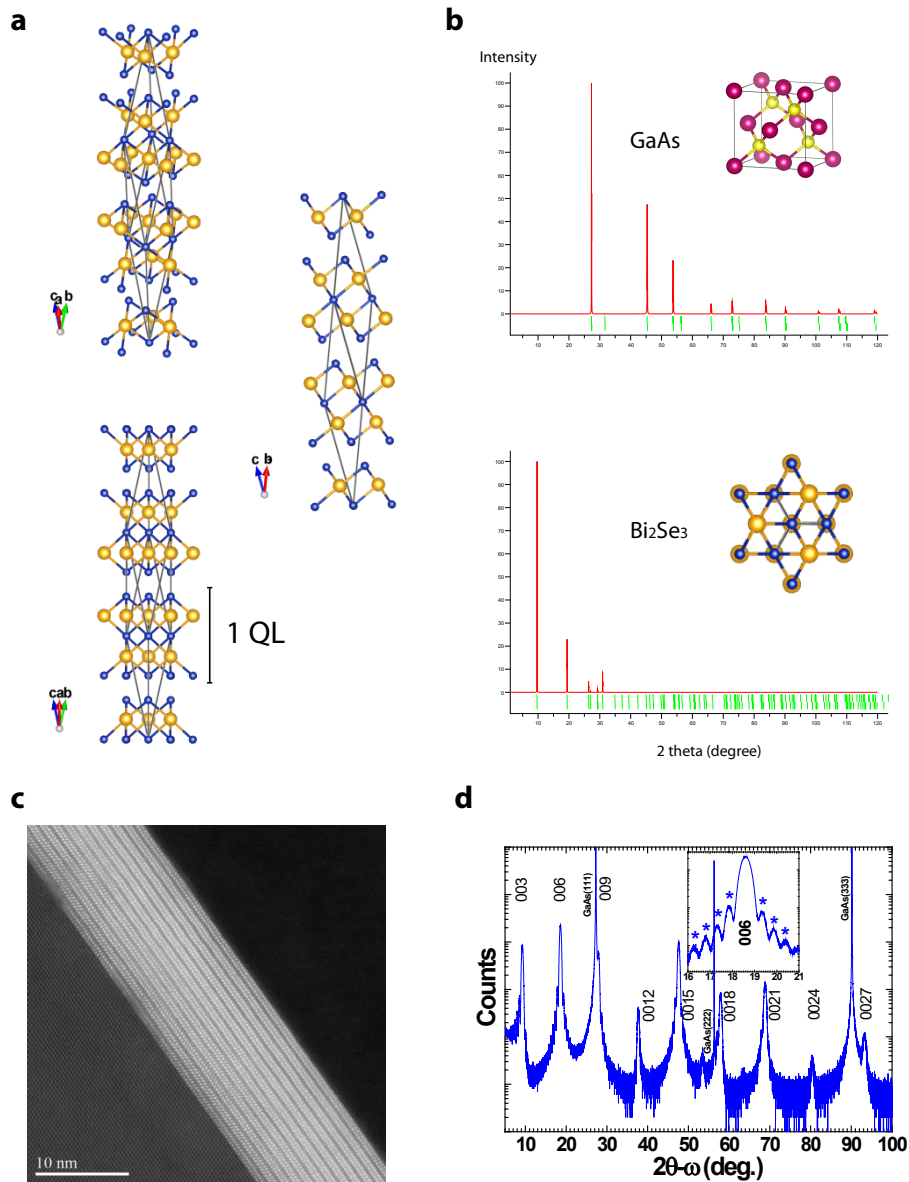


Fig. II.9 **Structure of the MBE grown  $\text{Bi}_2\text{Se}_3$  thin films.** **a** Crystallographic structure of  $\text{Bi}_2\text{Se}_3$  drawn with Vesta[87]. The structure is imported from the Crystallography Open Database. Bounds between Se (blue) and Bi (gold) are represented. A quintuple layer (QL) consists of 5 atomic planes. Van der Waals interaction weakly coupled the QLs together. **b** Powder diffraction pattern generated with Vesta. (Top) GaAs. (Down)  $\text{Bi}_2\text{Se}_3$ . **c** High-angle annular dark-field scanning transmission electron microscopy (HAADF-STEM) cross-section image of  $\text{Bi}_2\text{Se}_3$  film with 12 quintuple layers (1 QL  $\approx$  1 nm). Each QL is delineated by the fringes with darker contrast located between QL. **d** X-ray diffraction spectrum showing the crystalline structure of the films on the GaAs(111) substrate with highly directed 003-type reflections of the  $\text{Bi}_2\text{Se}_3$  film along 111-axis of GaAs. The (006) Bragg reflection is enlarged (in insert) with Kiessig fringes (indicated by stars) which are used to determine the film thickness, about 18 QLs for this film.

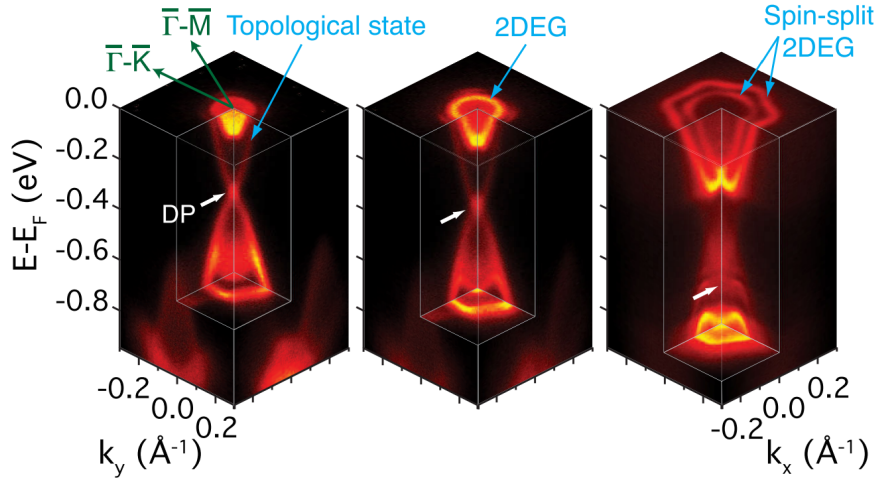


Fig. II.10 ARPES spectra of a  $\text{Bi}_2\text{Se}_3$  crystal from Ref.[33]. The sample is cleaved in the ARPES chamber in UHV, the three curves represent different time after cleaving. From left to right approximately : 20 min, 80 min and 8 hours. The Dirac cone where the energy is linear in momentum is visible. On the right spectra, a large Rashba spin-split of the conduction band is resolved.

layer present on the  $\text{Bi}_2\text{Se}_3$  surface needs to be removed before metal deposition. The first attempt to remove it was to heat the sample in the evaporator at 150 °C for one hour and then deposit the metal. This approach leads to high contact resistance between the electrodes and the  $\text{Bi}_2\text{Se}_3$  and we did not observed Josephson current at low temperature with this method. We did achieve to make good electrical contacts by removing the Se capping layer by dipping the sample in a solution of  $\text{Na}_2\text{S}$  diluted (1.5 %) in NMF<sup>1</sup>. The sample is loaded in the glove box, under nitrogen atmosphere, after development of the PMMA resist. It is dipped with the PMMA in the  $\text{Na}_2\text{S}$  solution for 45s and rinsed in IPA. This procedure removes the Se capping layer from the developed area. Then, inside the glovebox, the sample is locked in a waterproof container to protect it from air during transport to the evaporator. Thereby, the  $\text{Bi}_2\text{Se}_3$  surface is exposed to air only for less than a minute, which is the time needed to load it in the evaporator. In the Plassys, the surface is cleaned by the ion milling program QCL1, detailed in Fig. II.2a, for 40 s. Subsequently, 5 nm of Ti and 50 nm of Al are deposited. For some devices, we deposit only 20 nm of Aluminum in order to increase the parallel critical field of the superconducting electrodes. The resist is then lifted off in acetone, see section II.1.5. After this step, aluminum electrodes spaced by 100 nm define Josephson junctions on the  $\text{Bi}_2\text{Se}_3$  as shown in Fig. II.11.

As all the thin film surface is conducting, each Josephson junctions have to be isolated electrically from the rest of the sample. This is done by etching the  $\text{Bi}_2\text{Se}_3$

1. 75 mg of  $\text{Na}_2\text{S}$  in 5 mL of NMF gives a good amount of solution.

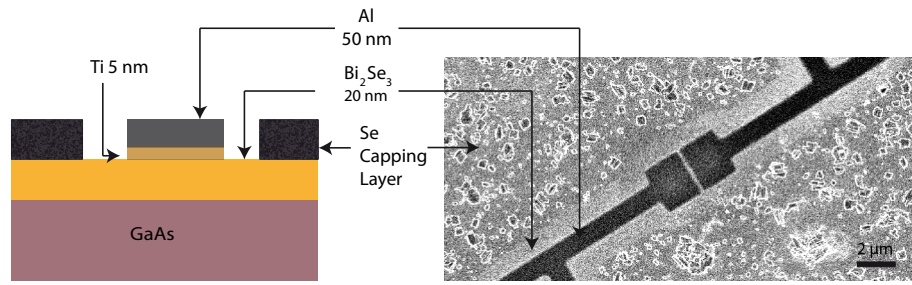


Fig. II.11 **Josephson junction device.** **Left** Sketch of a device section showing the different material layers. **Right** Scanning electron microscope image showing a top view of a Josephson junction device.

area around each junction. During etching, the areas containing Josephson junctions are protected by a resist mask. To do so, a lithography is performed using a negative tone resist, in contrast with PMMA which is a positive resist. In the case of a negative resist, the areas exposed to the electron beam are not removed by the developer. It is the unexposed areas which are removed. We spin-coat the negative resist ma-N 2403 at 3000 rpm for 30 s. This yields a resist thickness of 300 nm. The resist is then baked at 90 °C for 1 min. As ma-N resist is photosensitive, the spin coating is done at the ENS, in a clean room free from UV light. In the SEM, the exposure of the resist to the electron beam, see section II.1.2, is done with a current of 26 nA and an acceleration voltage of 20 kV. After lithography, the resist is developed at the clean room free from UV light, in a solution of MIF for 55s. Then, the sample is rinsed in deionized water for 3 min. As the resist does not stick strongly to the sample, it should be dipped in the solution softly. After development, the resist can be exposed to UV light. The etching of the sample area which is not protected by the resist is done in a reactive ion etching chamber, see Fig. II.12. We use first a physical etching program with Ar to etch the  $\text{Bi}_2\text{Se}_3$ . This etching also leads to an unwanted polymerization of the ma-N resist. This polymerized resist can not be fully removed with acetone. Therefore, in the RIE chamber, a second chemical etching program is used to remove the resist top layers which have been polymerized, it is done with  $\text{O}_2$  which reacts with the organic resist. Finally, the ma-N protective resist is removed by dipping the sample in acetone for 5 min at 60 °C after which the sample is rinsed in IPA for 2 min.

The Josephson devices are now isolated electrically and ready to be connected with large gold electrodes, which allow to wire bond the sample. This last lithography step is done with PMMA, see sections II.1.1, II.1.2 and II.1.3. In addition to large pads connected to the devices, we also pattern large pads not connected near the junction for electrolyte gating, as detailed in chapter 4. After development, before metal deposition, the surface is cleaned using the evaporator Ar ion milling program QCL1 for 3 min. This step is important to remove some,  $\text{Al}_2\text{O}_3$  oxide that forms on top of the aluminum, in order to have a good electrical contact between the gold and the aluminum. Then 5 nm of Ti and 75 nm of Au are deposited. The resist is removed

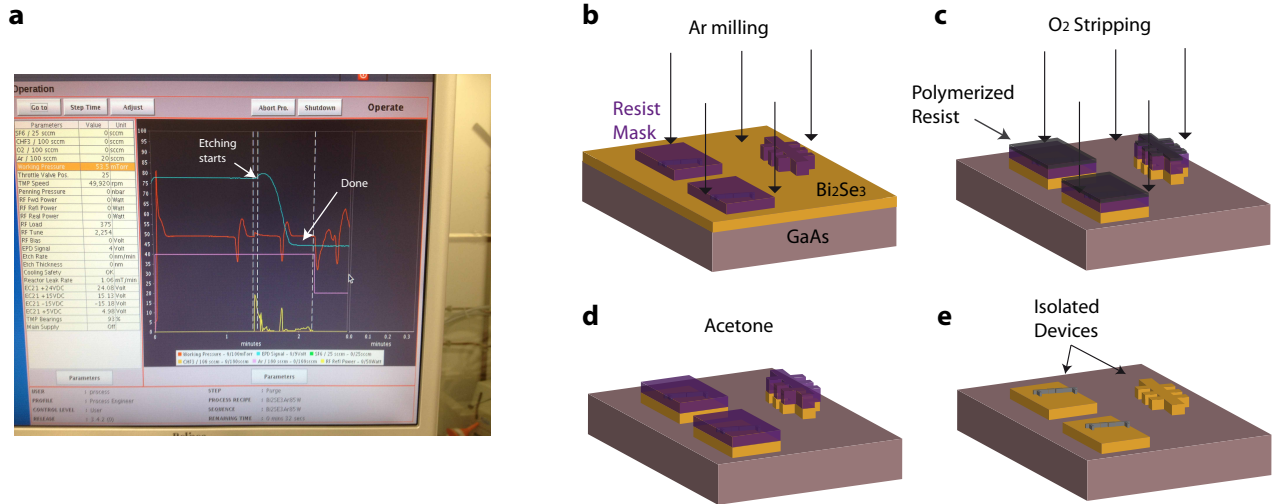


Fig. II.12 **Etching process.** **a** Picture of the reactive ion etching controller. Etching is monitored by a laser beam focused on the  $\text{Bi}_2\text{Se}_3$ . The intensity of the reflected beam is shown in blue. During etching the intensity changes due to change in the film thickness, when it becomes constant, all the  $\text{Bi}_2\text{Se}_3$  has been etched and we stop the plasma. **b** Sketch of the etching showing the  $\text{Bi}_2\text{Se}_3$  and the devices protected by a mask of *ma-N* resist (purple). A physical etching with argon ion removes the unprotected  $\text{Bi}_2\text{Se}_3$  surface and the Se capping layer (not shown). **c** After the physical etching, the resist is polymerized (black) and can not be removed by acetone. Therefore, we use a quick chemical etching with  $\text{O}_2$  to remove the top resist which has been polymerized. **d** The *ma-N* mask resist is removed by dipping the sample in hot acetone. **e** After the acetone, the resist is well removed and the devices electrically isolated.

in acetone and the sample is ready to be wire-bond. A final device is shown on the SEM images, Fig. II.13.

## II.5 Measurement stations

### II.5.1 Glove box

Samples are always kept in a glove box which contains a nitrogen atmosphere, in order to protect them from oxidation. The glove box also contains a probe station for rapid characterization. It consists in two metallic tips connected to measurement instruments. The sample is placed under a binocular microscope and the tips are moved using mechanical arms in contact with the sample electrodes. Thus, the sample two point resistance can be measured at room temperature in the glove box. The samples which show an appropriate resistance are wire-bonded and mounted on the dilution fridge.

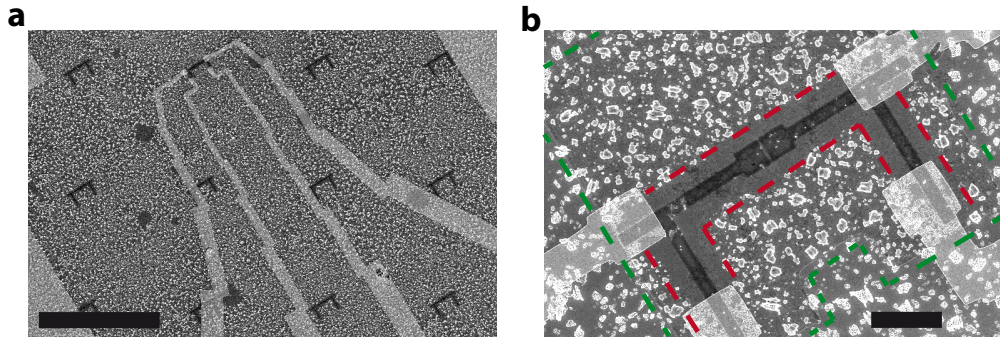


Fig. II.13 **SEM images of devices.** **a** Scale bar  $100\ \mu\text{m}$ . On these MBE grown films, many junctions are fabricated and examined by SEM. The best junctions are selected and connected by  $\text{Ti}5\ \text{nm}/\text{Au}75\ \text{nm}$  electrodes. **b** Scale bar  $10\ \mu\text{m}$ . The white grains at the surface are Se grains. Before deposition of the Al electrodes (dark area), the Se capping layer is removed by chemical etching in an NMF solution of  $\text{Na}_2\text{S}$ . Because of the undercut in the PMMA resist, the area on which Se is removed extends beyond the area where the Al electrodes are evaporated. This area where Se is removed, is clearly visible and indicated by dashed red lines. After evaporation of the superconducting Al electrodes, the  $\text{Bi}_2\text{Se}_3$  film is etched to isolate the junction, the etched contour is visible and highlighted by the dashed green line.

## II.5.2 Dilution fridge

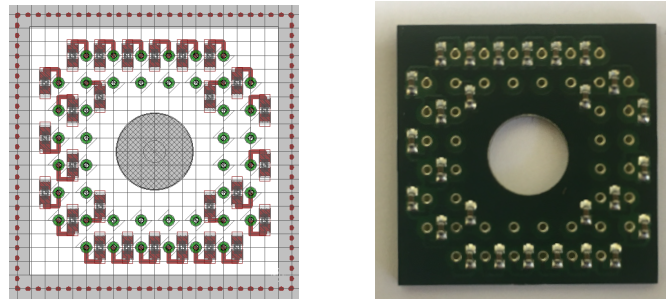


Fig. II.14 **Left** Design of a PCB with the Eagle software. **Right** Picture of the PCB fabricated by a company, the square side size is 2 cm. It contains capacitance connected to the ground to filter each measurements lines at 20 mK.

Measurements are done in a  $\text{He}_3/\text{He}_4$  dilution refrigerator which allows to cool down a sample to a temperature of 20 mK. A magnetic field up to 7 Tesla can be applied at low temperature. The measurement lines are filtered with  $\pi$  filters at room temperature at the input connections of the cryostat. They are also filtered on the sample stage at 20 mK with 1 nF capacitances connecting the measurements lines to the ground. These filters present at low temperature where designed using a software

called Eagle. It generates a file which can be sent directly to a company which fabricate PCB. A picture of the PCB containing the filters is shown in Fig. II.14. An RF cable has been added to the dilution fridge to provide a microwave signal on the sample stage. This RF line is attenuated if necessary. The measurement setup is shown in Fig. II.15.

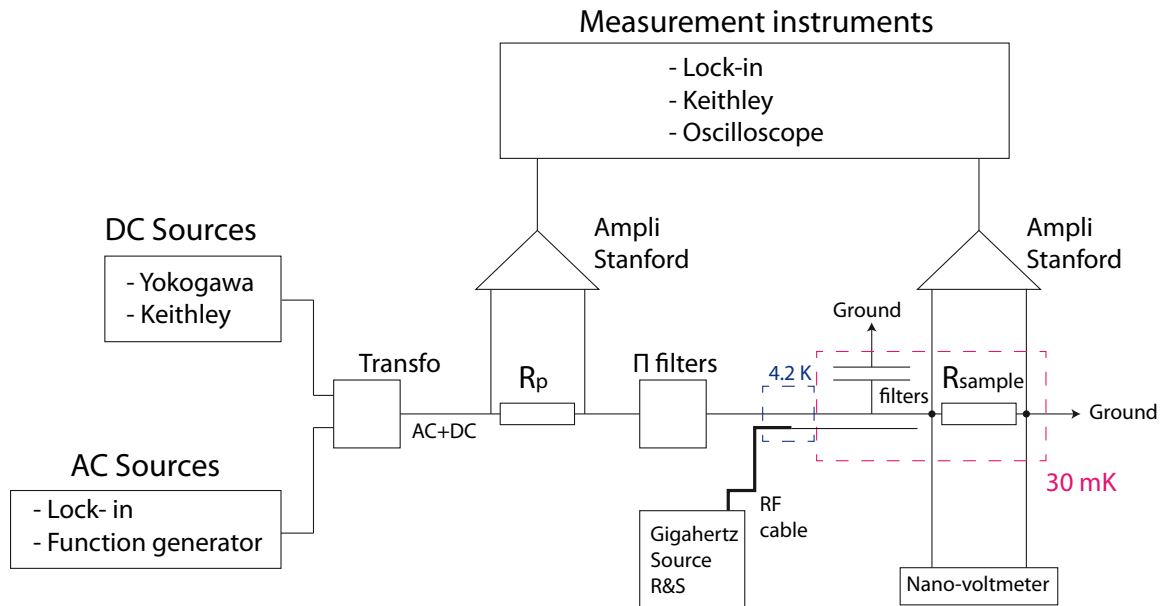


Fig. II.15 **Measurement setup.** We usually sum and control an AC and a DC current provided by a lock-in and a yokogawa, respectively, and measure the resulting AC and DC voltage across the sample after amplification with a lock-in and a keithley, respectively.

# III – Andreev Quantum Dot in doped InAs nanowire

As one reduces the size of a conductor, quantum confinement drastically modifies its optical and electronic properties. This is the case in Quantum dots (QDs) which present a discrete set of electronic energy levels. In these nanostructures, one can tune the number of electron one by one and address single transitions between energy levels[95]. QDs coupled to metallic leads have allowed to revisit the Kondo effect at the level of a single spin, when the number of electrons on the QD is odd[96, 97]. When coupled with a superconductor (S), the discrete energy spectrum of a QD is modified by Andreev reflections. Thereby, in S-QD-S junctions, Josephson current can flow and be controlled by changing the QD occupancy between even and odd number of electrons[75]. Devices based on Andreev QDs, such as nano-SQUIDs, promise improved sensors to detect the magnetization reversal of single molecules attached on the quantum dot[98]. Alternatively, they could be sensitive to atomic dopants implemented in the QD during growth. Andreev QDs are of fundamental interest as they can be used to test random matrix theory[99]. Moreover, Andreev QD chains could become a model system for realizing a Kitaev chain, where a one dimensional spin system with superconducting correlations host Majorana bound states at its edges[100, 101, 102]. In this chapter, we present a study of Andreev QDs fabricated with small-diameter (30 nm) Si-doped InAs nanowires where the Fermi level can be tuned across a mobility edge separating localized states from delocalized states. While at deeply localized levels only quasiparticle cotunneling is observed, for slightly delocalized levels Shiba bound states form and a parity-changing quantum phase transition is identified by a crossing of the bound states at zero energy. Finally, in the metallic regime, single Andreev resonances are observed. The study is reported in Ref.[103]. We conclude the chapter with a discussion on recent experiments related to Andreev QDs physics.

## III.1 Coulomb blockade transport

### III.1.1 Single electron transistors

Electron-electron interaction plays a major role in nanostructures weakly coupled to their environment. It is particularly the case when the Coulomb or charging energy,  $E_c$ , dominates all other energy scales of a system. The Coulomb energy accounts for the electrostatic energy rise when one adds an excess charge to a metallic island. If the island contains  $N$  electronic charges its electrostatic energy is given by :

$$E_{\text{el}}(N) = \frac{e^2 N^2}{2C}$$

with  $C$  the island capacitance. Adding one charge on the island requires an energy,  $E(N+1) - E(N) = \frac{e^2}{C}(N+1/2)$ , where  $E_c$  is defined as the Coulomb energy :

$$E_c = \frac{e^2}{C}$$

Thereby, charge transfer is suppressed when the island is connected to two electrodes subject to a potential difference,  $V_D$ , such that  $eV_D < E_c$ . This is the regime of Coulomb blockade.

At low temperature, we observed that the nanowires (NWs) coupled to metallic leads are naturally in the regime of Coulomb blockade without the need of engineering tunnel barriers between the metallic contacts and the NWs. Coulomb blockade takes place whenever the charging energy,  $E_c$ , corresponding to the energy difference,  $E(N+1) - E(N)$ , is larger than thermal broadening  $k_B T$ . Charging the NW with an additional charge takes a time,  $\Delta t = RC$ , where  $R$  is the NW resistance. Heisenberg's uncertainty relation,  $E_c \Delta t > h$ , sets a lower limit on the charging energy that can be resolved through the condition,  $R > \frac{h}{e^2}$ . Therefore, the charging energy of a system can be observed if the device resistance is higher than the resistance quantum,  $R_Q = \frac{h}{e^2}$ , which is the case in this study.

In this section, we will focus on the features of the Coulomb blockade regime. They are measured with a large AC bias corresponding to  $V_{AC} \approx 50 \mu\text{V}$  and on a large drain voltage range, making the superconducting features barely visible.

The device is sketched in Fig. III.1a. The potential along the NW is modified by the presence of metallic electrodes and the region in between defines a Quantum Dot (QD). A scanning electron microscope image of a NW device is shown in Fig. III.1b. The gate voltage changes the energy spectrum of the QD,  $E_N$ , via capacitive coupling. The energy of the QD,  $E_N$ , depends on the number  $N$  of electrons on the QD. At low temperature the electronic levels in the left  $L$  (right  $R$ ) lead are filled up to the chemical potential,  $\mu_L$  ( $\mu_R$ ), as shown by the gray region in Fig. III.1cd. The QD chemical potential,  $\mu_N$ , is defined as the energy required to add one electron in the QD :  $\mu_N(V_G) = E_N(V_G) - E_{N-1}(V_G)$ . A change in gate voltage,  $\Delta V_G$ , allows to tune the QD chemical potential,  $\mu_N(V_G + \Delta V_G) = \mu_N(V_G) + |e|\alpha_G \Delta V_G$  where  $\alpha_G$  is the

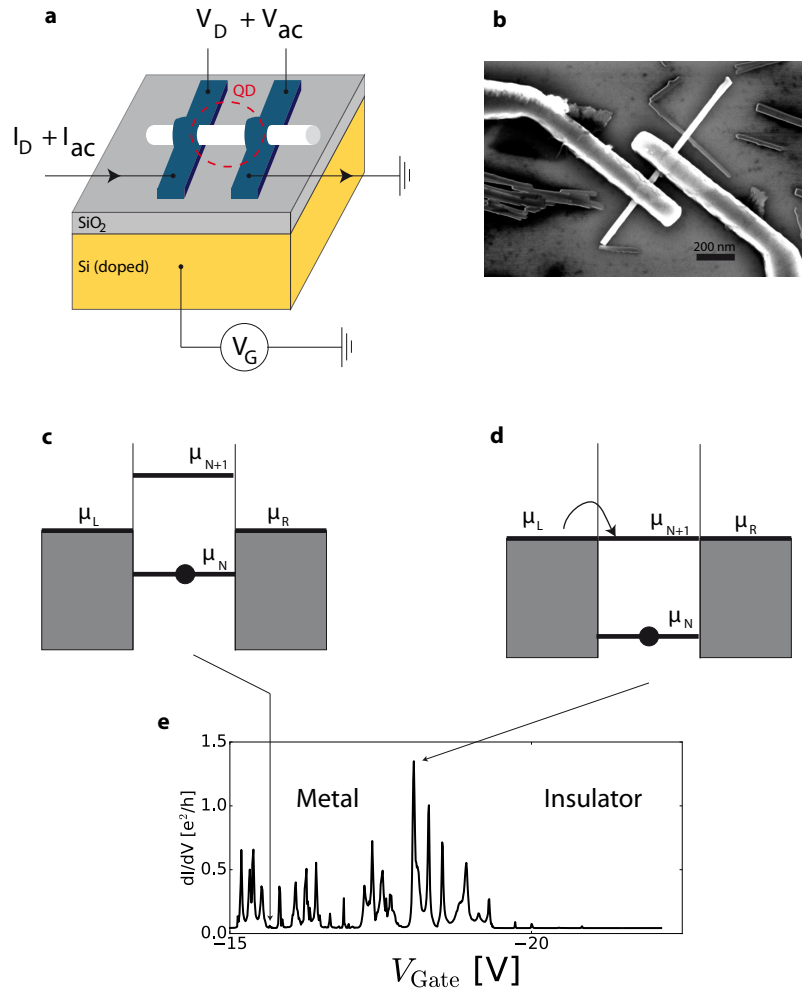


Fig. III.1 **Coulomb peaks.** **a** Sketch of the device. The nanowire is deposited on a silicon dioxide layer on top of a doped silicon substrate. It is contacted with Ti(5nm)/Al(50nm) electrodes. We inject a current,  $I_{DC} + I_{AC}$  and measure the resulting voltage across the device,  $V_{DC} + V_{AC}$ . A DC gate voltage,  $V_G$  can be applied on the doped Si substrate. **b** Scanning electron microscope image of a nanowire device. **c** Energy level structure of the system when transport is blocked. The left (L) and right (R) metallic leads have a continuum of energy level filled with electrons up to the chemical potential,  $\mu_L = \mu_R = E_F$ . The QD have a discrete set of energy levels. **d** When the QD and the electrode chemical potentials are aligned, a current can flow. **e** Conductance,  $dI/dV = I_{AC}/V_{AC}$  measured at zero DC bias, as a function of gate voltage,  $V_{Gate}$ . The conductance exhibits sharp peaks when the QD and the electrodes chemical potential are aligned.

so-called lever arm of the gate. At zero drain bias,  $V_D = 0$ , a low AC excitation provided by the lock-in allows to probe the conductance of the QD as a function of gate voltage,  $V_G$ . The conductance peaks observed experimentally, in Fig. III.1e, correspond to the situation where the chemical potential of the QD is aligned with the chemical potential of the electrodes. These peaks correspond to charge degeneracy points where the energy required to add one electron in the QD,  $\mu_{N+1}(V_G)$  is equal to the energy to remove or add an electron to the left (right) contact,  $\mu_L$  ( $\mu_R$ ). Therefore, electron transport through the QD is possible as long as it occurs electron per electron. Indeed the energy difference  $\mu_{N+2}$ , corresponding to the addition of two electrons in the QD, is significantly higher than  $\mu_{N+1}$  because of the large charging energy  $E_c$ .

The separation between two Coulomb peaks in gate voltage  $\Delta V_G$  can be linked with the energy states of the QD,  $E_N$ , providing that we know the lever arm,  $\alpha_G$ . The lever arm can be determined by applying a voltage  $V_D$  on the QD, which is what we do in the following.

Due to the large charging energy of the device, the number of charges,  $N$ , on the QD is fixed and can be tuned one by one. Therefore, such devices are called single-electron transistors. Their behaviour can be understood from classical arguments[104], and basic quantities such as the charging energy,  $E_c$ , and the lever arm  $\alpha_G$  can be obtained from their characteristics. Fig. III.2a shows different single electron transfers between the NW and the left and right electrodes. We consider an anti-symmetric applied bias such that  $\frac{V_D}{2} = V_L = -V_R$ . Also, we assume that both electrodes have the same capacitance  $C_L = C_R = C_e$  which will be later justified. The electrostatic energy is expressed :

$$E_{\text{el}} = \frac{e^2}{C} \left(N - \frac{q}{e}\right)^2$$

with the total capacitance  $C = 2C_e + C_G$  and an induced charge  $q = C_G V_G$  which depends only on the gate voltage  $V_G$ . The change in energy due to an electron transfer into the NW,  $(N + 1)$ , and outside the NW,  $(N - 1)$  are written :

$$\Delta E_{\text{el}}^{\pm}(N) = E_{\text{el}}(N \pm 1) - E_{\text{el}}(N) = E_C \left(\pm N + \frac{1}{2} \mp \frac{q}{e}\right)$$

At  $T = 0$  K the energy associated with an electron transfer, for example, from left (FL) or to right (TR), must be negative :

$$\begin{aligned} \Delta E_{FL}(N) &= E_C \left(N + \frac{1}{2} - \frac{q}{e}\right) - eV_D/2 < 0 \\ \Delta E_{TL}(N) &= E_C \left(-N + \frac{1}{2} + \frac{q}{e}\right) + eV_D/2 < 0 \\ \Delta E_{FR}(N) &= E_C \left(N + \frac{1}{2} - \frac{q}{e}\right) + eV_D/2 < 0 \\ \Delta E_{TR}(N) &= E_C \left(-N + \frac{1}{2} + \frac{q}{e}\right) - eV_D/2 < 0 \end{aligned}$$

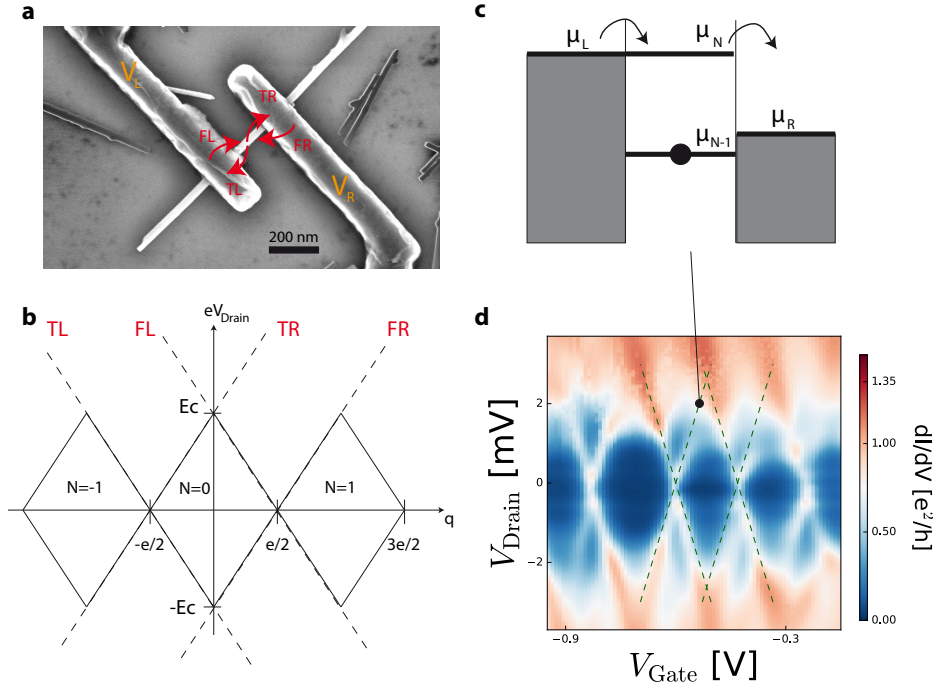


Fig. III.2 **Single electron transistor device and Coulomb diamonds.** **a** Single electron transfer between the NW and the electrodes represented in red. FL(R) denotes an electron transmitted to the NW from the left (right) electrode. TL(R) denotes an electron transmitted, from the NW, to the left (right) electrode. **b** For a given number of electron on the QD,  $N$ , the four energy conditions corresponding to the different electron transfer are represented as dashed line. These conditions are fulfilled within a diamond and transport can not occur in these regions. **c** Position of energy level that allows a current to flow when a voltage,  $V_{\text{Drain}}$ , is applied. **d** Conductance map as a function of drain bias and gate voltage. Low conductance regions define diamonds in the  $V_G, V_D$  plane.

These four conditions are represented as dashed line in Fig. III.2b for  $N = 0$ . For a given  $N$ , the transport is blocked in a region of the  $V$ - $q$  plane which has a diamond shape. We can directly read the value of the charging energy  $E_c$  from the height in  $V_D$  of the Coulomb diamond. From Fig. III.2d we obtain,  $E_c = 2.6$  meV. The capacitance of the gate,  $C_G = \frac{e}{\Delta V_G} = 1.10^{-18}$  F<sup>1</sup> is extracted from the separation between two Coulomb peaks in gate voltage,  $\Delta V_G = 160$  meV, at  $V_D = 0$ . At the voltage threshold,  $V_T = -20$  V where the conductance drops to zero in Fig. III.1, all the conducting electrons have been removed from the QD. Therefore, we can estimate the electronic

1. This value is consistent with an estimation considering a parallel plate capacitor with a rectangular QD, of area  $s = Ld$ , where  $L = 100$  nm and  $d = 30$  nm. Then,  $C_G = \epsilon_{\text{SiO}_2} \epsilon_0 s / d_{\text{SiO}_2} = 5.10^{-19}$  F, with  $\epsilon_{\text{SiO}_2} = 3.9$ . The value obtained from Coulomb diamond is much more accurate since it does not depend on the considered geometry.

density at zero gate voltage from :

$$n = \frac{4C_G V_T}{e\pi L d^2} = 1.8 \cdot 10^{18} \text{ cm}^{-3}$$

In this picture we have assumed that the capacitance of both electrodes were the same. This is justified because the Coulomb diamonds are symmetric with respect to  $V_D = 0$ . The capacitance model, detailed in the following, allows to describe a system with  $C_L \neq C_R$  and accounts for the observation of non-symmetric Coulomb diamonds.

More importantly, we have neglected the discrete energy spectrum in the QD due to quantum confinement of the electronic states. These effects are responsible for the different diamond size observed in Fig. III.2d. A full quantum treatment of the problem requires to solve Schrödinger equation,  $H_N \psi = E \psi$ , with the many-body Hamiltonian :

$$H_N = \sum_{n=1}^N h(\vec{r}_n) + \frac{1}{2} \sum_{n \neq m} V(\vec{r}_m, \vec{r}_n) \quad (\text{III.1})$$

where  $h$  denotes single particle operators and includes a kinetic term,  $\frac{p_n^2}{2m}$ , plus a confinement potential,  $U(\vec{r}_n)$ . The Coulomb potential between two electrons  $V(\vec{r}_m, \vec{r}_n) = \frac{e^2}{|\vec{r}_n - \vec{r}_m|}$  is responsible for the many-body nature of the problem. Nuclei do not appear in this equation as it is written within the effective mass approximation. An approximation to handle the problem is given by the capacitance model which separates the many-body part of the Hamiltonian from the single-particle part.

We will resume the main results of the capacitance model[21] which are useful for the data analysis. The charge  $Q_0$  on the QD is related to the different electrostatic potentials  $V_j$  by the equation :

$$Q_0 = \sum_{j=0}^3 C_{0j} V_j + Q_0^{(0)}$$

with  $j=0$  denotes the QD,  $j=1$  the gate electrode (G),  $j=2$  the source (S) and  $j=3$  the drain electrode (D). The capacitance of the QD,  $C_{00}$ , is related to the other capacitors by  $C_{00} = -\sum_{i=1}^3 C_{0i} > 0$ . The total energy of the QD,  $E$ , is written as a sum of the electrostatic term obtained from the charge,  $Q_0$ , and the energies,  $\epsilon_n^{(0)}$  of the single particle Schrödinger equation :

$$E(N) = \sum_{n=1}^N \epsilon_n^{(0)} + \frac{e^2 N^2}{2C_{00}} + |e| N \sum_{j=1}^3 \frac{C_{0j}}{C_{00}} (V_j - V_j^{(0)})$$

The electrochemical potential of the QD is defined as  $\mu_N = E(N) - E(N-1)$ . The conductance peaks occur when  $\mu_{N+1} = \mu_L = \mu_R$  that is at :

$$V_G(N+1) = \frac{1}{e\alpha_G} (\epsilon_{N+1} + E_c N - |e| \sum_{i=2,3} \alpha_i V_i - \mu_R)$$

with the gate voltage,  $V_G = V_{j=1}$ , the charging energy,  $E_c = \frac{e^2}{C_{00}}$ , and the lever arm of the gate,  $\alpha_G = -\frac{C_{01}}{C_{00}}$ . From this relation we can get the magnetic field dependence  $\epsilon_N(B)$  if we assume that the charging energy and the lever arm does not depend on B :

$$V_G(N)_B - V_G(N)_{B=0} = \frac{1}{e\alpha_G}(\epsilon_N(B) - \epsilon_N(B=0)) \quad (\text{III.2})$$

Also, at zero magnetic field, the separation of two subsequent conductance peaks contains both the single particle level separation and the charging energy :

$$\Delta V_G = \frac{1}{|e|\alpha_G}(\epsilon_{N+1} - \epsilon_N + E_c)$$

The different slopes of the Coulomb diamond boundaries represented as dashed line in Fig. III.2c are denoted  $m_1$  and  $m_2$ . Within the capacitance model their difference gives the lever arm of the gate :

$$|m_1 - m_2| = \frac{1}{\alpha_G}$$

The diamond boundaries intersect at  $V_D = \frac{1}{e}(\epsilon_{N+1}^{(0)} - \epsilon_N^{(0)} + \frac{e^2}{C_{00}})$ .

### III.1.2 Excited state spectroscopy

At large negative gate voltages, we observed sharp conductance lines due to a reduced coupling between the NW and the metallic electrodes. The first excited state of the QD can be resolved, as shown by the red arrow in Fig. III.3a. The difference in gate voltage,  $\Delta V_G = 50$  mV, between this conductance line and the diamond boundary, pointed by the black arrow, is linked to the difference between the first excited state  $\epsilon_N^1$  and the ground state  $\epsilon_N^0$  through the relation :

$$\Delta V_G = \frac{1}{|e|\alpha_G}(\epsilon_N^1 - \epsilon_N^0)$$

We find for the lever arm, calculated from the capacitance model with the slopes of the diamond boundaries,  $\alpha_G = 0.034$ , and the energy of the first excited state  $\epsilon_N^1 - \epsilon_N^0 = 1.7$  meV. An approximation for the mean level spacing of the single-particle spectrum,  $\delta = \langle \epsilon_N^1 - \epsilon_N^0 \rangle$ , is given by the density of states in the QD. The remaining electronic density is estimated from the gate voltage separation between the Coulomb peak and the voltage threshold where the NW is fully depleted,  $\Delta V_G \approx 2$  V, and,  $n = \frac{4C_G\Delta V_G}{e\pi d^2 L} = 4.4 \cdot 10^{16}$  cm<sup>-3</sup>. This corresponds to a Fermi energy of  $E_F = 17$  meV calculated with the effective mass of InAs,  $m^* = 0.026m_0$  with  $m_0$  the free electron mass. The mean level spacing is obtained from the density of states  $\rho(E_F)$  and the QD volume :

$$\delta = \frac{4}{\rho(E_F)\pi d^2 L} = 1.8 \text{ meV}$$

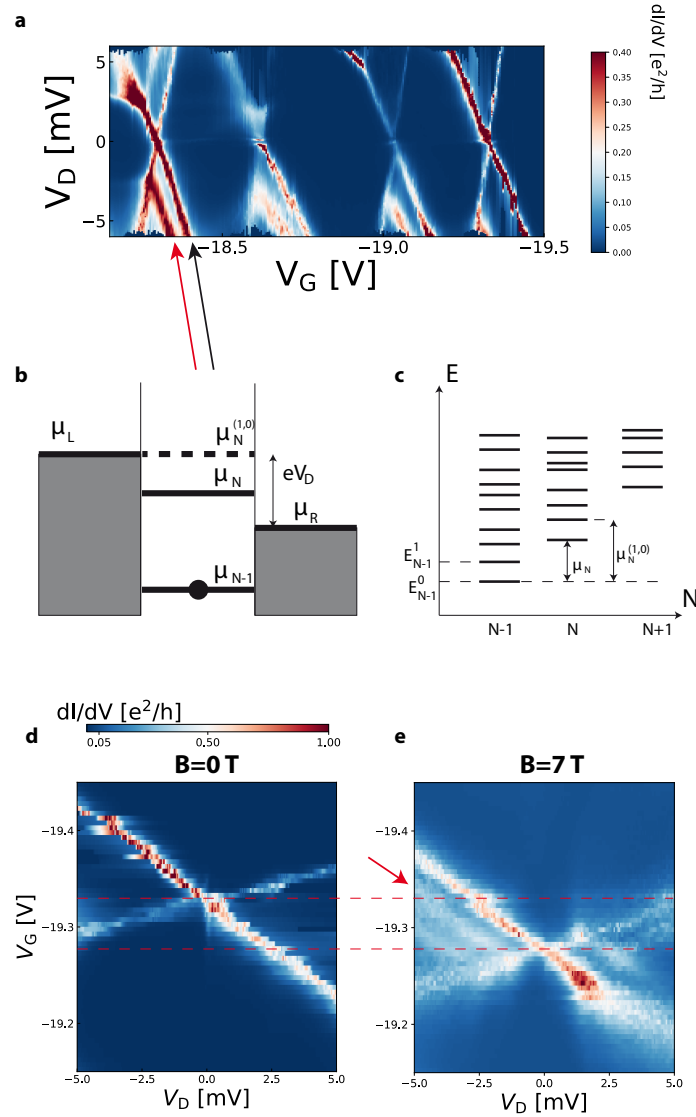


Fig. III.3 **Discrete energy spectrum due to quantum confinement.** **a** Conductance map as a function of gate voltage and drain bias. A Coulomb diamond boundary is shown by the black arrow. Additional line due to quantum confinement in the QD, is pointed by the red arrow. **b** Position of energy level showing the chemical potential corresponding to the transition between a ground state and an excited state of the QD. **c** Representation of the QD discrete energy spectrum  $E_N^n$ . The energy depends on the number of electron  $N$  present in the QD. For a given  $N$ , the different excited states are labelled by  $n$ . **d** Conductance map showing the diamond boundary at zero magnetic field. Note that the two axes are interchanged with respect to figure (a). **d** Same conductance map with a magnetic field applied perpendicular to the NW axis,  $B = 7$  T. The red dashed line shows the shift of the Coulomb node in gate voltage. An additional conductance line is pointed by the red arrow, it is due to the Zeeman splitting of the electronic states.

which is very close to the experimental value.

As shown by comparing Fig. III.3d and e, under large magnetic field we observed a shift of the conductance peak,  $\Delta V_G = 54$  mV, represented by the red dashed lines. The lever arm at zero field,  $\alpha_G^{B=0} = 0.038$ , and at  $B = 7$  T,  $\alpha_G^{B=7T} = 0.034$ , changes by 10%. We retain the value at zero field which is more precise due to sharper conductance peaks. From Eq. (III.2), we find a shift in energy of  $\epsilon_N(B = 7T) - \epsilon_N(0) = \alpha_G^{B=0} \Delta V_G = 2$  meV. Also the additional conductance line in Fig. III.3e, marked by the black dashed line, is found at  $\Delta V_D = 2$  mV from the diamond boundary. This exactly corresponds to the energy shift we just calculate using the gate voltage shift. This line is not present at zero field, see Fig. III.3d. It appears due to the Zeeman splitting of the electronic level by the magnetic field<sup>1</sup>. The Zeeman energy shift is  $E_z = \frac{1}{2}g\mu_B B$ . Thereby, we can extract the value for the Landé g-factor, we find  $g = 10$  consistent with previous study on InAs NW[105].

The energy spectra of QDs can be predicted when the number of electron in the QD is low and when the confinement potential is well known. In other words when the confinement potential  $U(\vec{r}_n)$  which enters in Eq. (III.1) is optimized. Remarkable agreements with theory has been obtained in InGaAs/AlGaAs quantum wells[106].

However, when the Thouless energy,  $E_T = \frac{\hbar D}{d^2} > 4$  meV, is larger than the mean level spacing, the system becomes extremely sensitive to the boundary conditions and the energy levels fluctuate around the mean level spacing value[107]. In that case, a statistical description of the level spacing is given by random matrix theory.

## III.2 Random matrix theory

As the typical mean level spacing is smaller than the Thouless energy, the addition energy will fluctuate as we sweep the gate voltage. The distribution function describing these fluctuations can give information about the fundamental symmetries present in the system. Within random matrix theory (RMT), the Hamiltonian,  $H$ , of a system is written with a random set of matrix elements. However, it satisfies symmetry requirements. Based on the work of Wigner[108], Dyson[109] showed that there is three ensembles of random matrices defined in term of the symmetry properties of the Hamiltonian<sup>2</sup>. These correspond to the Gaussian orthogonal (GOE), unitary (GUE) and symplectic ensembles (GSE). The ensemble which applies depends on the system symmetries. For example, if the system is invariant under time reversal and under rota-

---

1. The vector potential  $\vec{A}$ , associated with the magnetic field, can not affect the electron momentum,  $\vec{p}$ , because its component perpendicular to the NW axis,  $p_y$  and  $p_z$  are forbidden at low energy. Indeed, due to the boundaries of the NW, the wave vectors are discrete,  $k_{y,z} = \frac{2\pi}{d}n_{y,z}$ . Assuming a parabolic dispersion,  $E(k_y) - E(0) = \frac{\hbar^2}{2m}(\frac{2\pi}{d})^2 = 63$  meV. This is much higher than all the energies involved in the experiment. We can estimate the typical cyclotron energy for a free electron at  $B = 7$  T,  $\hbar\omega_c = \frac{\hbar e B}{m^*} = 30$  meV.

2. There is now 10 ensembles identified in physical context[110] due to the consideration of additional symmetries. For example, quantum chromodynamics and superconductivity requires to consider chiral and particle-hole symmetry, respectively.

tion symmetries, the Hamiltonian is a real symmetric matrix and the ensemble which applies is the GOE. With broken time reversal symmetry, the GUE applies. Finally, with strong spin-orbit coupling, the GSE applies. The symmetries corresponding to the three ensembles are summarized in Table. III.4 from Ref. [111].

TABLE I. Classical random matrix ensembles.<sup>a</sup>

	GOE	GUE	GSE
Symmetries	integer spins and/or even number of half-integer spins $T$ is good ( $T^2 = 1$ )	any spin $T$ is not good	odd number of half-integer spins $T$ is good ( $T^2 = -1$ )
Hamiltonian Structure	Real symmetric $H = H^t = H^*$	Complex hermitian $H = H^\dagger$	Quaternion real $H = H_0 \mathbf{I} + i \sum_{j=1}^3 H_j \sigma_j$ $H_0 = (H_0)^t = (H_0)^*$ $H_j = -(H_j)^t = (H_j)^*$
$N = 2$ Example	$H = \begin{bmatrix} a+b & c \\ c & a-b \end{bmatrix}$ $a, b, c \xrightarrow{\text{i.i.d.}} G(0, v^2)$	$H = \begin{bmatrix} a+b & c-id \\ c-id & a+b \end{bmatrix}$ $a, b, c, d \xrightarrow{\text{i.i.d.}} G(0, v^2)$	$H_0 = \begin{bmatrix} a & b \\ b & c \end{bmatrix}, H_1 = \begin{bmatrix} 0 & -d \\ d & 0 \end{bmatrix}$ $H_2 = \begin{bmatrix} 0 & e \\ -e & 0 \end{bmatrix}, H_3 = \begin{bmatrix} 0 & -f \\ f & 0 \end{bmatrix}$ $a, b, c, d, e, f \xrightarrow{\text{i.i.d.}} G(0, v^2)$

<sup>a</sup> Here,  $t$  denotes 'transpose' and  $*$  denotes 'complex conjugation' and  $\dagger$  denotes 'conjugate transpose' of the matrix respectively. For GSE,  $(\sigma_1, \sigma_2, \sigma_3)$  are Pauli spin matrices and  $\mathbf{I} = \begin{bmatrix} \mathbf{1} & 0 \\ 0 & \mathbf{1} \end{bmatrix}$  is the identity matrix.

Fig. III.4 From Ref. [111].

These different ensembles give different nearest-neighbor level spacing distribution  $P(s)$ , which can be compared with experiments. This function is the probability density for two neighboring levels,  $\epsilon_n$  and  $\epsilon_{n+1}$  having the spacing  $s$ .  $P(s)$  can be calculated for the different ensembles[112]. An approximation commonly used is given by the "Wigner surmises" which is exact for  $2 \times 2$  matrix :

$$P_\beta(s) = a_\beta s^\beta e^{-b_\beta s^2}$$

where  $a$  and  $b$  are constant,  $\beta$  depends on the ensemble.  $\beta = 1$  for the GOE,  $\beta = 2$  for the GUE and  $\beta = 4$  for the GSE. The  $\beta$  parameter characterizes the level repulsion because it describes the probability density when the spacing  $s \rightarrow 0$ , i.e the probability to find two levels at the same energy. The spacing distribution for the different ensembles is shown in Fig. III.5 from Ref. [112].

Thus, by identifying the probability density for the level spacing found experimentally with a Wigner probability density  $P_\beta(s)$ , one can obtain information about the system symmetries. Indeed, the probability density in our system is expected to be  $P_{\beta=1}$  or  $P_{\beta=4}$  depending on the presence of spin-orbit scattering[107].

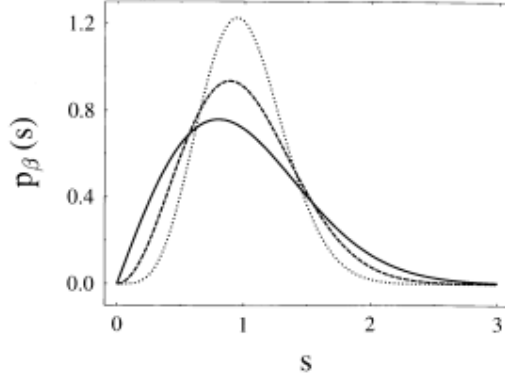


Fig. 12. The Wigner surmises  $p_\beta(s)$  for the nearest-neighbor spacing distribution. The solid line is the result for orthogonal symmetry ( $\beta = 1$ ), the dashed line is the result for unitary symmetry ( $\beta = 2$ ) and the dotted line is the result for symplectic symmetry ( $\beta = 4$ ). We notice the importance of the repulsion law  $s^\beta$  for small spacings.

Fig. III.5 From Ref. [112].

Fig. III.6a shows more than 140 Coulomb diamonds, measured on a large range of gate voltage around  $V_G = 0$ . At  $V_D = 0$ , the spacing between two Coulomb peaks in gate voltage  $\Delta V_G$  are extracted. From the lever arm obtained in Fig. III.2d near  $V_G = 0$ , we convert the spacing in gate voltage into an addition energy to add one electron to the QD,  $\epsilon = e\Delta V_G \alpha_G$ . The corresponding histogram of level spacing is shown in Fig. III.6b. This distribution is characterized by two maxima. One is at the Coulomb energy  $E_c = 2.6$  meV, the other at  $E_c + \delta$  where  $\delta = 1$  meV is the mean level spacing.  $\delta$  can be estimated from the density of states  $\rho(E_F)$  and the volume  $V$  of the QD. We find  $\delta = \frac{1}{\rho(E_F)V} = 1.1$  meV with a Fermi energy of  $E_F = 196$  meV.

Adding one electron in the QD requires an energy  $\epsilon = E_c + \delta$ , adding a second electron costs only  $\epsilon = E_c$  in the case of spin degenerate single particle state. Therefore, we expect a bimodal distribution[107] :

$$P(E) = \frac{1}{2}(\delta(E - E_c) + \frac{1}{2}P_\beta(\frac{E - E_c}{2}))$$

The distribution for  $\beta = 4$  is shown as red dashed line in Fig. III.6b as an example. Because of insufficient histogram resolution, we can not discriminate between the different Wigner distributions for the mean level-spacing. However, the dip in the probability density between  $E_c$  and  $E_c + \delta$  shows a departure from a Poissonian distribution which is characterized by  $P(0) = 1$ .

The Landauer formula for a single electronic mode,  $G = \frac{2e^2}{h}T$ , relates the conductance to the transmission coefficient of the mode,  $T$ . In a system described by RMT, the transmission coefficient,  $T$ , also follows a distribution related to the ensemble and to the system symmetries. In Fig. III.6c, we extracted the distribution of the conductance  $P(G)$  from the Coulomb peak heights. However, when the number of electronic mode is larger than 1, which is the case at zero gate voltage, the different conductance distri-

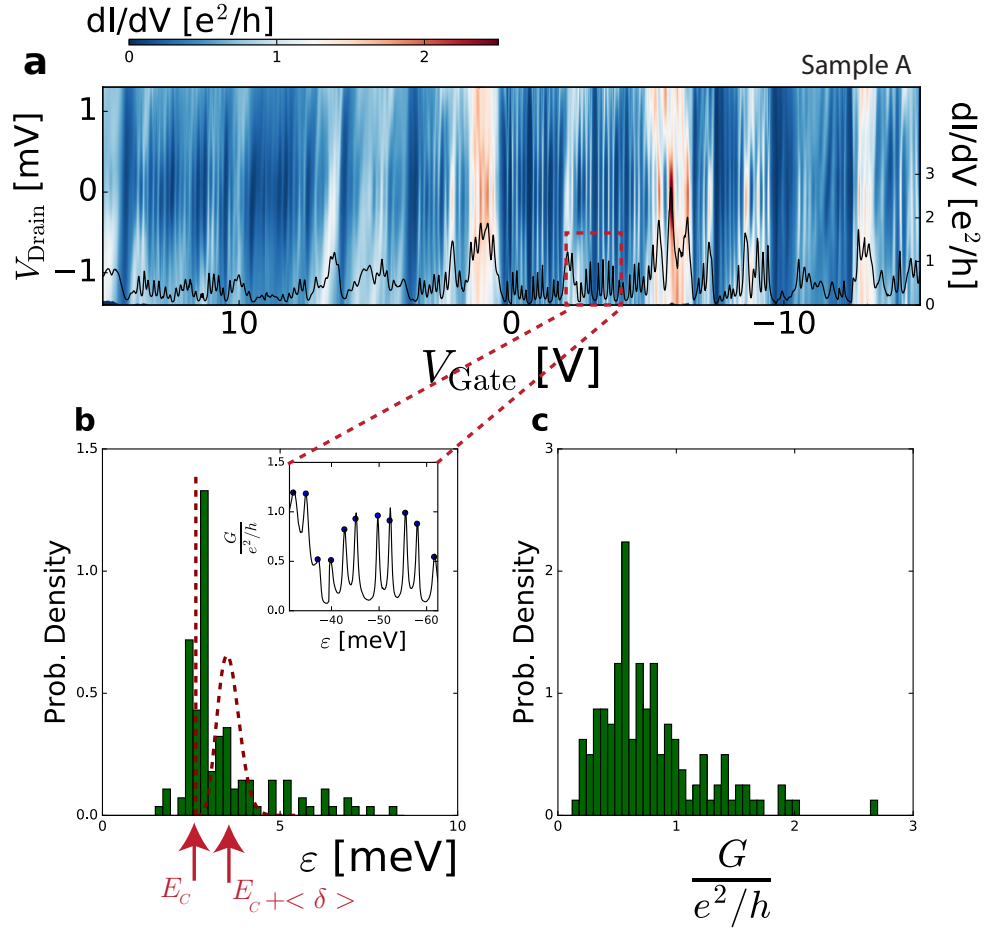


Fig. III.6 **Statistics on the Coulomb peaks spacing and conductance fluctuations.** **a** Conductance map showing more than 140 Coulomb diamonds. The conductance at zero drain bias  $V_D = 0$  is shown as a black continuous line. The spacing between two Coulomb peaks in gate voltage is converted in an energy  $\epsilon$ . **b** Probability density to find an energy in the range  $\epsilon + d\epsilon$ . The probability density is peaked at the QD charging energy  $E_c$ . A second smaller peak is observed at  $E_c + \delta$ . One of the Wigner bimodal distribution is represented as a red dashed line. **c** Probability density for the conductance.

bution predicted by RMT,  $P(G)$ , becomes almost equivalent, see Fig. 11 of Ref. [107] and a comparison between theory and experiment is challenging. Nevertheless, this broad conductance distribution indicates a fluctuating coupling parameter  $\Gamma$  between the electrodes and the NW. The conductance peaks are broadened by finite lifetime effect which depend on the coupling between the QD and the electrode. Therefore,  $\Gamma$  can be obtained by fitting a conductance peak with a Breit-Wigner function[113]. The large variation of  $\Gamma$  as a function of gate voltage will be important to understand the superconducting properties of the device in the last section of this chapter.

Following the pioneered work of Anderson[114], which showed that a metal becomes insulating by increasing disorder through a random on-site potential energy, random matrix theory is now widely used to describe the metal insulator transition.

### III.3 Mobility edge

A particularity of these narrow nanowires (NWs) is that they can be driven across a metal insulator transition with the gate voltage as shown in Fig. III.1e. This was never reported before for InAs NWs. It is because the use of relatively thick NWs in previous studies,  $d \approx 100$  nm prevent them from being fully depleted by a back-gate. Indeed, the gate induced electric field is screened over the Debye length  $\lambda_D$  and the NW can be fully depleted only if its diameter is such that :  $\lambda_D \approx d$ .

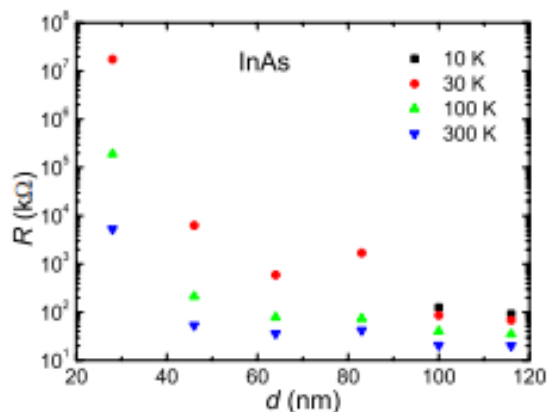


Fig. III.7 From Ref. [92]. Diameter dependence of the resistance of InAs nanowires at zero backgate voltage for different temperatures. The electrodes spacing is  $1 \mu\text{m}$ .

Previous studies have shown that the conductivity and the mobility of InAs nanowires decrease with decreasing their diameters[115, 92]. In particular in Fig. III.7, from Ref. [92], it is shown that InAs NWs becomes insulating below a typical diameter of  $d=50$  nm. By comparing the data point at  $d=45$  nm and 30 K,  $R \approx 7 \cdot 10^4$  kΩ (measured with an electrode spacing of  $L=1 \mu\text{m}$ ) with our NW resistance  $R \approx 30$  kΩ, we find that the conductivity,  $\sigma = \frac{4L}{R\pi d^2}$  is, at least,  $10^3$  times larger than for undoped

NWs. Thus, the NWs used for this study are conducting at low temperature due to the Si doping. In other words, all the conduction electrons come from the Si dopants. Assuming that each Si atom provides one electron, the density of Si dopants is equal to the electronic density extracted from Coulomb peaks measurement. Then, the mean dopant spacing is estimated,  $\langle r \rangle \approx \frac{1}{n^{(1/3)}} \approx 9$  nm. This average distance between dopants is smaller than the Bohr radius,  $a_0 = \frac{4\pi\epsilon_0\epsilon\hbar^2}{me^2} = 30.2$  nm, with  $\epsilon = 15.15$ . At this high dopant concentration, it is expected that an impurity band is formed, as expressed by the Mott criterion for metallicity,  $a_0N_c^{1/3} \approx 0.25$ .

When the impurity band is fully depleted by applying large negative gate voltage, a metal insulator transition occurs. On the metallic side,  $k_F l > 1$  while on the insulating side  $k_F l < 1$ . The mobility edge is defined as the critical potential,  $\mu_c$  where the metal insulator transition occurs.

We now turn to the superconducting features of the device which have been observed across the metal insulator transition.

### III.4 Superconducting correlations

The superconducting gap of bulk aluminum is known[116] to be  $\Delta_{Al} = 180 \mu\text{eV}$ . Superconducting features manifest in the conductance of the device at low voltage when  $eV_D/2 < \Delta_{Al}$ . In this section, the conductance is measured with a low AC excitation corresponding to  $V_{ac} < 10 \mu\text{V}$ .

At low gate voltage, where the NW is nearly depleted, we observed a conductance peak at  $V_D = 2\Delta/e$ , which corresponds to an effective superconducting gap  $\Delta \approx 150 \mu\text{eV}$ , as shown in Fig. III.8b. This peak corresponds to elastic quasiparticle cotunneling, where the peaks in the density of states of the two superconducting electrodes are aligned, as sketched in Fig. III.8a. At this gate voltage, on the insulating side of the metal insulator transition, the coupling between the NW and the superconducting lead is greatly reduced and the conductance is low. A conductance peak at  $eV_D = 2\Delta$  is also expected when two superconductors are separated by a tunnel barrier[50]. It is due to the sharp and large density of states in the superconductor at the gap edges. The value extracted for the superconducting gap,  $\Delta = 150 \mu\text{eV}$  is consistent with previous study, see for example the evaporated Al device in Ref. [117].

For larger gate voltage, in the metallic side of the metal insulator transition, above the mobility edge, we observed an additional conductance peak at  $eV_D = \Delta$  as shown in Fig. III.8d. As no states are accessible in the superconductor at voltage,  $eV_D < 2\Delta$ , transport occurs through Andreev reflection, as sketched in Fig. III.8c, and peaks are expected at  $eV_n = \frac{2\Delta}{n}$  where  $n=1,2,3..$  [118, 119] when the QD is well coupled with the superconducting electrodes. Conductance peak at  $eV_D = \Delta$  has been observed in small SNS structures such as atomic contact[120], InAs NW[121], InSb NW[122], carbon nanotube[123] and TI nanoribbon[124].

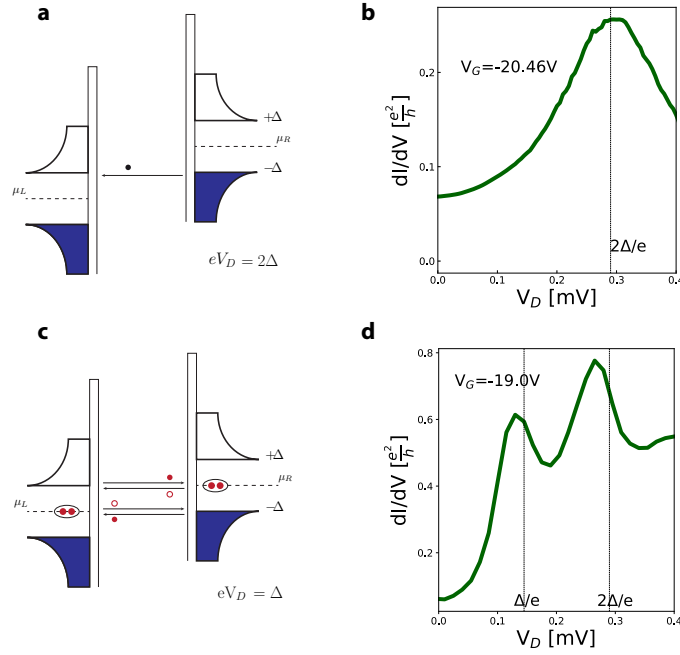


Fig. III.8 **Superconducting correlations.** **a** When two superconductors are separated by a barrier, a conductance peak is expected when the superconducting density of states of the two electrodes align. It corresponds to an apply drain voltage such that  $eV_D = 2\Delta$ . **b** Conductance of the device as a function of drain voltage measured at low gate voltage. **c** At low drain voltage,  $eV_D < 2\Delta$ , transport occurs through Andreev reflection where an electron is reflected as a hole, adding a Cooper pair to the superconducting condensate. Conductance peaks are expected at  $eV_D = \frac{2\Delta}{n}$  where  $n=1,2,3,\dots$  **d** A conductance peak is observed at  $eV_D = \Delta$ , due to Andreev reflection  $n = 2$ .

### III.4.1 Ground state transitions

The sub-gap resonances (SGRs) are probed at voltage such that  $eV_D < 2\Delta$ . Their formation and their position in energy depends on the different energy scales : the superconducting gap  $\Delta$ , the coupling between the QD and the superconductor  $\Gamma_s$ , the charging energy  $E_c$  and the energy of the QD level with respect to the Fermi energy  $\epsilon_0$ [69]. In particular in our experiment,  $\epsilon_0$  is tunable by the gate voltage. Furthermore, the coupling  $\Gamma_s$  fluctuates for different region of gate voltage as it is linked[68] with the normal coupling  $\Gamma$ , previously discussed.

For example, in the conductance map as a function of gate voltage, in Fig. III.9a, we observed the SGRs across a charge degeneracy point of the QD, which correspond to a Coulomb diamond node. As shown in Fig. III.9b the SGR conductance peaks are shifted at lower voltage  $V_D$ , but do not cross zero energy  $eV_D = 0$ . At another Coulomb node, such as the one shown in Fig. III.9c, the SGR crosses zero energy. This crossing result in a conductance peak at  $V_D = 0$  as shown in Fig. III.9d. In the next section, we

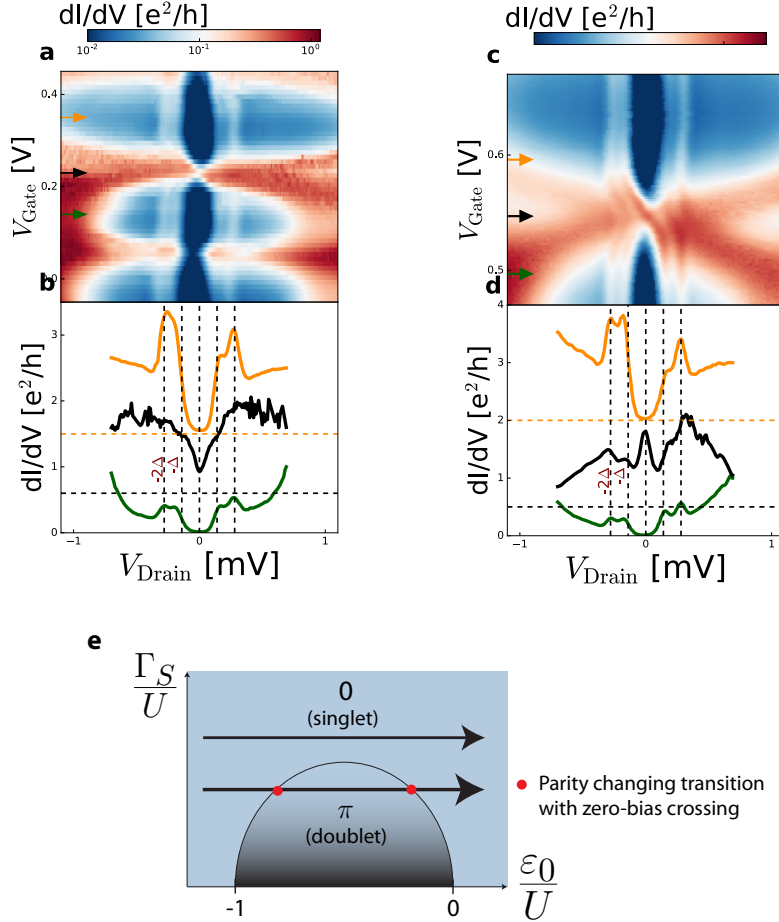


Fig. III.9 **Evolution of sub-gap resonance with the gate voltage.** The conductance maps **a**, **c** and the corresponding plots at selected gate voltages **b**, **d** show the spectra of the Andreev QDot for two regimes of weak and strong coupling  $\Gamma_s$ , respectively. In the strong coupling regime, only the conductance ridges at  $V_D = \Delta/e$  and  $V_D = 2\Delta/e$  are seen. In the weak coupling regime, SGRs form at energies below the superconducting gap energy  $eV_D < \Delta$ . **e** Phase diagram of the S-QD-S system as a function of the charging energy  $U$ , the QD level  $\epsilon_0$ , and the coupling to the lead  $\Gamma_s$ . At large coupling  $\Gamma_s$ , only the singlet ground state can be observed upon changing the gate voltage. At low coupling  $\Gamma_s$ , a parity-changing phase transition from the singlet phase to the doublet phase is identified as a zero bias crossing of the SGRs.

will see that the SGRs can also cross zero energy in the middle of a Coulomb diamond, far from the charge degeneracy point. The crossing of the SGR at zero energy signal a quantum phase transition of the Andreev QD ground state as shown in the phase diagram, Fig. III.9e. At large coupling with the superconducting leads,  $\Gamma_s > E_c$ , the ground state of the QD is a singlet non-degenerate BCS like states. In this regime, the SGRs result from Andreev reflection and no zero bias crossing are expected as a function of gate voltage. At low coupling  $\Gamma_s < E_c$ , the ground state depends on the relative position of the QD level  $\epsilon_0$  with respect to the Fermi energy and zero bias crossing can occur as a function of gate voltage. By equating the energy of the BCS singlet state and the energy of the spin degenerate doublet state one can draw a line in the parameter space which separates the two ground states[68], as discussed in chapter 1. This line defines the phase diagram in Fig. III.9e. Furthermore, at low coupling, the energy of the SGR depends on the ratio between the superconducting gap and the Kondo energy,  $k_B T_k$ .<sup>1</sup> Indeed, in the absence of Kondo screening  $k_B T_k \ll \Delta$ , a local moment due to the electron spin is present on the QD when it contains an odd number of electron. In this regime, a Shiba bound state is formed on the QD and is characterized by a conductance peak at zero voltage. The interaction between local magnetic moments and BCS states has been addressed theoretically by Yu, Shiba and Rusinov[76]. Shiba states have been observed by STM at magnetic impurities on top of superconductor[77, 125]. Their behaviour in a magnetic field has been observed in a NS junction on a InAs/InP NW[126]. An additional way to probe the singlet-doublet phase diagram is by controlling the phase between the two superconducting electrodes[127]. Remarkable agreements between theory and experiment have been obtained in nano-SQUIDS[70, 71].

### III.4.2 Shiba states across the mobility edge

The SGRs have been observed across the metal insulator transition as shown in Fig. III.10a. On the metallic side of the transition at high gate voltage  $V_G > -19.4$  V, the drain-voltage positions of the SGRs fluctuate due to fluctuation in the coupling parameter  $\Gamma_s$ . Across the transition, the four last QD levels, Fig. III.10bcde, show a remarkable evolution from the intermediate coupling regime to the weak coupling regime[128]. In Fig. III.10b, a peak corresponding to Andreev reflection is observed at  $V_D = \Delta/e$ . It corresponds to a relatively large coupling  $\Gamma_s$  on the phase diagram shown in Fig. III.9e where the system is in the BCS singlet state and no ground state transition is expected as a function of gate voltage. In Fig. III.10c and d, a Shiba resonance corresponding to a zero bias peak is resolved. For these more localized levels, the coupling  $\Gamma_s$  is low and the system ground state is switched by the gate voltage across a charge degeneracy point. The last localized level in Fig. III.10e is in the weak-coupling regime where only quasiparticle tunneling is observed as conductance peaks at  $V_D = 2\Delta/e$ .

---

1. The Kondo temperature,  $T_k$ , can be expressed as a function of  $\Gamma_s$  and  $E_c$ [68].

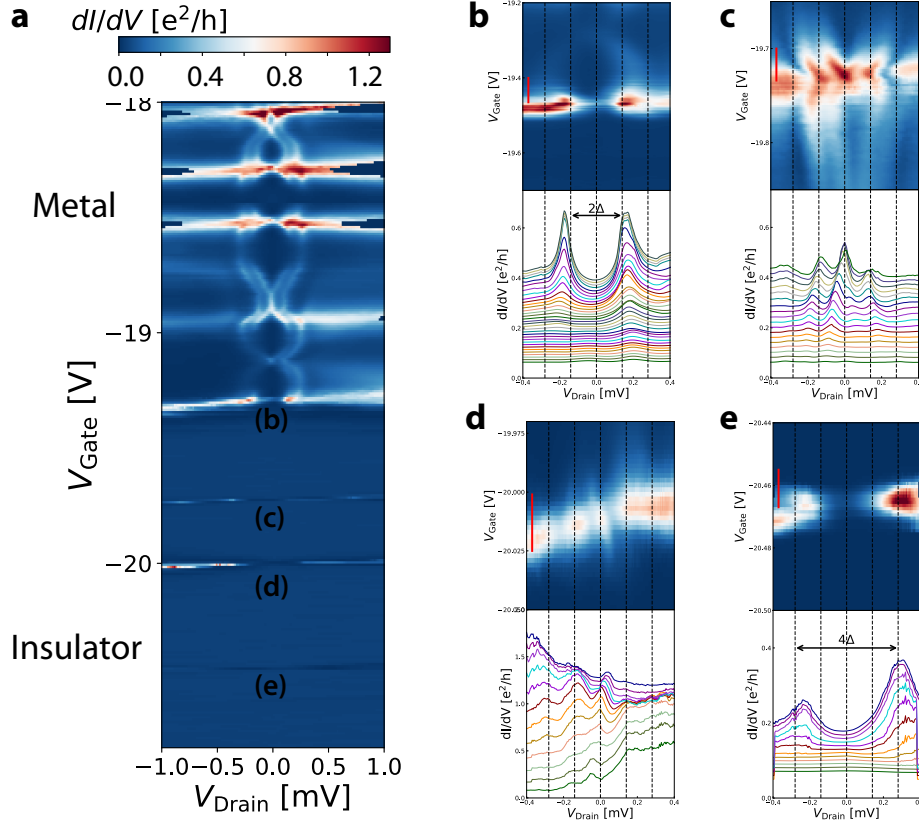


Fig. III.10 **Superconducting correlations across the metal insulator transition.** **a** Conductance map as a function of drain bias and gate voltage. **bcde** Enlargements on the last QD levels. The waterfall plots are shown for the range indicated by vertical red bars on the corresponding color maps. The shifts between curves are respectively of 0.01, 0.02, 0.1, 0.01  $e^2/h$ . **b** On this level, only conductance peaks at  $V_D = \Delta/e$  are observed, which are the signature of Andreev reflections and correspond to a large coupling  $\Gamma_s$  in the phase diagram. **cd** On these two more localized levels, the crossing of the conductance peaks at zero bias corresponding to the ground state transition is observed. **e** Finally, on the last localized level, only the conductance peaks at  $V_D = 2\Delta/e$ , are observed, indicating the absence of Andreev reflections and only the presence of quasiparticle cotunneling.

In the regime corresponding to intermediate coupling, the ground state of the system can be tuned by an electric or magnetic field effect, as discussed in chapter 1. This is interesting in the case of a measurable Josephson current through the system. The BCS singlet state minimizes its energy when the phase difference between the two superconductors is zero,  $\varphi = 0$ , this corresponds to a Josephson current phase relation,  $I_J = I_c \sin(\varphi)$ . When the ground state is changed to a spin doublet, the magnetic moment on the QD leads to a phase offset in the Josephson current phase relation,  $I_J = I_c \sin(\varphi + \pi)$ [75]. Therefore, the Josephson current is sensitive to small variations in the device electrostatic environment and the device can be used as a sensor[98]. Such a sensor, in contrast with conventional SQUID magnetometers, is suitable to measure the magnetization of small molecules.

The observation of the superconducting proximity effect, across the metal insulator transition, at such low carrier density make these doped NWs interesting in the context of Majorana physics[129]. Indeed, the formation of Majorana zero energy states can be obtained in one dimensional systems[100] coupled to superconductor. At the metal insulator transition, the NW likely contains a single spin degenerate electronic mode,  $\lambda_F \approx d$ . Furthermore, the large Lande g-factor reported in this study  $g = 10$ , make these NWs suitable to realize a sufficient Zeeman splitting of the spin states, corresponding to the condition necessary for the formation of Majorana zero energy modes,  $E_z > \sqrt{\mu^2 + \Delta^2}$ , while maintaining superconductivity.

The high-coupling regime  $\Gamma_s \gg E_c$  has not been observed in this study. It is antagonist with the Coulomb blockade regime. In the high coupling regime, higher order multiple Andreev reflection processes are observed[124] and Josephson current can flow across the device[11].

## III.5 State of the art

Quantum dots coupled to superconducting leads have been reviewed in 2011, from a theoretical[69] and an experimental[128] perspective. We will try to review research into Andreev quantum dot physics reported after 2010 with a focus on experiments.

Andreev bound states, discussed in chapter 1, have been observed in quantum dots by using a normal metal as a tunnel probe to infer the density of states of the quantum dot formed between two superconductors connected in a SQUID geometry. In this configuration, the phase dependence of the Andreev states can be probed by controlling the flux in the superconducting loop. Such a device is shown in Fig. III.11a from Ref. [70], it is conveniently done in a single lithography step by angle evaporation. Moreover, the gate voltage allows to study the phase periodicity of the Andreev states in the doublet and in the singlet ground states revealing the offset of  $\pi$  in the current phase relation. These experiments were done in carbon nanotubes[70, 72] and InAs nanowires[127], they are shown in Fig. III.11. The  $\pi$  offset in the Andreev spectrum implies that the Kondo effect is too weak to screen the magnetic spin of the doublet ground state.

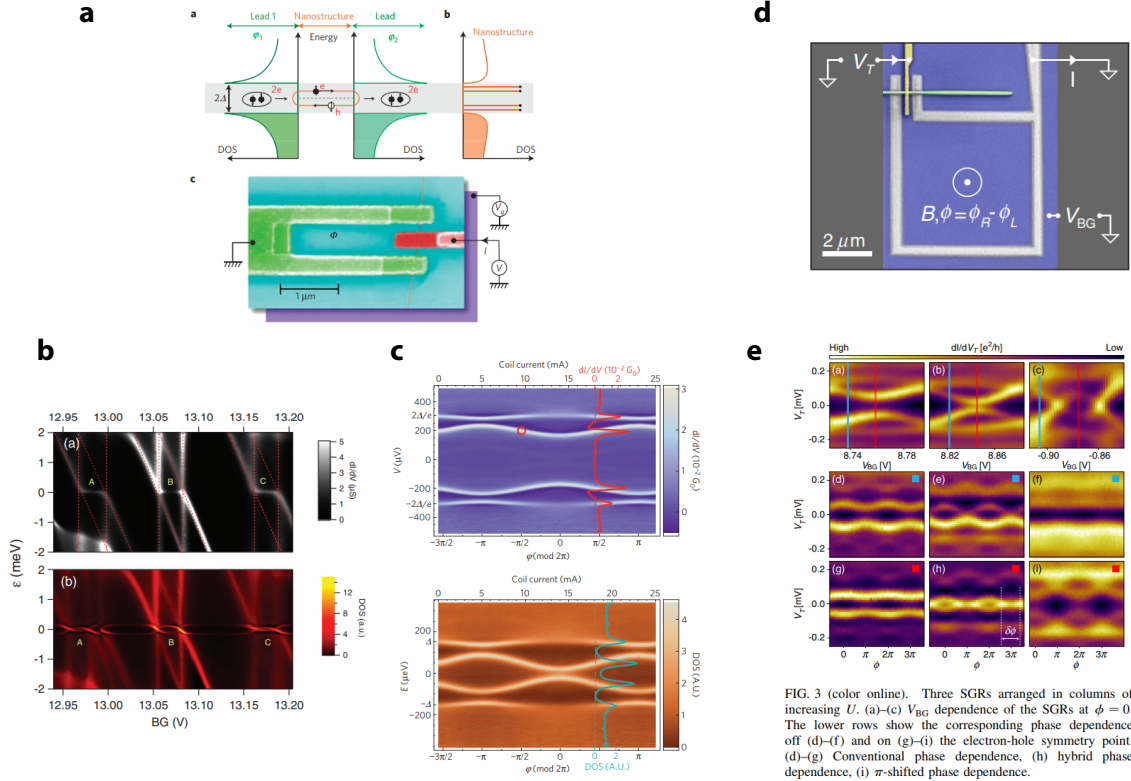


FIG. 3 (color online). Three SGRs arranged in columns of increasing  $U$ . (a)–(c)  $V_{\text{BG}}$  dependence of the SGRs at  $\phi = 0$ . The lower rows show the corresponding phase dependence off (d)–(f) and on (g)–(i) the electron-hole symmetry point. (d)–(g) Conventional phase dependence, (h) hybrid phase dependence, (i)  $\pi$ -shifted phase dependence.

Fig. III.11 **Andreev bound states in quantum dots.** **a** Sketch of Andreev bound states and SEM image of a carbon nanotube device from Ref. [70] **b** Transport maps in the normal (up) and superconducting (down) states from Ref. [72]. **c** Phase dependence of the Andreev bound states in quantum dot from Ref. [70]. **d** SEM image of an InAs nanowire device from Ref. [127]. **e** Phase periodicity of the Andreev bound states in the singlet and doublet ground states from Ref. [127].

The interplay between the Kondo effect and superconductivity has been studied in S-QD-S geometries where small Josephson current has been reported[130, 131, 132]. This interplay depends on the superconducting gap energy  $\Delta$  and the Kondo temperature  $T_K$ . The superconducting gap  $\Delta$  has been tuned by a magnetic field in InAs/InP nanowire quantum dot[131]. A side gate has been used to control the Kondo effect in InAs quantum dot[130]. In carbon nanotube[132], supercurrent has been measured in Coulomb diamond showing the Kondo effect in the normal states.

The Zeeman splitting of the sub gap resonance has been resolved in a N-QD-S geometry[126]. The use of vanadium as S electrode allows to apply relatively large magnetic field while maintaining superconductivity and to observe the splitting of the sub gap resonance. Remarkably, the splitting is only observed in the singlet ground state as shown in Fig. III.12.

An Andreev quantum dot has been realized in graphene simply by deposition of a

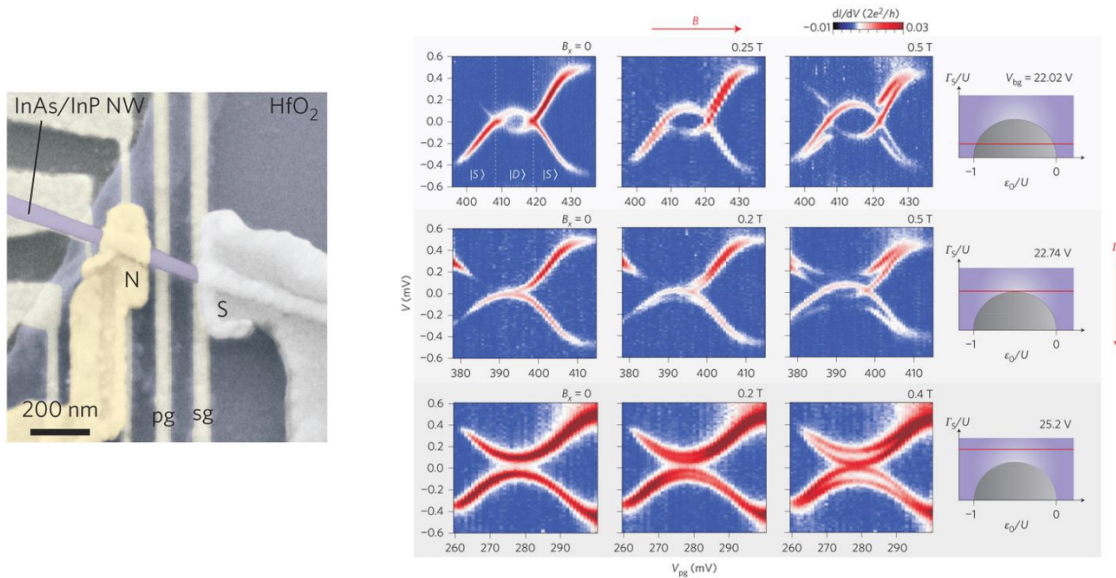


Fig. III.12 **Zeeman splitting.** From Ref. [126] **Left** InAs/InP core/shell nanowire device in a N-QD-S geometry. **Right** The different rows correspond to different coupling  $\Gamma_S$  between the QD and the superconductor. The gate voltage  $V_{pg}$  allows to sweep the phase diagram in the right of the figure, at constant coupling  $\Gamma_S/U$ . The Zeeman splitting of the sub gap resonance is observed only in the singlet ground state.

tunnel coupled superconductor at its surface[133]. As the lever arm of the device was very low, multiple charge states of the quantum dot could not be studied.

After the proposal aiming at detecting the magnetization reversal of single molecules[98, 9] attached on narrow (diameter 1 nm) carbon nanotubes embedded in SQUID loop, such nano-SQUIDs have been investigated[71]. A demonstration of a  $0-\pi$  transition in the doublet ground states by tuning the Kondo effect through the coupling to the lead has been demonstrated, the result is shown in Fig. III.13.

As entanglement between two electrons (or any massive particle) has never been demonstrated, Cooper pair splitter has been widely studied since 2010[134, 135, 136, 137, 138, 139, 140, 141]. These devices consists in two quantum dots coupled to a superconducting lead. Two spin entangled electrons forming a Cooper pair in the superconductor can be separated on the two quantum dots and remain entangled as they travel in normal leads attached to each quantum dot, over the spin coherence length[142] of the normal leads. Non-local Josephson current carried by spatially separated Cooper pairs across two quantum dots may have been measured[143]. Nevertheless, the multiple orders of co-tunneling events that can lead to the transport of a Cooper pair across a quantum dot[75] complicates the experiment interpretation.

Semiconductor nanowires are now grown in situ with an epitaxial Al shell[16]. A quantum dot can be defined, using electrostatic gate, in these nanowires by removing

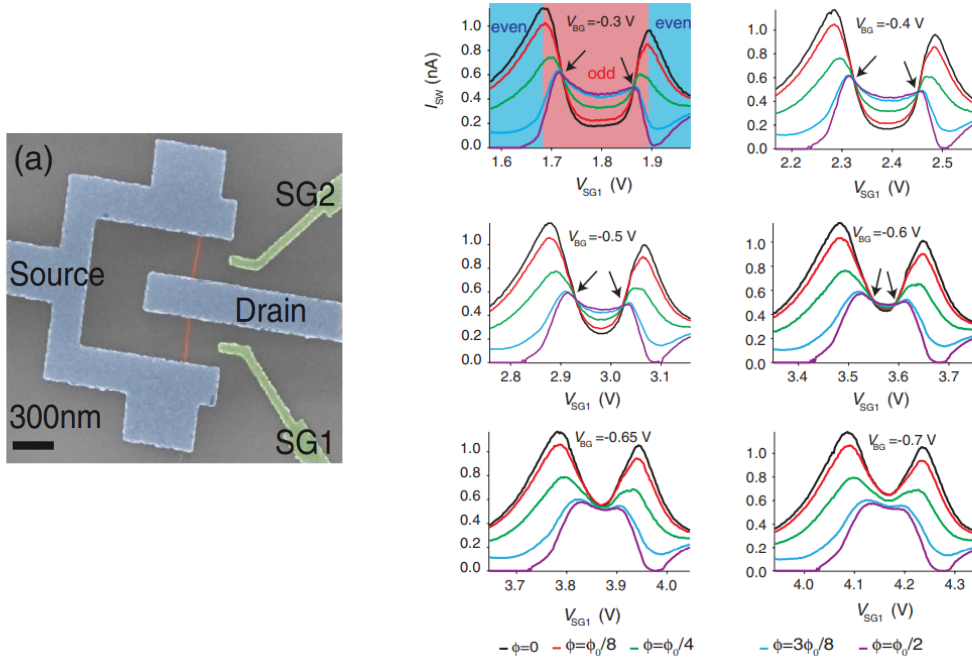


Fig. III.13 **Nano-SQUID**. From Ref. [71] **Left** Nano-SQUID device based on a carbon nanotube. **Right** Josephson critical current  $I_{sw}$  as a function of gate voltages. In a symmetric SQUID device  $I_{sw} \propto \cos(\phi/\phi_0)$  therefore  $\phi = 0$  (black curve) corresponds to a larger current than  $\phi = \pi/2$  (purple curve) in the '0' state. A transition to the ' $\pi$ ' state is achieved in the doublet ground state by tuning the Kondo effect.

some of the Al shell by chemical etching. Such nanowires coupled to superconductor acquires a hard superconducting gap[117] in their density of states due to the proximity effect and can be considered as superconducting island. Due to the pairing energy  $\Delta$ , the addition energy to add an electron on the island depends on the parity of the number of electron on the island :

$$E_{even,odd} = E_c \pm \Delta$$

In the group, we have resolved this even odd effect by STM on Pb nanocrystals deposited on InAs[144, 145]. Nevertheless, if  $\Delta \gg E_c$ , charges are added to the island two by two, this is the case in Ref. [146] where an InAs nanowire coupled to an Al shell is attached to normal leads and studied by tunneling spectroscopy. In this experiment, the system differs from a quantum dot as the mean level spacing  $\delta$  due to quantum confinement in the QD is small compared to the other energy scale. As shown in Fig. III.14, the periodicity of the conductance peaks, corresponding to the number of charge added to the island, is doubled when a magnetic field of  $B = 200$  mT is applied. As the critical field of the thin Al shell is about  $B_c = 1$  T, the superconducting gap  $\Delta$  of the electrode is practically unchanged at such low magnetic field. Thus, this

evolution is attributed to transport through Majorana zero modes at the edges of the Al shell.

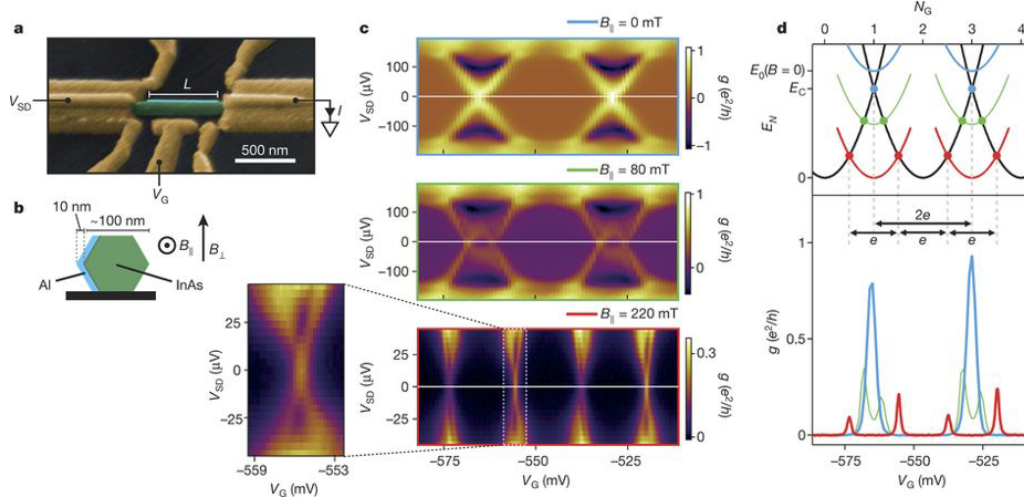


Fig. III.14 **Majorana island.** From Ref. [146]. An InAs nanowire with an epitaxial Al shell is studied by tunneling spectroscopy. The periodicity of the conductance peaks is doubled when a magnetic field of  $B = 200$  mT is applied. As the critical field of the thin Al shell is about  $B_c = 1$  T, this striking evolution is attributed to transport through Majorana zero modes at the edges of the Al shell.

The anomalous Josephson effect, discussed in the last section of chapter 1, has been probed in a quantum dot Josephson junction[147]. The quantum dot is formed by electrostatic gating in an InSb nanowire. It is embedded in a SQUID loop in order to detect the anomalous phase shift  $\varphi_0$  in the Josephson current phase relation, the device is shown in Fig. III.15a. In quantum dots, the anomalous Josephson effect is predicted to occur in the presence of spin-orbit coupling, when multiple orbitals are available for electron transport[148]. In Ref. [147] the critical current is very small  $I_c < 1$  nA and  $I_c\phi_0 < k_B T \approx 5$   $\mu$ eV, therefore, some dissipation remains at zero voltage and only voltage fluctuations can be studied to detect the  $\varphi_0$  phase shift. As shown in Fig. III.15c, an anomalous phase shift  $\varphi_0$  different from 0 or  $\pi$  is detected when a magnetic field of about 100 mT is applied in the sample plane. The phase shift depends on the angle between the magnetic field and the nanowire as shown in Fig. III.15c, no phase shift is detected when the magnetic field is along the nanowire.

### III.5.1 Conclusion

In summary, while past works on InAs-based Andreev QDots employed large diameter nanowires ( $>60$  nm), we found that Andreev QDots could be fabricated with smaller (30 nm) diameter nanowires provided that they are initially doped to a high carrier concentration of about  $n=10^{18}$   $\text{cm}^{-3}$ . We found that these nanowires could

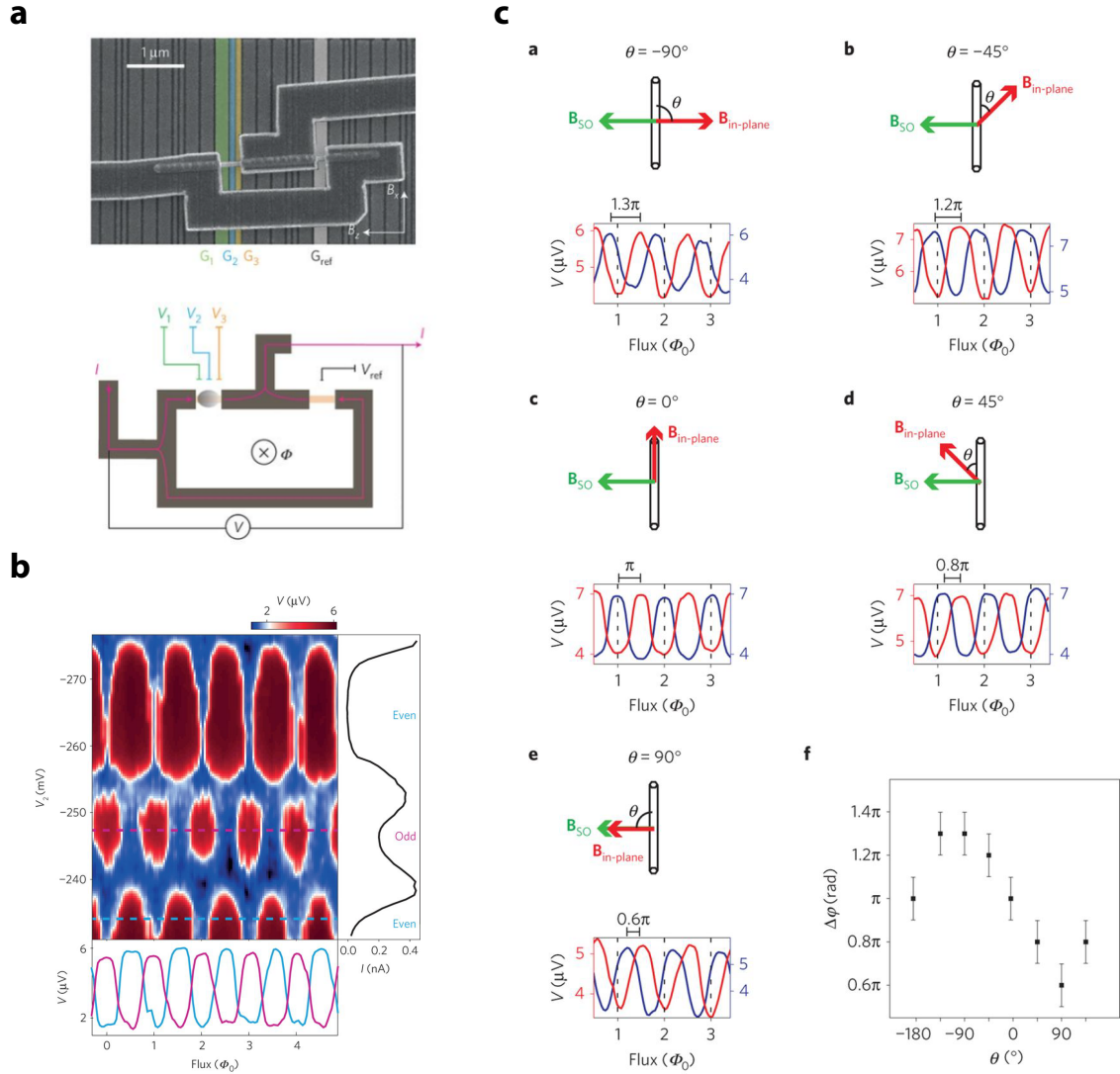


Fig. III.15 **Anomalous  $\varphi_0$  Josephson effect in quantum dot.** From Ref. [147] **a** SEM image and sketch of the InSb nanowire device. **b** At zero in-plane magnetic field, the Josephson current phase relation is offset by  $\pi$  when the dot occupancy changes from even to odd. **c** An anomalous phase shift  $\varphi_0$  different from 0 or  $\pi$  is obtained when a magnetic field  $B_{in-plane}$  is applied. It depends on the angle between the magnetic field and the nanowire. There is no anomalous phase shift when  $B_{in-plane}$  is along the nanowire, the phase shift is maximum when  $B_{in-plane}$  is perpendicular to the nanowire.

be driven across a metal insulator transition by applying a large negative back-gate voltage, and we observed a remarkable evolution of the superconducting sub gap resonances across the mobility edge, as a consequence of the rapidly changing coupling of the levels with the superconducting electrodes. Deeply localized levels do not allow for the presence of Andreev reflections or the formation of Shiba states, and only quasiparticle cotunneling is observed. For localized levels near the mobility edge, Shiba bound states form, and a parity-changing quantum phase transition is identified by a crossing of the sub gap resonances at zero energy. Finally, on the metallic side of the mobility edge, simple Andreev reflections at  $eV = \Delta$  are observed.

We have presented recent studies of Andreev quantum dots and showed the work reported in Ref. [147] where an anomalous phase shift different from 0 or  $\pi$  has been detected in the Josephson current phase relation. We have probed this effect in Josephson junctions based on  $\text{Bi}_2\text{Se}_3$  thin films.



# IV – Anomalous Josephson effect in $\text{Bi}_2\text{Se}_3$ thin films

As the Josephson effect in topological insulators has been investigated by many groups in the recent years, we shall start this chapter by presenting some experiments studying Josephson junctions based on materials with strong spin-orbit interaction. Then, we will detail our experiments realized on  $\text{Bi}_2\text{Se}_3$  thin films and our first attempts at identifying topologically protected transport in this system. As this will appear, our first experimental observations were in close agreement with the conventional theory describing the Josephson effect until we applied an in-plane magnetic field and observed an anomalous Fraunhofer pattern, possibly related to strong spin-orbit coupling and disorder. This first experiment with in-plane magnetic field was realized in a vectorial magnetic field in collaboration with M. Aprili at the Laboratoire de Physique des solides. Then, we will describe a simple model developed to reproduce these experimental observations. Finally, we designed and performed a superconducting interference experiment where the spin-orbit contribution could be well separated from the disorder contribution. We find experimental evidence of the anomalous Josephson effect, predicted in 2008[18], and show that spin-orbit coupling modifies the oscillation frequency of Josephson interferometer devices as reported in Ref. [149].

## IV.1 State of the art

In 2008, it was predicted that the proximity effect induced by a s-wave superconductor on the surface of a three dimensional topological insulator will result in a chiral p-wave superconductor, which host Majorana bound states at vortices[150]. Moreover, it was proposed that these vortices could be manipulated by tuning the phase between the different s-wave superconductors, thereby, realizing a platform for quantum processing with anyonic excitations[151].  $\text{Bi}_2\text{Se}_3$  and related compounds were predicted to be three dimensional topological insulators in 2009[47]. The Dirac cones were first observed by photoemission at the surface of  $\text{Bi}_2\text{Te}_3$  and  $\text{Sb}_2\text{Te}_3$  crystals[152], followed closely by  $\text{Bi}_2\text{Se}_3$  grown by MBE[48]. In these studies[33, 153], it was also shown that  $\text{Bi}_2\text{Se}_3$  gets doped after some hours in UHV. This undesirable doping has made difficult the separation of the contributions between the topological surface states and the

bulk states in experiments. In Ref. [154], an ionic liquid and a metallic gate capacitively coupled to  $\text{Bi}_2\text{Se}_3$  are used to reduce the number of carriers and to observe the sign reversal of the Hall coefficient, where the type of carrier changes from electron to hole as the Fermi level crosses a band gap. Josephson junctions were fabricated on  $\text{Bi}_2\text{Se}_3$ [155, 156, 157, 158, 159, 160]. While some of these studies manage to measure the Josephson current across the charge neutrality point, where the bulk is depleted and only the surface contribution should remain, no departure from the conventional theory describing the Josephson effect were reported. It has been predicted that the Josephson current mediated by topological states is  $4\pi$  periodic as function of the phase difference between the superconducting electrodes[161, 100, 162, 163]. This periodicity can be obtained from microwave measurements. Recently, a small  $4\pi$  periodic contribution to the Josephson current, in contrast with the conventional  $2\pi$  periodic contribution expected from trivial states, was reported in  $\text{Bi}_2\text{Se}_3$ [164]. Larger  $4\pi$  periodic contribution has been reported in InSb nanowire driven in the topological regime by a magnetic field[165], in the 3D topological insulator HgTe[166], in the 2D topological insulator HgTe quantum well[167] and in the Dirac semi-metal BiSb[168]. All these materials possess electronic states which have their spin locked perpendicular to their momentum. A comparison with graphene based Josephson junctions is interesting as graphene is also characterized by a linear dispersion in momentum but no spin momentum locking. Until now, no  $4\pi$  periodic contribution has been reported in graphene[169, 170], even though microwave measurements were not shown in the high quality samples[171, 172].

The dependence of the critical current on magnetic field can provide insight about where the current is flowing in the material. Measurements of  $I_c(B)$  has been used to identify a supercurrent flowing at the edges of the 2D topological insulator HgTe quantum well[173], InAs/GaSb heterostructure[174], Bi nanowires[175] and in graphene driven in the quantum Hall regime[176]. Nevertheless, a supercurrent flowing at the edge of the material does not imply that it is topologically protected from back scattering, as shown in InAs where current along the etched edge were also reported[177]. Therefore, both the magnetic field and microwave dependence of the Josephson current has been measured in HgTe quantum well[167], which shows convincing results of a  $4\pi$  periodic current with a spatial modulation of the current density, as shown in Fig. IV.1. Moreover, the  $4\pi$  periodicity has also been probed by detecting the microwave signal emitted by the Josephson junction[178].

Above a thickness of 50 nm, HgTe is a three dimensional topological insulator where a small gap ( $\approx 20$  meV) in the bulk electronic states can be induced by strain, simply by growing HgTe on a CdTe substrate[179]. As previously mentioned, a  $4\pi$  periodic Josephson current has been detected in this material[166]. Strain has been shown to alter the topological surface states in  $\text{Bi}_2\text{Se}_3$ [180, 181]. Recently, a critical current minimum at zero magnetic field has been reported in  $\text{Bi}_2\text{Te}_3$ , after having cooled down the sample twice[182]. The  $\text{Bi}_2\text{Te}_3$  is grown by MBE on GaAs(001) and then exfoliated on Si/SiO<sub>2</sub>. A critical current minimum at zero magnetic field is known from SFS junctions[183, 184] where the thickness of the F layer changes along the junction

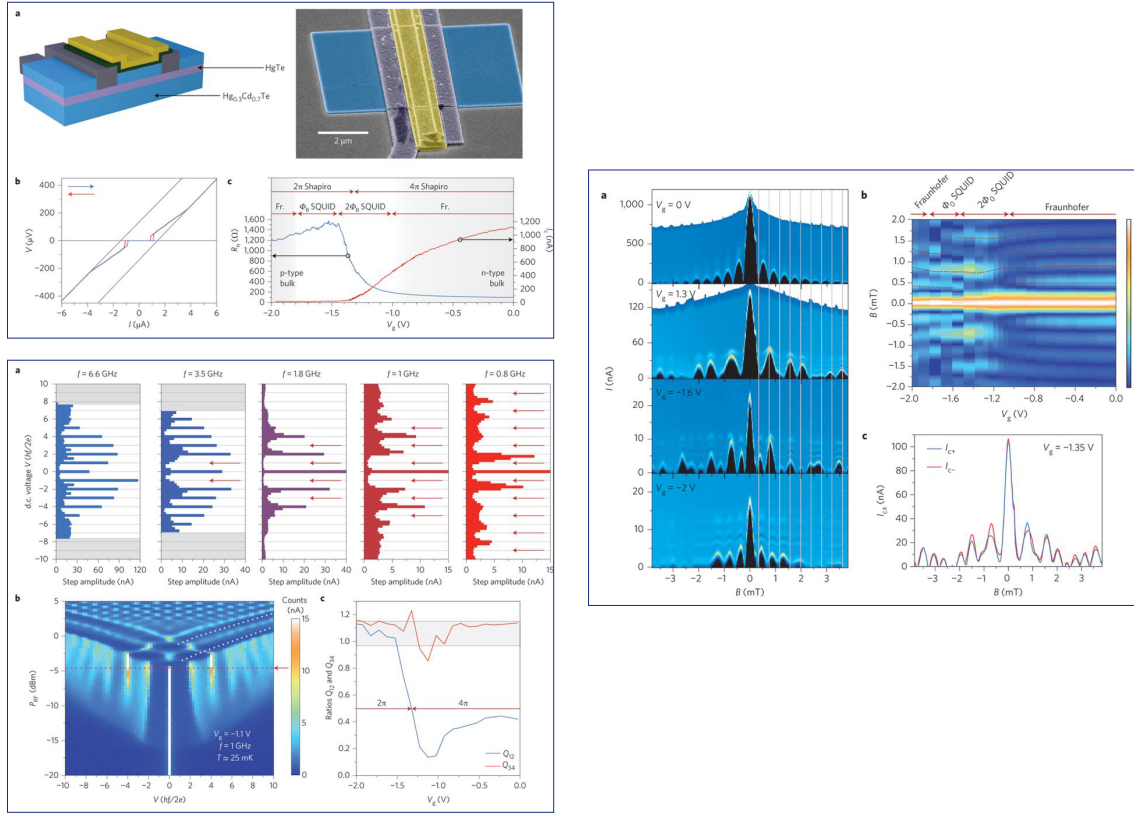


Fig. IV.1  **$4\pi$  periodic Josephson effect.** From Ref. [167] **up left** Sketch and SEM images of the HgTe quantum well Josephson junction. **down left** Microwave measurements which shows evidence of a  $4\pi$  periodic contribution to the supercurrent. **right** Magnetic field dependence which shows strong spatial modulation of the current density and of the magnetic field periodicity in the gate voltage range where the  $4\pi$  periodic contribution is present.

width, inducing a '0' and a ' $\pi$ ' coupling in the same junction. In absence of magnetism, the dip at zero field is also known from corner junction on high  $T_c$  superconductor and have been decisive to identify the unconventional order parameter in cuprates[185]. Therefore, the interpretation of this experiment in terms of an induced chiral p wave pairing is plausible[182], even though microwave measurements are unfortunately not discussed in this study. Nevertheless, no  $4\pi$  periodic current has been reported in  $\text{Bi}_2\text{Te}_3$  crystal exfoliated on Si/SiO<sub>2</sub> substrate[186, 187]. It is also worth mentioning that a dip of the critical current at zero field has also been reported in Josephson junction made on the Dirac semi-metal  $\text{Cd}_3\text{As}_2$ [188].

Besides topology, a new type of ' $\pi$ ' Josephson junctions have emerged and are interesting for superconducting spintronics[189, 190]. These junctions combine non magnetic material with large Landé g-factor and conventional superconductor to form a Josephson junction where the coupling '0' or ' $\pi$ ' is tunable with a magnetic field, as

discussed in chapter 1. Experiments on HgTe[63] and BiSb[168] are shown in Fig. IV.2. In these experiments a center of mass momentum is acquired by the Cooper pair due to the Zeeman field. It is also shown[63] that the center of mass momentum results in an unusual Fraunhofer diffraction pattern. This unusual pattern has been measured in  $\text{Bi}_2\text{Se}_3$ [191]. An interesting perspective is to generate spin triplet pair correlations. Indeed in diffusive system it should be possible to separate the singlet component which decays over  $\xi = \sqrt{\frac{\hbar D}{E_z}}$  and the triplet component which decays over  $\xi = \sqrt{\frac{\hbar D}{2\pi k_B T}}$ . In ballistic system it should be possible to use the oscillating character of the order parameter as the triplet component is maximum when the singlet component is zero and vice-versa.

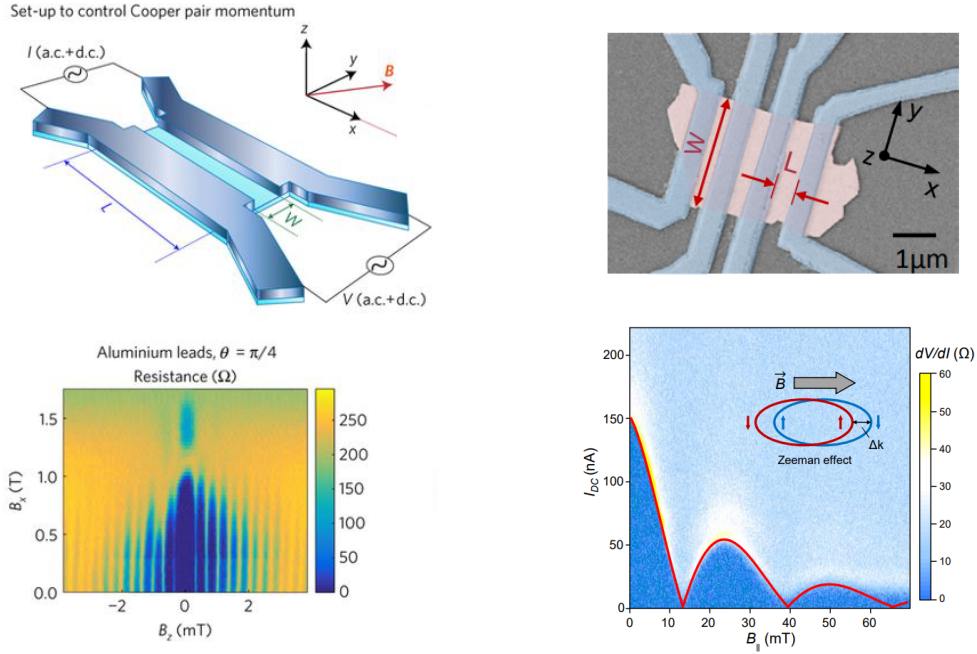


Fig. IV.2 **Zeeman  $\pi$  junctions.** **Left** From Ref. [63]. Josephson junction with HgTe ( $g \approx 10$ ), the electrodes spacing is 800 nm. A ' $\pi$ ' coupling is induced by an in-plane magnetic field due to the momentum acquired by the Cooper pairs in the Zeeman field. **Right** From Ref. [168]. Josephson junction on the Dirac semi-metal BiSb ( $g \approx 800$ ), the electrode spacing is 800 nm. Multiple  $0, \pi$  transition are observed. In this case the magnetic field is applied parallel to the current.

While these experiments rely on the Zeeman field induced by the magnetic field, another intriguing result has been obtained in[192] where the symmetry of the Fraunhofer pattern is broken due to an in-plane magnetic field, as shown in Fig. IV.3. The authors suggest that spin-orbit interaction could be involved. The asymmetry is also observed in Ref. [63] as shown in Fig. IV.2.

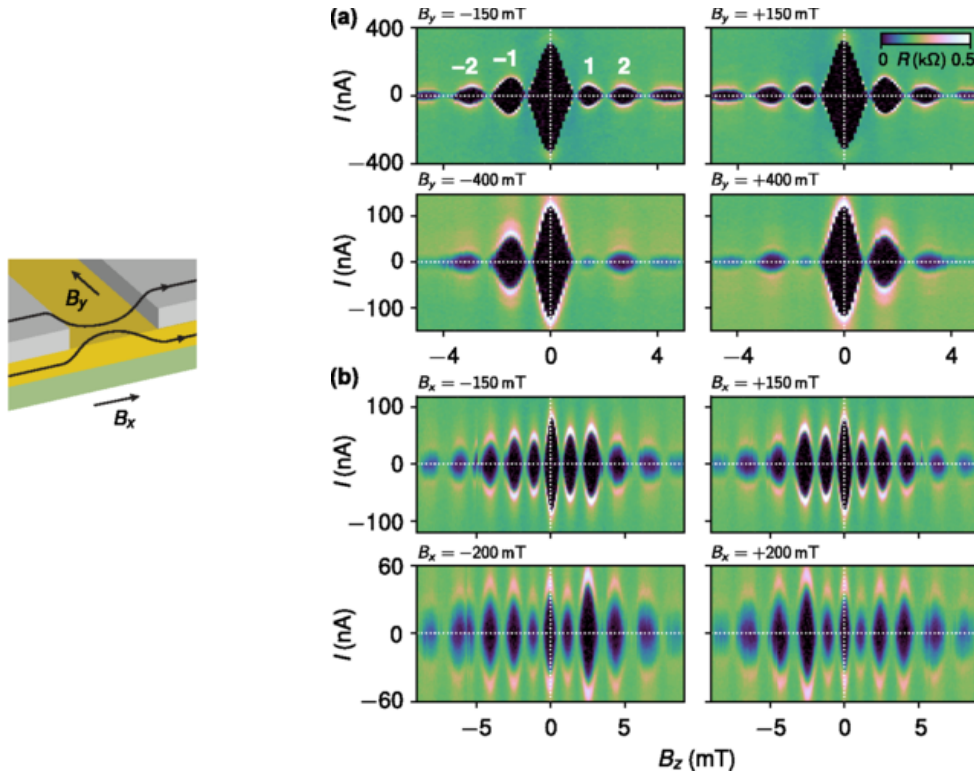


Fig. IV.3 **Anomalous Fraunhofer pattern.** From Ref. [192]. Josephson junction in InAs/InGaAs with epitaxial Al layer. The symmetry of the Fraunhofer pattern is broken by a magnetic field applied in the  $y$  direction. A magnetic field applied in the  $x$  direction seems to induce a spatial modulation of the current density.

The Rashba spin-orbit coefficient in  $\text{Bi}_2\text{Se}_3$  ( $\alpha \approx 0.4 \text{ eV\AA}$ ) is one of the largest ever reported especially at high doping[33, 153]. Moreover, a large value for the Landé  $g$ -factor has been measured recently by electron spin resonance ( $g \approx 20$ )[20]. Thus,  $\text{Bi}_2\text{Se}_3$  Josephson junctions are promising devices to observe new effects related to spin-orbit coupling.

## IV.2 Thin films characterization

We perform magnetoresistance measurements to characterize the  $\text{Bi}_2\text{Se}_3$  thin films. These measurements are directly linked to the electronic density in the film and to its mobility. We consider that the film is isotropic, and that only one type of carriers contribute to the transport signal. We did not attempt to separate the surface contribution from the bulk contribution in these measurements.

$\text{Bi}_2\text{Se}_3$  Hall bars are defined by lithography and sketched in Fig.IV.4a. They are

characterized using AC lock-in measurements at low frequency,  $f = 37$  Hz. An AC voltage, provided by a lock-in, is converted into an AC current through a large resistance,  $R_p$ , in series with the sample. We measure the voltage across this large resistance, it typically corresponds to an injected current,  $I = 100$  nA across the Hall bar. The corresponding longitudinal,  $V_{xx}$ , and transverse,  $V_{xy}$ , voltages are measured. We define the transverse resistance,  $R_{xy} = \frac{V_{xy}}{I}$ . The carrier density and the resistivity are obtained from the relations :

$$n_{3D} = \frac{1}{te} \left( \frac{dR_{xy}}{dB} \right)^{-1} \quad \rho = \frac{V_{xx}L}{ItW}$$

where  $B$  is the magnetic field applied perpendicular to the film,  $t$  is the film thickness,  $L$  is the length across which is measured the longitudinal voltage and  $W$  is the Hall bar width.

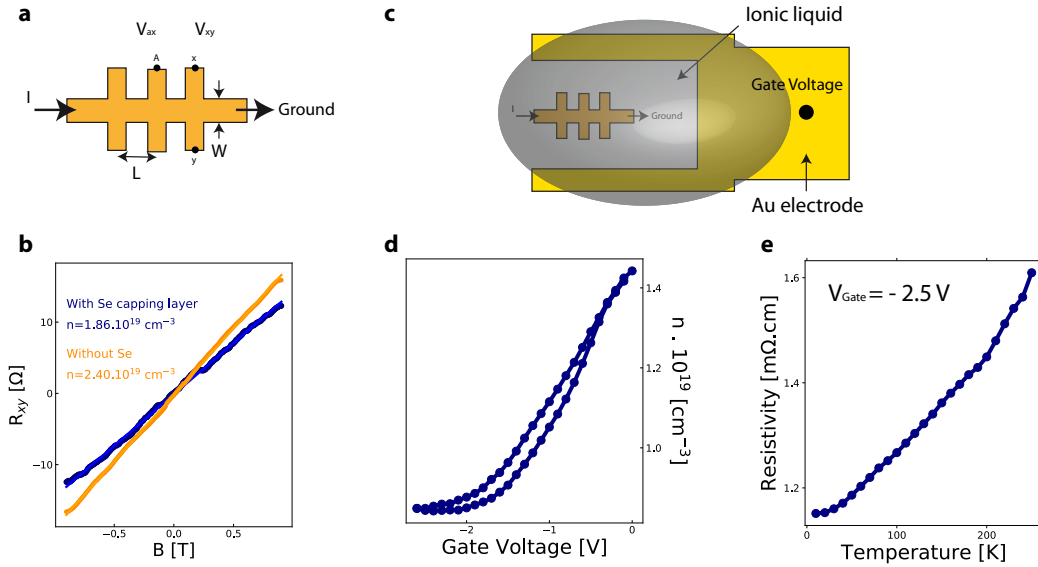


Fig. IV.4 **Hall measurements.** **a** Sketch of a  $\text{Bi}_2\text{Se}_3$  Hall bar. Length  $L=60 \mu\text{m}$ , width  $W=30 \mu\text{m}$ . **b** Transverse resistance as a function of magnetic field measured at room temperature. The curve slope is directly link with the carrier density. In blue, the  $\text{Bi}_2\text{Se}_3$  Hall bar is measured with the Se capping layer. In orange, it is measured after removal of the Se capping layer with the  $\text{Na}_2\text{S}$  solution. **c** An ionic liquid is deposited on top of a Hall bar and on top of a gold electrode. A gate voltage is applied on the gold electrode and allows to tune the carrier density of  $\text{Bi}_2\text{Se}_3$ . **d** Modulation of the carrier density by an electrolyte gate at  $T=250$  K. The two curves correspond to opposite directions for the gate voltage sweeping. As shown by the identical values at zero gate voltage, we observed no electro-chemical reaction at this temperature and in this gate voltage range. **e** Resistivity as a function of temperature at a gate voltage of  $-2.5$  V. It shows a metallic behaviour.

During the Josephson junction fabrication, we removed the Se protecting layer, just

before deposition of the superconducting electrodes, using an NMF solution of  $\text{Na}_2\text{S}$ . We checked the effect of this solution on  $\text{Bi}_2\text{Se}_3$ . Fig. IV.4b shows the carrier density before and after removal of the Se capping layer. We observed a slight increase in the carrier density after removal. However, the film electronic properties remain practically unchanged, as shown in Table IV.1.

The film which has been measured with in-plane magnetic field, as detailed in section IV.4, has been characterized in a Van Der Pauw geometry. For this configuration a  $\text{Bi}_2\text{Se}_3$  square of side,  $S=400 \mu\text{m}$ , is defined by lithography. Fig. IV.5a, shows the transverse measurement used to obtain the carrier density. In this configuration the resistivity  $\rho_{xx}$  of the film, measured as sketched in Fig. IV.5b, is obtained from the relation  $\rho_{xx} = \frac{V_{xx}t\pi}{I \ln(2)}$ . We retain some important values for this film. By taking an effective mass,  $m^*=0.25m_0$ [193], the Fermi velocity is found to be  $3.2 \cdot 10^5 \text{ m.s}^{-1}$ . The elastic diffusion time is  $\tau = \frac{m^*\sigma}{n_3De^2} = 0.13 \text{ fs}$  and the mean free path is  $l = v_F\tau = 40 \text{ nm}$ . The diffusion coefficient is  $D = \frac{1}{3}v_Fl = 4.4 \cdot 10^{-3} \text{ m}^2.\text{s}^{-1}$ . An important length for the superconducting proximity effect at a superconductor-normal interface is the coherence length in the normal material,  $\xi_N = \sqrt{\frac{\hbar D}{2\pi k_B T}} = 420 \text{ nm}$  at a temperature  $T=30 \text{ mK}$ . We fabricate junction with a superconducting electrode spacing  $L = 75 \text{ nm}$  to  $L = 300 \text{ nm}$ , therefore  $l < L < \xi_N$  which corresponds to the diffusive and short junction regime.

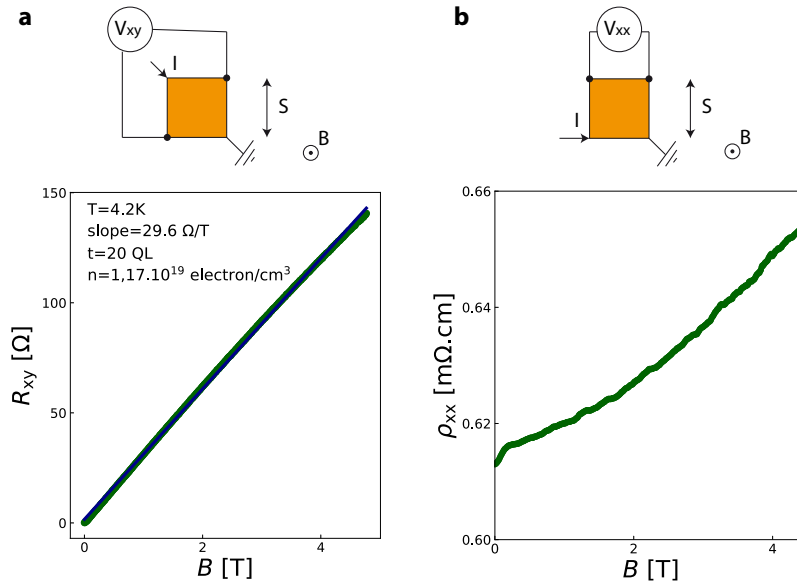


Fig. IV.5 **Van der Pauw measurements.** **a** Transverse resistance as a function of magnetic field (green curve). The carrier density is obtained from the slope of the fit (blue curve). **b** Resistivity of the film as a function of magnetic field measured at 4.2 K. A weak anti-localization dip is observed at zero magnetic field.

### IV.2.1 Carrier density modulation with an electrolyte gate

As  $\text{Bi}_2\text{Se}_3$  is naturally n-doped[33], the bulk of the material is conducting. We reduce this doping by using an electrolyte gate as sketch in Fig. IV.4c. A gold electrode is patterned on the sample near the Hall bar, by lithography. A small electrolyte<sup>1</sup> droplet is deposited on top of the gold electrode and the Hall bar. We apply a voltage on the gold electrode to tune the carrier density in  $\text{Bi}_2\text{Se}_3$  as shown in Fig. IV.4d. Each point corresponds to the slope of a  $R_{xy}$  vs  $B$  curve for a given gate voltage value. We observed a decrease in the carrier concentration by applying negative gate voltage which confirms the n-type nature of the doping. The maximum voltage that can be applied depends on the electrochemical stability of the ionic liquid. It is -2.6 V to 2.2 V for the electrolyte used during this thesis. Above this voltage, electrochemical processes occurs, such as the extraction of Se from the sample, and the sample resistance changes irreversibly. The electrochemical stability can be checked by measuring the gate current. When a gate voltage is applied, a gate current peak is observed because the electrolyte is charging. This gate current should decrease to zero as the sample is charging. If the gate current does not reach zero, but stay at a finite stationary value, that means that electrochemical processes are occurring. We found that the ionic mobility is sufficient at temperatures larger than 250 K to modulate the carrier density. At a temperature below 250 K, the ionic liquid freezes and it is no more possible to change the carrier density. Thus, to change the carrier density, the gate voltage should be applied at a temperature above 250 K. The film resistivity,  $\rho_{xx}$ , at low carrier density,  $V_{gate} = -2.5$  V, is shown in Fig. IV.4e, as a function of temperature. It shows a metallic behaviour.

We did not manage to induce such a carrier density modulation on a Josephson junction. Indeed, the gating method sketched in Fig. IV.4c was repeated on a Josephson junction. As we cannot directly measure the carrier density in a Josephson junction, we compared the change in resistivity induced by the gate voltage applied on the electrolyte. By applying a gate voltage of  $-2.5$  V the resistivity changes only by 5% while on the Hall bar it changes by 20%. We manage to measure the Josephson current at low temperature with the electrolyte, we report no distinct behaviour due to its presence. The anomalous Josephson effect reported in this chapter has been probed without electrolyte.

Tables IV.1, IV.2 and IV.3 summarize the electronic properties of the different  $\text{Bi}_2\text{Se}_3$  thin films used.

---

1. We tried two ionic liquids : 1-Ethyl-3-methylimidazolium-bis(trifluoromethylsulfonyl)imide and diethylmethyl(2-methoxyethyl)ammonium-bis(trifluoromethylsulfonyl)imide. As they show similar gating effect we mainly used the former which is more common.

Temperature [K]	Carrier density [ $10^{19} \text{ cm}^{-3}$ ]	Resistivity [ $\text{m}\Omega\cdot\text{cm}$ ]	Before/After $\text{Na}_2\text{S}$
300	1.9	1.1	Before
30	2.0	0.9	Before
300	2.4	0.9	After
60	2.7	0.6	After

Table IV.1 *Thin film 32m0258 (30QL). Before and after removal of the Se capping layer.*

Temperature [K]	Carrier density [ $10^{19} \text{ cm}^{-3}$ ]	Resistivity [ $\text{m}\Omega\cdot\text{cm}$ ]	$V_{\text{Gate}}$ [V]
250	1.4	1.1	off
250	0.8	1.4	-2.5 V
5	0.9	/	-2.5 V

Table IV.2 *Thin film 32m0236 (30QL). Effect of an electrolyte gate.*

Temperature [K]	Carrier density [ $10^{19} \text{ cm}^{-3}$ ]	Resistivity [ $\text{m}\Omega\cdot\text{cm}$ ]
300	/	1.1
4.2	1.2	0.6

Table IV.3 *Thin film 32m0272 (20QL). This film has been measured in a van der Pauw configuration.*

### IV.3 Josephson effect in $\text{Bi}_2\text{Se}_3$

Once the fabrication process was well established, we observed the Josephson current in most of the devices measured at low temperature  $T=30$  mK. A typical differential resistance curve measured with a lock-in is shown in Fig. IV.6a for a junction of width  $W=1.5 \mu\text{m}$  and electrode spacing  $L=150$  nm. At low current ( $I < 1 \mu\text{A}$ ), a Josephson superfluid current flows through the junction and the resistance is zero. The Josephson critical current  $I_c$  is defined as the current above which the junction becomes resistive. Above  $I_c$ , the resistance corresponds to the  $\text{Bi}_2\text{Se}_3$  resistance which differs from the normal state resistance due to Andreev reflections. At large current, the aluminum becomes resistive. As the aluminum resistance is negligible compared to  $\text{Bi}_2\text{Se}_3$ , the normal state resistance,  $R_N$ , corresponds to the resistance of the device at large current. For this junction we find  $R_N = 23 \Omega$ . It corresponds to a resistivity  $\rho_{xx} = R_N \frac{Wt}{L} = 0.7 \text{ m}\Omega\cdot\text{cm}$ , which is close to the value obtained from Hall bar measurement, see Table IV.1 after  $\text{Na}_2\text{S}$ . A value commonly reported in Josephson studies is the  $I_c R_N$  product, we find  $12 \mu\text{eV}$  for this junction. In Fig. IV.6b we report the  $I_c R_N$  product as a function of the electrode spacing for the devices measured at the LPEM. Due to slight adjustments in the fabrication process we did not attempt a quantitative

analysis between different junctions. These values for the  $I_c R_N$  product is consistent with previous studies summarized in Ref. [158].

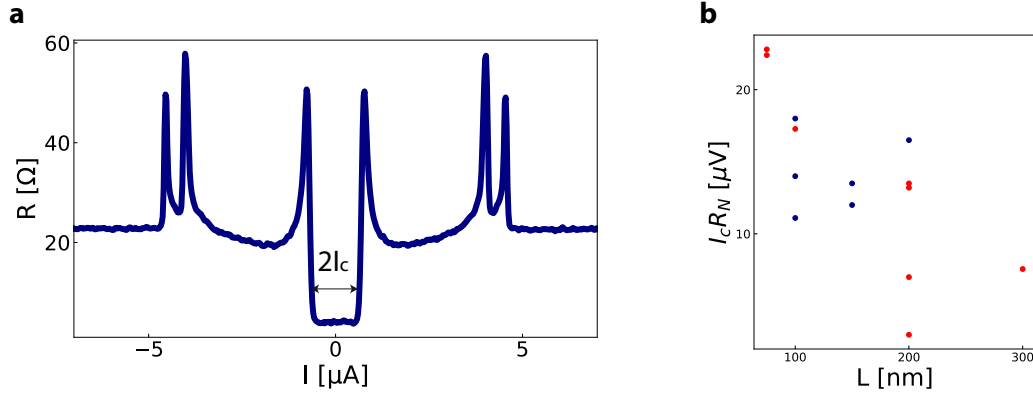


Fig. IV.6 **Josephson current in  $\text{Bi}_2\text{Se}_3$ .** **a** Resistance as a function of current across the junction. The Josephson critical current  $I_c$  is the current above which the junction becomes resistive. **b**  $I_c R_N$  product as a function of superconducting electrode spacing,  $L$ . The junction width is  $W$  and the  $\text{Bi}_2\text{Se}_3$  thickness is  $t$ . The red (blue) points correspond to a  $\text{Bi}_2\text{Se}_3$  thickness,  $t = 20 \text{ nm}$  ( $30 \text{ nm}$ ).

### IV.3.1 Supercurrent interferences

A hallmark of the Josephson effect is the Fraunhofer pattern which results from the spatial modulation of the supercurrent by the magnetic field. For single junction devices such as the one sketched in Fig. IV.7a, we observed the Fraunhofer pattern, Fig. IV.7b and c. These two patterns correspond to two different junctions with dimension  $L_1=100 \text{ nm}$  and  $W_1=1 \mu\text{m}$  for Fig. IV.7b,  $L_2=200 \text{ nm}$  and  $W_2=1.5 \mu\text{m}$  for Fig. IV.7c.

Due to the magnetic field  $B$  a phase gradient is present at the edges of both superconductor forming the junction. This phase gradient is expressed from the Ginzburg-Landau equation[194], and adds a position dependent phase difference along the junction width :

$$\varphi(y) = \frac{2\pi(L + 2\lambda_L)yB}{\phi_0}$$

where  $\lambda_L$  is the London penetration depth. This additional phase results in a position dependent Josephson current per unit length<sup>1</sup>  $J(y) = J_0(y) \sin(\varphi(y) + \varphi_b)$ . Here  $\varphi_b$  is the phase difference between the two bulk superconductors, this phase depends on the current which is applied in the junction.  $J_0(y)$  is the supercurrent per unit length without magnetic field which can be position dependent, for example due to

1. The current per unit length is found by integration of the current density  $J_{2D}(y, z)$  along the  $z$  direction  $J(y) = \int J_{2D}(y, z) dz$ .

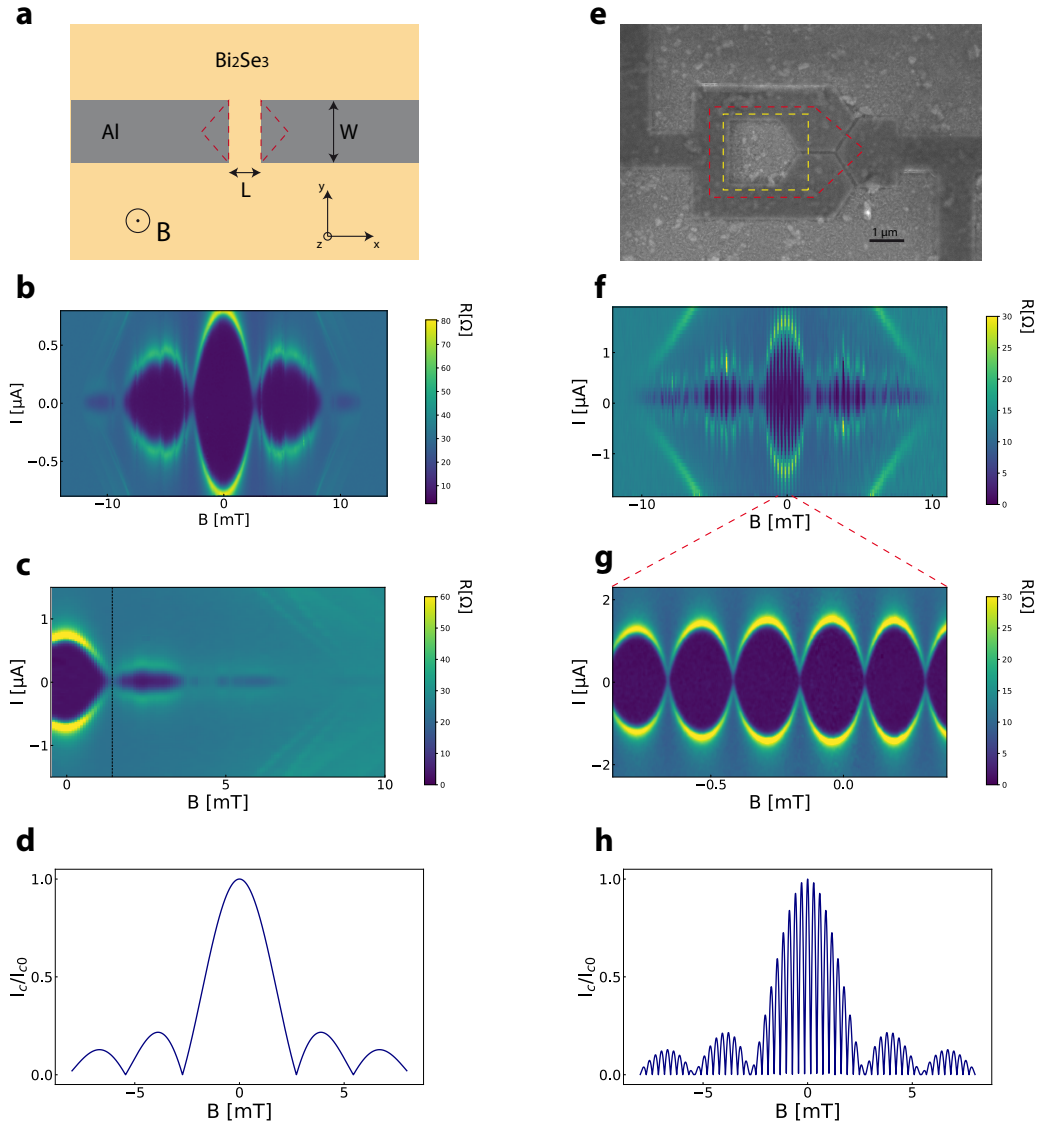


Fig. IV.7 **Supercurrent interferences in  $\text{Bi}_2\text{Se}_3$ .** **a** Sketch of a Josephson junction made with superconducting Al electrodes on top of  $\text{Bi}_2\text{Se}_3$ . In the red dashed region the magnetic flux lines are diverted in the junction due to the Meissner effect. **bc** Resistance as a function of current and magnetic field. The critical current corresponds to the current where the device becomes resistive. **e** Scanning electron microscope image of a SQUID device. The image is dark because this sample was fabricated before learning how to properly remove the ma-N mask resist. The effective SQUID area is shown by the red dashed line. The phase difference across the junction which is cut by the yellow dashed line is directly related to the magnetic field. **f** For a SQUID device the supercurrent envelope due to the single junction area is observed. **f** On a much lower magnetic field scale, fast critical current oscillation are due to the large SQUID area. **dh** Theoretical dependence of the critical current as a function of magnetic field for **d** a single junction and **h** a SQUID.

imperfections or edge states. The Josephson current across the junction is found by integrating the current per unit length along the junction width :  $I_J = \int_{-W/2}^{W/2} J(y)dy$ . To calculate the maximum supercurrent through the junction i.e the critical current,  $I_c$ , one must maximize the last expression with respect to the bulk phase difference  $\varphi_b$  that is  $I_c = \max_{\varphi_b} I_J$ . The final critical current expression is :

$$I_c(B) = \max_{\varphi_b} \text{Im} \left[ e^{i\varphi_b} \int_{-W/2}^{W/2} J_0(y) e^{i\varphi(y)} dy \right]$$

Where  $\text{Im}$  denotes the imaginary part. A Fourier transform of the current per unit length  $J_0(y)$  is clearly identify in this expression. Therefore, measurement of  $I_c(B)$  has been used to extract a position dependent supercurrent per unit length  $J_0(y)$  due to edge states in 2D topological insulator[174, 173], in the quantum Hall regime[176], and in InAs[177]. If  $J_0$  is constant along the junction width, expression IV.3.1 is always maximized for  $\varphi_b = [\pi]$  and we obtain the standard expression for the Fraunhofer pattern :

$$I_c(B) = J_0 W \left| \frac{\sin \frac{\pi\phi}{\phi_0}}{\frac{\pi\phi}{\phi_0}} \right|$$

where  $\phi = W(L + 2\lambda_L)B$  is the magnetic flux through the junction area. This relation is shown in Fig. IV.7d and we expect a first critical current minimum at  $B_0 = \frac{\phi_0}{W(L+2\lambda_L)}$ . We find experimentally  $B_{0,1} = 1.4$  mT as shown by the dashed line in Fig. IV.7c. This value is lower than expected from the junction area because the magnetic field in the junction is larger than the applied magnetic field due to flux focusing by the superconducting electrodes. An intuitive way to take this effect into account is given in Ref. [187] : when the electrode becomes superconducting, the magnetic flux lines in the dashed red region in Fig. IV.7a are diverted into the junction area. The effect is present at both electrodes and is equivalent as increasing the junction area by  $W^2/2$ . Thereby, we can estimate the London penetration depth from  $B_{0,1} = \frac{\phi_0}{S_{eff}}$  with  $S_{eff} = (L + 2\lambda_L)W + \frac{W^2}{2}$  the effective junction area. We find  $\lambda_L \approx 20$  nm which is close to the bulk value of aluminum. In Ref. [156] flux focusing is underestimated. Indeed by taking their junction dimensions  $L = 55$  nm and  $W = 1.5 \mu\text{m}$ , if we add the effective surface resulting from flux focusing  $\frac{W^2}{2}$  we find  $B_{0,1} = 1.7$  mT which is close to their experimental value (consideration of the London penetration depth barely affects the result). The non regular value of the magnetic field minimum in their Fraunhofer pattern, that we also observed in Fig. IV.7bcf, are probably due to trapped vortices which we discuss now.

In Fig. IV.7b, abrupt jumps in the critical current magnitude are observed for  $B > 2$  mT. Such jumps are expected in presence of trapped vortices. Similar behaviour has been observed in Josephson junctions fabricated with type II superconducting electrodes[195]. In our case, the aluminum is of type I and no vortices are expected in the electrodes ( $\xi > \lambda_L$ ). However, in hybrid Josephson junctions, the effective penetration depth in the semiconducting material is expected to be much larger

than for the superconducting electrodes because the carrier density in the semiconductor is much smaller than in the electrodes. Thus, it is quite plausible that vortices can be trapped inside the semiconducting material near the interface with the superconducting electrode and escape the junction. This probably explains the ubiquitous observation of flux-trapping effects in hybrids SNS junctions made from semiconducting materials[195, 156]. Due to these trapped vortices the second minimum of critical current occurs at a much larger field than expected from Eq. IV.3.1. We also note that the critical current of the electrode (not of the junction) observed as resistive line at large current and field in Fig. IV.7bcf does not show such abrupt jumps which supports that the jumps are related to the flux in the junction and not to superconductivity in the electrodes.

We also fabricated superconducting quantum interference devices (SQUID) consisting of two identical Josephson junctions in parallel as shown in Fig. IV.7e. The magnetic field dependence of the critical current is observed in Fig. IV.7f, and on a much lower field scale, in Fig. IV.7g. The critical current envelope (f) is due to the phase modulation along the junction width as previously discussed. In a SQUID the critical current is modulated by the magnetic flux in the normal area  $S_N$  enclosed by the superconductor which is  $\phi_L = BS_N$ . Indeed, the phase difference across the two junctions contributing to supercurrent between the two superconducting electrodes are linked by the relation  $\varphi_1 - \varphi_2 = \frac{2\pi\phi_L}{\phi_0}$ , in the case of negligible inductance[194]. The current is the sum the Josephson current across the two junctions in parallel  $I_J = I(\sin(\varphi_1) + \sin(\varphi_2)) = 2I \sin(\varphi_1 - \frac{\pi\phi_L}{\phi_0}) \cos(\frac{\pi\phi_L}{\phi_0})$ . The critical current is obtained<sup>1</sup> by maximizing this expression with respect to  $\varphi_1$ , which gives :

$$I_c(B) = 2I \left| \cos\left(\frac{\pi\phi_L}{\phi_0}\right) \right|$$

We find experimentally a periodicity  $B = 242 \mu\text{T}$  in Fig. IV.7g. From the normal area  $S_N$  enclosed by the superconductor, we expect  $B = 590 \mu\text{T}$ . This discrepancy is again due to flux focusing. By taking into account not the normal area but an effective area shown in Fig. IV.7f, we find  $B \approx 210 \mu\text{T}$  which is close to the experimental value. Flux focusing significantly changes the critical current sensitivity to an applied magnetic field. This effect is used to amplify the magnetic field in the loop of SQUID sensors[196].

Devices such as the one shown in Fig. IV.7e, fabricated on top of 3D topological insulator have been proposed to create Majorana bound states[150]. The device contains a third junction made of the same superconductor piece. This junction carries no current between the two separate superconductors. Across this junction, the phase difference is directly related to the flux enclosed in the SQUID area, see the yellow dashed line in Fig. IV.7e,  $\varphi_3 = \frac{2\pi\phi_L}{\phi_0}$ . When the phase is tuned to  $\varphi_3 = \pi$  a zero energy Andreev states is expected in the junction. Different techniques have been

---

1. In Fig. IV.7h we plot  $I_c(B) = I_0 \left| \frac{\sin(\frac{\pi\phi}{\phi_0})}{\frac{\pi\phi}{\phi_0}} \cos(\frac{\pi\phi_L}{\phi_0}) \right|$  with  $\phi$  and  $\phi_L$  the effective flux in one single junction and in the SQUID area respectively.

proposed to probe this zero energy state[197], one of them consists in using the right electrode as a tunnel probe and look for a conductance peak at zero voltage. This configuration requires an extra fabrication step. For the present device, we investigate the periodicity of the current phase relation through microwave measurements, see next section, at different magnetic field. We did not find anomalous behaviour of the Josephson effect in this device. Measurements on a tri-junction on top of  $Bi_2Se_3$  has been reported in Ref. [159, 160]. In these experiments the critical current does not vanish as a function of magnetic field. This is expected if the critical current of the two junctions are not equals i.e if the SQUID is not symmetric, see section IV.3.4. However, it is argued in these studies, that the temperature dependence of critical current shows an unexpected behaviour. The Josephson current carried by topological states is expected to be  $4\pi$  periodic in phase, in contrast with the conventional  $2\pi$  periodicity. The phase periodicity can be precisely probed by microwave measurements.

### IV.3.2 Shapiro steps

Microwave measurements can be used to determine precisely the phase periodicity of the Josephson current phase relation. Indeed considering a current phase relation with a general periodicity :

$$I_J = I_c \sin(\varphi p)$$

When a voltage,  $V = V_0 + V_1 \cos(\omega t)$ , where  $\omega$  is the microwave frequency is applied across the Josephson junction, its phase evolves in time according to the second Josephson relation :

$$\frac{d\varphi}{dt} = \frac{2eV}{\hbar}$$

Integrating to get  $\varphi$  and replacing in Eq. IV.3.2, one finds an AC current :

$$I_J = I_c \sin\left(\frac{2eV_0 p}{\hbar} t + \frac{2eV_1 p}{\hbar \omega} \sin(\omega t) + cst\right)$$

Using the expansion of the sine of a sine in term of Bessel functions[50], one obtains :

$$I_J = I_c \sum (-1)^n J_n\left(\frac{2eV_1 p}{\hbar \omega}\right) \sin\left(cst + \frac{2eV_0 p t}{\hbar} - n\omega t\right)$$

This current has a DC component when  $V_{0,n} = \frac{n\hbar\omega}{2ep}$  with n integer. Therefore, the current dependence on voltage shows supercurrent steps so-called Shapiro steps[7] for these voltage values. The position of these steps in voltage gives the periodicity of the current phase relation. If the current phase relation is conventional, that is  $2\pi$  periodic, then  $p = 1$  in Eq. IV.3.2 and we expect steps at voltages :

$$V_n = \frac{n\hbar\omega}{2e}$$

However, the supercurrent mediated by topological states is predicted to be  $4\pi$  periodic in phase[161, 100, 162, 163]. This result in  $p = \frac{1}{2}$  in Eq. IV.3.2 and the disappearance of odd Shapiro steps ( $n=1,3,5,\dots$ ). Therefore microwave measurements of the Josephson current is a powerful tool to make the distinction between supercurrent mediated by conventional and topological states. Disappearance of the first Shapiro step  $n = 1$  has been reported in InSb nanowire driven in the topological regime by a magnetic field[165], in the 3D topological insulator HgTe[166], in the 2D topological insulator HgTe quantum well[167] (where multiple odd steps disappear) and in the Dirac semi-metal BiSb[168].

The Dirac cone, which is a predicted characteristic of 3D topological insulators[47], has been observed by photoemission in our thin films[49]. Therefore, we investigate the phase periodicity of the supercurrent by illuminating the junctions with microwaves. An RF cable has been added in the dilution fridge to apply a microwave signal on the gold plate on which the sample is glued. The resulting resistance maps as a function of current and microwave power are shown in Fig. IV.8abc for different microwave frequencies. The IV curve at a fixed microwave power shows the Shapiro steps, see Fig. IV.8d. Regular steps are observed at voltage  $V_n = nhf/2e$  and  $f = 4.236GHz$  is the microwave frequency. For some values of microwave power, the first Shapiro step disappears as observed in the lower panel of Fig. IV.8d. Nevertheless, this behaviour is well captured by the resistively shunted junction (RSJ) model with a conventional,  $2\pi$  periodic, current phase relation. In the experiments mentioned above[165, 166, 167, 168], the disappearance of the Shapiro step occurs for all values of the microwave power.

### IV.3.3 RSJ model

The microwave response of Josephson junctions can be captured by the RSJ model. The equivalent circuit of a SNS junction consists of a Josephson junction of critical current  $I_c$  in parallel with a resistor  $R_N$ . The current across the resistor is  $I_R = \frac{V}{R_N}$ . The microwave signal is added in the model in the form of an AC current,  $I_{RF}\sin(2\pi ft)$ , with  $f$  the microwave frequency. The voltage  $V$  is linked to the phase difference according to the second Josephson relation and the total current in the circuit is :

$$I = \frac{h}{2eR_N} \frac{d\varphi}{dt} + I_c \sin(\varphi) + I_{RF} \sin(2\pi ft) \quad (IV.1)$$

This differential equation is solved numerically with Python for each pair of  $I$  and  $I_{RF}$ . The voltage  $V$  is found from the second Josephson relation by a time average  $\langle \rangle_t$  of the phase solution derivative :

$$V = \frac{h}{2e} \left\langle \frac{d\varphi}{dt} \right\rangle_t$$

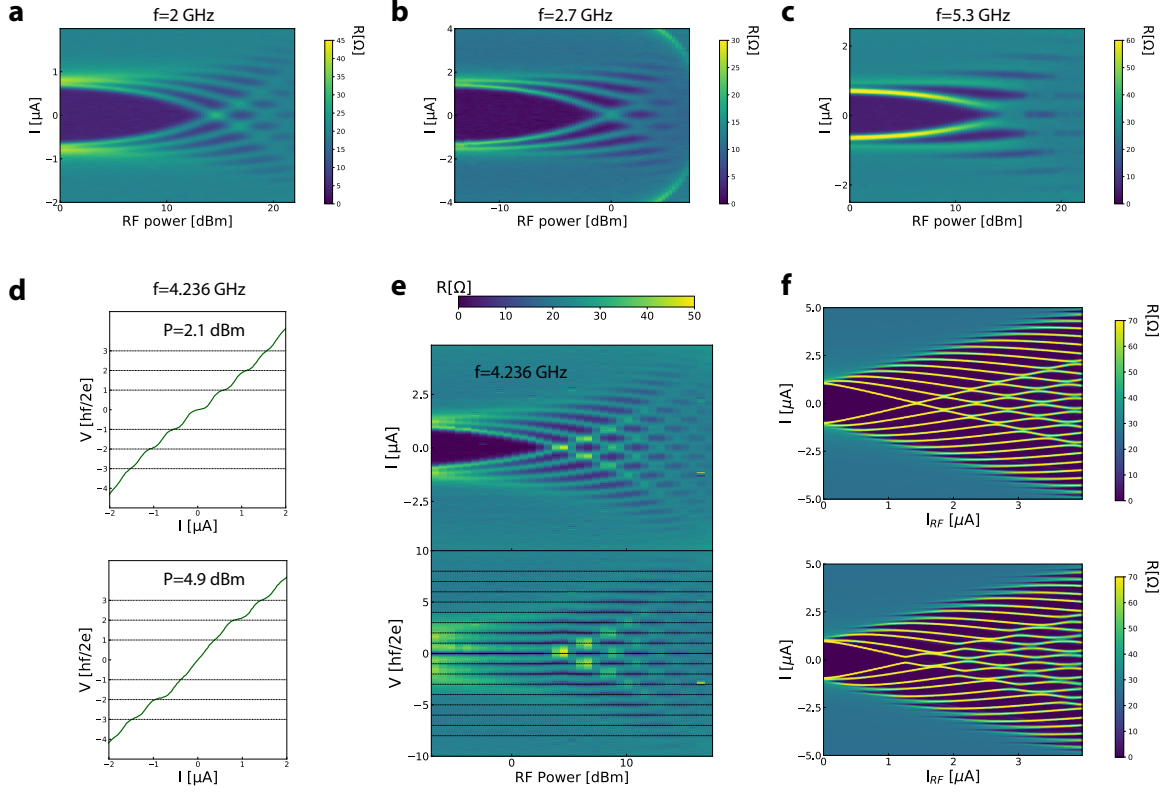


Fig. IV.8 **AC Josephson effect in  $\text{Bi}_2\text{Se}_3$ .** *abc* Resistance maps as a function of current and RF power for different microwave frequencies (a)  $f=2$  GHz, (b) 2.7 GHz and (c) 5.3 GHz. The zero resistance regions correspond to voltage plateaus. *d* IV curves showing the Shapiro steps for two values of the microwave power. The  $n^{\text{th}}$  current step appears at a voltage  $V_n = \frac{nhf}{2e}$ . *e* Resistance maps as a function of current (upper panel) or voltage (lower panel) and RF power at the frequency  $f=4.236$  GHz. In the lower panel as a function of voltage, dashed line are plotted at  $V_n = \frac{nhf}{2e}$ . *f* Theoretical curves calculated at  $f=4.236$  GHz with Eq. (IV.1) using two different CPRs : A conventional  $2\pi$  periodic current phase relation  $I_J = I_c \sin(\varphi)$  is used for the upper panel, it reproduces properly the experimental data. In the lower panel an unconventional current phase relation  $I_J = I_c(\frac{4}{5} \sin(\varphi) + \frac{1}{5} \sin(\varphi/2))$  is used. The odd steps have a lower current amplitude.

The result for a conventional  $2\pi$  periodic CPR is plotted in the upper panel of Fig. IV.8f. It reproduces well the observation.

We also used the RSJ model to see the effect of a Josephson current containing a large conventional and a small topological component :

$$I_J = I_c \left( \frac{4}{5} \sin(\varphi) + \frac{1}{5} \sin(\varphi/2) \right)$$

The result is shown in the lower panel of Fig. IV.8f, the odd Shapiro steps have a lower current magnitude than the even steps. This method has been used in an extended RSJ model to understand the role of thermal effect which can mask the  $4\pi$  periodic contribution to the supercurrent in  $Bi_2Se_3$ [164]. In this study, a small  $4\pi$  periodic contribution is reported. They used exfoliated  $Bi_2Se_3$  crystal of carrier concentration larger than our thin films. However, the thickness of the film is larger  $\approx 80$  nm, which may result in a better decoupling of the two surfaces. Indeed, the spin momentum locking at one surface is expected to protect the electronic states from back-scattering, if the film is too thin, an electronic states can possibly be back-scattered on the other surface.

As discussed in the first chapter for short junctions, high transmission across the normal material can lead to a non-sinusoidal current phase relation, as observed in atomic contacts[198], HgTe[199], InAs nanowire[200] and Bi nanowire[175].

### IV.3.4 Current phase relation

The Josephson current phase relation[201] (CPR) can be directly measured with a Josephson interferometer[194, 198]. Such device consists in two Josephson junctions in parallel as shown in Fig. IV.9a. The two junctions have widths  $W_1 = 600$  nm and  $W_2 = 60$  nm. The Josephson current is obtained by summing the current through the junctions :

$$I_j = f_{cpr}(I_{c,1}, \varphi_1) + f_{cpr}(I_{c,2}, \varphi_2)$$

where  $f_{cpr}$  is the current phase relation which we assume periodic with value between  $[-I_c, I_c]$ . The phase differences  $\varphi_1$  and  $\varphi_2$  for the two junctions are linked by the relation  $\varphi_1 - \varphi_2 = 2\pi \frac{\phi}{\phi_0}$ . Therefore, one can express the critical current as a function of a single phase difference and the magnetic flux  $\phi$  :

$$I_c = \max_{\varphi_1} \left[ f_{cpr}(I_{c,1}, \varphi_1) + f_{cpr}(I_{c,2}, \varphi_1 - 2\pi \frac{\phi}{\phi_0}) \right]$$

As the critical current  $I_{c_1}$  is much higher than  $I_{c_2}$ , the phase  $\varphi_1$  stays fixed at a value  $\varphi_{cst}$  to insure a maximum current through the large junction and :

$$I_c(B_z) = I_{c_1} + f_{cpr} \left( I_{c_2}, \varphi_{cst} - \frac{2\pi S B_z}{\phi_0} \right)$$

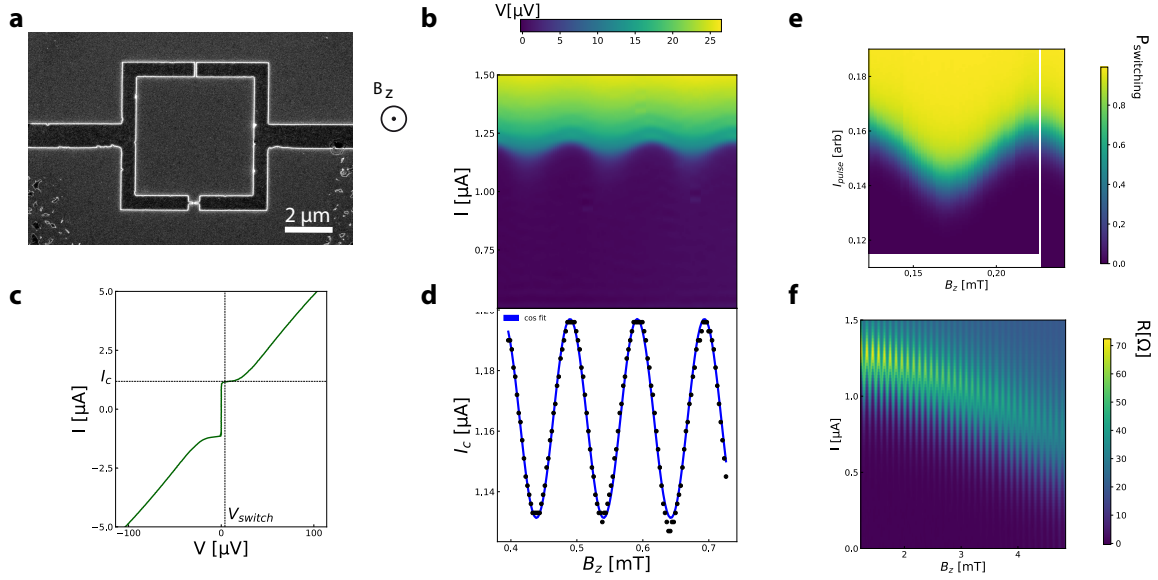


Fig. IV.9 **Measurement of the current phase relation in  $\text{Bi}_2\text{Se}_3$ .** **a** SEM image of a Josephson interferometer device. This device consists of two Josephson junctions in parallel and enables to probe the CPR of the smaller junction. **b** **c** These curves are measured with a nanovoltmeter, the noise at DC is 200 nV. **b** Voltage map as a function of current and magnetic field  $B_z$  showing zero voltage below a critical current value. The critical current of the small junctions oscillates with the magnetic flux in the superconducting loop. **c** IV curve of the device. The critical current value  $I_c$  is extracted when the junction develops a finite voltage defined as  $V_{\text{switch}}$  and indicated by the dashed vertical line. **d** Critical current extracted from (c) as a function of  $B_z$ . The oscillations are properly described by the function  $I_c(B_z) = I_{c_1} + I_{c_2} \cos(\omega B_z)$ , indicating a sinusoidal current phase relation. **e** Switching probability as a function of magnetic field and magnitude of current square pulses. We did not measure the magnitude of the current pulse, the unit is arbitrary. **f** Resistance measured with a lock-in on a large magnetic field scale.

Thus, a measurement of the critical current  $I_c$  as a function of magnetic field  $B_z$  provides a measure of the current  $I_{c2}$  as function of  $\varphi_2$ . In other words, it provides a measure of the current phase relation.

From the voltage map as a function of current  $I$  and  $B_z$ , shown Fig. IV.9b, the critical current  $I_c$  is extracted when the voltage across the device exceeds a value defined as  $V_{\text{switch}} = 4 \mu\text{V}$ , as shown by the dashed lines in Fig. IV.9c. The critical current as a function of magnetic field is fitted in Fig. IV.9 d, we find that the CPR displays a conventional sinusoidal form  $I_J = I_c \sin(\varphi)$ <sup>1</sup>. Measurements b and c were done with a nanovoltmeter connected through a voltage divider on the junction. Such measurements avoid to use the Stanford amplifier which have a noise of about  $2 \mu\text{V}$  at DC. We also measured this device by replacing the Yokogawa source by a function generator, as shown in Fig. IV.9e. It generates square voltage pulses at a frequency  $f=863$  Hz, which are converted into current pulses through a large resistor. These pulses generate a voltage difference across the sample if the current pulse exceed the critical current. We define a voltage threshold and a counter counts how many time this voltage threshold is exceeded. The switching probability corresponds to  $N_{\text{switch}}/N$  where  $N_{\text{switch}}$  is the number of counts and  $N = 3452$  is the number of pulses. We also measured the device using standard lock-in method on a large field scale as shown in Fig. IV.9f. The overall decrease of the critical current is due to the flux in the large junction which results in a Fraunhofer pattern, see section IV.3.1.

The Josephson effect in  $\text{Bi}_2\text{Se}_3$  shows a conventional behaviour. As discussed in the first chapter and in section IV.1, phenomena directly related to the Zeeman field and to spin-orbit coupling in the junction are observable with a significant applied magnetic field. This requires the fabrication of device with higher critical magnetic field.

## IV.4 Josephson effect with in-plane magnetic field

The critical field of the superconducting electrodes is  $B_c = 10$  mT, as shown by the resistive lines at large magnetic field in Fig. IV.7bcf. From the Ginzburg-Landau theory, it is shown that the critical field for a magnetic field applied in the y direction, see sketch Fig. IV.7a, is[50],  $B_{c//} = 2\sqrt{6}\frac{B_c\lambda_L(d)}{d}$  where  $d = 60$  nm is the aluminum thickness. To increase this parallel field while maintaining superconductivity[202], we fabricate Josephson junction with an aluminum thickness  $d = 20$  nm.

In Ref. [202], it is shown that the critical temperature of Al film increases by decreasing the Al thickness. It is not the case for our Al films, see Fig. IV.10. We argue that it is due to the inverse proximity effect[203] of the 5 nm of Ti which is used as a sticking layer. Indeed, near the interface between a normal material and a superconductor, the superconducting gap  $\Delta$  is affected by the normal material over the coherence length,  $\xi \approx 1 \mu\text{m}$ , on the superconducting side. Therefore, if the aluminum

---

1. That is  $f_{\text{cpr}}(I, \varphi) = I \sin(\varphi)$  and  $\varphi_{\text{cst}} = \frac{\pi}{2}$ . Which result in  $I_c(B_z) = I_{c1} + I_{c2} \cos\left(\frac{2\pi s B_z}{\phi_0}\right)$

thickness  $d_s$  is smaller than  $\xi$ , the change in the superconducting gap value is non negligible. For a bulk superconductor at zero temperature the BCS relation gives,  $\Delta = 2\Omega e^{-\frac{1}{N_0V}}$ , where  $\Omega \approx 400k_B$  T and  $N_0V \approx 0.17$  for Al. An estimation of the superconducting gap for a bi-layer is provided by L. Cooper, which is valid when  $\xi \gg d_s, d_n$ , see Ref. [204] : As electrons are part of the time in the normal material and the other part in the superconductor they feel an effective potential  $V_{\text{eff}} = \frac{d_s}{d_s+d_n}V$  as the potential in the normal material is zero. Thus, the superconducting gap is reduced  $\Delta = 2\Omega e^{-\frac{d_n+d_s}{N_0Vd_s}}$ . The new critical temperature is obtained from the BCS relation  $\Delta = 1.8k_B T_c$ . We neglect the superconducting gap in Ti which is much smaller than in Al. For the same Ti thickness of 5 nm, we find  $T_c \approx 0.7$  K for 60 nm of Al and  $T_c \approx 0.3$  K for 20 nm of Al, which agree with the experimental points. See also Ref. [205] for the critical temperature of Al/Ti bi-layer for different Ti thickness.

As the Ti/Al bi-layer is deposited on  $\text{Bi}_2\text{Se}_3$  we could consider Cooper's argument to calculate the reduction of the critical temperature due to the inverse proximity effect arising from the proximity with the semiconductor. However, this argument was formulated for a metal superconductor bi-layer, where the normal density of states at the Fermi energy of both materials are of the same order of magnitude. For a superconductor deposited on top of a semiconductor, the changes in the critical temperature is weak because the electronic density in a semiconductor is generally much smaller than in a metal. Thus, we replace the probability to find an electron in the aluminum  $\frac{d_s}{d_s+d_N}$  by the probability taking into account the density of states in both materials  $\frac{N_0d_s}{N_0d_s+N_{0,n}d_n}$ . When  $N_0 = N_{0,n}$ , we recover Cooper formula. We find no correction to the critical temperature as  $N_0 \propto m^{3/2}\sqrt{E_F}$ , and the Fermi energy in Al ( $\approx 11$  eV) is much larger than in  $\text{Bi}_2\text{Se}_3$  (60 meV).

#### IV.4.1 Anomalous Fraunhofer pattern

A Josephson junction with an aluminum thickness of 20 nm is shown in Fig. IV.11a. Defects created during the fabrication process are more visible below the electrodes when the aluminum is thin. We recall that the selenium capping layer is only removed where the aluminum is deposited. We measured such a junctions in a dilution fridge, equipped with a 3D vectorial magnetic field, which allows the application of a magnetic field in any direction. The base temperature of the fridge is 80 mK. As shown in Fig. IV.11bf, the modulation of the critical current is symmetric with respect to the perpendicular magnetic field  $B_z$ . It becomes asymmetric upon increasing an in-plane magnetic field  $B_y$ , as shown in Fig. IV.11cdeg. The in-plane magnetic field is much larger than the perpendicular one. These measurements were acquired with an oscilloscope. The current source is a function generator which generates current ramps at  $f = 77$  Hz. We define a voltage threshold  $V_T = 1\mu\text{V}$  to extract the critical current from the data. This technique allows to record the critical current map shown in Fig. IV.11h as a function of both magnetic fields in a single day.

Similar behaviour for the Fraunhofer pattern has been observed in InAs Josephson

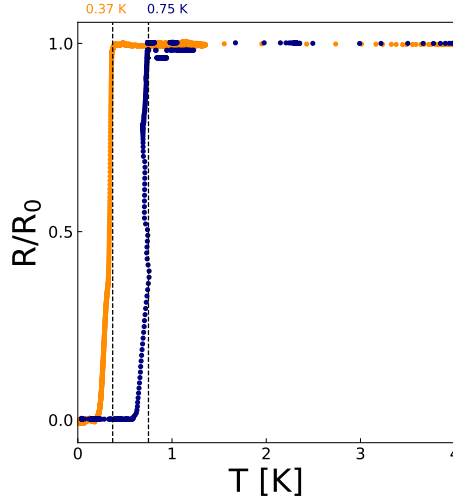


Fig. IV.10 **Critical temperature.** Normalized resistance as a function of temperature for two different thicknesses of aluminum deposited on  $\text{Ti}/\text{Bi}_2\text{Se}_3$ . The resistance is normalized with respect to the value at 4 K. In blue, the aluminum thickness is 60 nm, the critical temperature is 0.75 K. In orange, the thickness is 20 nm, the critical temperature 0.37 K. For both curves, the thickness of  $\text{Bi}_2\text{Se}_3$  and Ti is respectively 20 nm and 5 nm.

junctions[192]. Following this study, we define a parameter to quantify the Fraunhofer pattern asymmetry :

$$\frac{I_{c,L} - I_{c,R}}{I_{c,L} + I_{c,R}}$$

where  $I_{c,L}$  ( $I_{c,R}$ ) is the critical current of the left (right) side lobe, as shown in Fig. IV.12b. As the Fraunhofer pattern is symmetric when no in-plane magnetic field is applied, this parameter is equal to zero when  $B=0$ , as shown in Fig. IV.12a. As in Ref. [192], we find a linear dependence for the asymmetry parameter as a function of in-plane magnetic field. The asymmetry is more pronounced when the field is applied perpendicular to the current than parallel.

Before we discuss the simulation of an anomalous Fraunhofer pattern, it is important to understand what must be included in a simulation to generate an asymmetry. It was shown in Ref. [206], from a symmetry analysis of a general Hamiltonian  $H$  describing hybrid Josephson junctions, which parameters must be included to generate an asymmetric Fraunhofer pattern. The Hamiltonian  $H$  include spin-orbit coupling, Zeeman splitting and an asymmetric disorder with respect to the junction center, denoted  $V_x, V_y$ . The generation of an asymmetry in the pattern requires breaking all symmetry operations  $U$  leaving  $UH(B_z)U^\dagger = H(-B_z)$ . These symmetry operations are shown in Table IV.4 from Ref.[206], together with the parameters breaking those symmetries. We removed the Dresselhaus coefficient from the original Table[206] as  $\text{Bi}_2\text{Se}_3$  is centrosymmetric.

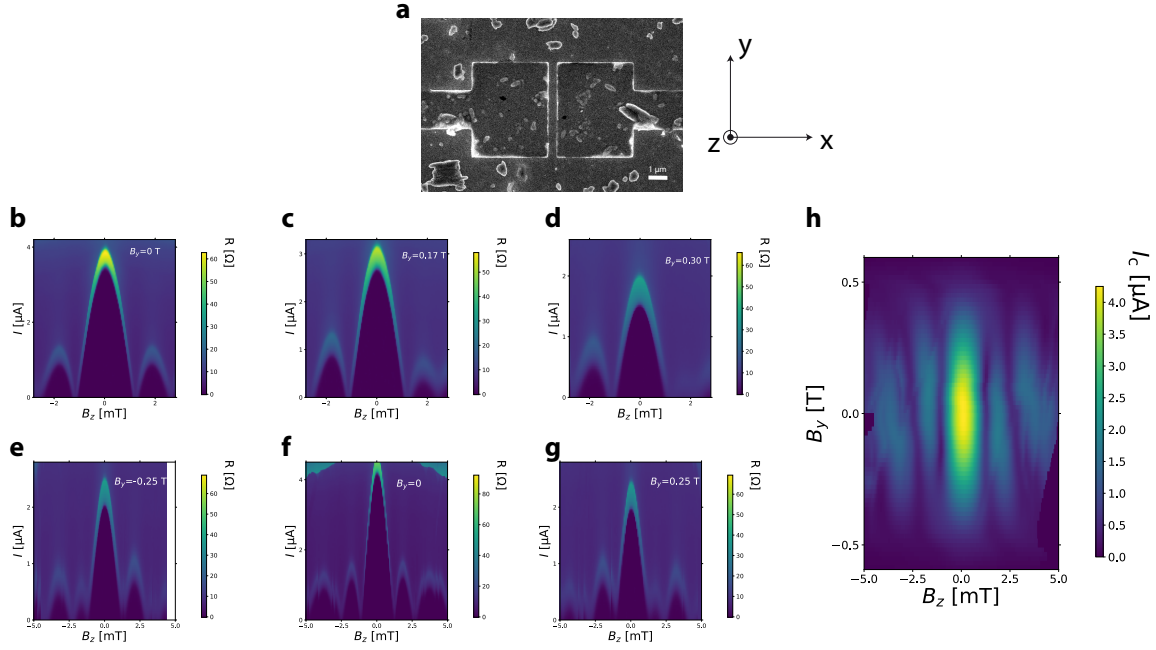


Fig. IV.11 **Fraunhofer pattern with in-plane magnetic field** **a** SEM image of a Josephson junction device. The aluminum thickness is 20 nm. Measurements are shown for two different junctions with the same dimensions, **bcd** corresponds to one junction while **efgh** to the other. **bf** The Fraunhofer pattern is symmetric with respect to perpendicular magnetic field  $B_z$  when no in-plane magnetic field is applied. **cd** It becomes asymmetric when a magnetic field  $B_y$  is applied in the  $y$  direction. **eg** The asymmetry is reversed by changing the direction of the magnetic field. **eg** Critical current map as a function of magnetic field  $B_y$  and  $B_z$ .

$UH(B_z, \varphi)U^\dagger = H(-B_z, \varphi)$	Broken by
$\sigma_x P_y$	$B_y, \alpha, V_y$
$\sigma_y P_y$	$B_x, V_y$
$P_x P_y T$	$B_x, B_y, \alpha, V_x, V_y$
$\sigma_z P_x P_y T$	$V_x, V_y$

Table IV.4 Symmetry operations  $U$  protecting the symmetry of the Fraunhofer pattern  $H(B_z) = H(-B_z)$ , see Ref. [206].  $P_{x,y}$  are the parity operator which correspond to a spatial inversion in the  $x$  or  $y$  direction.  $\sigma_{x,y}$  are the spin operators.  $T$  is the time reversal operator. A symmetry operation in the left column is broken by one of the parameters in the right column. These parameters include the in-plane magnetic fields  $B_x, B_y$ , the asymmetric disorder potentials  $V_x, V_y$  and the spin-orbit coefficient  $\alpha$ .

An asymmetric disorder  $V_y$  along the junction width is enough to break all symmetries and generate an asymmetric pattern. Indeed, asymmetric Fraunhofer pattern in

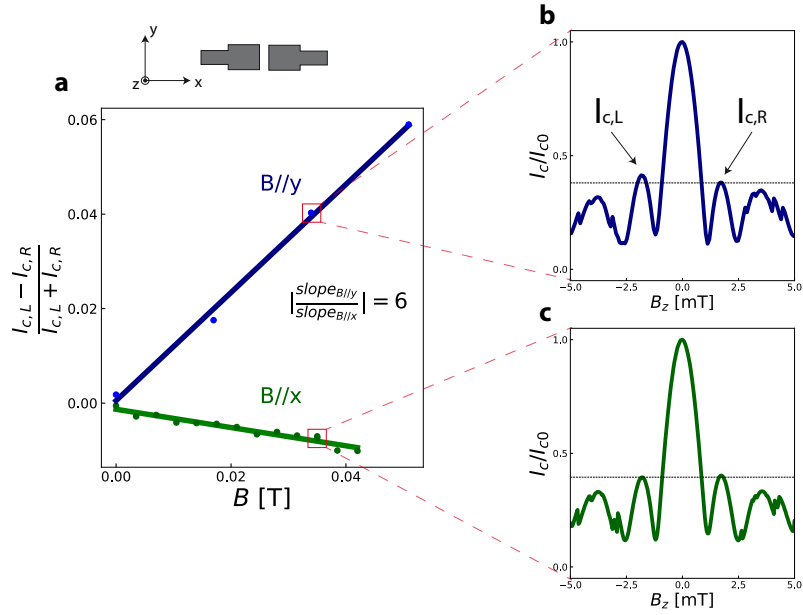


Fig. IV.12 **Asymmetry parameter.** **a** An asymmetry parameter  $\frac{I_{c,L} - I_{c,R}}{I_{c,L} + I_{c,R}}$  is extracted from the Fraunhofer pattern and shown as a function of magnetic field. We observed a more pronounced asymmetry for a magnetic field in the  $y$  direction. **b** Critical current as a function of magnetic field  $B_z$  for finite  $B_y$  and  $B_x = 0$ . The critical current of the side lobe of the Fraunhofer pattern are extracted to calculate the asymmetry parameter. **c** Same for finite  $B_x$  and  $B_y = 0$ . The asymmetry is less pronounced.

the absence of in-plane magnetic field has been reported[177]. However, we measured a symmetric Fraunhofer pattern in the absence of in-plane magnetic field, which shows that disorder  $V_y$  is not enough to break all symmetries of Table IV.4 and that the magnetic field  $B_y$  must play a role in the asymmetry.

#### IV.4.2 Simulation of an anomalous pattern

Due to the magnetic field  $B_z$  the phase difference changes linearly along the junction width according to  $\varphi(y) = \frac{2\pi(L+2\lambda_L)yB_z}{\phi_0}$ . An asymmetric Fraunhofer pattern can be generated, Fig. IV.13b, simply by adding a phase jump along the junction width as shown in Fig. IV.13c. We consider that the in-plane magnetic field is responsible for this phase jump, as the Fraunhofer pattern is symmetric at  $B_y=0$ . An in-plane magnetic field also induced a position dependent phase difference along the thickness of the film, which is considered as superconducting by proximity with the electrodes<sup>1</sup>, as sketched in Fig. IV.13a. The phase is modulated according to  $\varphi(z) = \frac{2\pi(L+2\lambda_L)zB_y}{\phi_0}$ . If the thickness of the film changes (along the  $z$  direction), it produces a phase offset

1. The film thickness, 20 nm is much smaller than the coherence length in the normal material  $\xi_N = 420$  nm, see section IV.2.

along the junction width. A first attempt to simulate our observation, has been to consider this thickness variation using the standard relation for tunnel junction[194] :

$$I_c(B_z, B_y) = \max_{\varphi} \int_0^W \int_0^{t(y)} j_0 \sin \left( \varphi + \frac{2\pi(L + 2\lambda_L)yB_z}{\phi_0} + \frac{2\pi(L + 2\lambda_L)zB_y}{\phi_0} \right) dydz \quad (IV.2)$$

AFM measurement of the film, Fig. IV.13ef, shows thickness  $t$  variation of about  $t' \approx 1$  nm over a length  $l_d \approx 1 \mu\text{m}$ . We consider the thickness variation of the film along the  $y$  direction with the function :  $t(y) = t + t' \sin(2\pi y/l_d)$ , with  $t = 20$  nm the film thickness. The calculated pattern at  $B_y = 0.25$  T is shown in blue in Fig IV.13g. It shows a much less pronounced asymmetry than the measured pattern, shown in Fig. IV.13d, measured at the same field.

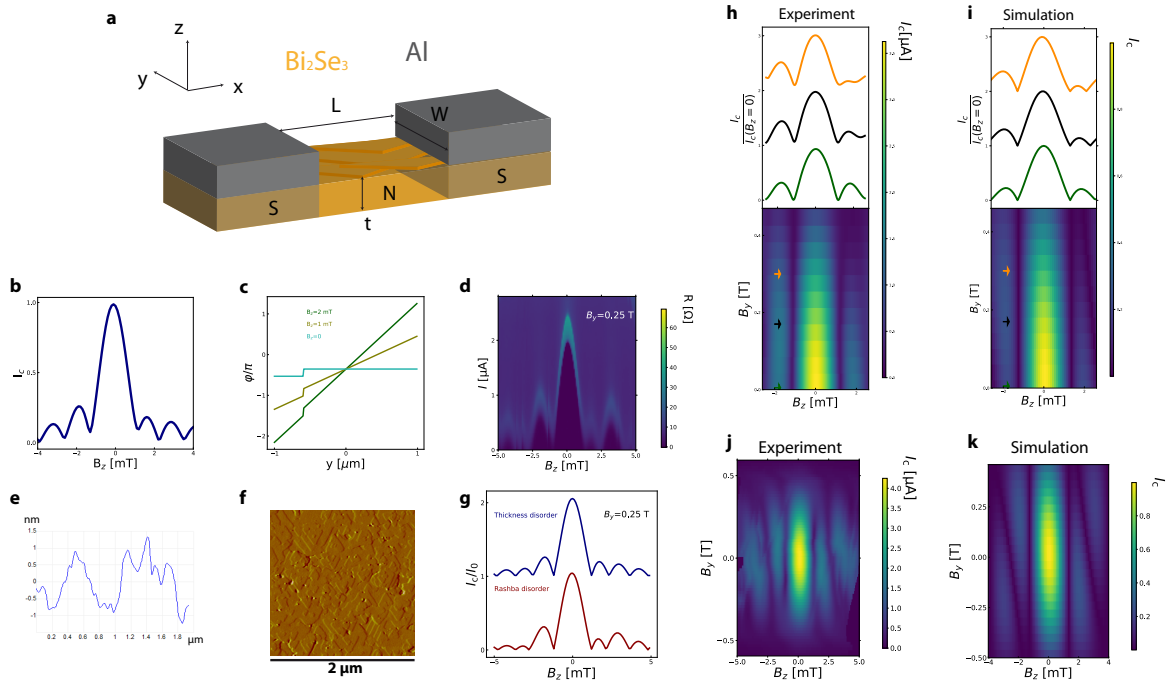


Fig. IV.13 **Simulation of the anomalous Fraunhofer pattern.** **b** An asymmetric Fraunhofer pattern can be generated simply by **c** a phase jump along the junction width. If it occurs symmetrically with respect to the junction center  $y=0$  it does not generate an asymmetric pattern. **d** Experimental Fraunhofer pattern with an in-plane magnetic field  $B_y = 0.25$  T. **e** AFM measurement showing thickness variation of the film of about  $\pm 1$  nm over a length  $l_d \approx 1 \mu\text{m}$ . **f** AFM topographic image of the  $Bi_2Se_3$  surface. **g** Simulation of an asymmetric pattern by considering spin-orbit induced phase jump due to the film thickness variation. **hj** Experimental critical current maps as a function of  $B_y$  and  $B_z$ . **ik** Simulation of the critical current maps.

Thus, we consider an additional disorder that can manifest through spin-orbit

coupling. As discussed in the first chapter and shown in Ref. [18], an in-plane magnetic field generates an anomalous phase difference between the two superconductors due to spin-orbit coupling in the weak link. In the ballistic regime this anomalous phase is given by :

$$\varphi_0 = \frac{4E_z L \alpha}{(\hbar v_F)^2}$$

where  $E_z = \frac{1}{2}g\mu_B B$  is the Zeeman energy. It is strongly generated in  $\text{Bi}_2\text{Se}_3$  due to its large Landé g-factor and Rashba spin-orbit coefficient  $\alpha$ . Nevertheless, in absence of disorder, the anomalous phase has no effect on the Fraunhofer pattern. It is understood because the arbitrary bulk phase difference between the two superconductors masks the anomalous phase  $\varphi_0$ . However, if the anomalous phase is spatially varying due to disorder in the junction it can generate an asymmetric Fraunhofer pattern. In Ref. [207] it is shown, from ARPES measurements, that the Rashba coefficient can change due to a thickness variation of 1 QL (1 nm). We consider a variation of  $\alpha' \approx 0.01 \text{ eV\AA}$  with the function  $\alpha(y) = \alpha + \alpha' \sin(2\pi y/l_d)$ . The mere existence of a large value for  $\alpha \approx 0.4 \text{ eV\AA}$ , does not lead to an asymmetric Fraunhofer pattern in absence of disorder, as the induced anomalous phase-shift  $\varphi_0$  can always be compensated by the arbitrary phase  $\varphi$ . In other words, because in Eq. IV.4.2, the critical current is obtained by maximizing over the arbitrary phase  $\varphi$ , a global change of  $\varphi_0$  will be compensated by an equivalent change of the arbitrary phase  $\varphi$ . Only the spatial variation of the anomalous phase due to disorder along the y direction can generate an asymmetric Fraunhofer pattern, in agreement with Table IV.4 indicating that finite disorder  $V_y$  must be present for the asymmetry to be present. We calculate the pattern by adding the anomalous phase in the usual relation :

$$I_c(B_z, B_y) = \max_{\varphi} \int_{-W/2}^{W/2} j_0 \sin \left( \varphi + \frac{2\pi(L + 2\lambda_L)yB_z}{\phi_0} + \varphi_0(y) \right) dy$$

We use the expression from Ref. [208] for the anomalous phase in the diffusive regime as the electrode spacing  $L=150 \text{ nm}$  is larger than the mean free path  $l=40 \text{ nm}$  :

$$\varphi_0 = \frac{\tau m^{*2} E_z (\alpha L)^3}{3\hbar^6 D} \quad (\text{IV.3})$$

where  $\tau = 0.13 \text{ ps}$  is the elastic scattering time,  $D = \frac{1}{3}v_F^2\tau = 40 \text{ cm}^2\text{s}^{-1}$  is the diffusion constant and  $m^* = 0.25 m_e$  is the effective electron mass[193]. The value of the Lande g-factor,  $g=19.5$ , is taken from electron spin resonance measurements[20]. The result for  $B_y = 0.25 \text{ T}$  is shown in red in Fig. IV.13g and agrees with the measured pattern. We also calculated the critical current maps shown in Fig. IV.13i and k which reproduce the experimental map Fig. IV.13h and j respectively. These maps are calculated using Eq. (IV.2), including the anomalous phase.

While a spatially varying anomalous phase provides a natural explanation for the asymmetric Fraunhofer pattern in these SNS junctions made from  $\text{Bi}_2\text{Se}_3$  with strong spin-orbit coupling, we also showed that disorder along the junction width in combina-

tion with  $B_y$ , is sufficient to generate an asymmetric Fraunhofer pattern. To unambiguously demonstrate that an anomalous phase shift  $\varphi_0$  is generated by finite spin-orbit coefficient  $\alpha$  and finite magnetic field  $B_y$ , a direct measurement of the current phase relation with in-plane magnetic field is required.

### IV.4.3 Detection of the anomalous Josephson effect

A remarkable consequence of the anomalous Josephson effect is that the current oscillation frequency of a superconducting loop interrupted by a Josephson junction does not depend solely on its surface, as shown in section IV.7.

To probe the anomalous Josephson effect, we measured simultaneously two Josephson interferometers, oriented as sketched in Fig. IV.14a, differing only by the orientation of the small junctions with respect to the in-plane magnetic field. According to Ref. [18] an anomalous phase manifests only in the small junction of the upper device in Fig. IV.14a. This is because the anomalous phase is generated perpendicular to the magnetic field. As the anomalous phase generates a current, the  $\varphi_0$  Josephson effect can be seen as the superconducting analogue of the spin galvanic effect (or inverse Edelstein effect)[80], where a spin polarization generates a transverse current. Therefore, we call the device where the anomalous phase is expected, the anomalous device while the other is the reference device where no anomalous phase is expected. This experiment were done in a dilution fridge equipped with a single magnetic coil at a base temperature  $T = 30$  mK. The sample is mounted in the fridge such that the sample plane is parallel to the magnetic field  $B$ . The sample plane can be mechanically tilted by about  $1^\circ$  with respect to the magnetic field. Thus, the magnetic field  $B$  produces an in-plane  $B_y = B \cos(\theta)$  and a perpendicular  $B_z = B \sin(\theta)$  magnetic field, as sketched in Fig. IV.14c. In this situation, the critical current for the reference device changes as  $I_c \propto \cos(\omega_{\text{ref}} B)$  with  $\omega_{\text{ref}} = \frac{2\pi S_{\text{ref}}}{\phi_0} \sin(\theta)$  where  $S_{\text{ref}}$  is the normal surface enclosed by the superconductor. For the anomalous device, the critical current changes as  $I_c \propto \cos(\omega B)$  with :

$$\omega = \frac{2\pi S}{\phi_0} \sin \theta + \dot{\varphi}_0 \cos(\theta) \quad (\text{IV.4})$$

with  $\dot{\varphi}_0 = \frac{\tau m^* 2g\mu_B (\alpha L)^3}{6\hbar^6 D}$

In Eq. (IV.4), the first term arises from the flux within the Josephson interferometer of area  $S$ , the second term arises from the anomalous phase shift in the diffusive regime  $\varphi_0 = \dot{\varphi}_0 B \cos(\theta)$ , which is expressed in the previous section.

Fig. IV.14b shows voltage maps for two different angle  $\theta$ . At low  $B$ , the two devices are in-phase and become out-of-phase at higher magnetic field, indicating that the frequency  $\omega$  of the anomalous device is slightly larger than the reference device, as expected from Eq. (IV.4) where the anomalous phase leads to an enhanced frequency  $\omega$  with respect to the reference device.

One also sees that the frequency of both devices decreases with increasing  $B$ . This is due to flux focusing that makes the effective device area larger at low magnetic field.

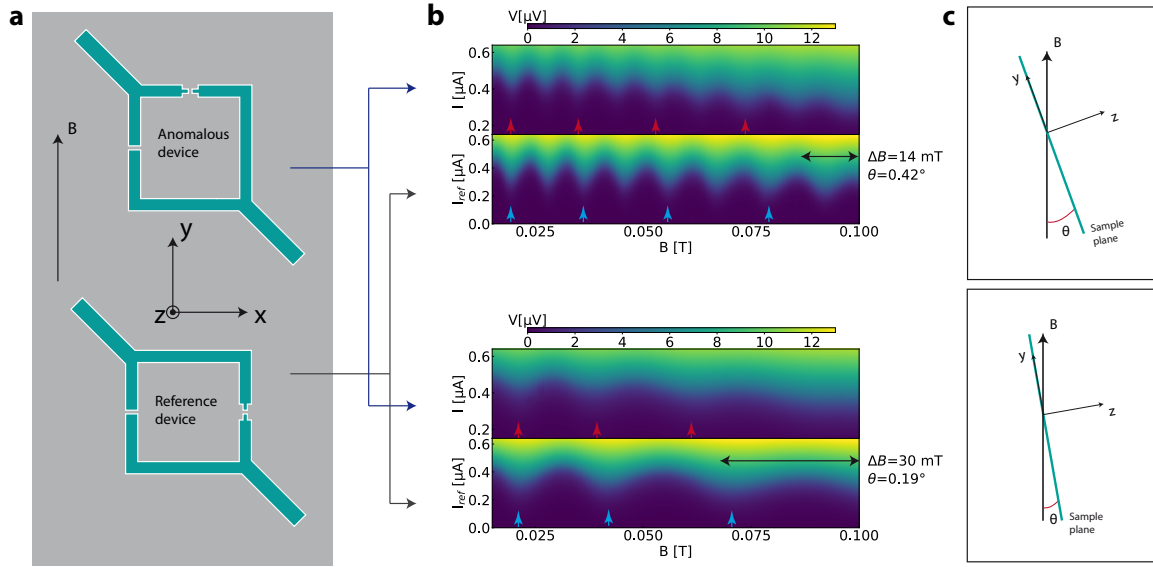


Fig. IV.14 **Probing the anomalous  $\phi_0$  Josephson effect** **a** Sketch of the setup consisting of two Josephson interferometers fabricated on the same chip. An anomalous phase induced by Rashba spin-orbit and a magnetic field  $B_y$  can only be generated in the small junction of the anomalous device, as it is correctly oriented with respect to  $B$ . **b** Voltage maps, showing the critical current oscillation of the two devices as a function of magnetic field  $B$ , for two different angle  $\theta$  between the magnetic field and the sample plane. The angle  $\theta$  is determined from the last oscillation period, as shown by the black arrow. The frequency of the anomalous device is larger than the reference as a consequence of the anomalous phase shift. The colored arrows are guide to the eyes, to help visualizing the increased phase shift in the anomalous device. **c** The oscillation frequency can be changed by mechanically tilting the sample, i.e by changing the perpendicular component of the magnetic field  $B_z = B \sin \theta$ .

As flux focusing decreases upon increasing the in-plane magnetic field, the effective areas of the devices are reduced and so are their frequencies.

The angle  $\theta$  is determined from the last oscillation period  $\Delta B$  of the reference device by the relation :

$$\theta = \arcsin\left(\frac{\phi_0}{S\Delta B}\right)$$

We choose the last oscillation period as it is the one where the effective area of the device is the closest from the area defined by lithography. The error on the determination of the angle  $\delta\theta$  is due to the error  $\delta(\Delta B)$  which is estimated as the difference between the last oscillation period and the before last oscillation period. The error on the angle is given by the relation :

$$\delta\theta = \frac{d\theta}{d\Delta B} \delta(\Delta B) = \frac{\phi_0 \delta(\Delta B)}{S \Delta B^2 \sqrt{1 - \left(\frac{\phi_0}{S \Delta B}\right)^2}}$$

To compare precisely the oscillation frequencies, the critical current plot, Fig. IV.15a, is extracted from the voltage maps. The average critical current, shown as a continuous line in Fig. IV.15a, is removed from the critical current curve and the result is shown in Fig. IV.15b for the two devices. These curves show that the anomalous device has a frequency larger than the reference as expected from Eq. (IV.4) where the anomalous phase leads to an enhanced frequency  $\omega$  with respect to the reference device.

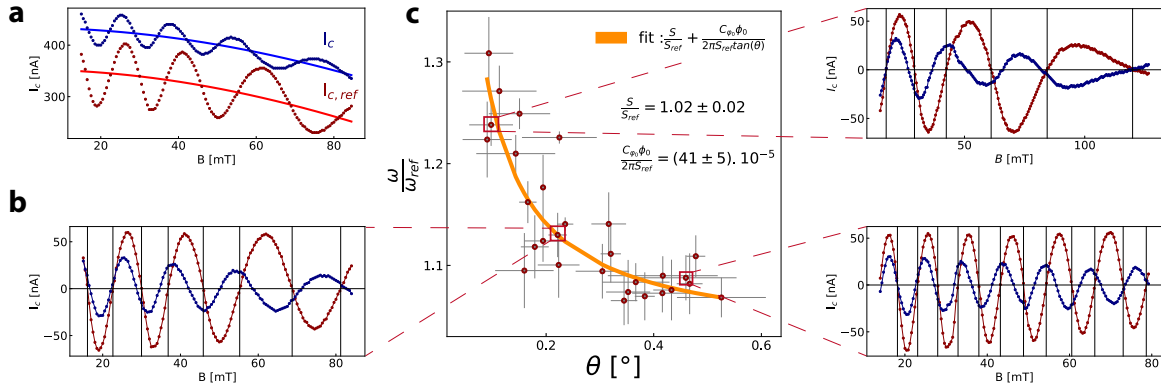


Fig. IV.15 **Comparison of the device frequencies as a function of the angle  $\theta$ .** **a** The critical current is extracted and shown as a function of magnetic field. The red and blue curves correspond to the reference and anomalous device respectively. The anomalous device shows a larger oscillation frequency than the reference device. As the critical current of the large junction decreases with the magnetic field, a decreasing background is fitted for both devices and shown by the continuous lines. **b** Critical current as function of magnetic field. The background is subtracted to compare precisely the oscillation frequency of the two devices. Each period are compared one by one and the average of the single period ratios provides a value  $\frac{\omega}{\omega_{ref}}$ . **c** The ratio of the oscillation frequencies is plotted as a function of the angle  $\theta$ . Without the generation of an anomalous phase this ratio should be constant and equal to the surface ratio  $\frac{S}{S_{ref}} \simeq 1$ . This ratio diverges as  $\frac{1}{\theta}$  for small  $\theta$ , as shown by Eq. (IV.5). Fitting the curve with Eq. (IV.5) provides the spin-orbit coefficient  $\alpha$ .

While the two devices have been fabricated with nominally identical areas, to exclude that the observed difference in frequencies between the two is due to a difference of areas, we plot in Fig. IV.15c, the frequency ratio  $\frac{\omega}{\omega_{ref}}(\theta)$  measured at different angles  $\theta$ . Because each curve contains several periods  $T_i$ , the frequency ratio is obtained from the average between N period ratio as  $\omega/\omega_{ref} = \frac{1}{N} \sum_{i=1}^N \frac{T_{i,ref}}{T_i}$ , where  $T_{i,ref}$  and  $T_i$  are the  $i^{th}$  oscillation period for the reference and for the anomalous device, respectively. This method enables ignoring the flux focusing effect because the ratio is taken between

two periods measured at about the same magnetic field. We find that the experimental data follows the relation :

$$\frac{\omega}{\omega_{\text{ref}}}(\theta) = \frac{S}{S_{\text{ref}}} + \frac{\dot{\varphi}_0 \phi_0}{2\pi S_{\text{ref}} \tan(\theta)} \quad (\text{IV.5})$$

At large  $\theta$ , this ratio is equal to the ratio of areas  $S/S_{\text{ref}} \simeq 1$ , however, for small  $\theta$ , this ratio increases as  $1/\tan(\theta)$ , indicating the presence of an anomalous phase shift  $\varphi_0$ . Indeed if there were no anomalous phase shift, this ratio should not depend on the angle and stays constant at the value  $\frac{S}{S_{\text{ref}}}$ .

Another method has been used to compare the frequency ratio. The initial procedure of removing the decreasing critical current background is the same as for the first method as shown in Fig. IV.16ab. As the oscillation frequency of the devices should not vary with the magnetic field in the absence of flux focusing, we create a new magnetic field scale,  $B_{\text{cor}}$ . On this field scale, flux focusing is corrected and the reference signal is periodic as shown in the lower panel of Fig. IV.16c. Furthermore, the oscillation frequency of the anomalous device is also periodic on this field scale as shown in the upper panel of Fig. IV.16c. In this corrected field scale, the frequency ratio  $\frac{\omega}{\omega_{\text{ref}}}$  is extracted from sinusoidal fit and plotted Fig. IV.16d. It provides the same result as the first method : at large  $\theta$ , the ratio is equal to the ratio of areas  $S/S_{\text{ref}} \simeq 1$ , however, for small  $\theta$ , this ratio increases as  $1/\tan(\theta)$ , indicating the presence of an anomalous phase shift.

We retain the value extracted from the fit  $\frac{\dot{\varphi}_0 \phi_0}{2\pi S_{\text{ref}}} = 4.1 \cdot 10^{-4}$  using the first method, without flux focusing correction, to calculate the Rashba coefficient  $\alpha$ . Using the expression of  $\dot{\varphi}_0$  given above, we calculate a spin-orbit coefficient  $\alpha = 0.38 \text{ eV\AA}$ . This value of the Rashba coefficient is consistent with the value extracted from spin-splitting conduction band observed by photoemission measurements [153, 33]. A contribution from the Dirac states is possible, however, despite their large effective Rashba coefficient, see chapter 1 section spin-orbit, about  $4 \text{ eV\AA}$ , their larger Fermi velocity makes their contribution to the anomalous phase shift smaller than the spin-splitting bulk states.

The symmetry analysis of Ref. [206], discussed in the previous section, also enumerates the parameters required for the appearance of an anomalous phase. Table IV.5 from Ref. [206] shows that the anomalous phase observed here must be the consequence of finite Rashba coefficient  $\alpha$  and in-plane magnetic field  $B_y$ . Indeed, while Table IV.5 shows that disorder alone  $V_y$  is sufficient to generate an anomalous phase shift, this disorder-induced anomalous phase shift should exist even at low magnetic field and should not change with magnetic field. In contrast, the data in Fig. IV.14b shows that the two devices are in-phase at low magnetic field and that the anomalous phase shift is induced by the in-plane magnetic field. Thus, this observation implies that disorder  $V_y$  is absent, which is plausible as the small Josephson junction is only  $150 \text{ nm} \times 150 \text{ nm}$ , which is much smaller than the disorder length  $l_d \approx 1 \mu\text{m}$  observed in AFM, see previous section. In the absence of disorder  $V_y$ , Table IV.5 shows that the only way for an anomalous phase shift to be present is that the coefficient  $\alpha$  be

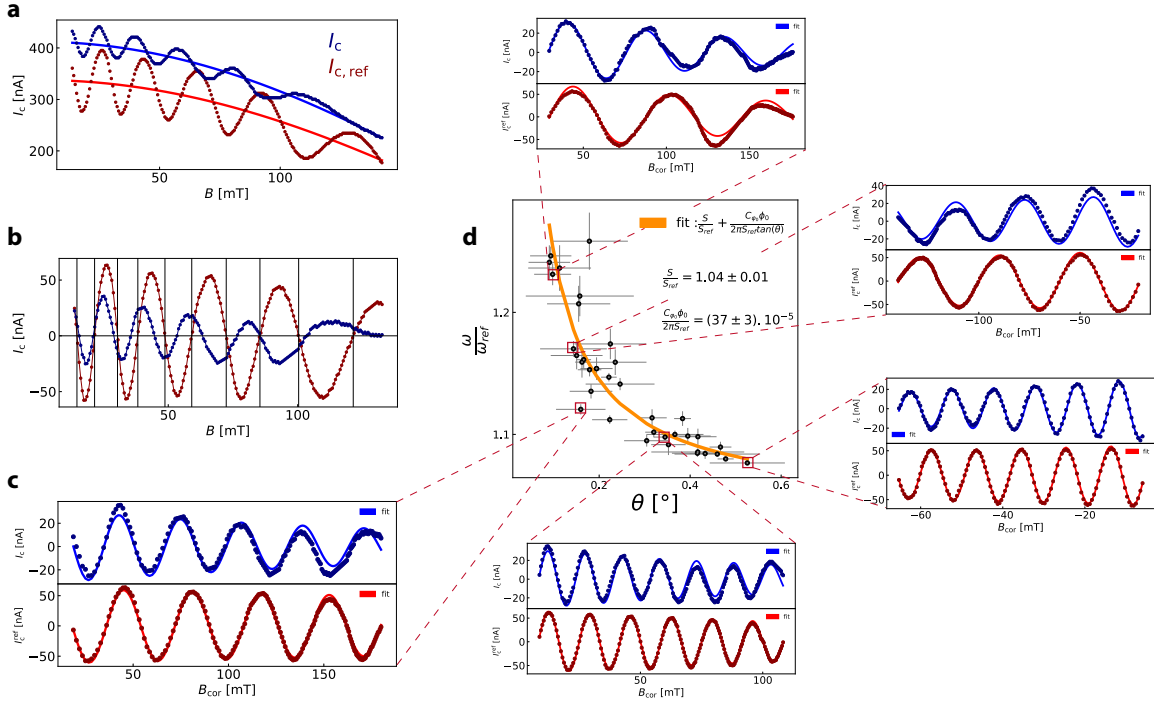


Fig. IV.16 **Comparison of the device frequencies : second method.** **a** The critical current is extracted and shown as a function of magnetic field. The red and blue curves correspond to the reference and anomalous device respectively. **b** Critical current as function of magnetic field. The background is subtracted to compare precisely the oscillation frequencies of the two devices. The zeros of critical current of the reference (red) are not regularly spaced due to flux focusing. **c** Critical current of the anomalous (upper panel) and reference (lower panel) devices as a function of the corrected magnetic field,  $B_{cor}$ . The zeros of critical current are now regularly spaced. The frequencies for the reference and the anomalous devices are extracted from sinusoidal fit shown as continuous lines. **d** Ratio of the oscillation frequencies  $\frac{\omega}{\omega_{ref}}$  as a function of the angle  $\theta$ . This ratio diverges as  $\frac{1}{\theta}$  for small  $\theta$  due to the anomalous phase generated by spin-orbit coupling.

non-zero. Indeed, if  $\alpha$  were zero, the first and third symmetry operations of Table IV.5 would not be broken even with finite  $B_y$ .

$UH(\varphi)U^\dagger=H(-\varphi)$	Broken by
$P_y P_x$	$\alpha, V_x, V_y$
$\sigma_z P_y P_x$	$B_x, B_y, V_x, V_y$
$\sigma_x P_y T$	$B_x, \alpha, V_y$
$\sigma_y P_y T$	$B_y, V_y$

Table IV.5 From Ref. [206], symmetry operations  $U$  protecting  $H(\varphi) = H(-\varphi)$ . Which in turn results in  $\varphi_0 = 0$ . The symmetry operations on the left column are broken by one of the parameters on the right column. These parameters include the in-plane magnetic fields  $B_x, B_y$ , the asymmetric disorder potentials  $V_x, V_y$  and the spin-orbit term  $\alpha$  which is the consequence of the structural inversion asymmetry (Rashba). To generate an anomalous phase  $\varphi_0$ , each symmetry operator, one per line of the table, must be broken. For example, the combination of the magnetic field  $B_y$  and the spin orbit coupling  $\alpha$  is enough to break all the symmetries.

An interesting perspective would be to generate an anomalous phase through spin-orbit coupling without magnetic field. Indeed, several studies have shown that injecting a normal current through a material with strong spin-orbit coupling result in a spin polarization at the surface, an effect known as the Edelstein effect[209]. It could potentially be used to replace the magnetic field in Table IV.5 and generates an anomalous phase.

## IV.5 Current injection across a $\text{Bi}_2\text{Se}_3$ Josephson junction

### IV.5.1 Current induced spin polarization

We fabricate single junction and interferometer devices with additional gold electrodes on top of the  $\text{Bi}_2\text{Se}_3$  to inject a normal current across the Josephson junction. Such device is sketched in Fig. IV.17c.

Similar devices have been fabricated with Nb-Au-Nb Josephson junction where a normal current was injected in the region carrying the supercurrent[210, 61]. In Ref. [61] a transition to a  $\pi$  junction has been induced by changing the electron energy distribution in the junction. This is achievable when the time spent by an injected electron between the two reservoirs is smaller than the inelastic scattering time. It is not the case in our experiment, as we did not try to reduce the spacing between the reservoirs. We used a different approach where the injected current generates a spin polarization at the surface. Indeed as sketched in Fig. IV.17ab, the electronic bands of  $\text{Bi}_2\text{Se}_3$  are spin textured at the surface, as discussed in the first chapter. When no

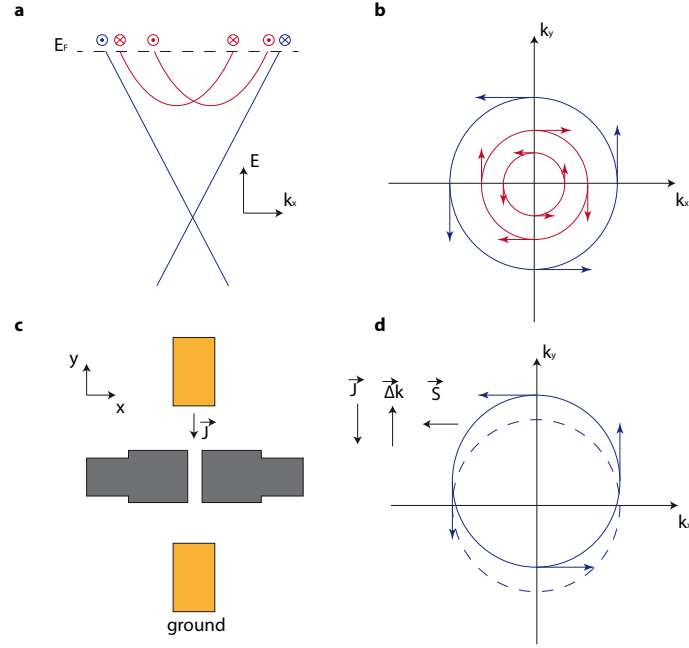


Fig. IV.17 **Current induced spin polarization.** **a** Dirac cone (blue) and spin split Rashba states (red). **b** Electronic bands at the Fermi energy in the  $k_x$ - $k_y$  plane. **c** Sketch of a Josephson junction (gray) and two gold electrodes (yellow) used for current injection. **d** A current shifts the Fermi surface in opposite direction. It results in a net spin polarization perpendicular to the current. The Rashba states are not represented for simplicity.

current is applied, the summation over the spin of all  $k$  vectors results in zero net spin polarization[211] :

$$S = \frac{1}{2\pi^2} \int_{E(\vec{k}) < E_F} s(\vec{k}) dk_x dk_y = 0$$

A finite current density  $\vec{j}$  induces a shift of the Fermi surface in reciprocal space  $\Delta\vec{k}$ , as shown in Fig. IV.17d. Thus, the summation over the spin of all  $k$  vectors results in a net spin accumulation. This current induced spin accumulation has been detected by spin-torque measurements where a ferromagnetic electrode is deposited on top of  $\text{Bi}_2\text{Se}_3$ [212, 213].

To estimate the energy associated with the spin accumulation, we approximate the shift in momentum as  $\Delta\vec{k} \approx \frac{m^* \vec{j}}{en\hbar}$  and the associated energy as  $\alpha\Delta\vec{k} \approx 10 \mu\text{V}$  for a current  $I = 10 \mu\text{A}$  across an area  $4 \mu\text{m} \times 20 \text{nm}$ . This energy is larger than the thermal energy at 30 mK. Also, it corresponds to a Zeeman energy induced by a magnetic field of 10 mT with a Landé factor  $g=20$ .

### IV.5.2 Effect of heating

We show the result of current injection for the Josephson interferometer shown in Fig. IV.18a. An additional Yokogawa source is used to inject a current  $I_{\text{control}}$  in the  $\text{Bi}_2\text{Se}_3$ . Its ground is different and isolated from that of the junction. It insures that the injected current which enters by the top electrode is equal to the current which exits by the bottom electrode denoted "ground yoko" in Fig. IV.18a. The critical current of the junction is shown as a function of the control current  $I_{\text{control}}$  in Fig. IV.18b. The Josephson current vanished above  $2 \mu\text{A}$  and superconductivity above  $3 \mu\text{A}$ . We attribute this effect to an increase in temperature due to dissipation in the film. The resistance between the two electrodes used for current injection is  $R = 1.1 \text{ k}\Omega$ . Thus, an electrical power  $P = RI_{\text{control}}^2$  is dissipated by phonons through electron-phonon coupling. It is expressed with the relation[214] :

$$P = \Gamma V(T_{\text{el}}^5 - T_{\text{ph}}^5)$$

where  $\Gamma$  is the electron-phonon coupling strength and is typically  $1 \text{ nW} \cdot \mu\text{m}^{-3} \cdot \text{K}^{-5}$ ,  $V = 4\mu\text{m} \times 25\mu\text{m} \times 20\text{nm}$  is the volume of the film and  $T_{\text{el}}$  ( $T_{\text{ph}}$ ) is the electron (phonon) temperature. If we consider  $T_{\text{el}} \gg T_{\text{ph}}$  or  $T_{\text{ph}} = 0$ , we find, for a current  $I_{\text{control}} = 2 \mu\text{A}$ , an electron temperature  $T_{\text{el}} \approx 1.2 \text{ K}$  which is larger than the critical temperature of the aluminum  $T_c = 0.75 \text{ K}$ . Therefore at low temperature, electron-phonon coupling is weak and it is easy to increase the electron temperature. This imposes a serious limitation on the current induced spin polarization for device made with aluminum.

We compare the critical current oscillation of the device without current injection in Fig. IV.18c and with an injected current  $I_{\text{control}} = 0.5 \mu\text{A}$  in Fig. IV.18d. We only observed a drop in the critical current of both junctions, no shift in magnetic field were detected for the oscillation. We also checked the effect of current injection on the Fraunhofer pattern of single junction. No anomalous behaviour were observed.

## IV.6 Anomalous Shapiro steps

Due to the anomalous Josephson effect it should be possible to observe Shapiro steps induced by the coupling of a Josephson junction to the magnetic field instead of the electric field. If the microwave energy  $\hbar\omega$  matches the Zeeman energy, transition between the two spin states can be induced at the microwave frequency. Therefore, the anomalous phase will oscillate,  $\varphi_0(t) = A(1 + C \cos(\omega t))$ , with  $A = \frac{E_z L \alpha}{(\hbar v_F)^2}$  and  $AC$  the oscillation amplitude. The usual expression for the Shapiro steps, see Eq. IV.3.2, becomes :

$$I_J = I_c \sum (-1)^n J_n \left( \frac{2eV_1}{\hbar\omega} + AC \right) \sin \left( cst + \frac{2eV_0 t}{\hbar} - n\omega t \right)$$

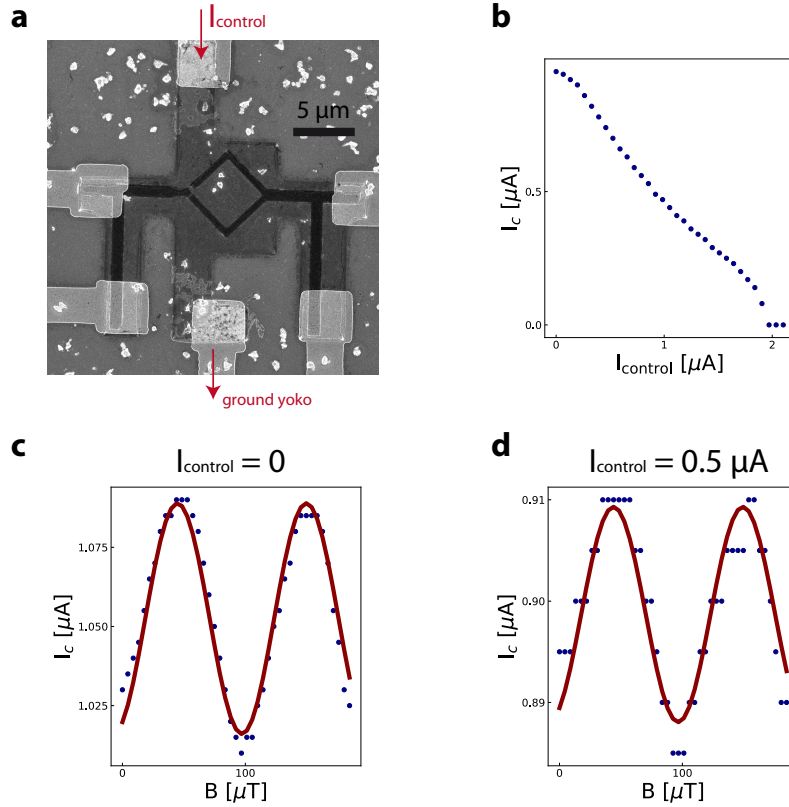


Fig. IV.18 **Heating effect.** **a** SEM image of a Josephson interferometer. Two additional gold electrodes are present to inject a current  $I_{\text{control}}$  in the  $\text{Bi}_2\text{Se}_3$ . **b** Critical current of the device as a function of the control current. **c** Critical current as a function of perpendicular magnetic field measured without current injection. **d** Critical current as a function of magnetic field for a finite control current corresponding to  $V_{\text{control}} = 20$  mV.

By placing the junction in a tunable cavity[215] the usual Shapiro steps will be observed at an electric field maximum corresponding to  $\frac{2eV_1}{\hbar\omega} \gg AC$ . By tuning the cavity such that the junction is at an electric field node and a magnetic field maximum  $\frac{2eV_1}{\hbar\omega} \ll AC$ , Shapiro steps resulting from the coupling to the magnetic field could be observed.

## IV.7 Conclusion and perspectives

To summarize, the simultaneous measurements of the CPR in two Josephson interferometers, making an angle of  $90^\circ$  with respect to the in-plane magnetic field, enabled the identification of the anomalous phase shift  $\varphi_0$  induced by the combination of the strong spin-orbit coupling and in-plane magnetic field. We estimated that an in-plane magnetic field of 0.25 T generates an anomalous phase shift of  $2\pi$ . This anomalous

phase shift can be employed to fabricate a phase battery, a device of intense interest for the design and fabrication of superconducting circuits[216, 217].

It will be worth trying to measure the Shapiro steps on thicker  $\text{Bi}_2\text{Se}_3$  films. Indeed, the  $4\pi$  phase periodicity of the Josephson current in three dimensional topological insulators has only been detected in thick samples[166, 164]; possibly due to a better decoupling of the two surfaces.

As discussed in section IV.5, an interesting perspective will be to probe spin-orbit related phenomena without magnetic field. We encounter a heating problem when trying to induce a spin polarization by injecting a current in  $\text{Bi}_2\text{Se}_3$ . This difficulty could be overcome in a non-local geometry in the spirit of Ref. [218]. Indeed, by using a material with a long spin coherence length, like InAs, one could inject a current far ( $\approx 1 \mu\text{m}$ [219]) from the junction and detect the phase shift induced by the spin polarization, as sketch in Fig. IV.19.

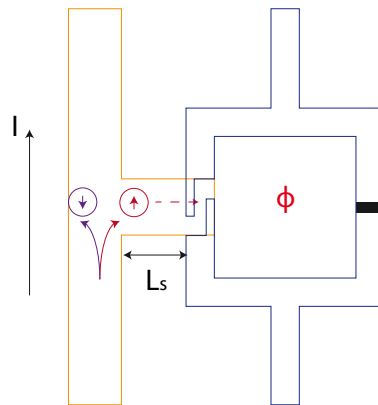


Fig. IV.19 **Non local spin injection in a Josephson junction.** A current  $I$  is injected across a material with spin-orbit coupling (yellow). In blue, a SQUID device with a tunnel junction (black) and a SNS junction on the spin-orbit coupled material. Due to the spin Hall effect, a spin current is induced in the SNS junction and can result in a detectable flux in the SQUID.  $L_s$  should be of the order of the spin coherence length.

It has been proposed that the edges of quantum spin Hall insulator should carry an anomalous Josephson current with an in-plane magnetic field[220]. As discussed in section IV.1, signatures of supercurrent at the edges of  $\text{HgTe}/\text{CdTe}$ [167] and  $\text{InAs}/\text{GaSb}$ [174] hetero-structures have been reported. Even in the non topological regime, the anomalous Josephson effect in these systems should be measurable as the g-factor is large ( $g \approx 10$ ) as well as the Rashba coefficient  $\alpha \approx 0.1 \text{ eV}\cdot\text{\AA}$  for  $\text{InAs}/\text{GaSb}$ [221] and  $\alpha \approx 0.2 \text{ eV}\cdot\text{\AA}$  for  $\text{HgTe}/\text{CdTe}$ [222]. Moreover, in the quantum spin Hall insulator regime, which is accessible by tuning the gate voltage, the anomalous phase shift should be controlled by an effective Rashba coefficient, solely related to the Fermi velocity  $v_F$ . The quasi one dimensional edge states could also be used as

Dayem bridges in nano-SQUID devices[9].

# Conclusion

In this thesis, we studied the electronic properties of semiconductor junctions between two superconductors.

We presented the theory describing these devices. In the case where the semiconductor is a quantum dot, the ground state of the system depends on the coupling with the superconductor, the charging energy and the energy difference between the quantum dot level and the Fermi energy. In the case of negligible Kondo screening, the ground state of the system determines the sign of the Josephson current and a ground state transition can induced an offset of  $\pi$  in the Josephson current phase relation. When the semiconductor is a two dimensional system with strong spin-orbit coupling, applying a magnetic field results in an offset  $\varphi_0$  different from 0 or  $\pi$  in the current phase relation. Thus, the  $\varphi_0$  offset is related to the spin-orbit coupling parameters of the semiconductor.

We have presented the fabrication of superconducting devices based on Si doped InAs nanowires and Bi<sub>2</sub>Se<sub>3</sub> thin films coupled to superconducting aluminium electrodes.

At low temperature, we observed that the InAs nanowires were in the regime of Coulomb blockade. We observed a discrete energy spectrum due to quantum confinement of the electronic states. The mean level spacing of this spectrum, extracted from Coulomb peak measurements, was in agreement with a quantum dot of volume corresponding to the nanowire between the superconducting leads. We have probed the sub gap resonances at voltages  $eV < 2\Delta$ , which result from Andreev reflections and observed transition between ground states when changing the occupancy of the quantum dot or the coupling with the superconducting leads. By applying large negative gate voltage, we induced a metal insulator transition and observed an evolution of the sub gap resonances in agreement with the theoretical phase diagram describing Andreev quantum dots.

Within the field of hybrid semiconducting-superconducting devices, numerous theoretical works have appeared proposing different means of breaking time-reversal and inversion symmetry to induce an anomalous phase shifts  $\varphi_0$  in Josephson junctions. We presented recent studies of Andreev quantum dots and showed that an anomalous phase shift, has been reported in Josephson interferometers based on nanowires by the Kouwenhoven's group.

For this thesis, we fabricated Josephson junctions and SQUIDs based on Bi<sub>2</sub>Se<sub>3</sub> thin

films. The Josephson current dependence to microwave irradiation and magnetic field was studied. An asymmetric Fraunhofer pattern has been observed by applying an in-plane magnetic field. We developed a simple model, involving disorder and spin-orbit coupling, to reproduce the experimental observations. We designed and performed an experiment where the disorder contribution could be well separated from the spin-orbit contribution. An anomalous phase shift  $\varphi_0$  in the current phase relation of Josephson interferometer devices was detected. We showed that this offset  $\varphi_0$  is solely related to the interplay between the magnetic field and spin-orbit coupling. The observation of this phase offset, in systems where the band structure can be modulated by strain, or where the position of the Fermi energy can be changed by a field effect, will be of great interest to identify distinct topological phases within the Josephson junctions.

## A - Josephson $\varphi_0$ interferometer

Consider a Josephson junction with the current phase relation  $I_{c,1} \sin(\varphi_1)$ , in parallel with another junction described by the anomalous Josephson current phase relation  $I_{c,2} \sin(\varphi_2 + \varphi_0)$ , the total current reads :

$$I = I_{c,1} \sin(\varphi_1) + I_{c,2} \sin(\varphi_2 + \varphi_0)$$

If the device inductance can be neglected, the two phase differences are linked by the relation :

$$\varphi_1 - \varphi_2 = \frac{2\pi\phi}{\phi_0}$$

and the critical current is obtained by maximizing over one of the phase difference :

$$I_c = \max_{\varphi_1} \left[ I_{c,1} \sin(\varphi_1) + I_{c,2} \sin\left(\varphi_1 - \frac{2\pi\phi}{\phi_0} + \varphi_0\right) \right]$$

If  $I_{c,1} \gg I_{c,2}$ , the phase  $\varphi_1$  stays fixed at  $\pi/2$  to insure a maximum current through the junction of larger critical current. The flux is  $\phi = BS$  where S is the surface enclosed by the device. Then :

$$I_c = I_{c,1} + I_{c,2} \cos\left(\frac{2\pi BS}{\phi_0} + \varphi_0\right)$$

If  $\varphi_0$  depends linearly on the magnetic field B,  $\varphi_0 = aB$  with  $a$  constant, the oscillation frequency of the device is modified due to the anomalous phase :

$$I_c = I_{c,1} + I_{c,2} \cos\left(\left(\frac{2\pi S}{\phi_0} + a\right)B\right)$$



# Publications

1. Alexandre Assouline, Cheryl Feuillet-Palma, Alexandre Zimmers, Marco Aprili, Jean-Christophe Harmand, and Hervé Aubin. “Shiba bound states across the mobility edge in doped InAs nanowires.” [Physical Review Letters 119, 097701\(2017\)](#)
2. Alexandre Assouline, Cheryl Feuillet-Palma, Nicolas Bergeal, Tianzhen Zhang, Alireza Mottaghizadeh, Alexandre Zimmers, Emmanuel Lhuillier, Mahmoud Eddrief, Paola Atkinson, Marco Aprili, and Hervé Aubin. “Spin-orbit induced phase-shift in  $\text{Bi}_2\text{Se}_3$  Josephson junctions.” [Preprint arXiv :1806. 01406.   
https://arxiv.org/abs/1806.01406. \(2018\)](#)
3. Wasim J. Mir, Alexandre Assouline, Clément Livache, Bertille Martinez, Nicolas Goubet, Xiang Zhen Xu, Gilles Patriarche, Sandrine Ithurria, Hervé Aubin, and Emmanuel Lhuillier. “Electronic properties of  $(\text{Sb};\text{Bi})_2\text{Te}_3$  colloidal heterostructured nanoplates down to the single particle level.” [Scientific Reports, volume 7, Article number : 9647 \(2017\)](#)
4. Sergio Vlaic, Stéphane Pons, Tianzhen Zhang, Alexandre Assouline, Alexandre Zimmers, Christophe David, Guillemain Rodary, Jean-Christophe Girard, Dimitri Roditchev, and Hervé Aubin. “Superconducting parity effect across the Anderson limit.” [Nature Communications 8 \(2\) : 14549\(2017\)](#)
5. Tianzhen Zhang, Sergio Vlaic, Stéphane Pons, Alexandre Assouline, Alexandre Zimmers, Dimitri Roditchev, Guy Allan, Christophe Delerue, Christophe David, Guillemain Rodary, Jean-Christophe Girard, and Hervé Aubin. “Quantum confinement effects in Pb nanocrystals grown on InAs.” [Physical Review B 97\(21\) : 214514\(2018\)](#) (Editor’s suggestion)



# Bibliographie

- [1] R. L. FAGALY ; «Superconducting quantum interference device instruments and applications» ; Rev. Sci. Instrum. **77**, p. 101 101 (2006). [v](#)
- [2] K. ENPUKU, Y. TSUJITA, K. NAKAMURA, T. SASAYAMA & T. YOSHIDA ; «Bio-sensing utilizing magnetic markers and superconducting quantum interference devices» ; Supercond. Sci. Technol. **30**, p. 053 002 (2017). [v](#)
- [3] G. WENDIN & V. S. SHUMEIKO ; «Quantum bits with Josephson junctions (Review Article)» ; Low Temp. Phys. **33**, p. 724–744 (2007). [v](#)
- [4] G. WENDIN ; «Quantum information processing with superconducting circuits : a review» ; Rep. Prog. Phys. **80**, p. 106 001 (2017). [v](#)
- [5] B. D. JOSEPHSON ; «Possible new effects in superconductive tunnelling» ; Physics Letters **1**, p. 251–253 (1962). [v](#), [25](#)
- [6] P. W. ANDERSON & J. M. ROWELL ; «Probable Observation of the Josephson Superconducting Tunneling Effect» ; Phys. Rev. Lett. **10**, p. 230–232 (1963). [v](#)
- [7] S. SHAPIRO ; «Josephson Currents in Superconducting Tunneling : The Effect of Microwaves and Other Observations» ; Phys. Rev. Lett. **11**, p. 80–82 (1963). [v](#), [88](#)
- [8] R. C. JAKLEVIC, J. LAMBE, A. H. SILVER & J. E. MERCEREAU ; «Quantum Interference Effects in Josephson Tunneling» ; Phys. Rev. Lett. **12**, p. 159–160 (1964). [v](#)
- [9] V. BOUCHIAT ; «Detection of magnetic moments using a nano-SQUID : limits of resolution and sensitivity in near-field SQUID magnetometry» ; Supercond. Sci. Technol. **22**, p. 064 002 (2009). [v](#), [69](#), [110](#)
- [10] C. NAYAK, S. H. SIMON, A. STERN, M. FREEDMAN & S. DAS SARMA ; «Non-Abelian anyons and topological quantum computation» ; Rev. Mod. Phys. **80**, p. 1083–1159 (2008). [v](#)
- [11] Y.-J. DOH, J. A. VAN DAM, A. L. ROEST, E. P. A. M. BAKKERS, L. P. KOUWENHOVEN & S. DE FRANCESCHI ; «Tunable supercurrent through semiconductor nanowires» ; Science **309**, p. 272–275 (2005). [v](#), [67](#)
- [12] Z. HAN, A. ALLAIN, H. ARJMANDI-TASH, K. TIKHONOV, M. FEIGEL'MAN, B. SACÉPÉ & V. BOUCHIAT ; «Collapse of superconductivity in a hybrid tin-graphene Josephson junction array» ; Nat. Phys. **10**, p. 380 (2014). [v](#)

- [13] C. G. L. BØTTCHER, F. NICHELE, M. KJAERGAARD, H. J. SUOMINEN, J. SHABANI, C. J. PALMSTRØM & C. M. MARCUS; «Superconducting, Insulating, and Anomalous Metallic Regimes in a Gated Two-Dimensional Semiconductor-Superconductor Array»; (2017)[1711.01451](#). [v](#)
- [14] B. VAN HECK, S. MI & A. R. AKHMEROV; «Single fermion manipulation via superconducting phase differences in multiterminal Josephson junctions»; *Phys. Rev. B Condens. Matter* **90**, p. 155 450 (2014). [v](#)
- [15] R.-P. RIWAR, M. HOUZET, J. S. MEYER & Y. V. NAZAROV; «Multi-terminal Josephson junctions as topological matter»; *Nat. Commun.* **7**, p. 11 167 (2016). [v](#)
- [16] P. KROGSTRUP, N. L. B. ZIINO, W. CHANG, S. M. ALBRECHT, M. H. MADSEN, E. JOHNSON, J. NYGÅRD, C. M. MARCUS & T. S. JESPERSEN; «Epitaxy of semiconductor-superconductor nanowires»; *Nat. Mater.* **14**, p. 400–406 (2015). [v](#), [69](#)
- [17] R. YAN, G. KHALSA, S. VISHWANATH, Y. HAN, J. WRIGHT, S. ROUVIMOV, D. S. KATZER, N. NEPAL, B. P. DOWNEY, D. A. MULLER, H. G. XING, D. J. MEYER & D. JENA; «GaN/NbN epitaxial semiconductor/superconductor heterostructures»; *Nature* **555**, p. 183–189 (2018). [v](#)
- [18] A. BUZDIN; «Direct coupling between magnetism and superconducting current in the Josephson  $\phi_0$  junction»; *Phys. Rev. Lett.* **101**, p. 107 005 (2008). [vi](#), [25](#), [26](#), [75](#), [99](#), [100](#)
- [19] H. KOSAKA, A. A. KISELEV, F. A. BARON, K. W. KIM & E. YABLONOVITCH; «Electron g-factor Engineering in III-V Semiconductors for Quantum Communications»; (2001)[quant-ph/0102056](#). [4](#)
- [20] A. WOLOS, S. SZYSZKO, A. DRABINSKA, M. KAMINSKA, S. G. STRZELECKA, A. HRUBAN, A. MATERNA, M. PIERSA, J. BORYSIUK, K. SOB CZAK & M. KONCZYKOWSKI; «g -factors of conduction electrons and holes in  $B i_2 S e_3$  three-dimensional topological insulator»; *Phys. Rev. B Condens. Matter* **93**, p. 3023 (2016). [4](#), [79](#), [99](#)
- [21] T. IHN; *Semiconductor Nanostructures : Quantum States and Electronic Transport* (Oxford University Press) (2010). [4](#), [54](#)
- [22] L. W. MOLENKAMP, G. SCHMIDT & G. E. W. BAUER; «Rashba Hamiltonian and electron transport»; *Phys. Rev. B Condens. Matter* **64**, p. 121 202 (2001). [5](#)
- [23] S. MURAKAMI, N. NAGAOSA & S.-C. ZHANG; «Dissipationless quantum spin current at room temperature»; *Science* **301**, p. 1348–1351 (2003). [6](#)
- [24] J. SINOVA, D. CULCER, Q. NIU, N. A. SINITSYN, T. JUNGWIRTH & A. H. MACDONALD; «Universal intrinsic spin Hall effect»; *Phys. Rev. Lett.* **92**, p. 126 603 (2004). [6](#)

- [25] D. XIAO, M.-C. CHANG & Q. NIU; «Berry phase effects on electronic properties»; *Rev. Mod. Phys.* **82**, p. 1959–2007 (2010). 6
- [26] Y. K. KATO, R. C. MYERS, A. C. GOSSARD & D. D. AWSCHALOM; «Observation of the spin Hall effect in semiconductors»; *Science* **306**, p. 1910–1913 (2004). 6
- [27] V. M. EDELSTEIN; «Spin polarization of conduction electrons induced by electric current in two-dimensional asymmetric electron systems»; *Solid State Commun.* **73**, p. 233–235 (1990). 6, 27
- [28] S. D. GANICHEV, M. TRUSHIN & J. SCHLIEMANN; «Spin polarisation by current»; (2016) [1606.02043](#). 6
- [29] S. D. GANICHEV, E. L. IVCHENKO, V. V. BEL'KOV, S. A. TARASENKO, M. SOLLINGER, D. WEISS, W. WEGSCHEIDER & W. PRETTL; «Spin-galvanic effect»; *Nature* **417**, p. 153–156 (2002). 6
- [30] M. B. LUNDEBERG & J. A. FOLK; «Spin-resolved quantum interference in graphene»; *Nat. Phys.* **5**, p. 894 (2009). 6
- [31] L. BAWDEN, J. M. RILEY, C. H. KIM, R. SANKAR, E. J. MONKMAN, D. E. SHAI, H. I. WEI, E. B. LOCHOCKI, J. W. WELLS, W. MEEVASANA, T. K. KIM, M. HOESCH, Y. OHTSUBO, P. LE FÈVRE, C. J. FENNIE, K. M. SHEN, F. CHOU & P. D. C. KING; «Hierarchical spin-orbital polarization of a giant Rashba system»; *Sci Adv* **1**, p. e1500495 (2015). 7
- [32] Y. M. KOROTEEV, G. BIHLMAYER, J. E. GAYONE, E. V. CHULKOV, S. BLÜGEL, P. M. ECHENIQUE & P. HOFMANN; «Strong spin-orbit splitting on bi surfaces»; *Phys. Rev. Lett.* **93**, p. 046403 (2004). 7
- [33] P. D. C. KING, R. C. HATCH, M. BIANCHI, R. OVSYANNIKOV, C. LUPULESCU, G. LANDOLT, B. SLOMSKI, J. H. DIL, D. GUAN, J. L. MI, E. D. L. RIENKS, J. FINK, A. LINDBLAD, S. SVENSSON, S. BAO, G. BALAKRISHNAN, B. B. IVERSEN, J. OSTERWALDER, W. EBERHARDT, F. BAUMBERGER & P. HOFMANN; «Large tunable Rashba spin splitting of a two-dimensional electron gas in Bi<sub>2</sub>Se<sub>3</sub>»; *Phys. Rev. Lett.* **107**, p. 096802 (2011). 7, 42, 44, 75, 79, 82, 103
- [34] C. R. AST, J. HENK, A. ERNST, L. MORESCHINI, M. C. FALUB, D. PACILÉ, P. BRUNO, K. KERN & M. GRIONI; «Giant spin splitting through surface alloying»; *Phys. Rev. Lett.* **98**, p. 186807 (2007). 7
- [35] P. D. C. KING, T. D. VEAL, C. F. MCCONVILLE, J. ZÚÑIGA-PÉREZ, V. MUÑOZ-SANJOSÉ, M. HOPKINSON, E. D. L. RIENKS, M. F. JENSEN & P. HOFMANN; «Surface band-gap narrowing in quantized electron accumulation layers»; *Phys. Rev. Lett.* **104**, p. 256803 (2010). 7
- [36] M.-C. CHANG; «Effect of in-plane magnetic field on the spin Hall effect in a Rashba-Dresselhaus system»; *Phys. Rev. B Condens. Matter* **71**, p. 085315 (2005). 7

- [37] C. H. L. QUAY, T. L. HUGHES, J. A. SULPIZIO, L. N. PFEIFFER, K. W. BALDWIN, K. W. WEST, D. GOLDHABER-GORDON & R. DE PICCIOTTO ; «Observation of a one-dimensional spin-orbit gap in a quantum wire» ; Nat. Phys. **6**, p. 336 (2010). 7
- [38] J. KAMMhubER, M. C. CASSIDY, F. PEI, M. P. NOWAK, A. VUIK, Ö. GÜL, D. CAR, S. R. PLISSARD, E. P. A. M. BAKKERS, M. WIMMER & L. P. KOUWENHOVEN ; «Conductance through a helical state in an Indium antimonide nanowire» ; Nat. Commun. **8**, p. 478 (2017). 7
- [39] C. L. KANE & E. J. MELE ; «Quantum spin Hall effect in graphene» ; Phys. Rev. Lett. **95**, p. 226 801 (2005). 7
- [40] B. A. BERNEVIG, T. L. HUGHES & S.-C. ZHANG ; «Quantum spin Hall effect and topological phase transition in HgTe quantum wells» ; Science **314**, p. 1757–1761 (2006). 8
- [41] M. KÖNIG, S. WIEDMANN, C. BRÜNE, A. ROTH, H. BUHMANN, L. W. MOLENKAMP, X.-L. QI & S.-C. ZHANG ; «Quantum spin hall insulator state in HgTe quantum wells» ; Science **318**, p. 766–770 (2007). 8
- [42] I. KNEZ, R.-R. DU & G. SULLIVAN ; «Evidence for helical edge modes in inverted InAs/GaSb quantum wells» ; Phys. Rev. Lett. **107**, p. 136 603 (2011). 8
- [43] L. FU, C. L. KANE & E. J. MELE ; «Topological insulators in three dimensions» ; Phys. Rev. Lett. **98**, p. 106 803 (2007). 8
- [44] L. FU & C. L. KANE ; «Topological insulators with inversion symmetry» ; Phys. Rev. B Condens. Matter **76**, p. 045 302 (2007). 8
- [45] X.-L. QI & S.-C. ZHANG ; «Topological insulators and superconductors» ; Rev. Mod. Phys. **83**, p. 1057–1110 (2011). 8
- [46] H. ZHANG, C.-X. LIU & S.-C. ZHANG ; «Spin-orbital texture in topological insulators» ; Phys. Rev. Lett. **111**, p. 066 801 (2013). 8
- [47] H. ZHANG, C.-X. LIU, X.-L. QI, X. DAI, Z. FANG & S.-C. ZHANG ; «Topological insulators in Bi<sub>2</sub>Se<sub>3</sub>, Bi<sub>2</sub>Te<sub>3</sub> and Sb<sub>2</sub>Te<sub>3</sub> with a single Dirac cone on the surface» ; Nat. Phys. **5**, p. 438 (2009). 9, 75, 89
- [48] K. HE, Y. ZHANG, K. HE, C.-Z. CHANG, C.-L. SONG, L.-L. WANG, X. CHEN, J.-F. JIA, Z. FANG, X. DAI, W.-Y. SHAN, S.-Q. SHEN, Q. NIU, X.-L. QI, S.-C. ZHANG, X.-C. MA & Q.-K. XUE ; «Crossover of the three-dimensional topological insulator Bi<sub>2</sub>Se<sub>3</sub> to the two-dimensional limit» ; Nat. Phys. **6**, p. 584–588 (2010). 9, 75
- [49] F. VIDAL, M. EDDRIEF, B. RACHE SALLES, I. VOBORNIK, E. VELEZ-FORT, G. PANACCIONE & M. MARANGOLO ; «Photon energy dependence of circular dichroism in angle-resolved photoemission spectroscopy of Bi<sub>2</sub>Se<sub>3</sub> Dirac states» ; Phys. Rev. B Condens. Matter **88**, p. 241 410 (2013). 9, 42, 89
- [50] M. TINKHAM ; *Introduction to Superconductivity* (Courier Corporation) (1996). 9, 16, 19, 26, 62, 88, 93

- [51] A. V. DMITRIEV & W. NOLTING ; «On details of the thermodynamical derivation of the Ginsburg–Landau equations» ; (2003) [cond-mat/0312094](#). 10
- [52] J. BARDEEN, L. N. COOPER & J. R. SCHRIEFFER ; «Theory of Superconductivity» ; Phys. Rev. **108**, p. 1175–1204 (1957). 12
- [53] P. G. DE GENNES ; *Superconductivity Of Metals And Alloys* (CRC Press) (2018). 14
- [54] G. E. BLONDER, M. TINKHAM & T. M. KLAPWIJK ; «Transition from metallic to tunneling regimes in superconducting microconstrictions : Excess current, charge imbalance, and supercurrent conversion» ; Phys. Rev. B Condens. Matter **25**, p. 4515–4532 (1982). 16
- [55] S. DATTA ; *Electronic Transport in Mesoscopic Systems* (Cambridge University Press) (1997). 17
- [56] C. W. BEENAKKER ; «Universal limit of critical-current fluctuations in mesoscopic Josephson junctions» ; Phys. Rev. Lett. **67**, p. 3836–3839 (1991). 17, 19
- [57] C. W. J. BEENAKKER ; «Random-matrix theory of quantum transport» ; Rev. Mod. Phys. **69**, p. 731–808 (1997). 17
- [58] L. BRETHERAU, Ç. Ö. GIRIT, H. POTHIER, D. ESTEVE & C. URBINA ; «Exciting Andreev pairs in a superconducting atomic contact» ; Nature **499**, p. 312–315 (2013). 18
- [59] D. J. VAN WOERKOM, A. PROUTSKI, B. VAN HECK, D. BOUMAN, J. I. VÄYRYNEN, L. I. GLAZMAN, P. KROGSTRUP, J. NYGÅRD, L. P. KOUWENHOVEN & A. GERESDI ; «Microwave spectroscopy of spinful Andreev bound states in ballistic semiconductor Josephson junctions» ; Nat. Phys. **13**, p. 876 (2017). 18
- [60] H. VAN HOUTEN & C. W. J. BEENAKKER ; «Andreev reflection and the Josephson effect in a quantum point contact : An analogy with phase-conjugating resonators» ; Physica B Condens. Matter **175**, p. 187–197 (1991). 19
- [61] J. J. A. BASELMANS, A. F. MORPURGO, B. J. VAN WEES & T. M. KLAPWIJK ; «Reversing the direction of the supercurrent in a controllable Josephson junction» ; Nature **397**, p. 43 (1999). 20, 105
- [62] T. YOKOYAMA, M. ETO & Y. V. NAZAROV ; «Josephson Current through Semiconductor Nanowire with Spin–Orbit Interaction in Magnetic Field» ; J. Phys. Soc. Jpn. **82**, p. 054703 (2013). 20
- [63] S. HART, H. REN, M. KOSOWSKY, G. BEN-SHACH, P. LEUBNER, C. BRÜNE, H. BUHMANN, L. W. MOLENKAMP, B. I. HALPERIN & A. YACOBY ; «Controlled finite momentum pairing and spatially varying order parameter in proximitized HgTe quantum wells» ; Nat. Phys. **13**, p. 87 (2016). 20, 78
- [64] C. LI, J. C. DE BOER, B. DE RONDE, S. V. RAMANKUTTY, E. VAN HEUMEN, Y. HUANG, A. DE VISSER, A. A. GOLUBOV, M. S. GOLDEN &

- A. BRINKMAN; « $4\pi$  periodic Andreev bound states in a Dirac semimetal»; (2017) [Preprint at <http://arxiv.org/abs/1707.03154>](http://arxiv.org/abs/1707.03154). 20
- [65] A. I. BUZDIN; «Proximity effects in superconductor-ferromagnet heterostructures»; *Rev. Mod. Phys.* **77**, p. 935–976 (2005). 21, 26, 27
- [66] T. KONTOS, M. APRILI, J. LESUEUR, F. GENËT, B. STEPHANIDIS & R. BOURSIER; «Josephson junction through a thin ferromagnetic layer : negative coupling»; *Phys. Rev. Lett.* **89**, p. 137 007 (2002). 21
- [67] E. A. DEMLER, G. B. ARNOLD & M. R. BEASLEY; «Superconducting proximity effects in magnetic metals»; *Phys. Rev. B Condens. Matter* **55**, p. 15 174–15 182 (1997). 21
- [68] T. MENG, S. FLORENS & P. SIMON; «Self-consistent description of Andreev bound states in Josephson quantum dot devices»; *Phys. Rev. B Condens. Matter* **79**, p. 224 521 (2009). 21, 23, 24, 63, 65
- [69] A. MARTÍN-RODERO & A. LEVY YEYATI; «Josephson and Andreev transport through quantum dots»; *Adv. Phys.* **60**, p. 899–958 (2011). 22, 24, 63, 67
- [70] J.-D. PILLET, C. H. L. QUAY, P. MORFIN, C. BENA, A. L. YEYATI & P. JOYEZ; «Andreev bound states in supercurrent-carrying carbon nanotubes revealed»; *Nat. Phys.* **6**, p. 965 (2010). 22, 65, 67, 68
- [71] R. MAURAND, T. MENG, E. BONET, S. FLORENS, L. MARTY & W. WERNSDORFER; «First-Order -Quantum Phase Transition in the Kondo Regime of a Superconducting Carbon-Nanotube Quantum Dot»; *Phys. Rev. X* **2**, p. 011 009 (2012). 22, 65, 69, 70
- [72] J.-D. PILLET, P. JOYEZ, R. ŽITKO & M. F. GOFFMAN; «Tunneling spectroscopy of a single quantum dot coupled to a superconductor : From Kondo ridge to Andreev bound states»; *Phys. Rev. B Condens. Matter* **88**, p. 045 101 (2013). 22, 67, 68
- [73] E. VECINO, A. MARTÍN-RODERO & A. L. YEYATI; «Josephson current through a correlated quantum level : Andreev states and junction behavior»; *Phys. Rev. B Condens. Matter* **68**, p. 035 105 (2003). 22, 23
- [74] L. I. GLAZMAN & K. A. MATVEEV; «Resonant Josephson current through Kondo impurities in a tunnel barrier»; *JETP Lett.* **49** (1989). 22
- [75] J. A. VAN DAM, Y. V. NAZAROV, E. P. A. M. BAKKERS, S. DE FRANCESCHI & L. P. KOUWENHOVEN; «Supercurrent reversal in quantum dots»; *Nature* **442**, p. 667–670 (2006). 22, 49, 67, 69
- [76] A. V. BALATSKY, I. VEKHTER & J.-X. ZHU; «Impurity-induced states in conventional and unconventional superconductors»; *Rev. Mod. Phys.* **78**, p. 373–433 (2006). 25, 65
- [77] G. C. MÉNARD, S. GUISSART, C. BRUN, S. PONS, V. S. STOLYAROV, F. DEBONTRIDDER, M. V. LECLERC, E. JANOD, L. CARIO, D. RODITCHEV, P. SIMON

- & T. CREN ; «Coherent long-range magnetic bound states in a superconductor» ; Nat. Phys. **11**, p. 1013 (2015). 25, 65
- [78] V. BRAUDE & Y. V. NAZAROV ; «Fully developed triplet proximity effect» ; Phys. Rev. Lett. **98**, p. 077 003 (2007). 25
- [79] K. SHEN, G. VIGNALE & R. RAIMONDI ; «Microscopic theory of the inverse Edelstein effect» ; Phys. Rev. Lett. **112**, p. 096 601 (2014). 27
- [80] F. KONSCHELLE, I. V. TOKATLY & F. S. BERGERET ; «Theory of the spin-galvanic effect and the anomalous phase shift  $\phi_0$  in superconductors and Josephson junctions with intrinsic spin-orbit coupling» ; Phys. Rev. B Condens. Matter **92**, p. 125 443 (2015). 27, 100
- [81] O. V. DIMITROVA & M. V. FEIGEL'MAN ; «Two-dimensional S-N-S junction with Rashba spin-orbit coupling» ; J. Exp. Theor. Phys. **102**, p. 652–660 (2006). 27, 28
- [82] B. BÉRI, J. H. BARDARSON & C. W. J. BEENAKKER ; «Splitting of Andreev levels in a Josephson junction by spin-orbit coupling» ; Phys. Rev. B Condens. Matter **77**, p. 045 311 (2008). 27
- [83] T. YOKOYAMA, M. ETO & Y. V. NAZAROV ; «Anomalous Josephson effect induced by spin-orbit interaction and Zeeman effect in semiconductor nanowires» ; Phys. Rev. B Condens. Matter **89**, p. 195 407 (2014). 28
- [84] M. TCHERNYCHEVA, L. TRAVERS, G. PATRIARCHE, F. GLAS, J.-C. HARMAND, G. E. CIRLIN & V. G. DUBROVSKII ; «Au-assisted molecular beam epitaxy of InAs nanowires : Growth and theoretical analysis» ; J. Appl. Phys. **102**, p. 094 313 (2007). 35
- [85] V. G. DUBROVSKII, G. E. CIRLIN, N. V. SIBIREV, F. JABEEN, J. C. HARMAND & P. WERNER ; «New mode of vapor-liquid-solid nanowire growth» ; Nano Lett. **11**, p. 1247–1253 (2011). 35
- [86] M. KJAERGAARD, F. NICHELE, H. J. SUOMINEN, M. P. NOWAK, M. WIMMER, A. R. AKHMEROV, J. A. FOLK, K. FLENSBERG, J. SHABANI, C. J. PALMSTRØM & C. M. MARCUS ; «Quantized conductance doubling and hard gap in a two-dimensional semiconductor-superconductor heterostructure» ; Nat. Commun. **7**, p. 12 841 (2016). 36
- [87] K. MOMMA & F. IZUMI ; «VESTA3 for three-dimensional visualization of crystal, volumetric and morphology data» ; J. Appl. Crystallogr. **44**, p. 1272–1276 (2011). 37, 41, 43
- [88] M. DE LUCA, G. LAVENUTA, A. POLIMENI, S. RUBINI, V. GRILLO, F. MURA, A. MIRIAMETRO, M. CAPIZZI & F. MARTELLI ; «Excitonic recombination and absorption in  $\text{In}_x\text{Ga}_{1-x}\text{As}/\text{GaAs}$  heterostructure nanowires» ; Phys. Rev. B Condens. Matter **87**, p. 235 304 (2013). 36
- [89] M. B. ROTA, A. S. AMERUDDIN, H. A. FONSEKA, Q. GAO, F. MURA, A. POLIMENI, A. MIRIAMETRO, H. H. TAN, C. JAGADISH & M. CAPIZZI ; «Bandgap Energy of Wurtzite InAs Nanowires» ; Nano Lett. **16**, p. 5197–5203 (2016). 36

- [90] M. HJORT, S. LEHMANN, J. KNUTSSON, A. A. ZAKHAROV, Y. A. DU, S. SAKONG, R. TIMM, G. NYLUND, E. LUNDGREN, P. KRATZER, K. A. DICK & A. MIKKELSEN; «Electronic and structural differences between wurtzite and zinc blende InAs nanowire surfaces : experiment and theory»; ACS Nano **8**, p. 12 346–12 355 (2014). 36
- [91] T. CAMPOS, P. E. FARIA JUNIOR, M. GMITRA, G. M. SIPAHI & J. FABIAN; «Spin-orbit coupling effects in zinc-blende InSb and wurtzite InAs nanowires : Realistic calculations with multiband kp method»; Phys. Rev. B Condens. Matter **97**, p. 245 402 (2018). 36
- [92] M. SCHEFFLER, S. NADJ-PERGE, L. P. KOUWENHOVEN, M. T. BORGSTRÖM & E. P. A. M. BAKKERS; «Diameter-dependent conductance of InAs nanowires»; J. Appl. Phys. **106**, p. 124 303 (2009). 38, 61
- [93] W. J. MIR, A. ASSOULINE, C. LIVACHE, B. MARTINEZ, N. GOUBET, X. Z. XU, G. PATRIARCHE, S. ITHURRIA, H. AUBIN & E. LHUILLIER; «Electronic properties of (Sb;Bi)<sub>2</sub>Te<sub>3</sub> colloidal heterostructured nanoplates down to the single particle level»; Sci. Rep. **7**, p. 9647 (2017). 41
- [94] C.-X. LIU, X.-L. QI, H. ZHANG, X. DAI, Z. FANG & S.-C. ZHANG; «Model Hamiltonian for topological insulators»; Phys. Rev. B Condens. Matter **82**, p. 045 122 (2010). 42
- [95] D. PRESS, T. D. LADD, B. ZHANG & Y. YAMAMOTO; «Complete quantum control of a single quantum dot spin using ultrafast optical pulses»; Nature **456**, p. 218–221 (2008). 49
- [96] S. M. CRONENWETT, T. H. OOSTERKAMP & L. P. KOUWENHOVEN; «A tunable kondo effect in quantum dots»; Science **281**, p. 540–544 (1998). 49
- [97] D. GOLDHABER-GORDON, H. SHTRIKMAN, D. MAHALU, D. ABUSCH-MAGDER, U. MEIRAV & M. A. KASTNER; «Kondo effect in a single-electron transistor»; Nature **391**, p. 156 (1998). 49
- [98] J.-P. CLEUZIQU, W. WERNSDORFER, V. BOUCHIAT, T. ONDARÇUHU & M. MONTHIOUX; «Carbon nanotube superconducting quantum interference device»; Nat. Nanotechnol. **1**, p. 53–59 (2006). 49, 67, 69
- [99] A. ALTLAND & M. R. ZIRNBAUER; «Random matrix theory of a chaotic Andreev quantum dot»; Phys. Rev. Lett. **76**, p. 3420–3423 (1996). 49
- [100] A. YU KITAEV; «Unpaired Majorana fermions in quantum wires»; Phys.-Usp. **44**, p. 131 (2007). 49, 67, 76, 89
- [101] J. D. SAU & S. D. SARMA; «Realizing a robust practical Majorana chain in a quantum-dot-superconductor linear array»; Nat. Commun. **3**, p. 964 (2012). 49
- [102] I. C. FULGA, A. HAIM, A. R. AKHMEROV & Y. OREG; «Adaptive tuning of Majorana fermions in a quantum dot chain»; New J. Phys. **15**, p. 045 020 (2013). 49

- [103] A. ASSOULINE, C. FEUILLET-PALMA, A. ZIMMERS, H. AUBIN, M. APRILI & J.-C. HARMAND ; «Shiba Bound States across the Mobility Edge in Doped InAs Nanowires» ; Phys. Rev. Lett. **119**, p. 097 701 (2017). 49
- [104] Y. V. NAZAROV & Y. M. BLANTER ; *Quantum Transport : Introduction to Nanoscience* (Cambridge University Press) (2009). 52
- [105] S. CSONKA, L. HOFSTETTER, F. FREITAG, S. OBERHOLZER, C. SCHÖNENBERGER, T. S. JESPERSEN, M. AAGESEN & J. NYGÅRD ; «Giant fluctuations and gate control of the g-factor in InAs nanowire quantum dots» ; Nano Lett. **8**, p. 3932–3935 (2008). 57
- [106] L. P. KOUWENHOVEN, D. G. AUSTING & S. TARUCHA ; «Few-electron quantum dots» ; Rep. Prog. Phys. **64**, p. 701 (2001). 57
- [107] Y. ALHASSID, P. JACQUOD & A. WOBST ; «Random matrix model for quantum dots with interactions and the conductance peak spacing distribution» ; Phys. Rev. B Condens. Matter **61**, p. R13 357–R13 360 (2000). 57, 58, 59, 61
- [108] E. P. WIGNER ; «On the statistical distribution of the widths and spacings of nuclear resonance levels» ; Math. Proc. Cambridge Philos. Soc. **47**, p. 790–798 (1951). 57
- [109] F. J. DYSON ; «The Threefold Way. Algebraic Structure of Symmetry Groups and Ensembles in Quantum Mechanics» ; J. Math. Phys. **3**, p. 1199–1215 (1962). 57
- [110] C. W. J. BEENAKKER ; «Random-matrix theory of Majorana fermions and topological superconductors» ; Rev. Mod. Phys. **87**, p. 1037–1066 (2015). 57
- [111] M. VYAS & T. H. SELIGMAN ; «Random Matrix Ensembles For Many-Body Quantum Systems» ; (2017)1710.07712. 58
- [112] T. GUHR, A. MÜLLER-GROELING & H. A. WEIDENMÜLLER ; «Random-matrix theories in quantum physics : common concepts» ; Phys. Rep. **299**, p. 189–425 (1998). 58, 59
- [113] J. GRAMICH, A. BAUMGARTNER & C. SCHÖNENBERGER ; «Resonant and Inelastic Andreev Tunneling Observed on a Carbon Nanotube Quantum Dot» ; Phys. Rev. Lett. **115**, p. 216 801 (2015). 61
- [114] P. W. ANDERSON ; «Absence of Diffusion in Certain Random Lattices» ; Phys. Rev. **109**, p. 1492–1505 (1958). 61
- [115] A. C. FORD, J. C. HO, Y.-L. CHUEH, Y.-C. TSENG, Z. FAN, J. GUO, J. BOKOR & A. JAVEY ; «Diameter-dependent electron mobility of InAs nanowires» ; Nano Lett. **9**, p. 360–365 (2009). 61
- [116] I. GIAEVER ; «Energy Gap in Superconductors Measured by Electron Tunneling» ; Phys. Rev. Lett. **5**, p. 147–148 (1960). 62
- [117] W. CHANG, S. M. ALBRECHT, T. S. JESPERSEN, F. KUEMMETH, P. KROGSTROP, J. NYGÅRD & C. M. MARCUS ; «Hard gap in epitaxial semiconductor-superconductor nanowires» ; Nat. Nanotechnol. **10**, p. 232–236 (2015). 62, 70

- [118] K. FLENSBERG, J. B. HANSEN & M. OCTAVIO ; «Subharmonic energy-gap structure in superconducting weak links» ; Phys. Rev. B Condens. Matter **38**, p. 8707–8711 (1988). 62
- [119] A. L. YEYATI, J. C. CUEVAS, A. LÓPEZ-DÁVALOS & A. MARTÍN-RODERO ; «Resonant tunneling through a small quantum dot coupled to superconducting leads» ; Phys. Rev. B Condens. Matter **55**, p. R6137–R6140 (1997). 62
- [120] E. SCHEER, N. AGRAÏT, J. C. CUEVAS, A. L. YEYATI, B. LUDOPH, A. MARTÍN-RODERO, G. R. BOLLINGER, J. M. VAN RUITENBEEK & C. URBINA ; «The signature of chemical valence in the electrical conduction through a single-atom contact» ; Nature **394**, p. 154 (1998). 62
- [121] T. SAND-JESPERSEN, J. PAASKE, B. M. ANDERSEN, K. GROVE-RASMUSSEN, H. I. JØRGENSEN, M. AAGESEN, C. B. SØRENSEN, P. E. LINDELOF, K. FLENSBERG & J. NYGÅRD ; «Kondo-enhanced Andreev tunneling in InAs nanowire quantum dots» ; Phys. Rev. Lett. **99**, p. 126 603 (2007). 62
- [122] S. LI, N. KANG, P. CAROFF & H. Q. XU ; «-» ; Phys. Rev. B Condens. Matter **95**, p. 014 515 (2017). 62
- [123] A. EICHLER, M. WEISS, S. OBERHOLZER, C. SCHÖNENBERGER, A. LEVY YEYATI, J. C. CUEVAS & A. MARTÍN-RODERO ; «Even-odd effect in Andreev transport through a carbon nanotube quantum dot» ; Phys. Rev. Lett. **99**, p. 126 602 (2007). 62
- [124] L. A. JAUREGUI, M. KAYYALHA, A. KAZAKOV, I. MIOTKOWSKI, L. P. ROHKINSON & Y. P. CHEN ; «Gate-tunable supercurrent and multiple Andreev reflections in a superconductor-topological insulator nanoribbon-superconductor hybrid device» ; Appl. Phys. Lett. **112**, p. 093 105 (2018). 62, 67
- [125] K. J. FRANKE, G. SCHULZE & J. I. PASCUAL ; «Competition of superconducting phenomena and Kondo screening at the nanoscale» ; Science **332**, p. 940–944 (2011). 65
- [126] E. J. H. LEE, X. JIANG, M. HOUZET, R. AGUADO, C. M. LIEBER & S. DE FRANCESCHI ; «Spin-resolved Andreev levels and parity crossings in hybrid superconductor-semiconductor nanostructures» ; Nat. Nanotechnol. **9**, p. 79–84 (2014). 65, 68, 69
- [127] W. CHANG, V. E. MANUCHARYAN, T. S. JESPERSEN, J. NYGÅRD & C. M. MARCUS ; «Tunneling spectroscopy of quasiparticle bound states in a spinful Josephson junction» ; Phys. Rev. Lett. **110**, p. 217 005 (2013). 65, 67, 68
- [128] S. DE FRANCESCHI, L. KOUWENHOVEN, C. SCHÖNENBERGER & W. WERNSDORFER ; «Hybrid superconductor-quantum dot devices» ; Nat. Nanotechnol. **5**, p. 703–711 (2010). 65, 67
- [129] H. ZHANG, C.-X. LIU, S. GAZIBEGOVIC, D. XU, J. A. LOGAN, G. WANG, N. VAN LOO, J. D. S. BOMMER, M. W. A. DE MOOR, D. CAR, R. L. M. OP HET VELD, P. J. VAN VELDHoven, S. KOELLING, M. A. VERHEIJEN, M. PENDHARKAR,

- D. J. PENNACHIO, B. SHOJAEI, J. S. LEE, C. J. PALMSTRØM, E. P. A. M. BAKKERS, S. D. SARMA & L. P. KOUWENHOVEN; «Quantized Majorana conductance»; *Nature* **556**, p. 74–79 (2018). 67
- [130] Y. KANAI, R. S. DEACON, A. OIWA, K. YOSHIDA, K. SHIBATA, K. HIRAKAWA & S. TARUCHA; «Electrical control of Kondo effect and superconducting transport in a side-gated InAs quantum dot Josephson junction»; *Phys. Rev. B Condens. Matter* **82**, p. 054512 (2010). 68
- [131] E. J. H. LEE, X. JIANG, R. AGUADO, G. KATSAROS, C. M. LIEBER & S. DE FRANCESCHI; «Zero-bias anomaly in a nanowire quantum dot coupled to superconductors»; *Phys. Rev. Lett.* **109**, p. 186802 (2012). 68
- [132] B.-K. KIM, Y.-H. AHN, J.-J. KIM, M.-S. CHOI, M.-H. BAE, K. KANG, J. S. LIM, R. LÓPEZ & N. KIM; «Transport measurement of Andreev bound states in a Kondo-correlated quantum dot»; *Phys. Rev. Lett.* **110**, p. 076803 (2013). 68
- [133] T. DIRKS, T. L. HUGHES, S. LAL, B. UCHOA, Y.-F. CHEN, C. CHIALVO, P. M. GOLDBART & N. MASON; «Transport through Andreev bound states in a graphene quantum dot»; *Nat. Phys.* **7**, p. 386 (2011). 69
- [134] L. HOFSTETTER, S. CSONKA, J. NYGÅRD & C. SCHÖNENBERGER; «Cooper pair splitter realized in a two-quantum-dot Y-junction»; *Nature* **461**, p. 960–963 (2009). 69
- [135] L. G. HERRMANN, F. PORTIER, P. ROCHE, A. L. YEYATI, T. KONTOS & C. STRUNK; «Carbon nanotubes as cooper-pair beam splitters»; *Phys. Rev. Lett.* **104**, p. 026801 (2010). 69
- [136] L. HOFSTETTER, S. CSONKA, A. BAUMGARTNER, G. FÜLÖP, S. D’HOLLOSY, J. NYGÅRD & C. SCHÖNENBERGER; «Finite-bias Cooper pair splitting»; *Phys. Rev. Lett.* **107**, p. 136801 (2011). 69
- [137] J. SCHINDELE, A. BAUMGARTNER & C. SCHÖNENBERGER; «Near-unity Cooper pair splitting efficiency»; *Phys. Rev. Lett.* **109**, p. 157002 (2012). 69
- [138] A. DAS, Y. RONEN, M. HEIBLUM, D. MAHALU, A. V. KRETININ & H. SHTRIKMAN; «High-efficiency Cooper pair splitting demonstrated by two-particle conductance resonance and positive noise cross-correlation»; *Nat. Commun.* **3**, p. 1165 (2012). 69
- [139] G. FÜLÖP, F. DOMÍNGUEZ, S. D’HOLLOSY, A. BAUMGARTNER, P. MAKK, M. H. MADSEN, V. A. GUZENKO, J. NYGÅRD, C. SCHÖNENBERGER, A. LEVY YEYATI & S. CSONKA; «Magnetic Field Tuning and Quantum Interference in a Cooper Pair Splitter»; *Phys. Rev. Lett.* **115**, p. 227003 (2015). 69
- [140] Z. B. TAN, D. COX, T. NIEMINEN, P. LÄHTEENMÄKI, D. GOLUBEV, G. B. LESOVIK & P. J. HAKONEN; «Cooper pair splitting by means of graphene quantum dots»; *Phys. Rev. Lett.* **114**, p. 096602 (2015). 69

- [141] S. BABA, C. JÜNGER, S. MATSUO, A. BAUMGARTNER, Y. SATO, H. KAMATA, K. LI, S. JEPPESEN, L. SAMUELSON, H. Q. XU, C. SCHÖNENBERGER & S. TARUCHA ; «Cooper-pair splitting in two parallel InAs nanowires» ; *New J. Phys.* **20**, p. 063 021 (2018). [69](#)
- [142] P. RECHER, E. V. SUKHORUKOV & D. LOSS ; «Andreev tunneling, Coulomb blockade, and resonant transport of nonlocal spin-entangled electrons» ; *Phys. Rev. B Condens. Matter* **63**, p. 165 314 (2001). [69](#)
- [143] R. S. DEACON, A. OIWA, J. SAILER, S. BABA, Y. KANAI, K. SHIBATA, K. HIRAKAWA & S. TARUCHA ; «Cooper pair splitting in parallel quantum dot Josephson junctions» ; *Nat. Commun.* **6**, p. 7446 (2015). [69](#)
- [144] S. VLAIC, S. PONS, T. ZHANG, A. ASSOULINE, A. ZIMMERS, C. DAVID, G. RODARY, J.-C. GIRARD, D. RODITCHEV & H. AUBIN ; «Superconducting parity effect across the Anderson limit» ; *Nat. Commun.* **8**, p. 14 549 (2017). [70](#)
- [145] T. ZHANG, S. VLAIC, S. PONS, A. ASSOULINE, A. ZIMMERS, D. RODITCHEV, H. AUBIN, G. ALLAN, C. DELERUE, C. DAVID, G. RODARY & J.-C. GIRARD ; «Quantum confinement effects in Pb nanocrystals grown on InAs» ; *Phys. Rev. B Condens. Matter* **97**, p. 214 514 (2018). [70](#)
- [146] S. M. ALBRECHT, A. P. HIGGINBOTHAM, M. MADSEN, F. KUEMMETH, T. S. JESPERSEN, J. NYGÅRD, P. KROGSTRUP & C. M. MARCUS ; «Exponential protection of zero modes in Majorana islands» ; *Nature* **531**, p. 206–209 (2016). [70](#), [71](#)
- [147] D. B. SZOMBATI, S. NADJ-PERGE, D. CAR, S. R. PLISSARD, E. P. A. M. BAKKERS & L. P. KOUWENHOVEN ; «Josephson 0-junction in nanowire quantum dots» ; *Nat. Phys.* **12**, p. 568 (2016). [71](#), [72](#), [73](#)
- [148] A. ZAZUNOV, R. EGGER, T. JONCKHEERE & T. MARTIN ; «Anomalous Josephson current through a spin-orbit coupled quantum dot» ; *Phys. Rev. Lett.* **103**, p. 147 004 (2009). [71](#)
- [149] A. ASSOULINE, C. FEUILLET-PALMA, N. BERGEAL, T. ZHANG, A. MOTTAGHIZADEH, A. ZIMMERS, E. LHUILLIER, M. MARANGOLO, M. EDDRIEF, P. ATKINSON, M. APRILI & H. AUBIN ; «Spin-Orbit induced phase-shift in Bi<sub>2</sub>Se<sub>3</sub> Josephson junctions» ; (2018)[1806.01406](#). [75](#)
- [150] L. FU & C. L. KANE ; «Superconducting proximity effect and majorana fermions at the surface of a topological insulator» ; *Phys. Rev. Lett.* **100**, p. 096 407 (2008). [75](#), [87](#)
- [151] A. Y. KITAEV ; «Fault-tolerant quantum computation by anyons» ; *Ann. Phys.* **303**, p. 2–30 (2003). [75](#)
- [152] D. HSIEH, Y. XIA, D. QIAN, L. WRAY, F. MEIER, J. H. DIL, J. OSTERWALDER, L. PATTHEY, A. V. FEDOROV, H. LIN, A. BANSIL, D. GRAUER, Y. S. HOR, R. J. CAVA & M. Z. HASAN ; «Observation of time-reversal-protected single-dirac-cone topological-insulator states in Bi<sub>2</sub>Te<sub>3</sub> and Sb<sub>2</sub>Te<sub>3</sub>» ; *Phys. Rev. Lett.* **103**, p. 146 401 (2009). [75](#)

- [153] Z.-H. ZHU, G. LEVY, B. LUDBROOK, C. N. VEENSTRA, J. A. ROSEN, R. COMIN, D. WONG, P. DOSANJH, A. UBALDINI, P. SYERS, N. P. BUTCH, J. PAGLIONE, I. S. ELFIMOV & A. DAMASCELLI; «Rashba spin-splitting control at the surface of the topological insulator Bi<sub>2</sub>Se<sub>3</sub>»; *Phys. Rev. Lett.* **107**, p. 186 405 (2011). [75](#), [79](#), [103](#)
- [154] D. KIM, S. CHO, N. P. BUTCH, P. SYERS, K. KIRSHENBAUM, S. ADAM, J. PAGLIONE & M. S. FUHRER; «Surface conduction of topological Dirac electrons in bulk insulating Bi<sub>2</sub>Se<sub>3</sub>»; *Nat. Phys.* **8**, p. 459 (2012). [76](#)
- [155] B. SACÉPÉ, J. B. OOSTINGA, J. LI, A. UBALDINI, N. J. G. COUTO, E. GIANNINI & A. F. MORPURGO; «Gate-tuned normal and superconducting transport at the surface of a topological insulator»; *Nat. Commun.* **2**, p. 575 (2011). [76](#)
- [156] J. R. WILLIAMS, A. J. BESTWICK, P. GALLAGHER, S. S. HONG, Y. CUI, A. S. BLEICH, J. G. ANALYTIS, I. R. FISHER & D. GOLDBABER-GORDON; «Unconventional Josephson effect in hybrid superconductor-topological insulator devices»; *Phys. Rev. Lett.* **109**, p. 056 803 (2012). [76](#), [86](#), [87](#)
- [157] S. CHO, B. DELLABETTA, A. YANG, J. SCHNEELOCH, Z. XU, T. VALLA, G. GU, M. J. GILBERT & N. MASON; «Symmetry protected Josephson supercurrents in three-dimensional topological insulators»; *Nat. Commun.* **4**, p. 1689 (2013). [76](#)
- [158] L. GALLETTI, S. CHARPENTIER, M. IAVARONE, P. LUCIGNANO, D. MASSAROTTI, R. ARPAIA, Y. SUZUKI, K. KADOWAKI, T. BAUCH, A. TAGLIACOZZO, F. TAFURI & F. LOMBARDI; «Influence of topological edge states on the properties of AlBi<sub>2</sub>Se<sub>3</sub>Al hybrid Josephson devices»; *Phys. Rev. B Condens. Matter* **89**, p. 134 512 (2014). [76](#), [84](#)
- [159] C. KURTER, A. D. K. FINCK, P. GHAEMI, Y. S. HOR & D. J. VAN HARLINGEN; «Dynamical gate-tunable supercurrents in topological Josephson junctions»; *Phys. Rev. B Condens. Matter* **90**, p. 014 501 (2014). [76](#), [88](#)
- [160] C. KURTER, A. D. K. FINCK, Y. S. HOR & D. J. VAN HARLINGEN; «Evidence for an anomalous current-phase relation in topological insulator Josephson junctions»; *Nat. Commun.* **6**, p. 7130 (2015). [76](#), [88](#)
- [161] M. SNELDER, M. VELDHORST, A. A. GOLUBOV & A. BRINKMAN; «Andreev bound states and current-phase relations in three-dimensional topological insulators»; *Phys. Rev. B Condens. Matter* **87**, p. 104 507 (2013). [76](#), [89](#)
- [162] H.-J. KWON, K. SENGUPTA & V. M. YAKOVENKO; «Fractional ac Josephson effect in p- and d-wave superconductors»; *The European Physical Journal B - Condensed Matter and Complex Systems* **37**, p. 349–361 (2004). [76](#), [89](#)
- [163] L. FU & C. L. KANE; «Josephson current and noise at a superconductor/quantum-spin-Hall-insulator/superconductor junction»; *Phys. Rev. B Condens. Matter* **79**, p. 161 408 (2009). [76](#), [89](#)
- [164] K. LE CALVEZ, L. VEYRAT, F. GAY, P. PLAINDOUX, C. WINKELMANN, H. COURTOIS & B. SACÉPÉ; «Joule overheating poisons the fractional ac

- Josephson effect in topological Josephson junctions»; (2018) [Preprint at http://arxiv.org/abs/1803.07674](http://arxiv.org/abs/1803.07674). 76, 91, 109
- [165] L. P. ROKHINSON, X. LIU & J. K. FURDYNA; «The fractional a.c. Josephson effect in a semiconductor–superconductor nanowire as a signature of Majorana particles»; *Nat. Phys.* **8**, p. 795 (2012). 76, 89
- [166] J. WIEDENMANN, E. BOCQUILLON, R. S. DEACON, S. HARTINGER, O. HERRMANN, T. M. KLAPWIJK, L. MAIER, C. AMES, C. BRÜNE, C. GOULD, A. OIWA, K. ISHIBASHI, S. TARUCHA, H. BUHMANN & L. W. MOLENKAMP; « $4\pi$ -periodic Josephson supercurrent in HgTe-based topological Josephson junctions»; *Nat. Commun.* **7**, p. 10303 (2016). 76, 89, 109
- [167] E. BOCQUILLON, R. S. DEACON, J. WIEDENMANN, P. LEUBNER, T. M. KLAPWIJK, C. BRÜNE, K. ISHIBASHI, H. BUHMANN & L. W. MOLENKAMP; «Gapless Andreev bound states in the quantum spin Hall insulator HgTe»; *Nat. Nanotechnol.* **12**, p. 137–143 (2017). 76, 77, 89, 109
- [168] C. LI, J. C. DE BOER, B. DE RONDE, S. V. RAMANKUTTY, E. VAN HEUMEN, Y. HUANG, A. DE VISSER, A. A. GOLUBOV, M. S. GOLDEN & A. BRINKMAN; « $4\pi$ -periodic Andreev bound states in a Dirac semimetal»; *Nat. Mater.* **17**, p. 875–880 (2018). 76, 78, 89
- [169] H. B. HEERSCHE, P. JARILLO-HERRERO, J. B. OOSTINGA, L. M. K. VANDERSYPEN & A. F. MORPURGO; «Bipolar supercurrent in graphene»; *Nature* **446**, p. 56–59 (2007). 76
- [170] D. JEONG, J.-H. CHOI, G.-H. LEE, S. JO, Y.-J. DOH & H.-J. LEE; «Observation of supercurrent in PbIn-graphene-PbIn Josephson junction»; *Phys. Rev. B Condens. Matter* **83**, p. 094503 (2011). 76
- [171] V. E. CALADO, S. GOSWAMI, G. NANDA, M. DIEZ, A. R. AKHMEROV, K. WATANABE, T. TANIGUCHI, T. M. KLAPWIJK & L. M. K. VANDERSYPEN; «Ballistic Josephson junctions in edge-contacted graphene»; *Nat. Nanotechnol.* **10**, p. 761–764 (2015). 76
- [172] J. PARK, J. H. LEE, G.-H. LEE, Y. TAKANE, K.-I. IMURA, T. TANIGUCHI, K. WATANABE & H.-J. LEE; «Short Ballistic Josephson Coupling in Planar Graphene Junctions with Inhomogeneous Carrier Doping»; *Phys. Rev. Lett.* **120**, p. 077701 (2018). 76
- [173] S. HART, H. REN, T. WAGNER, P. LEUBNER, M. MÜHLBAUER, C. BRÜNE, H. BUHMANN, L. W. MOLENKAMP & A. YACOBY; «Induced superconductivity in the quantum spin Hall edge»; *Nat. Phys.* **10**, p. 638 (2014). 76, 86
- [174] V. S. PRIBIAG, A. J. A. BEUKMAN, F. QU, M. C. CASSIDY, C. CHARPENTIER, W. WEGSCHEIDER & L. P. KOUWENHOVEN; «Edge-mode superconductivity in a two-dimensional topological insulator»; *Nat. Nanotechnol.* **10**, p. 593–597 (2015). 76, 86, 109
- [175] A. MURANI, A. KASUMOV, S. SENGUPTA, Y. A. KASUMOV, V. T. VOLKOV, I. I. KHODOS, F. BRISSET, R. DELAGRANGE, A. CHEPELIANSKII, R. DEBLOCK,

- H. BOUCHIAT & S. GUÉRON; «Ballistic edge states in Bismuth nanowires revealed by SQUID interferometry»; *Nat. Commun.* **8**, p. 15 941 (2017). 76, 91
- [176] F. AMET, C. T. KE, I. V. BORZENETS, J. WANG, K. WATANABE, T. TANIGUCHI, R. S. DEACON, M. YAMAMOTO, Y. BOMZE, S. TARUCHA & G. FINKELSTEIN; «Supercurrent in the quantum Hall regime»; *Science* **352**, p. 966–969 (2016). 76, 86
- [177] F. K. DE VRIES, T. TIMMERMAN, V. P. OSTROUKH, J. VAN VEEN, A. J. A. BEUKMAN, F. QU, M. WIMMER, B.-M. NGUYEN, A. A. KISELEV, W. YI, M. SOKOLICH, M. J. MANFRA, C. M. MARCUS & L. P. KOUWENHOVEN; «h/e Superconducting Quantum Interference through Trivial Edge States in InAs»; *Phys. Rev. Lett.* **120**, p. 047 702 (2018). 76, 86, 97
- [178] R. S. DEACON, J. WIEDENMANN, E. BOCQUILLON, F. DOMÍNGUEZ, T. M. KLAPWIJK, P. LEUBNER, C. BRÜNE, E. M. HANKIEWICZ, S. TARUCHA, K. ISHIBASHI, H. BUHMANN & L. W. MOLENKAMP; «Josephson Radiation from Gapless Andreev Bound States in HgTe-Based Topological Junctions»; *Phys. Rev. X* **7**, p. 021 011 (2017). 76
- [179] J. B. OOSTINGA, L. MAIER, P. SCHÜFFELGEN, D. KNOTT, C. AMES, C. BRÜNE, G. TKACHOV, H. BUHMANN & L. W. MOLENKAMP; «Josephson Supercurrent through the Topological Surface States of Strained Bulk HgTe»; *Phys. Rev. X* **3**, p. 021 007 (2013). 76
- [180] W. LIU, X. PENG, C. TANG, L. SUN, K. ZHANG & J. ZHONG; «Anisotropic interactions and strain-induced topological phase transition in  $\text{Sb}_2\text{Se}_3$  and  $\text{Bi}_2\text{Se}_3$ »; *Phys. Rev. B Condens. Matter* **84**, p. 245 105 (2011). 76
- [181] Y. LIU, Y. Y. LI, S. RAJPUT, D. GILKS, L. LARI, P. L. GALINDO, M. WEINERT, V. K. LAZAROV & L. LI; «Tuning Dirac states by strain in the topological insulator  $\text{Bi}_2\text{Se}_3$ »; *Nat. Phys.* **10**, p. 294 (2014). 76
- [182] S. CHARPENTIER, L. GALLETTI, G. KUNAKOVA, R. ARPAIA, Y. SONG, R. BAGHDADI, S. M. WANG, A. KALABOUKHOV, E. OLSSON, F. TAFURI, D. GOLUBEV, J. LINDER, T. BAUCH & F. LOMBARDI; «Induced unconventional superconductivity on the surface states of  $\text{Bi}_2\text{Te}_3$  topological insulator»; *Nat. Commun.* **8**, p. 2019 (2017). 76, 77
- [183] M. WEIDES, M. KEMMLER, H. KOHLSTEDT, R. WASER, D. KOELLE, R. KLEINER & E. GOLDOBIN; «0- $\pi$  Josephson tunnel junctions with ferromagnetic barrier»; *Phys. Rev. Lett.* **97**, p. 247 001 (2006). 76
- [184] S. M. FROLOV, D. J. VAN HARLINGEN, V. V. BOLGINOV, V. A. OBOZNOV & V. V. RYAZANOV; «Josephson interferometry and Shapiro step measurements of superconductor-ferromagnet-superconductor -junctions»; *Phys. Rev. B Condens. Matter* **74**, p. 020 503 (2006). 76
- [185] D. J. VAN HARLINGEN; «Phase-sensitive tests of the symmetry of the pairing state in the high-temperature superconductors—Evidence for  $d_x^2-y^2$  symmetry»; *Rev. Mod. Phys.* **67**, p. 515–535 (1995). 77

- [186] M. VELDHORST, M. SNELDER, M. HOEK, T. GANG, V. K. GUDURU, X. L. WANG, U. ZEITLER, W. G. VAN DER WIEL, A. A. GOLUBOV, H. HILGENKAMP & A. BRINKMAN ; «Josephson supercurrent through a topological insulator surface state» ; Nat. Mater. **11**, p. 417–421 (2012). 77
- [187] C. G. MOLENAAR, D. P. LEUSINK, X. L. WANG & A. BRINKMAN ; «Geometric dependence of Nb-Bi<sub>2</sub>Te<sub>3</sub>-Nb topological Josephson junction transport parameters» ; Supercond. Sci. Technol. **27**, p. 104 003 (2014). 77, 86
- [188] W. YU, W. PAN, D. L. MEDLIN, M. A. RODRIGUEZ, S. R. LEE, Z.-Q. BAO & F. ZHANG ; « $\pi$  and  $4\pi$  Josephson Effects Mediated by a Dirac Semimetal» ; Phys. Rev. Lett. **120**, p. 177 704 (2018). 77
- [189] M. ESCHRIG ; «Spin-polarized supercurrents for spintronics : a review of current progress» ; Rep. Prog. Phys. **78**, p. 104 501 (2015). 77
- [190] J. LINDER & J. W. A. ROBINSON ; «Superconducting spintronics» ; Nat. Phys. **11**, p. 307 (2015). 77
- [191] A. Q. CHEN, M. J. PARK, S. T. GILL, Y. XIAO, G. J. MACDOUGALL, M. J. GILBERT & N. MASON ; «Finite momentum Cooper pairing in 3D topological insulator Josephson junctions» ; (2018)1801.08504. 78
- [192] H. J. SUOMINEN, J. DANON, M. KJAERGAARD, K. FLENSBERG, J. SHABANI, C. J. PALMSTRØM, F. NICHELE & C. M. MARCUS ; «Anomalous Fraunhofer interference in epitaxial superconductor-semiconductor Josephson junctions» ; Phys. Rev. B Condens. Matter **95**, p. 035 307 (2017). 78, 79, 95
- [193] G. R. HYDE, R. O. DILLON, H. A. BEALE, I. L. SPAIN, J. A. WOOLLAM & D. J. SELLMYER ; «Shubnikov-de Haas effects in Bi<sub>2</sub>Se<sub>3</sub> with high carrier concentrations» ; Solid State Commun. **13**, p. 257–263 (1973). 81, 99
- [194] A. BARONE & G. PATERNO ; *Physics and applications of the Josephson effect* ; authoriz. facs., new york [u.a.] wiley, 1982 édition (Wiley, New York) (1981). 84, 87, 91, 98
- [195] B.-K. KIM, H.-S. KIM, Y. YANG, X. PENG, D. YU & Y.-J. DOH ; «Strong Superconducting Proximity Effects in PbS Semiconductor Nanowires» ; ACS Nano **11**, p. 221–226 (2017). 86, 87
- [196] P. F. VOHRALIK & S. K. H. LAM ; «NanoSQUID detection of magnetization from ferritin nanoparticles» ; Supercond. Sci. Technol. **22**, p. 064 007 (2009). 87
- [197] C. SPÅNSLÄTT, E. ARDONNE, J. C. BUDICH & T. H. HANSSON ; «Topological aspects of  $\pi$  phase winding junctions in superconducting wires» ; J. Phys. Condens. Matter **27**, p. 405 701 (2015). 88
- [198] M. L. DELLA ROCCA, M. CHAUVIN, B. HUARD, H. POTHIER, D. ESTEVE & C. URBINA ; «Measurement of the current-phase relation of superconducting atomic contacts» ; Phys. Rev. Lett. **99**, p. 127 005 (2007). 91
- [199] I. SOCHNIKOV, L. MAIER, C. A. WATSON, J. R. KIRTLEY, C. GOULD, G. TKA-CHOV, E. M. HANKIEWICZ, C. BRÜNE, H. BUHMANN, L. W. MOLENKAMP &

- K. A. MOLER; «Nonsinusoidal current-phase relationship in Josephson junctions from the 3D topological insulator HgTe»; *Phys. Rev. Lett.* **114**, p. 066 801 (2015). 91
- [200] E. M. SPANTON, M. DENG, S. VAITIEKĖNAS, P. KROGSTRUP, J. NYGÅRD, C. M. MARCUS & K. A. MOLER; «Current-phase relations of few-mode InAs nanowire Josephson junctions»; *Nat. Phys.* **13**, p. 1177 (2017). 91
- [201] A. A. GOLUBOV, M. Y. KUPRIYANOV & E. IL'ICHEV; «The current-phase relation in Josephson junctions»; *Rev. Mod. Phys.* **76**, p. 411–469 (2004). 91
- [202] R. MESERVEY & P. M. TEDROW; «Properties of Very Thin Aluminum Films»; *J. Appl. Phys.* **42**, p. 51–53 (1971). 93
- [203] J. CLARKE; «THE PROXIMITY EFFECT BETWEEN SUPERCONDUCTING AND NORMAL THIN FILMS IN ZERO FIELD»; *Le Journal de Physique Colloques* **29**, p. C2–3–C2–16 (1968). 93
- [204] N. R. WERTHAMER; «Theory of the Superconducting Transition Temperature and Energy Gap Function of Superposed Metal Films»; *Phys. Rev.* **132**, p. 2440–2445 (1963). 94
- [205] L. LOLLI, E. TARALLI, C. PORTESI, M. RAJTERI & E. MONTICONE; «Aluminum-Titanium Bilayer for Near-Infrared Transition Edge Sensors»; *Sensors* **16** (2016). 94
- [206] A. RASMUSSEN, J. DANON, H. SUOMINEN, F. NICHELE, M. KJAERGAARD & K. FLENSBERG; «Effects of spin-orbit coupling and spatial symmetries on the Josephson current in SNS junctions»; *Phys. Rev. B Condens. Matter* **93**, p. 155 406 (2016). 95, 96, 103, 105
- [207] Y. ZHANG, K. HE, C.-Z. CHANG, C.-L. SONG, L.-L. WANG, X. CHEN, J.-F. JIA, Z. FANG, X. DAI, W.-Y. SHAN, S.-Q. SHEN, Q. NIU, X.-L. QI, S.-C. ZHANG, X.-C. MA & Q.-K. XUE; «Crossover of the three-dimensional topological insulator Bi<sub>2</sub>Se<sub>3</sub> to the two-dimensional limit»; *Nat. Phys.* **6**, p. 584 (2010). 99
- [208] F. S. BERGERET & I. V. TOKATLY; «Theory of diffusive  $\varphi_0$  Josephson junctions in the presence of spin-orbit coupling»; *EPL* **110**, p. 57 005 (2015). 99
- [209] Y. ANDO & M. SHIRAISHI; «Spin to Charge Interconversion Phenomena in the Interface and Surface States»; *J. Phys. Soc. Jpn.* **86**, p. 011 001 (2016). 105
- [210] A. F. MORPURGO, T. M. KLAPWIJK & B. J. VAN WEES; «Hot electron tunable supercurrent»; *Appl. Phys. Lett.* **72**, p. 966–968 (1998). 105
- [211] F. YANG, S. GHATAK, A. A. TASKIN, K. SEGAWA, Y. ANDO, M. SHIRAISHI, Y. KANAI, K. MATSUMOTO, A. ROSCH & Y. ANDO; «Switching of charge-current-induced spin polarization in the topological insulator BiSbTeSe<sub>2</sub>»; *Phys. Rev. B Condens. Matter* **94**, p. 075 304 (2016). 106
- [212] C. H. LI, O. M. J. VAN 'T ERVE, J. T. ROBINSON, Y. LIU, L. LI & B. T. JONKER; «Electrical detection of charge-current-induced spin polarization due

- to spin-momentum locking in Bi<sub>2</sub>Se<sub>3</sub>»; *Nat. Nanotechnol.* **9**, p. 218–224 (2014). 106
- [213] A. R. MELLNIK, J. S. LEE, A. RICARDELLA, J. L. GRAB, P. J. MINTUN, M. H. FISCHER, A. VAEZI, A. MANCHON, E.-A. KIM, N. SAMARTH & D. C. RALPH; «Spin-transfer torque generated by a topological insulator»; *Nature* **511**, p. 449–451 (2014). 106
- [214] F. GIAZOTTO, T. T. HEIKKILÄ, A. LUUKANEN, A. M. SAVIN & J. P. PEKOLA; «Opportunities for mesoscopics in thermometry and refrigeration : Physics and applications»; *Rev. Mod. Phys.* **78**, p. 217–274 (2006). 107
- [215] A. PALACIOS-LALOY, F. NGUYEN, F. MALLET, P. BERTET, D. VION & D. ESTEVE; «Tunable Resonators for Quantum Circuits»; *J. Low Temp. Phys.* **151**, p. 1034–1042 (2008). 108
- [216] T. ORTLEPP, ARIANDO, O. MIELKE, C. J. M. VERWIJS, K. F. K. FOO, H. ROGALLA, F. H. UHLMANN & H. HILGENKAMP; «Flip-flopping fractional flux quanta»; *Science* **312**, p. 1495–1497 (2006). 109
- [217] A. K. FEOFANOV, V. A. OBOZNOV, V. V. BOL'GINOV, J. LISENFELD, S. POLETTO, V. V. RYAZANOV, A. N. ROSSOLENKO, M. KHABIPOV, D. BALASHOV, A. B. ZORIN, P. N. DMITRIEV, V. P. KOSHELETS & A. V. USTINOV; «Implementation of superconductor/ferromagnet/ superconductor  $\pi$ -shifters in superconducting digital and quantum circuits»; *Nat. Phys.* **6**, p. 593 (2010). 109
- [218] A. ROTH, C. BRÜNE, H. BUHMANN, L. W. MOLENKAMP, J. MACIEJKO, X.-L. QI & S.-C. ZHANG; «Nonlocal transport in the quantum spin Hall state»; *Science* **325**, p. 294–297 (2009). 109
- [219] R. L. KALLAHER, J. J. HEREMANS, W. VAN ROY & G. BORGHES; «Spin and phase coherence lengths in InAs wires with diffusive boundary scattering»; *Phys. Rev. B Condens. Matter* **88**, p. 205407 (2013). 109
- [220] F. DOLCINI, M. HOUZET & J. S. MEYER; «Topological Josephson  $\pi$  junctions»; *Phys. Rev. B Condens. Matter* **92**, p. 035428 (2015). 109
- [221] J. LUO, H. MUNEKATA, F. F. FANG & P. J. STILES; «Effects of inversion asymmetry on electron energy band structures in GaSb/InAs/GaSb quantum wells»; *Phys. Rev. B Condens. Matter* **41**, p. 7685–7693 (1990). 109
- [222] M. SCHULTZ, F. HEINRICHS, U. MERKT, T. COLIN, T. SKAULI & S. LØVOLD; «Rashba spin splitting in a gated HgTe quantum well»; *Semicond. Sci. Technol.* **11**, p. 1168 (1999). 109



---

## Sujet : Transport d'Andreev dans des boîtes quantiques et effet Josephson dans des couches minces à fort couplage spin-orbite

---

**Résumé :** Les jonctions Josephson sont les briques de base des circuits supraconducteurs. Elles sont constituées de deux supraconducteurs séparés par une barrière isolante. Dans cette thèse, nous présentons deux expériences où la barrière isolante est remplacée par un semi-conducteur. Dans la première, nous étudions des nanofils dans le régime du blocage de Coulomb, où le nombre d'électrons peut être contrôlé, un par un, jusqu'à induire une transition entre un régime métallique et un régime isolant. A travers cette transition, nous avons observé qu'un spin électronique se comporte comme une impureté magnétique et donne lieu à la formation d'états électroniques discrets entre les électrodes supraconductrices. La compréhension de ces dispositifs est essentielle pour le développement de la nanoélectronique à base de supraconducteur.

Dans la seconde expérience, nous étudions l'effet Josephson dans des couches minces où le mouvement des électrons dépend de leur orientation de spin. Ce couplage spin-orbite est essentiel dans un grand nombre de travaux théoriques visant à découvrir des nouvelles phases de la matière. Nous démontrons par cette expérience que le couplage spin-orbite peut être sondé par des mesures sensibles à la différence de phase entre les électrodes supraconductrices qui forment la jonction Josephson.

**Mots clés :** Josephson, Andreev, Boîtes quantiques, Spin-orbite, Supraconducteurs, Semi-conducteurs, Nanofils, InAs, Couches minces,  $\text{Bi}_2\text{Se}_3$

---

## Subject : Andreev transport in quantum dots and Josephson effect in spin-orbit coupled thin films

---

**Abstract:** Josephson junctions are the building blocks of superconducting electronics. They are made of two superconductors separated by an insulating barrier. In this thesis, we present two experiments where the insulating barrier is replaced by a semiconductor.

In the first one, we study nanowires in the regime of Coulomb blockade, where the number of electrons can be controlled, one by one, until a metal-insulator transition is induced. Across this transition, we observed that a single electronic spin behaves like a magnetic impurity and leads to the formation of discrete electronic states between the superconducting electrodes. The understanding of such devices is crucial for the development of superconducting nanoelectronics. In the second experiment, we study the Josephson effect in thin films where the electron motion is coupled to its spin. This spin-orbit interaction is essential in a wide number of theoretical works aiming at discover new phases of matter. We demonstrate that spin-orbit coupling can be probed by phase sensitive measurements of the Josephson current.

**Keywords :** Josephson, Andreev, Quantum dots, Spin-orbit, Superconductors, Semiconductors, Nanowires, InAs, Thin films,  $\text{Bi}_2\text{Se}_3$